Radio Science Bulletin

ISSN 1024-4530

INTERNATIONAL
UNION OF
RADIO SCIENCE

UNION
RADIO-SCIENTIFIQUE
INTERNATIONALE

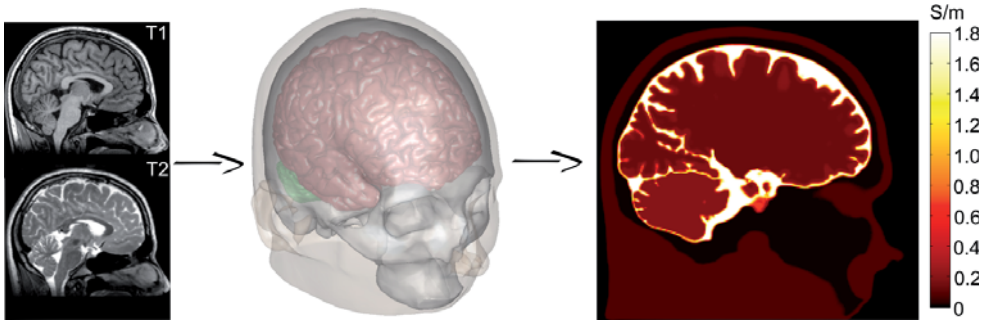

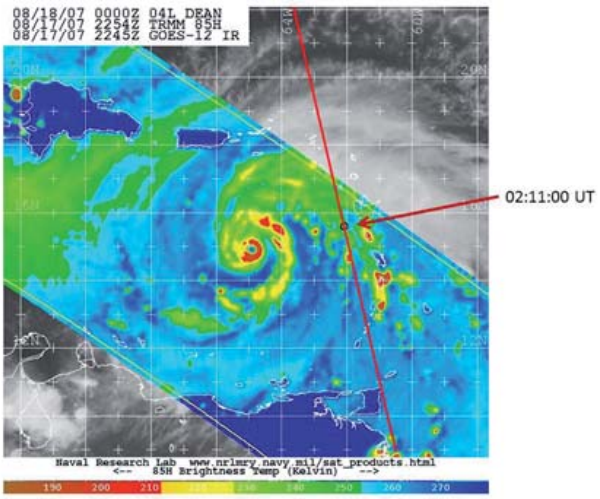

No 360
March 2017

URSI, c/o Ghent University (INTEC)
St.-Pietersnieuwstraat 41, B-9000 Gent (Belgium)

Contents

Cover: (Upper figure) The steps used to create the volume conductor models used for the paper. The MRI data were first segmented, and then the surfaces obtained were used to voxelize the segmented model. See the paper by Marko Mikkonen and Ilkka Laakso in the special section on "The Best Papers from the EMTS 2016 Young Scientist Awards", pp. 13-18.

(Lower figure) Passive microwave imagery from the NASA TRMM satellite, depicting the eyewall replacement cycle in Hurricane Dean on August 17, 2007, at 2254 UTC. All images are from the 85 GHz channel, in which ice scattering reveals areas of deep convection displayed in the red shades (image courtesy of the Naval Research Laboratory, NRL). See the paper by Michel Parrot in the special section on "Radio Science for Humanity: URSI-France 2017 Workshop", pp. 75-79.

The International Union of Radio Science (URSI) is a foundation Union (1919) of the International Council of Scientific Unions as direct and immediate successor of the Commission Internationale de Télégraphie Sans Fil which dates from 1914.

Radio Science Bulletin Staff

Editor

W. R. Stone
Stoneware Limited
840 Armada Terrace
San Diego, CA 92106, USA
Tel: +1-619 222 1915, Fax: +1-619 222 1606
E-mail: r.stone@ieee.org

Editor-in-Chief

P. Lagasse
URSI Secretariat
Ghent University - INTEC
Technologiepark - Zwijnaarde 15
B-9052 Gent, BELGIUM
Tel: +32 9-264 33 20, Fax: +32 9-264 42 88
E-mail: lagasse@intec.ugent.be

Production Editors

I. Lievens
I. Heleu
URSI Secretariat / Ghent University - INTEC
Technologiepark - Zwijnaarde 15
B-9052 Gent, BELGIUM
Tel: +32 9-264.33.20, Fax: +32 9-264.42.88
E-mail: ingeursi@intec.ugent.be, info@ursi.org

Senior Associate Editors

A. Pellinen-Wannberg
Department of Physics
Umea University
BOX 812
SE-90187 Umea, SWEDEN
Tel: +46 90 786 74 92, Fax: +46 90 786 66 76
E-mail: asta.pellinen-wannberg@umu.se

O. Santolik
Institute of Atmospheric Physics
Academy of Sciences of the Czech Republic
Bocni II
1401, 141 31 Prague 4, CZECH REPUBLIC
Tel: +420 267 103 083, Fax +420 272 762 528
E-mail os@ufa.cas.cz, santolik@gmail.com

Associate Editors, Commissions

Commission A

P. Tavella
INRIM
Strada delle Cacce 91
10135 Torino, ITALY
Tel: +39 011 3919235, Fax: +39 011 3919259
E-mail: tavella@inrim.it

P. M. Duarte Cruz
Instituto de Telecomunicações
Campus Universitário de Santiago
P-3810-193 Aveiro, PORTUGAL
Tel: +351 234377900
E-mail: pcruz@av.it.pt

Commission B

K. Kobayashi
Dept. of Electrical, and Communication Engineering
Chuo University
1-13-27 Kasuga, Bunkyo-ku
Tokyo, 112-8551, JAPAN
Tel: +81 3 3817 1846/69, Fax: +81 3 3817 1847
E-mail: kazuya@tamacc.chuo-u.ac.jp

L. Li
School of EECS
Peking University
Room 2843N, Science Building#2
Beijing 100871, CHINA CIE
Tel: +86-10-62754409-2 , Fax: +86-10-62754409
E-mail: lianlin.li@pku.edu.cn

Commission C

S. E. El-Khamy
Dept. of Electrical Engineering
Alexandria University - Faculty of Engineering
Abou-Keer Street
Alexandria 21544, EGYPT
Tel: +2010-1497360, Fax: +203 5971853
E-mail: elkhamy@ieee.org, said.elkhamy@gmail.com

A. I. Zaghloul
Ece, Virginia Tech
7054 Haycock Rd
22043 Falls Church, USA
Tel: +1-703-538-8435, Fax: +1-703-538-8450
E-mail: amirz@vt.edu

Commission D

G. Gradoni
School of Mathematical Sciences
University of Nottingham
University Park
Nottingham NG7 2RD, UNITED KINGDOM
Tel: +44(0)7745368300, Fax: +44(0)1159514951
E-mail: gabriele.gradoni@gmail.com, gabriele.gradoni@nottingham.ac.uk

Commission E

F. Gronwald
Hamburg University of Technology
Harburger Schloss Strasse 20
21079 Hamburg, GERMANY
Tel: +49-40-42878-2177
E-mail: gronwald@tuhh.de

G. Gradoni
School of Mathematical Sciences
University of Nottingham
University Park
Nottingham NG7 2RD, UNITED KINGDOM
Tel: +44(0)7745368300, Fax: +44(0)1159514951
E-mail: gabriele.gradoni@gmail.com, gabriele.gradoni@nottingham.ac.uk

Commission F

V. Chandrasekar
Engineering B117
Colorado State University
Fort Collins, Colorado 80523 , USA
Tel: +1 970 491 7981, Fax: +1 970 491 2249
E-mail: chandra@engr.colostate.edu, chandra.ve@gmail.com

M. Kurum
Department of Electrical and Computer Engineering
Mississippi State University
406 Hardy Rd., Simrall Bldg., Room: 236
Mississippi State, MS 39762, USA
Tel: +1 662 325 2148
E-mail: kurum@ece.msstate.edu, mkurum@gmail.com

Commission G

P. Doherty
Institute for Scientific Research
Boston College
140 Commonwealth Avenue
Chestnut Hill, MA 02467, USA
Tel: +1 617 552 8767, Fax: +1 617 552 2818
E-mail: Patricia.Doherty@bc.edu

Commission H

J. Lichtenberger
Eötvös University
Pazmany Peter Setany 1/a
H-1111 Budeapest
HUNGARY
Tel: +36 1 209 0555 x6654, Fax +36 1 372 2927
E-mail lityi@sas.elte.hu

W. Li
UCLA
7127 Math Sciences Bldg
405 Hilgard Avenue
Los Angeles, CA, 90095, USA
E-mail: moonli@atmos.ucla.edu

Commission J

J. W. M. Baars
Mm-astronomy
Max Planck Institute for Radio Astronomy
Auf dem Hügel 69
53121 Bonn, GERMANY
Tel: +49-228-525303
E-mail: jacobbaars@arcor.de

Commission K

P. Mojabi
Room E3-504B, EITC Building
Electrical and Computer Engineering Department
University of Manitoba
Winnipeg, R3T5V6, CANADA
Tel: +1 204 474 6754 , Fax: +1 204 261 4639
E-mail: Puyan.Mojabi@umanitoba.ca

Associate Editors, Columns

Book Reviews

G. Trichopoulos
Electrical, Computer & Energy Engineering ISTB4 555D
Arizona State University
781 E Terrace Road, Tempe, AZ, 85287 USA
Tel: +1 (614) 364-2090
E-mail: gtrichop@asu.edu

Historical Papers

J. D. Mathews
Communications and Space Sciences Lab (CSSL)
The Pennsylvania State University
323A, EE East
University Park, PA 16802-2707, USA
Tel: +1(814) 777-5875, Fax: +1 814 863 8457
E-mail: JDMathews@psu.edu

Et Cetera

T. Akgül
Dept. of Electronics and Communications Engineering
Telecommunications Division
Istanbul Technical University
80626 Maslak Istanbul, TURKEY
Tel: +90 212 285 3605, Fax: +90 212 285 3565
E-mail: tayfunakgul@itu.edu.tr.

Women in Radio Science

A. Pellinen-Wannberg
Department of Physics and Swedish Institute of Space Physics
Umeå University
S-90187 Umeå, Sweden
Tel: +46 90 786 7492
E-mail: asta.pellinen-wannberg@umu.se

Ethically Speaking

R. L. Haupt
Colorado School of Mines
Brown Building 249
1510 Illinois Street, Golden, CO 80401 USA
Tel: +1 (303) 273 3721
E-mail: rhaupt@mines.edu

A. J. Shockley
E-mail: aj4317@gmail.com

Solution Box

Ö. Ergül
Department of Electrical and Electronics Engineering
Middle East Technical University
TR-06800, Ankara, Turkey
E-mail: ozgur.ergul@eee.metu.edu.tr

Telecommunications Health & Safety

J. C. Lin
University of Illinois at Chicago
851 South Morgan Street, M/C 154
Chicago, IL 60607-7053 USA
Tel: +1 312 413 1052, Fax: +1 312 996 6465
E-mail: lin@uic.edu

Historical Column

G. Pelosi
Department of Information Engineering
University of Florence
Via di S. Marta, 3, 50139 Florence, Italy
E-mail: giuseppe.pelosi@unifi.it

Early Career Representative Column

S. J. Wijnholds
Netherlands Institute for Radio Astronomy
Oude Hoogeveensedijk 4
7991 PD Dwingeloo, The Netherlands
E-mail: wijnholds@astron.nl

URSI Officers and Secretariat

Current Officers triennium 2014-2017

President

P. S. Cannon
Gisbert Kapp Building
University of Birmingham
Edgbaston , Birmingham, B15 2TT,
UNITED KINGDOM
Tel: +44 (0) 7990 564772
Fax: +44 (0)121 414 4323
E-mail: p.cannon@bham.ac.uk
president@ursi.org

Vice President

M. Ando
Dept. of Electrical & Electronic Eng.
Graduate School of Science and Eng.
Tokyo Institute of Technology
S3-19, 2-12-1 O-okayama, Meguro
Tokyo 152-8552
JAPAN
Tel: +81 3 5734-2563
Fax: +81 3 5734-2901
E-mail: mando@antenna.ee.titech.ac.jp

Past President

P. Wilkinson
Bureau of Meteorology
P.O. Box 1386
Haymarket, NSW 1240
AUSTRALIA
Tel: +61 2-9213 8003
Fax: +61 2-9213 8060
E-mail: p.wilkinson@bom.gov.au

Vice President

Y. M. M. Antar
Electrical Engineering Department
Royal Military College
POB 17000, Station Forces
Kingston, ON K7K 7B4
CANADA
Tel: +1-613 541-6000 ext.6403
Fax: +1-613 544-8107
E-mail: antar-y@rmc.ca

Secretary General

P. Lagasse
URSI Secretariat
Ghent University - INTEC
Technologiepark - Zwijnaarde 15
B-9052 Gent
BELGIUM
Tel: +32 9-264 33 20
Fax: +32 9-264 42 88
E-mail: lagasse@intec.ugent.be

Vice President

U. S. Inan
Director, STAR Laboratory
Electrical Eng. Dept
Stanford University
Packard Bldg. Rm. 355
350 Serra Mall
Stanford, CA 94305, USA
Tel: +1-650 723-4994
Fax: +1-650 723-9251
E-mail: inan@stanford.edu
uinan@ku.edu.tr

Vice President

S. Ananthakrishnan
Electronic Science Department
Pune University
Ganeshkhind, Pune 411007
INDIA
Tel: +91 20 2569 9841
Fax: +91 20 6521 4552
E-mail: subra.anan@gmail.com

URSI Secretariat

Secretary General

P. Lagasse
URSI Secretariat
Ghent University - INTEC
Technologiepark - Zwijnaarde 15
B-9052 Gent
BELGIUM
Tel: +32 9-264 33 20
Fax: +32 9-264 42 88
E-mail: lagasse@intec.ugent.be

Assistant Secretary General AP-RASC

K. Kobayashi
Dept. of Electr and Commun. Eng,
Chuo University
1-13-27 Kasuga, Bunkyo-ku
Tokyo, 112-8551
JAPAN
Tel: +81 3 3817 1846/69
Fax: +81 3 3817 1847

Assistant Secretary General

P. Van Daele
INTEC- IBBT
Ghent University
Technologiepark - Zwijnaarde 15
B-9052 Gent
BELGIUM
Tel: +32 9 331 49 06
Fax +32 9 331 48 99
E-mail peter.vandaele@intec.Ugent.be

Executive Secretary

I. Heleu
URSI Secretariat
Ghent University - INTEC
Technologiepark - Zwijnaarde 15
B-9052 Gent
BELGIUM
Tel. +32 9-264.33.20
Fax +32 9-264.42.88
E-mail info@ursi.org

Assistant Secretary General Publications & GASS

W. R. Stone
840 Armada Terrace
San Diego, CA 92106
USA
Tel: +1-619 222 1915
Fax: +1-619 222 1606
E-mail: r.stone@ieee.org

Administrative Secretary

I. Lievens
URSI Secretariat
Ghent University - INTEC
Technologiepark - Zwijnaarde 15
B-9052 Gent
BELGIUM
Tel: +32 9-264.33.20
Fax: +32 9-264.42.88
E-mail: ingeursi@intec.ugent.be

Assistant Secretary General AT-RASC

P. L. E. Uslenghi
Dept. of ECE (MC 154)
University of Illinois at Chicago 851
S. Morgan Street
Chicago, IL 60607-7053
USA
Tel: +1 312 996-6059
Fax: +1 312 996 8664
E-mail: uslenghi@uic.edu

Editor's Comments

W. Ross Stone
Stoneware Limited
840 Armada Terrace
San Diego, CA 92106, USA
Tel: +1-619 222 1915, Fax: +1-619 222 1606
E-mail: r.stone@ieee.org

The Radio Science Bulletin is on IEEE Xplore!

Beginning with this issue, current issues of the *URSI Radio Science Bulletin* and the archives back to September 2002 are available on IEEE Xplore. In fact, starting with the next (June) issue, the link you receive in your e-mail alert when the issue becomes available will point to the issue on Xplore. If you go to http://ieeexplore.ieee.org/Xplore/home.jsp, choose Browse...Journals and Magazines, and type in URSI, you will find the archives of the *Bulletin*. This (June) issue will be available on Xplore about one to two weeks after you receive the e-mail announcement of the issue. The contents of each issue are all available for downloading as PDFs. The current and past issues of the *Bulletin* are available on Xplore as a free, open-access publication: anyone can access it, without a subscription.

All of the material in the current and past issues of the *Bulletin* has been fully indexed on Xplore (and therefore, also by Google, which "crawls" Xplore). That means that anyone searching for a topic will find all of the material related to that topic that has appeared in any issue of the *Bulletin* back to September 2002. This will hopefully result in a substantial increase in the number of people reading the *Bulletin*, as well as an increase in the number of authors citing material that appears in the *Bulletin*.

The archives and current issues of the *Radio Science Bulletin* will still also be available on the URSI Web site, www.ursi.org, and it will still be possible to download a PDF of the complete issue from there.

Special thanks go to Inge Lievens of the URSI Secretariat; Michael Porch, Naveen Maddali, Ira Polans, Karen Hawkens, and John Baillieul of the IEEE; and the URSI Board for their efforts and support in making this happen. Yes, there were costs involved in converting the archives to go onto Xplore, and there will be costs associated with having the future issues of the *Bulletin* appear on Xplore. However, the costs are reasonable, and the Board feels that this is a good investment in our authors and the visibility of URSI.

This Issue and the URSI GASS

This issue is quite late. I'm sorry. The reason is because I have spent the time from the start of this year through August totally consumed with the organization of the XXXIInd URSI General Assembly and Scientific Symposium (GASS), held in Montreal, Canada, August 19-26. The GASS was a record-setting success by every measure, with about 1400 attendees, 1463 accepted papers, 56 countries represented, and an excellent program. Tremendous thanks go to Fabrice Labeau, Ahmed Kishk, Paul Cannon, Paul Lagasse, Peter Van Daele, and all of the members of the Organizing Committee, the Commission Chairs and Vice Chairs, and the session conveners, who worked so hard to make it such a success.

Our Two Special Sections

We have two special sections this time.

The first is a special section containing three invited papers by the recipients of the Young Scientist Best Paper Awards from the URSI Commission B International Symposium on Electromagnetic Theory (EMTS 2016) that was held at Espoo, Finland, August 14-18, 2016. The guest editors for this special section are Kazuya Kobayashi and Ari Sihvola, and their contributions are greatly appreciated. They describe the topics of the papers in their foreword to the special section.

The second special section is based on the URSI-France 2017 workshop, "Les radiosciences au service de l'humanité" (Radio Science for Humanity), held in February of this year. This special section is in two parts. The first part appears in this issue, and includes a report on the workshop

and three invited papers. The second part will appear in the next issue of the *Radio Science Bulletin*. The papers in this issue are again discussed in the foreword to the special issue, written by the guest editors, Tullio Tanzi and Joël Hamelin. Their contributions are also greatly appreciated.

Our Contributed Paper

Our contributed paper, by J. Gavan and M. Haridim, is both unusual and interesting. The authors consider the (admittedly somewhat speculative) possibility that hornets may use a biological equivalent of radar for detection, tracking, direction finding, and long-distance communication. It is noted that biological structures on the hornets may be capable of operating as a dielectric phased-array antenna. Using the measured characteristics, the authors perform an analysis of the possible operating frequencies and range of a hornet-based tracking radar. They also analyze the possibility of the use of these structures for communication and direction finding. The results are compared with available preliminary measurements. Although the measurements currently available can only partially confirm the hypotheses, the analyses do point the way for what additional measurements would enable more definitive confirmation. I think you will find this a fascinating article, and it will hopefully motivate some further research in this area.

Our Other Contributions

In the History Corner, Giuseppe Pelosi has brought us an article from Stefano Selleri. This describes the first telecommunication network, which operated *without* electricity.

Jacob Baars provides a review of an unusual new book on the history of radio astronomy in The Netherlands. It turns out the politics and the people were as interesting as the science.

In their Ethically Speaking column, Randy Haupt and Amy Shockley provide an insightful perspective on the processes of getting and giving directions. Of course, there are implications for ethics in radio science.

In his Solution Box, Özgür Ergül brings us a problem and one possible solution by Aşkın Altınoklu and Özgür Ergül to an optimization problem involving nanocubes at optical frequencies.

Jim Lin reviews recent developments in microwave sensing and monitoring for biological and medical applications in his column. He was inspired by what he observed at a recent International Microwave Symposium.

In her Women in Radio Science column, Asta Pellinen Wannberg has a contribution from Mariá Hajduková. It is not every issue that has an article from someone who is in a family where the father, mother, and daughter all have comets named after them.

URSI Awards

The URSI awards are presented every three years at the GASS. They are traditionally announced immediately before the GASS, in the June issue of the *Radio Science Bulletin*. Because we're running late, we've included them in this issue. These are the highest awards URSI gives. Take note of them: they are special.

Start Preparing Your Papers Now for AT-RASC 2018

URSI has a flagship meeting every year. The meeting in the year following the General Assembly and Scientific Symposium is the URSI Atlantic Radio Science Conference: AT-RASC. AT-RASC 2018 will be the second edition of this conference, and it will be held May 28-June 1, 2018, in the same venue as in 2015: the ExpoMeloneras Convention Centre, Gran Canaria, in the Canary Islands, Spain. This is an amazingly beautiful location for a conference, and it also has a very good conference facility. The deadline for paper submission is **January 10, 2018**. Details are available at the Web site: **www.at-rasc.org**. There is a program for young scientists and a student paper competition. I urge you to start planning now to attend.

Special Section: The Best Papers from the EMTS 2016 Young Scientist Awards

The URSI Commission B International Symposium on Electromagnetic Theory (EMTS 2016) was held on the campus of Aalto University, Espoo, Finland, during August 14-18, 2016 [1, 2]. This special section is a collection of papers by the recipients of the EMTS 2016 Young Scientist Best Paper Awards.

According to tradition, Commission B organized the Young Scientist (YS) program at EMTS 2016, which consisted of the Young Scientist Award (YSA) and the Young Scientist Best Paper Award. In order to review the Young Scientist applications, we formed the Young Scientist Program Committee (YSPC):

Kazuya Kobayashi, Japan (Chair)
Henrik Wallén, Finland (Secretary)
Pasi Ylä-Oijala, Finland (Secretary)
Ludger Klinkenbusch, Germany
Lianlin Li, China
Ismo Lindell, Finland
Giuliano Manara, Italy
Sembiam Rengarajan, USA
Yury Shestopalov, Sweden
Daniel Sjöberg, Sweden
Sergei Tretyakov, Finland
John Volakis, USA

The Young Scientist Program Committee selected 20 Young Scientist Award recipients from among 43 Young Scientist applicants before the conference. All the Young Scientist Award recipients were given free registration for the conference, free accommodations, and free tickets for the conference banquet. During the conference, all 20 Young Scientist Award recipients made presentations at a special Young Scientist poster session, in addition to presentations at regular sessions. The Young Scientist Program Committee further carefully reviewed presentations by the 20 Young Scientist Award recipients, and selected the three winners (first, second, and third prizes), and the two honorable-mention recipients, as follows:

First Prize: Simon B. Adrian, Technical University of Munich, Germany, and Télécom Bretange, France

Second Prize: Marko Mikkonen, Aalto University, Finland

Third Prize: Alberto Favaro, Imperial College, UK

Honorable Mention: Dmitry Valovik, Penza State University, Russia

Honorable Mention: Xiaoyan Xiong, the University of Hong Kong, Hong Kong

Figure 1. The EMTS 2016 officials and the recipients of the Young Scientist Best Paper Awards (r-l): Kazuya Kobayashi, Commission B Vice Chair; Xiaoyan Xiong, Honorable Mention; Marko Mikkonen, second prize; Simon B. Adrian, first prize; Dmitry Valovik, honorable mention; Alberto Favaro, third prize; Ari Sihvola, Commission B Chair.

The award ceremony for the Young Scientist Best Paper Award was held during the conference banquet on August 17. There, the first, second, and third prize winners received certificates with prizes of 1,000 Euros, 750 Euros, and 500 Euros, respectively. The two honorable-mention recipients received certificates. Figure 1 shows a group photo of the five recipients of the Young Scientist Best Paper Awards.

The following three invited papers by the recipients of the Young Scientist Best Paper Awards appear in this special section of the *Radio Science Bulletin*:

1. "Sub-Voxel Refinement Method for Tissue Boundary Conductivities in Volume Conductor Models"
   Marko Mikkonen and Ilkka Laakso, Aalto University, Finland

2. "How Kerr Nonlinearity Influences Polarized Electromagnetic Wave Propagation"
   Dmitry Valovik, Penza State University, Russia

3. "Sum-Frequency and Second-Harmonic Generation from Plasmonic Nonlinear Nanoantennas"
   Xiaoyan Y. Z. Xiong, Li Jun Jiang, Wei E. I. Sha, Yat Hei Lo, and Weng Cho Chew,
   The University of Hong Kong, Hong Kong; Weng Cho Chew is also with the University of Illinois at Urbana-Champaign, USA

We were happy that the Young Scientist Program at EMTS 2016 was a great success. This success was due to the constant efforts by the various committees, including the Commission B Technical Advisory Board (B-TAB), the Young Scientist Program Committee (YSPC), the Local Scientific Committee (together with a number of reviewers), and the Local Organizing Committee. We were indebted to all the members of these committees for their hard work. In addition, Congress Bureau Tavicon Ltd. did an outstanding job as the conference secretariat. Finally, we would like to express our appreciation to the recipients of the Young Scientist Best Paper Awards who contributed to this special section.

References

1. EMTS 2016 Web site, http://emts2016.org/

2. Ari Sihvola, "EMTS 2016 Conference in Espoo, Finland," *Radio Science Bulletin*, No. 359, December 2016, pp. 76-77.

Guest Editors:

Kazuya Kobayashi
Vice-Chair, URSI Commission B
Chuo University, Tokyo, Japan
E-mail: kazuya@tamacc.chuo-u.ac.jp

Ari Sihvola
Chair, URSI Commission B
Aalto University, Finland
E-mail: ari.sihvola@aalto.fi

Sub-Voxel Refinement Method for Tissue Boundary Conductivities in Volume Conductor Models

Marko Mikkonen and Ilkka Laakso

School of Electrical Engineering
Aalto University
Finland
E-mail: marko.mikkonen@aalto.fi

Abstract

The resolution and element type of the mesh used in the Finite-Element Method modeling of transcranial direct-current stimulation (tDCS) greatly affect both the accuracy of the solution and the computational time. Tetrahedral meshing is usually used in these models as it well approximates curvature, but the models are slow to solve. Using a voxel grid as the mesh significantly reduces the computational time, but the cubical elements are not the most suitable option for curved surfaces. Tissue boundaries can be modeled as a layer of voxels with an average conductivity of the surrounding tissues. However, as the boundary being modeled only rarely divides a voxel into two equally sized portions, this approach is often erroneous, and in particular, with low resolutions. In this paper, we propose a novel method for improving the accuracy of anatomically correct Finite-Element Method simulations by enhancing the tissue boundaries in voxel models. In our method, a voxel model is created from a set of polygonal surfaces segmented from magnetic-resonance imaging (MRI) data. This is done by first voxelizing with a fine resolution, and then increasing the voxel size to the target resolution, and calculating the ratio of fine voxels in and outside the surface within each coarse voxel. More-accurate proportions for the volume of a coarse voxel inside and outside the tissue boundary are thus achieved, and the tissue boundary's conductivity can be better approximated. To test the performance of this method, a series of simulations of motor cortical tDCS were performed using resolutions from 0.2 mm to 2 mm, scaled to zero, two, or four times finer resolution. Based on the results, the voxel size could be doubled with a cost of 3% in relative error by using our method. The model's degrees of freedom (DOF) could thus be decreased by 87%, and the simulation times could be decreased by 82%.

1. Introduction

Transcranial direct current stimulation is a noninvasive method for applying electric currents onto the brain via an intact scalp [1, 2]. These currents are capable of eliciting changes in the activity of the brain that outlast the stimulation. The modification of the brain's function can be taken advantage of in the treatment of psychiatric and neurological diseases [3], such as stroke recovery [4], depression [5], and chronic pain [3]. As a well-tolerated and affordable method, tDCS has potential in becoming a widely used clinical technique [5-8].

Despite its potential, tDCS has a significant limitation, as its efficacy varies among individuals [9-12]. Only approximately half of the subjects have been shown to respond to tDCS as expected [9, 10]. These variations have been shown to arise from the varying anatomical features among individuals [13]. In order to optimize the stimulation for each individual, and to thus obtain the best possible treatment, individual modeling of the subject becomes necessary. For this to be clinically feasible, the computational costs of the process should be optimized to give a result that is accurate enough, with the least possible memory and time consumption.

The Finite-Element Method (FEM), employing tetrahedral meshes of the brain, has been used to solve tDCS-evoked electric fields with computational times of the order of hours [14, 15]. Using voxels of a volume conductor model as elements has been shown to provide a significant speed increase in simulating electric fields evoked by transcranial magnetic stimulation [16]. However, cubical voxels are not the most suitable option for approximating curved surfaces, as the area and the thickness of the surface overestimate reality.

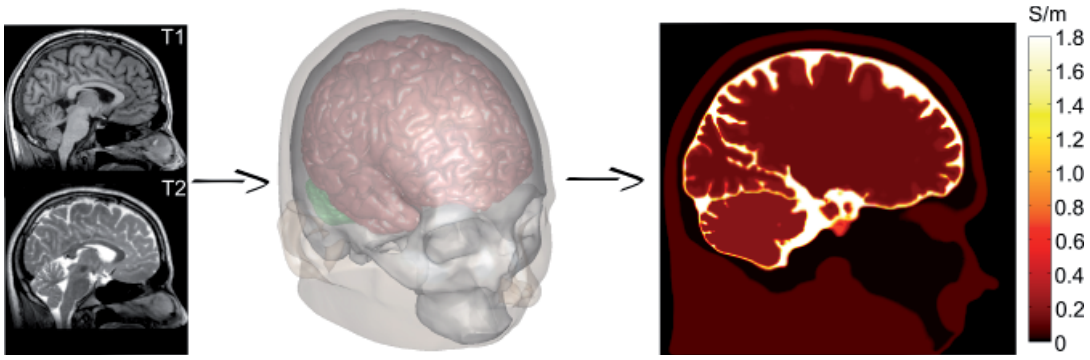

Figure 1. The steps used to create the volume conductor models used for this paper. The MRI data were first segmented, and then the surfaces obtained were used to voxelize the segmented model.

In this paper, we present a method for improving the accuracy of the FEM solution of tDCS-evoked electric fields by enhancing the conductivity of tissue boundaries via a sub-resolution approximation of the boundary conductivity when voxels are used as elements. The effects of refining the tissue boundary conductivity were studied by comparing the FEM simulation results of motor cortical tDCS-evoked electric fields using anatomically accurate volume conductor models with resolutions from 0.2 mm to 2 mm.

2. Methods

2.1 Subjects

Structural T1- and T2-weighted MRI data of a 36-year-old male subject were obtained from a freely available repository (NAMIC: Brain Multimodality, subject case01025). The images were obtained with a 3T MRI scanner, the voxel size being 1 mm. Imaging parameters and subject data can be found online (http://hdl.handle.net/1926/1687).

2.2 Volume Conductor Model

In-house software [13], employing *FreeSurfer* image-analysis software [17-19] (version 5.3.0, available at http://surfer.nmr.mgh.harvard.edu) was used to segment the MRI data of the subject. The polygonal surfaces of scalp, inner and outer surfaces of the skull, cortex, white matter, and cerebellum obtained from the segmentation process were used to build volume conductor models with varying sub-voxel refinement factors and resolutions using in-house software built with the *C* language. The process is demonstrated in Figure 1.

Tissue conductivities were assumed to be linear and isotropic. For the scalp, the conductivity used was 0.08 S/m [20]. For the skull, we used a value of 0.0175 S/m, averaged from the conductivities of dense and cancellous

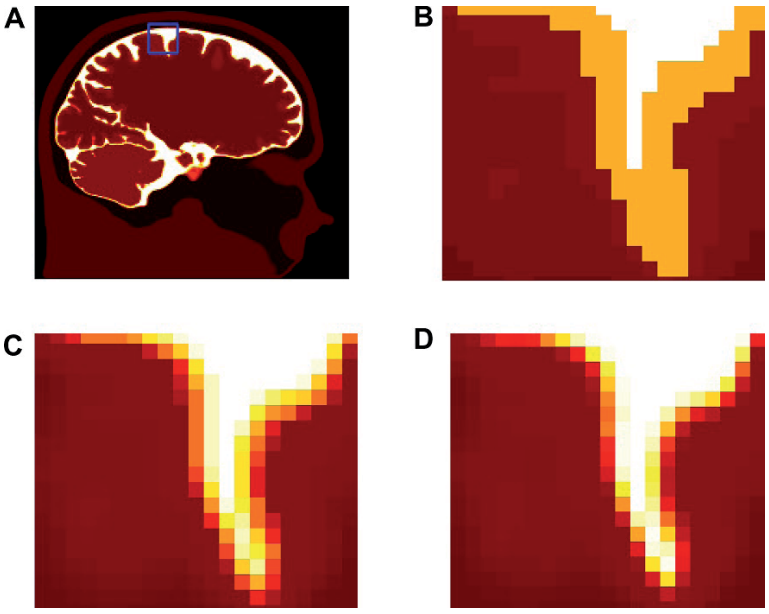

Figure 2. The effect of sub-voxel refinement on the conductivity of tissue boundaries: (a) presents the area from which (b) - (d) were enlarged, each showing the tissue boundaries between CSF (white) and grey matter (red). The resolution for each figure was 1 mm, with the sub-voxel refinement factors being zero, one, and two for (b) - (d), respectively.

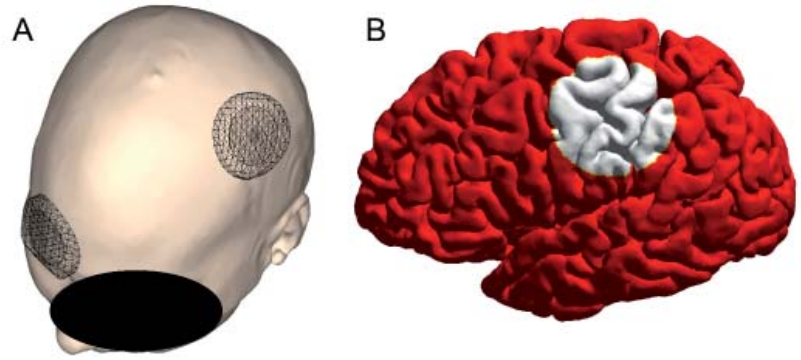

Figure 3. (a) The locations of stimulating electrodes at C3 and Fp2 of the EEG 10/10 system. (b) The left hemisphere, and the area with 2.5 cm radius around C3 used for the comparison of induced electric fields.

bone of 0.008 S/m and 0.027 S/m, respectively [21].The conductivities for dense and cancellous bone were increased by 30% to compensate for the original measurements at room temperature. The conductivity of cerebrospinal fluid (CSF) was 1.8 S/m [22]. For grey matter, conductivities in the literature varied from 0.1 S/m to 0.3 S/m [23-28], and therefore an average conductivity of 0.2 S/m was used. The conductivity of white matter used in the literature was often 70% of the conductivity of grey matter [23-25], and therefore a value of 0.14 S/m was used.

2.3 Sub-Voxel Refinement

A box encapsulating the head was created and divided into cubical voxels of 2^n times the object resolution, where n is the sub-voxel refinement factor. For each surface in the model, voxels crossing the surface were found, and the volume was divided into three parts: voxels that were inside the surface, voxels that were on the surface, and the voxels that were outside the surface. The result was then down-scaled to the desired resolution by combining 2^{3n} refined voxels into one, and assigning a number in $[0,1]$ for the new voxel to represent how large a portion of the voxel was within the surface. In the case of $n = 0$ – meaning that no refinement was used – the proportion of the voxel inside the surface was assigned to be 0.5. Figure 2 presents the effect of refinement on tissue boundary conductivities.

In total, 48 volume conductor models were built. Resolutions of 0.2 mm to 2 mm were used without refinement, resolutions of 0.5 mm to 2 mm were used with $n = 1$, and resolutions of 0.8 mm to 2 mm were used with $n = 2$.

2.4 Electric Field Modeling

In order to assess the effects of the sub-voxel refinement method, the electric scalar potential, ϕ, evoked by tDCS stimulation was determined using a Finite-Element Method solver employing cubical elements and piecewise-linear basis functions [16]. Each voxel of the volume conductor model was considered a cubical element with the electric scalar potentials at the vertices as the degrees of freedom.

tDCS stimulation was applied to the hand area of the left primary motor cortex, so that the center of the stimulating electrode was placed at position C3 of the EEG 10/10 system. The area of the sponge electrode used was $25\ \mathrm{cm}^2$, the conductivity was 1.6 S/m, and the input current was 1 mA. The reference electrode was placed at the contralateral orbit (Fp2). The electrode locations are presented in Figure 3a.

The electric fields induced 1 mm within the grey matter of the left hemisphere were calculated from the solved-for ϕ. In order to be able to compare the results, the relative error between each volume conductor model and the reference model (non-refined 0.2 mm) was approximated with

$$\text{Relative Error} = \frac{\sqrt{\sum \left| {}^{i}E_n - {}^{0}E_n \right|^2}}{\sqrt{\sum \left| {}^{0}E_n \right|^2}}, \qquad (1)$$

where ${}^{i}E_n$ and ${}^{0}E_n$ are the electric fields in node n for the voxel model i and for the reference, respectively. The error was approximated over the left hemisphere and within a 2.5 cm radius around the closest point to C3 on the left hemisphere, as presented in Figure 3b.

All the simulations in this work were run with *MATLAB* (version 2014a, MathWorks, Inc.) on the same computer with a 3.4 GHz eight-core Intel Xeon processor and 32 GB memory running Ubuntu *Linux 14.04 LTS*.

3. Results

3.1 Electric Field Distributions

The evoked electric fields were solved for C3-Fp2 tDCS with varying resolutions and refinement factors. Four of these results plotted onto the left hemisphere are presented in Figure 4.

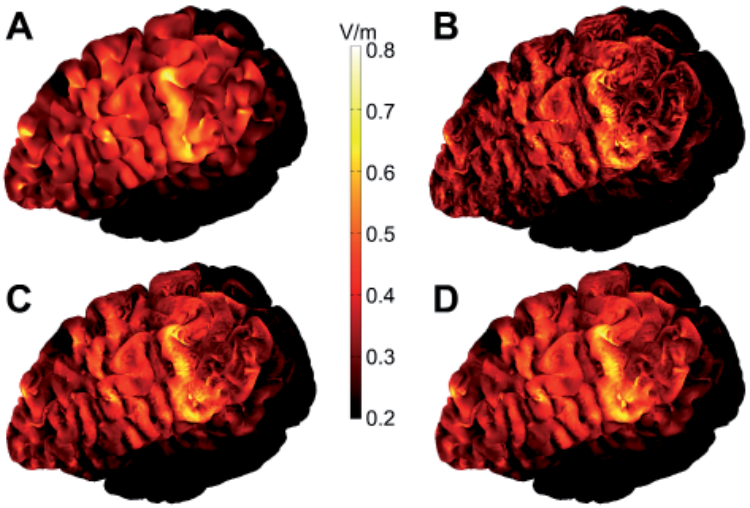

Figure 4. The calculated electric fields on the left hemisphere using (a) 0.2 mm unrefined voxels, (b) 1 mm unrefined voxels, and 1 mm voxels, with a refinement factor of one (d) and a refinement factor of two (d).

Visually, the electric-field distributions in the brain resembled each other, aside from the apparent roughness of the distribution with low resolutions, as expected. Refinement of the tissue boundaries could be observed to smoothen the electric-field distribution.

3.2 Effect of Refinement on Error

The relative error of each volume conductor model used is presented in Figure 5 for the left hemisphere. The sub-voxel refinement exhibited a significant reduction in the relative error for each modeled resolution: The reduction with a 1 mm voxel size was 38.2% when a refinement factor of one was used, increasing to 53.8% with refinement factor of two. This effect became more prominent as the resolution was increased. With 0.5 mm voxels, the error reduction with a refinement factor of one was 51.5%, and with 0.8 mm voxels it was 59.5% when refined by a factor of two.

Similar behavior could also be observed by studying an area with a radius of 2.5 cm around C3, as presented in Figure 6. In this case, the corresponding error reductions were 43.9% to 55.5% with a refinement factor of one and voxel sizes of 1 mm and 0.5 mm, respectively. By doubling the refinement factor, these reductions increased to 60.9% and 65.7% for voxel sizes of 1 mm and 0.8 mm, respectively.

3.3 Computational Costs

Aside from reducing the error of a given resolution, the sub-voxel refinement method also enables the use of a lower resolution without affecting the accuracy of the results.

A volume conductor model with 0.4 mm unrefined voxel size took 55.9 s to solve with 65.76×10^{6} DOFs (degrees of freedom) employing a geometric multi-grid in the solver. The relative residual of the solution was 10^{-6}. As can be seen from Figure 5, the relative errors obtained with a model employing 0.6 mm with a refinement of one and 0.8 mm with a refinement of 2 were within ±5% of the relative errors of the 0.4 mm unrefined solution. However, the computational costs of both of these solutions were significantly reduced, due to the lower resolution used. The solution time was reduced by 63.3% (to 20.48 s) with a refinement of one and a voxel size of 0.6 mm, and by

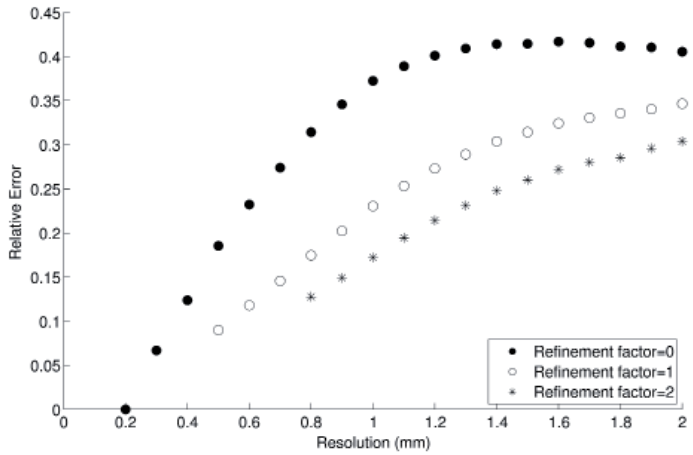

Figure 5. The relative errors calculated for the left hemisphere according to Equation (1).

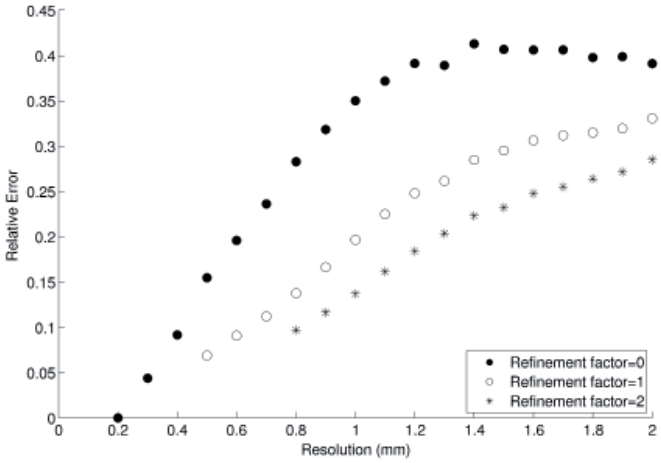

Figure 6. The relative errors calculated for the area within a 2.5 cm radius around C3 according to Equation (1).

81.9% (to 10.11 s) with a refinement of 2 and a voxel size of 0.8 mm. The degrees of freedom in the models decreased by 70.0% and 87.2% when refined by factors of one (0.6 mm voxel) and two (0.8 mm voxel), respectively.

4. Discussion

Based on the results, sub-voxel refinement was found to provide a significant improvement in the accuracy of solved electric fields due to tDCS stimulation. By using a refinement factor of two, the resolution of a volume conductor model could be halved to obtain up to an 87% decrease in the model's degrees of freedom, and an 81.9% decrease in the computational time, with a cost of the relative error rising only 3%.

One can thus obtain the accuracy of 0.5 mm resolution used in the literature [13] by using an accuracy of 1 mm refined by a factor of two and solving for the induced electric fields due to a tDCS stimulation in less than 5 s. This enables individual modeling to be effectively used in personally optimizing each stimulation setup for a patient.

A limiting factor for the factor of refinement arises from the memory consumption of the refinement process, itself. The number of voxels used to create the volume conductor model is 2^{3n} times higher than the resulting volume conductor model size, where n is the refinement factor. The time for creating a voxel model also rapidly increases with increasing n: with 1 mm voxels, it takes 3.2 s; with 0.5 mm voxels, the creation takes 18.8 s; and with 0.25 mm voxels, the creation takes 145.6 s. However, the voxel model only has to be created once, and it then can be freely used to optimize the tDCS treatment.

In conclusion, our sub-voxel refinement method can be a useful tool in the optimization of individualized tDCS. It significantly improves the accuracy of tDCS-evoked electric fields solved with the Finite-Element Method, while optimizing the computational costs of the process.

5. References

1. A. Priori, A. Berardelli, S. Rona, N. Accornero, and M. Manfredi, "Polarization of the Human Motor Cortex Through the Scalp," *NeuroReport*, **9**, 10, July 1998, pp. 2257-2260.

2. M. A. Nitsche and W. Paulus, "Excitability Changes Induced in the Human Motor Cortex by Weak Transcranial Direct Current Stimulation," *The Journal of Physiology*, **527**, 3, September 2000, pp. 633-639.

3. M.-F. Kuo, W. Paulus, and M. A. Nitsche, "Therapeutic Effects of Noninvasive Brain Stimulation with Direct Currents (tDCS) in Neuropsychiatric Diseases," *NeuroImage*, **85**, 3, January 2014, pp. 948-960.

4. J. Marquez, P. van Vliet, P. McElduff, J. Lagopoulos, and M. Parsons, "Transcranial Direct Current Stimulation (tDCS): Does It Have Merit in Stroke Rehabilitation? A Systematic Review," *International Journal of Stroke*, **10**, 3, October 2015, pp. 306-316.

5. D. Meron, N. Hedger, M. Garner, and D. S. Baldwin, "Transcranial Direct Current Stimulation (tDCS) in the Treatment of Depression: Systematic Review and Meta-Analysis of Efficacy and Tolerability," *Neuroscience & Biobehavioral Reviews*, **57**, October 2015, pp. 46-62.

6. F. C. Hummel, P. Celnik, A. Pascual-Leone, F. Fregni, W. D. Byblow, C. M. Buetefisch, J. Rothwell, L. G. Cohen, and C. Gerloff, "Controversy: Noninvasive and Invasive Cortical Stimulation Show Efficacy in Treating Stroke Patients," *Brain Stimulation*, **1**, 4, October 2008, pp. 370-382.

7. S. Tanaka and K. Watanabe, "Transcranial Direct Current Stimulation – A New Tool for Human Cognitive Neuroscience," *Brain and Nerve*, **61**, 1, January 2009, pp. 53-64.

8. A. R. Brunoni, M. A. Nitsche, N. Bolognini, M. Bikson, T. Wagner, L. Merabet, D. J. Edwards, A. Valero-Cabre, A. Rotenberg, A. Pascual-Leone, R. Ferrucci, A. Priori, P. S. Boggio, and F. Fregni, "Clinical Research with Transcranial Direct Current Stimulation (tDCS): Challenges and Future Directions," *Brain Stimulation*, **5**, 3, July 2012, pp. 175-195.

9. S. Wiethoff, M. Hamada, and J. C. Rothwell, "Variability in Response to Transcranial Direct Current Stimulation of the Motor Cortex," *Brain Stimulation*, **7**, 3, June 2014, pp. 468-475.

10. V. López-Alonso, B. Cheeran, D. Rio-Rodriguez, and M. Fernández-Del-Olmo, "Inter-individual Variability in Response to Non-invasive Brain Stimulation Paradigms," *Brain Stimulation*, **7**, 3, February 2014, pp. 372-380.

11. T. Chew, K.-A. Ho, and C. K. Loo, "Inter- and Intra-individual Variability in Response to Transcranial Direct Current Stimulation (tDCS) at Varying Current Intensities," *Brain Stimulation*, **8**, 6, December 2015, pp. 1130-1137.

12. V. López-Alonso, M. Fernández-Del-Olmo, A. Costantini, J. J. Gonzalez-Henriquez, and B. Cheeran, "Intra-individual Variability in the Response to Anodal Transcranial Direct Current Stimulation," *Clinical Neurophysiology*, **126**, 6, December 2015, pp. 2342-2347.

13. I. Laakso, S. Tanaka, S. Koyama, V. De Santis, and A. Hirata, "Intersubject Variability in Electric Fields of Motor Cortical tDCS," *Brain Stimulation*, **8**, 5, October 2015, pp. 906-913.

14. M. Windhoff, A. Opitz, and A. Thielscher, "Electric Field Calculations in Brain Stimulation Based on Finite Elements: An Optimized Processing Pipeline for the Generation and Usage of Accurate Individual Head Models," *Human Brain Mapping*, **34**, 4, November 2013, pp. 923-935.

15. P. C. Miranda, A. Mekonnen, R. Salvador, and G. Ruffini, "The Electric Field in the Cortex During Transcranial Current Stimulation," *NeuroImage*, **70**, April 2013, pp. 48-58.

16. I. Laakso and A. Hirata, "Fast Multigrid-Based Computation of the Induced Electric Field for Transcranial Magnetic Stimulation," *Physics in Medicine and Biology*, **57**, 23, December 2012, pp. 7753-7765.

17. A. M. Dale, B. Fischl, and M. I. Sereno, "Cortical Surface-Based Analysis. I. Segmentation and Surface Reconstruction." *NeuroImage*, **9**, 2, February 1999, pp. 179-194.

18. B. Fischl, M. I. Sereno, R. B. Tootell, and A. M. Dale, "High-Resolution Intersubject Averaging and a Coordinate System for the Cortical Surface," *Human Brain Mapping*, **8**, 4, November 1999, pp. 272-284.

19. B. Fischl and A. M. Dale, "Measuring the Thickness of the Human Cerebral Cortex from Magnetic Resonance Images," Proceedings of the National Academy of Sciences of the United States of America, **97**, 20, July 2000, pp. 11 050-11 055.

20. C. Gabriel, A. Peyman, and E. H. Grant, "Electrical Conductivity of Tissue at Frequencies Below 1 MHz," *Physics in Medicine and Biology*, **54**, 16, July 2009, pp. 4863-4878.

21. M. Akhtari, H. Bryant, A. Mamelak, E. Flynn, L. Heller, J. Shih, M. Mandelkem, A. Matlachov, D. Ranken, E. Best et al., "Conductivities of Three-layer Live Human Skull," *Brain Topography*, **14**, 3, March 2002, pp. 151-167.

22. S. Baumann, D. Wozny, S. Kelly, and F. Meno, "The Electrical Conductivity of Human Cerebrospinal Fluid at Body Temperature," *IEEE Transactions on Biomedical Engineering*, **44**, 3, March 1997, pp. 220-223.

23. W. Freygang Jr. and W. Landau, "Some Relations Between Resistivity and Electrical Activity in the Cerebral Cortex of the Cat," *Journal of Cellular and Comparative Physiology*, **45**, 3, June 1955, pp. 377-392.

24. R. D. Stoy, K. R. Foster, and H. P. Schwan, "Dielectric Properties of Mammalian Tissues from 0.1 to 100 MHz; A Summary of Recent Data," *Physics in Medicine and Biology*, **27**, 4, April 1982, p. 501-513.

25. S. Gabriel, R. Lau, and C. Gabriel, "The Dielectric Properties of Biological Tissues: II. Measurements in the Frequency Range 10 Hz to 20 GHz," *Physics in Medicine and Biology*, **41**, 11, November 1996, p. 2251-2269.

26. J. B. Ranck, "Specific Impedance of Rabbit Cerebral Cortex," *Experimental Neurology*, **7**, 2, February 1963, pp. 144-152.

27. J. Latikka, T. Kuurne, and H. Eskola, "Conductivity of Living Intracranial Tissues," *Physics in Medicine and Biology*, **46**, 6, June 2001, pp. 1611-1616.

28. M. Akhtari, N. Salamon, R. Duncan, I. Fried, and G. W. Mathern, "Electrical Conductivities of the Freshly Excised Cerebral Cortex in Epilepsy Surgery Patients; Correlation with Pathology, Seizure Duration, and Diffusion Tensor Imaging," *Brain Topography*, **18**, 4, July 2006, pp. 281-290.

How Kerr Nonlinearity Influences Polarized Electromagnetic Wave Propagation

D. V. Valovik

Department of Mathematics and Supercomputing
Penza State University
Krasnaya Str., 40 Penza, Russia, 440026
E-mail: dvalovik@mail.ru

Abstract

The propagation of electromagnetic TE waves along boundaries of a plane dielectric layer filled with a Kerr medium is studied for all possible cases of the problem's parameters. The layer is located between two half-spaces with constant permittivities. The problem is reduced to a nonlinear transmission eigenvalue problem for Maxwell's equations, in which each eigenvalue is a propagation constant of a guided wave. The exact dispersion equation with respect to the eigenvalues (propagation constants) is derived and studied. It is proven that in the presence of the Kerr effect, several novel wave-guiding regimes arise, including regimes that have no counterparts in the linear theory. An infinite number of eigenvalues arise in the focusing case, even if the corresponding linear problem has no solutions (the linear problem always has no more than a finite number of solutions). In the defocusing case, only those solutions arise that tend to linear solutions when the nonlinearity coefficient vanishes. It is also proven that in the nonlinear case, an infinite number of eigenvalues do not reduce to the solutions of the corresponding linear problem, even if the nonlinearity coefficient tends to zero. Numerical illustrations for the results obtained are provided.

1. Introduction

Nonlinear wave propagation phenomena give rise to a number of qualitatively different nonlinear mathematical models. Optical materials demonstrate many different effects associated with various applications: for the general theory, see [1-5]. Among different types of nonlinearities that are actively studied, one of the most important is the Kerr nonlinearity. This arises in different fields of mathematical physics, in particular, in nonlinear optics [6-12] and in plasma physics [6].

However, in mathematical formulations, nonlinear wave-propagation problems are usually difficult to study. Until now, only a few of the simplest wave-guiding problems for polarized waves, plane geometry, and nonlinear permittivities have been rigorously studied in detail. To be exact, problems with one interface between two half-spaces filled with linear/nonlinear media were well investigated [6, 9, 13]. The next step was to investigate wave-guiding problems with two interfaces: a dielectric layer sandwiched between two half-spaces. If the permittivity of the layer is constant and the permittivities of the half-spaces are constant or nonlinear, then these problems were also sufficiently well studied [9, 13-15]. The main issue relating to these two sorts of wave-guiding problems is that such models are not very realistic (however, these models are excellent fits for mathematical analysis). Indeed, on the one hand, it is not clear where to find a half-space filled with a nonlinear medium. On the other hand, since the fields must vanish at infinity, the nonlinear equations (with cubic-quintic nonlinearities) acquire a much simpler form in the half-spaces (due to the fact that a constant of integration in the first integral must be zero). After this simplification, a general solution of the nonlinear equation degenerates to a simpler solution (e.g., an elliptic function degenerates to a trigonometric or hyperbolic function), which hardly helps in the understanding of more complicated problems, where one must study the non-degenerated solutions.

In this paper, we concentrate on a widely known and rather physically realistic problem in nonlinear optics, which we completely solve. To be more precise, the paper focuses on studying the propagation of polarized monochromatic electromagnetic waves along a plane dielectric layer, sandwiched between two half-spaces with constant permittivities. The permittivity of the layer is described by the Kerr law. We look for guided waves that decay when they move off from the boundaries of the waveguide. Here, we consider only transverse electric (TE) waves. This problem was studied by many authors: see, e.g., [13, 16-25] and the bibliographies therein (some generalizations were also considered in the cited papers). In particular in [13], one found a deep and comprehensive background for the considered problem and many related

problems. In spite of the fact that many papers have been published, the first "purely nonlinear" results were only recently obtained in [25], where a novel wave-guiding regime was theoretically predicted and analyzed. However, in [25], only one of several possible opportunities was studied. In fact, this problem was one of those that forms a basis for the theory of self-action effects in nonlinear optics. For this reason, we decided to give a complete study of this problem. Using an original technique [26], we found results that to the best of our knowledge have not previously been found. The results found explain the influence of the Kerr nonlinearity on the wave-propagation process.

A strict electromagnetic statement of this problem, called $P(\alpha)$, implies a necessary inference about the (theoretical) existence of novel types of guided waves. We call these waves purely nonlinear TE guided waves. Let the permittivity inside the layer be $\varepsilon = \varepsilon_2 + \alpha|\mathbf{E}|^2$, where ε_2 and α are real constants, and $\mathbf{E}$ is the complex amplitude of the electric field. In this case, there are several types of waves: nonlinear waves of the first type become waves of the linear problem when $\alpha \to 0$ (this case is expected); waves of the second type stay away from any linear solutions even when $\alpha \to 0$ (in other words, some of the effects obtained are non-perturbative). In particular, among the waves of the latter case there are waves that are periodic but do not possess zero value (the corresponding linear problem does not admit such kinds of solutions).

From the mathematical standpoint, problem $P(\alpha)$ is a nonlinear boundary eigenvalue problem for Maxwell's equations, with appropriate transmission conditions on the boundaries of the layer, and the radiation condition at infinity. The eigenvalues of the problem $P(\alpha)$ are *propagation constants* (PCs) for the guided waves considered. If $\alpha = 0$ we obtain the linear problem $P(0)$, which has been well studied [27, 28]. It is known that $P(0)$ has a finite number of eigenvalues, and each eigenvalue corresponds to a guided mode. Problem $P(0)$ is usually reduced to determining roots of a transcendental equation called the *dispersion equation* (DE). In this paper, we not only demonstrate that an analog of such a dispersion equation can be derived in the nonlinear case, but show theoretically that there exist several novel types of purely nonlinear TE guided waves. Additional discussion and introductory remarks can be found in the upcoming paper [29].

It should be noted that the problem $P(\alpha)$ is exactly integrable, and the dispersion equation can be expressed through elliptic functions. Many researchers have gone this way: [13, 16-21, 23, 24, 30-32]. However, the dispersion equation in such a form is rather difficult to investigate. To be exact, the main problem with the dispersion equation expressed through elliptic functions consists in the absence of equivalency between the original wave-guiding problem and the dispersion equation. It is worth noticing that after [31], at least two papers, [23, 24] were published in which it was pointed out that the dispersion equation from [31] had spurious roots. The existence of spurious roots resulted from the absence of the afore-said equivalency.

We have developed an original, straightforward approach that allows us to derive the dispersion equation, which is equivalent to the problem $P(\alpha)$. Using the dispersion equation thus found, we derive all necessary information about the spectrum of the problem $P(\alpha)$. As is well known in wave-guiding problems, the spectrum (and its properties) are the most important aspects, as they define the properties of the waveguide. The technique given here was already generalized to the case of transverse-magnetic (TM) waves and Kerr nonlinearity [33]. From the theoretical point of view, for the TM case, the dispersion equation can be expressed in terms of hyperelliptic functions, but no one hardly has the courage to do it.

In the problem under investigation, the simplest one-dimensional nonlinear Schrödinger operator arises, which cannot be completely studied using perturbation theory. The problem was originally formulated in the whole space. However, using explicit solutions in the half-spaces and transmission conditions for the electromagnetic field, it is possible to reformulate the setting as a nonlinear Sturm-Liouville problem on a segment with the third-type boundary conditions. The aforementioned Schrödinger operator will thus be considered in a bounded domain.

We hope that the results presented will also be helpful for researchers who study spectral problems for Schrödinger operators with nonlinear unbounded potentials, especially in bounded domains.

Throughout the paper, the terms *eigenvalues* and *eigenfunction* have the same meanings as *propagation constant* and *eigenmode*, respectively.

2. Statement of the Problem

We begin with the non-stationary Maxwell's equations, given in the form [34]

$$\operatorname{rot} \tilde{\mathbf{H}} = \partial_t \tilde{\mathbf{D}}, \qquad (1)$$

$$\operatorname{rot} \tilde{\mathbf{E}} = -\partial_t \tilde{\mathbf{B}},$$

where $\tilde{\mathbf{D}} = \varepsilon \tilde{\mathbf{E}}$, $\tilde{\mathbf{B}} = \mu \tilde{\mathbf{H}}$, $\partial_t \equiv \dfrac{\partial}{\partial t}$. It follows from Equation (1) that

$$\operatorname{rot} \tilde{\mathbf{E}} = -\partial_t \left(\mu \tilde{\mathbf{H}}\right), \qquad (2)$$

$$\operatorname{rot} \tilde{\mathbf{H}} = \partial_t \left(\varepsilon \tilde{\mathbf{E}}\right).$$

The real monochromatic electromagnetic field $\left(\tilde{\mathbf{E}},\tilde{\mathbf{H}}\right)$ can be written in the form

$$\tilde{\mathbf{E}}(x,y,z,t)=\mathbf{E}^{+}(x,y,z)\cos\omega t+\mathbf{E}^{-}(x,y,z)\sin\omega t\,, \quad (3)$$

$$\tilde{\mathbf{H}}(x,y,z,t)=\mathbf{H}^{+}(x,y,z)\cos\omega t+\mathbf{H}^{-}(x,y,z)\sin\omega t\,,$$

where ω is the circular frequency, and $\mathbf{E}^{\pm}$ and $\mathbf{H}^{\pm}$ are real vector-functions. The vector-functions $\mathbf{E}^{\pm}$ and $\mathbf{H}^{\pm}$ are solutions to the system of Equation (2). Using the quantities

$$\mathbf{E}=\mathbf{E}^{+}+i\mathbf{E}^{-}\,, \quad (4)$$

$$\mathbf{H}=\mathbf{H}^{+}+i\mathbf{H}^{-}\,,$$

which are called the complex amplitudes [13, 35], the fields of Equation (3) can be written in the form

$$\tilde{\mathbf{E}}=\mathrm{Re}\left\{\mathbf{E}e^{-i\omega t}\right\}, \quad (5)$$

$$\tilde{\mathbf{H}}=\mathrm{Re}\left\{\mathbf{H}e^{-i\omega t}\right\}.$$

Here, we consider the case

$$\varepsilon\left(\tilde{\mathbf{E}}\right)=\varepsilon\left[\mathbf{E}^{+}(x,y,z)\cos\omega t+\mathbf{E}^{-}(x,y,z)\sin\omega t\right] \quad (6)$$

$$=\varepsilon\left[\left(\mathbf{E}^{+}\right)^{2}+\left(\mathbf{E}^{-}\right)^{2}\right]=\varepsilon\left(|\mathbf{E}|^{2}\right).$$

The dependence of ε on the field in the form of Equation (6) is widely used in optics (e.g., self-focusing and self-defocusing effects) [6, 9, 13, 35-37]. This results from the following assumptions:

- The dielectric's permittivity has an optical response that is local in space and time;
- The time dependence of the optical response of the nonlinear medium is described by one frequency;
- Phase matching is assumed to be absent, so that small amplitudes of higher harmonics can be neglected.

This dependence leads to various particular nonlinear laws for the permittivity: cubic (Kerr), quintic, cubic-quintic, polynomial nonlinearities, power nonlinearity with non-integer degree, saturated nonlinearities, and so on. These nonlinearities were actively experimentally [4, 5, 38-46] as well as theoretically [2, 6, 9, 13, 21, 32, 35-37, 47-56] studied.

Assuming that the permittivity, ε, satisfies Equation (6), and substituting the fields from Equation (3) into Equation (2), one arrives at the system

$$\mathrm{rot}\,\mathbf{H}=-i\omega\varepsilon\mathbf{E}\,, \quad (7)$$

$$\mathrm{rot}\,\mathbf{E}=i\omega\mu\mathbf{H}\,,$$

where $\mathbf{E}$, $\mathbf{H}$ are the complex amplitudes of Equation (4), ε depends on $|\mathbf{E}|^{2}$, and μ is a constant.

Consider a monochromatic TE wave $(\mathbf{E},\mathbf{H})e^{-i\omega t}$, where ω is a circular frequency and

$$\mathbf{E}=\left(0,E_{y},0\right)^{\mathrm{T}}, \quad (8)$$

$$\mathbf{H}=\left(H_{x},0,H_{z}\right)^{\mathrm{T}},$$

are the complex amplitudes from Equation (4). The TE wave propagates along the surface of the plane dielectric waveguide:

$$\Sigma:=\left\{(x,y,z)\in\mathbb{R}^{3}:\ 0\leqslant x\leqslant h,\ -\infty<y,\,z<+\infty\right\},$$

where $h>0$ (see Figure 1). The half-spaces $x<0$ and $x>h$ are filled with homogeneous isotropic nonmagnetic media with constant permittivities ε_1 and $\varepsilon_3\geqslant\varepsilon_0>0$,

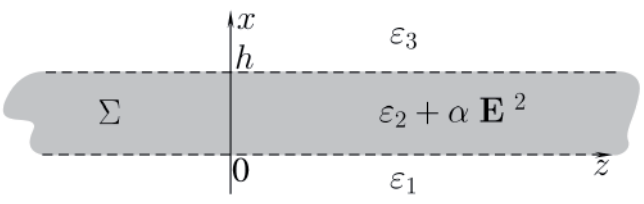

Figure 1. The geometry of the problem.

respectively, where ε_0 is the permittivity of free space. Without loss of generality, $\varepsilon_1 \geqslant \varepsilon_3$. The waveguide, Σ is located in Cartesian coordinates $Oxyz$ and filled with homogeneous isotropic nonmagnetic medium. The permittivity, ε, inside the layer Σ is described by the Kerr law [6, 9, 57]: $\varepsilon = \varepsilon_2 + \alpha|\mathbf{E}|^2$, where ε_2 and α are real constants. All the media contain no sources. Everywhere $\mu = \mu_0 > 0$ is the permeability of free space.

The complex amplitudes of Equation (8) must satisfy the time-harmonic Maxwell's equations of Equation (7), where

$$\varepsilon = \begin{cases} \varepsilon_3, & x > h, \\ \varepsilon_2 + \alpha|\mathbf{E}|^2, & 0 \leqslant x \leqslant h, \\ \varepsilon_1, & x < 0, \end{cases}$$

the continuity condition for the tangential components of the field on the boundaries $x = 0$ and $x = h$, and the radiation condition at infinity: the electromagnetic field decays as $O\left(|x|^{-1}\right)$ when $|x| \to \infty$.

It is supposed that the sought-for waves depend harmonically on z. Substituting Equation (8) into Equation (7), one finds that the components of Equation (8) do not depend on y. The components therefore have the form

$$E_y = \mathrm{E}_y(x)e^{i\gamma z}, \quad H_x = \mathrm{H}_x(x)e^{i\gamma z}, \quad H_z = \mathrm{H}_z(x)e^{i\gamma z}, \tag{9}$$

where γ is an unknown (real) spectral parameter, and E_y is a real function.

In the following, if it does not lead to misunderstanding, the explicit dependence on the arguments/parameters is often omitted.

2.1 Remark 1

Obviously, in the corresponding linear problem ($\alpha = 0$), the spectral parameter γ can be real as well as complex. However, only real eigenvalues correspond to guided modes (nevertheless, the case of complex eigenvalues has also been studied) [27, 28]. In addition, if γ is complex valued, then the permittivity can have losses (which is more realistic). In the considered nonlinear problem, the spectral parameter can be only real. Indeed, it follows from Equations (8) and (9) that

$$|\mathbf{E}|^2 = \left|\mathrm{E}_y(x)e^{i\gamma z}\right|^2 = \left|\mathrm{E}_y(x)\right|^2\left|e^{i\gamma z}\right|^2.$$

Let $\gamma = \gamma' + i\gamma''$ and $\gamma'' \neq 0$: then, $\left|e^{i\gamma z}\right| = \left|e^{i\gamma' z}\right|\left|e^{-\gamma'' z}\right| = e^{-\gamma'' z}$ This implies that Equations (7) and, therefore, their solutions E_y, H_x, and H_z, given by Equation (9), depend on z. This contradicts the choice of Equation (9).

Substituting the complex amplitudes of Equation (8) with the components of Equation (9) into Equation (7), normalizing the system obtained in accordance with the Equation $\tilde{x} = k_0 x$, $\tilde{\gamma} = \gamma k_0^{-1}$, $\tilde{\varepsilon}_j = \varepsilon_j \varepsilon_0^{-1}$ $(j = 1,2,3)$, $\tilde{\alpha} = \alpha\varepsilon_0^{-1}$, where $k_0^2 := \omega^2\mu_0\varepsilon_0$, denoting $Y(\tilde{x}) := \mathrm{E}_y(\tilde{x})$, and omitting the tilde symbol, one arrives at the equation

$$Y''(x) = \left(\gamma^2 - \varepsilon\right)Y(x), \tag{10}$$

where $\varepsilon = \varepsilon_2 + \alpha Y^2$ inside Σ and $\varepsilon = \varepsilon_1, \varepsilon_3$ in the half-spaces $x < 0$, $x > h$, respectively.

Transmission conditions for the tangential components E_y, H_z imply transmission conditions for Y and Y':

$$[Y]\big|_{x=0} = [Y]\big|_{x=h} = [Y']\big|_{x=0} = [Y']\big|_{x=h} = 0, \tag{11}$$

where $[f]\big|_{x=x_0} = \lim\limits_{x \to x_0 - 0} f(x) - \lim\limits_{x \to x_0 + 0} f(x)$.

As γ is real and Equation (10) depends on γ^2, only positive eigenvalues are sought.

Problem $P(\alpha)$ is to determine real positive eigenvalues $\hat{\gamma}$ for which nontrivial eigenfunctions $Y\left(x;\hat{\gamma}\right)$ exist; these eigenfunctions must satisfy Equations (10) and (11), and must decay as $O\left(|x|^{-1}\right)$ when $|x| \to \infty$.

3. The Nonlinear Sturm-Liouville Problem

Let the notation $k_1^2 := \gamma^2 - \varepsilon_1 > 0$, $k_2^2 := \varepsilon_2 - \gamma^2$, $k_3^2 := \gamma^2 - \varepsilon_3 > 0$, where k_2^2 is not necessarily positive, be introduced. Solving Equation (10) in the half-spaces $x < 0$, $x > h$, and taking into account the radiation condition at infinity, one finds

$$Y(x) = Be^{-k_3(x-h)} \text{ for } x > h \tag{12a}$$

and

$$Y(x) = Ae^{k_1 x} \text{ for } x < 0, \tag{12b}$$

where the constant $A \neq 0$ is supposed to be known (without loss of generality, $A > 0$), and the constant $Y(h) = B$ is determined using the transmission conditions at the boundary $x = h$.

The decay of the solutions in Equations (12) is guaranteed by the necessary condition

$$\gamma^2 > \varepsilon_1. \tag{13}$$

In order to reduce the number of parameters, we introduce the normalized coefficient $\bar{\alpha} = \alpha A^2$ and the normalized function $y = Y/A$. Using Equations (11) and (12), the problem $P(\alpha)$ is equivalently reformulated as the following nonlinear Sturm- Liouville problem for the equation

$$y''(x) = -\left[k_2^2 + \bar{\alpha} y^2(x)\right] y(x), \quad x \in [0,h], \tag{14}$$

with the third-kind boundary conditions

$$k_1 y(0) - y'(0) = 0, \quad k_3 y(h) + y'(h) = 0, \tag{15}$$

where $y(0) = 1$ and γ is an unknown real positive spectral parameter.

It is supposed that the function y is sufficiently smooth:

$$y(x) \in C^1[0,h] \cap C^2(0,h). \tag{16}$$

3.1 Definition 1

If for $\gamma = \hat{\gamma}$ there is a nonzero solution $y \equiv y(x;\hat{\gamma})$ satisfying Equations (14)-(16), then $\hat{\gamma}$ is called an eigenvalue; the function $y(x;\hat{\gamma})$ is called an eigenfunction.

The problem $P(\alpha)$ is now treated as a problem of proving the existence of eigenvalues $\hat{\gamma}$ satisfying Definition 1.

4. Preliminary Analysis of the Problem

Equation (14) has a first integral that can be written in the form

$$y'^2 + k_2^2 y^2 + 0.5\bar{\alpha} y^4 \equiv C, \tag{17}$$

where C is a constant of integration. Using the integral of Equation (17) at the point $x = 0$ and Equation (15), one calculates

$$C = \varepsilon_2 - \varepsilon_1 + 0.5\bar{\alpha}. \tag{18}$$

A simple analysis of Equation (17) allows us to state the following

- If there is a point $x = x^*$ in which $y(x^*) = 0$, then $y'^2(x^*) = C$. Obviously, if $C < 0$, then y does not vanish. If $C > 0$ and $y(x^*) = 0$, then $y'^2(x^*)$ stays bound.

- If there is a point $x = x^*$ in which $\lim_{x \to x^*} y(x) = \infty$ then $\lim_{x \to x^*} y^{-2} (y'/y)^2 = -0.5\bar{\alpha}$, and therefore $\lim_{x \to x^*} y'/y = \infty$. To be more precise, in this case $y'/y = O(y)$ and $y' = O(y^2)$. Obviously, if $\alpha > 0$, then the function y can not possess the infinite value for fixed γ
- If there is a point $x = x^*$ in which $\lim_{x \to x^*} y'(x) = \infty$ then we obtain the latter case.

For further investigation, we use the new variables $\tau(x) = y^2(x)$, $\eta(x) = y'(x)/y(x)$. Using Equation (15), one finds

$$\eta(0) = k_1 > 0, \tag{19}$$

$$\eta(h) = -k_3 < 0.$$

Equation (14) is rewritten as a system in the normal form:

$$\tau' = 2\tau\eta, \tag{20}$$

$$\eta' = -\left(\eta^2 + k_2^2 + \bar{\alpha}\tau\right).$$

A first integral of this system can be determined from Equation (17) (or from Equation (20)), and has the form

$$\bar{\alpha}\tau^2 + 2\left(\eta^2 + k_2^2\right)\tau - 2C = 0, \tag{21}$$

where C is defined by Equation (18).

Taking into account the analysis of Equation (17), we can state that

- If there is a point $x = x^*$ in which $\tau\left(x^*\right) = 0$, then $\tau\left(x^*\right)\eta^2\left(x^*\right) = C$. Obviously, if $C < 0$, then τ does not vanish. If $C > 0$ and $\tau\left(x^*\right) = 0$, then $\lim_{x\to x^*}\eta(x) = \infty$.

- If there is a point $x = x^*$ in which $\lim_{x\to x^*}\tau(x) = \infty$ then $\lim_{x\to x^*}\eta^2(x)/\tau(x) = -0.5\bar{\alpha}$. Obviously, if $\alpha > 0$, then the function τ can not possess the infinite value for fixed γ. If $\alpha < 0$ and $\lim_{x\to x^*}\tau(x) = \infty$, then $\lim_{x\to x^*}\eta(x) = \infty$.

- If there is a point $x = x^*$ in which $\lim_{x\to x^*}\eta(x) = \infty$, then we obtain the latter case.

4.1 Statement 1

The second equation in the system of Equation (20) can be written in the form $\eta' = w(\eta;\gamma)$ for

$$\bar{\alpha} \in (0, \bar{\alpha}_-) \quad \varepsilon_2 < \varepsilon_3 \quad (\bar{\alpha} > 0,\ C < 0) \quad (22)$$

or $\eta' = -w(\eta;\gamma)$ for

$$\bar{\alpha} \in (0, +\infty) \quad \varepsilon_2 > \varepsilon_1 \quad (\bar{\alpha} > 0,\ C > 0) \quad (23)$$

$$\bar{\alpha} \in \left[2(\varepsilon_1 - \varepsilon_2), +\infty\right] \quad \varepsilon_2 < \varepsilon_1 \quad (\bar{\alpha} > 0,\ C > 0) \quad (24)$$

$$\bar{\alpha} \in \left[-(\varepsilon_2 - \varepsilon_1), 0\right] \quad \varepsilon_2 > \varepsilon_1 \quad (\bar{\alpha} < 0,\ C > 0) \quad (25)$$

$$\bar{\alpha} \in \left[\bar{\alpha}_+, 2(\varepsilon_1 - \varepsilon_2)\right] \quad \varepsilon_2 < \varepsilon_3 \quad (\bar{\alpha} > 0,\ C < 0) \quad (26)$$

or $\eta' = -w_0(\eta;\gamma)$ for

$$\bar{\alpha} = 0 \quad \varepsilon_2 > \varepsilon_1 \quad C = \varepsilon_2 - \varepsilon_1 \quad (27)$$

or $\eta' = w_0(\eta;\gamma)$ for

$$\bar{\alpha} = -2(\varepsilon_2 - \varepsilon_1) \quad C = 0 \quad (28)$$

where $w = \sqrt{\left(\eta^2 + k_2^2\right)^2 + 2\bar{\alpha}C}$, $w_0 = \eta^2 + k_2^2$, and $\bar{\alpha}_\pm = \varepsilon_1 - \varepsilon_2 \pm \sqrt{(\varepsilon_1 - \varepsilon_2)^2 - (\varepsilon_3 - \varepsilon_2)^2}$.

4.2 Proof

Taking into account that τ must be nonnegative because $\tau = y^2$ (y is a real function), and solving Equation (21) with respect to τ for $(\bar{\alpha} \neq 0) \wedge (C \neq 0)$ one finds

$$\tau_\pm = \alpha^{-1}\left[\pm\sqrt{\left(\eta^2 + k_2^2\right)^2 + 2\bar{\alpha}C} - \left(\eta^2 + k_2^2\right)\right]. \quad (29)$$

The cases $\bar{\alpha} = 0$ and $C = 0$ will be discussed separately.

Obviously, it is necessary to choose the branch in Equation (29) that gives $\tau\left[\eta(0)\right] = 1$. Let us analyze the radicand, which clearly must be nonnegative for all possible η (we take into account that the right-hand side of the second equation in Equation (20) must not vanish). We study the radicand conditionally on the sign of $\bar{\alpha}C$, and therefore distinguish three cases: $\bar{\alpha}C > 0$, $\bar{\alpha}C < 0$, and $\bar{\alpha}C = 0$. It is easy to derive that

$$\bar{\alpha}C > 0 \text{ for } \bar{\alpha} \in \left[-\infty, -2(\varepsilon_2 - \varepsilon_1)\right] \cup (0, +\infty),\ \varepsilon_2 > \varepsilon_1 \quad (30)$$

$$\bar{\alpha}C > 0 \text{ for } \bar{\alpha} \in (-\infty, 0) \cup \left[2(\varepsilon_1 - \varepsilon_2), +\infty\right],\ \varepsilon_1 > \varepsilon_2 \quad (31)$$

$$\bar{\alpha}C < 0 \text{ for } \bar{\alpha} \in \left[-2(\varepsilon_2 - \varepsilon_1), 0\right],\ \varepsilon_2 > \varepsilon_1 \quad (32)$$

$$\bar{\alpha}C < 0 \text{ for } \bar{\alpha} \in \left[0, 2(\varepsilon_1 - \varepsilon_2)\right],\ \varepsilon_1 > \varepsilon_2 \quad (33)$$

$$\bar{\alpha}C = 0 \text{ for } \bar{\alpha} = 0 \text{ or } C = 0. \quad (34)$$

Calculating $\tau_\pm(0) = \tau_\pm\left[\eta(0)\right]$ using Equations (18), (19), and (29), one finds

$$\tau_\pm(0) = \bar{\alpha}^{-1}\left[\pm\sqrt{(\varepsilon_2 - \varepsilon_1)^2 + 2\bar{\alpha}C} - (\varepsilon_2 - \varepsilon_1)\right]$$

$$= \bar{\alpha}^{-1}\left[\pm\sqrt{(\varepsilon_2 - \varepsilon_1 + \bar{\alpha})^2} - (\varepsilon_2 - \varepsilon_1)\right]. \quad (35)$$

Calculating $\tau_\pm(h) = \tau_\pm\left[\eta(h)\right]$ using Equations (19) and (29), one finds

$$\tau_{\pm}(h)=\bar{\alpha}^{-1}\left[\pm\sqrt{(\varepsilon_2-\varepsilon_3)^2+2\bar{\alpha}C}-(\varepsilon_2-\varepsilon_3)\right]. \quad (36)$$

Under the condition of Equation (30), it is clear that $\tau_-(0)=1$ for $\bar{\alpha}\in\left[-\infty,-2(\varepsilon_2-\varepsilon_1)\right]$ and $\tau_+(0)=1$ for $\bar{\alpha}\in(0,+\infty)$. It is also clear that $\eta'>0$ in the case $\bar{\alpha}\in\left[-\infty,-2(\varepsilon_2-\varepsilon_1)\right]$, that is, the function $\eta(x)$ increases for $x\in(0,h)$. Taking into account the formulas in Equation (19), one arrives at the conclusion that η has at least one breakpoint when $x\in(0,h)$. Since in this case $\bar{\alpha}<0$, $C<0$, then taking into account the analyses given at the beginning of this section, one finds that there is a point $x=x^*\in(0,h)$ in which $\lim_{x\to x^*}y(x)=\infty$. Since only continuous and bounded solutions are being sought, this case is then not interesting, and is not considered. It is important to note that since $\bar{\alpha}C>0$, then w has no branch points on the real axis; therefore, $\mathrm{Re}\left[\int_a^{\eta}\frac{ds}{w(s;\gamma)}\right]$ is a single-valued function. From this consideration, one obtains the case covered by the formulas in Equation (23). It can be checked that $\tau_+(h)$ is positive for $\bar{\alpha}\in(0,+\infty)$.

Under the condition of Equation (31), it is clear that $\tau_-(0)=1$ for $\bar{\alpha}\in(-\infty,0)$ and $\tau_+(0)=1$ for $\bar{\alpha}\in\left[2(\varepsilon_1-\varepsilon_2),+\infty\right]$. Repeating the arguments given in the preceding paragraph, one arrives at the conclusion that the case with $\bar{\alpha}\in(-\infty,0)$ also drops out from further analysis. From this consideration, one obtains the case covered by Equation (24). It can be checked that $\tau_+(h)$ is positive for $\bar{\alpha}\in(0,+\infty)$.

Analyzing Equation (35) under the condition of Equation (32), one must choose τ_+ if $\bar{\alpha}>-(\varepsilon_2-\varepsilon_1)$ or τ_- if $\bar{\alpha}<-(\varepsilon_2-\varepsilon_1)$. Choosing τ_- for $\bar{\alpha}\in\left[-2(\varepsilon_2-\varepsilon_1),-(\varepsilon_2-\varepsilon_1)\right]$, one obtains $\eta'>0$. This means that η increases for $x\in(0,h)$. Taking into account Equation (19), one arrives at the conclusion that η has at least one breakpoint when $x\in(0,h)$. Since in this case $\bar{\alpha}<0$, $C>0$, then taking into account the analyses given in the beginning of this section, one finds that there is a point $x=x^*\in(0,h)$ at which either $\lim_{x\to x^*}y(x)=0$ or $\lim_{x\to x^*}y(x)=\infty$. Since $y(0)=1>0$ and $\eta'>0$, then one comes to the conclusion that $\lim_{x\to x^*}y(x)=\infty$. Since only continuous and bounded solutions are sought, then this case is not interesting, as well.

Carrying out similar considerations for the branch τ_+ and $\bar{\alpha}\in\left[-(\varepsilon_2-\varepsilon_1),0\right]$, one finds that breakpoints of η – if they arise – arise due to y vanishing at some points (in this case, $\eta'<0$). The radicand in Equation (36) is positive under the condition of Equation (32). Exclusion of the point $\bar{\alpha}=-(\varepsilon_2-\varepsilon_1)$ will be explained in Section 5 (see Equation (48)). From this consideration, one obtains the case covered by Equation (25).

Analyzing Equation (35) under the condition of Equation (33), one must choose τ_+ if $\bar{\alpha}>\varepsilon_1-\varepsilon_2$ or τ_- if $\bar{\alpha}<\varepsilon_1-\varepsilon_2$. It is also clear that $\eta'>0$ in the case $\bar{\alpha}\in(0,\varepsilon_1-\varepsilon_2)$, that is, the function $\eta(x)$ increases for $x\in(0,h)$. Taking into account Equation (19), one arrives at the conclusion that η has at least one breakpoint when $x\in(0,h)$. Since in this case $\bar{\alpha}>0$, $C<0$, then taking into account the analyses given in the beginning of this section, one finds that there is no point $x=x^*\in(0,h)$ in which $\lim_{x\to x^*}y(x)=0$ or $\lim_{x\to x^*}y(x)=\infty$. This means that η cannot possess an infinite value. At first sight, this case must be excluded from further consideration. However, the function w has branch points on the real axis, and therefore $\mathrm{Re}\left[\int_a^{\eta}\frac{ds}{w(s;\gamma)}\right]$ is multivalued. This case must therefore also be studied. Considering Equation (36), one finds that the conditions $\bar{\alpha}>0$, $C<0$ lead to the inequality $\varepsilon_2<\varepsilon_3$. The radicand in Equation (36) must be positive. This is true if $\bar{\alpha}\in(0,\bar{\alpha}_-)\cap\left[\bar{\alpha}_+,2(\varepsilon_1-\varepsilon_2)\right]$. Obviously, $\alpha_-\leqslant\varepsilon_1-\varepsilon_2\leqslant\alpha_+$. If $\bar{\alpha}=\varepsilon_1-\varepsilon_2$, then the radicand in Equation (36) takes the form $(\varepsilon_2-\varepsilon_3)^2-(\varepsilon_2-\varepsilon_1)^2$. This formula implies that $\varepsilon_1>\varepsilon_3$ and $\varepsilon_2>\varepsilon_3$. The latter formula contradicts the inequality $\varepsilon_2<\varepsilon_3$ given earlier in this paragraph. For this reason, the point $\bar{\alpha}=\varepsilon_1-\varepsilon_2$ is excluded. One thus obtains the cases covered by Equations (22) and (26).

If $\bar{\alpha}=0$ (this is the well-known linear case), then from Equation (21), one finds that $\tau(\eta)=\frac{\varepsilon_2-\varepsilon_1}{\eta^2+k_2^2}$. From this one obtains $\tau(0)=1$, $\tau(h)=\frac{\varepsilon_2-\varepsilon_1}{\varepsilon_2-\varepsilon_3}$. It is easy to show that $\varepsilon_2>\varepsilon_1$ must be satisfied. Indeed, let us get back to Equation (14) with the conditions of Equation (15). Multiplying by y and integrating from 0 to h, one finds from Equation (14) that

$$\left(\varepsilon_2-\gamma^2\right)\int_0^h y^2(x)\,dx=k_1y^2(0)+k_3y^2(h)+\int_0^h y'^2(x)\,dx \quad (37)$$

Using Equation (37) and taking into account Equation (13), one finds that the inequality $\varepsilon_1<\gamma^2<\varepsilon_2$ must be fulfilled.

If $C=0$, then $\bar{\alpha}=-2(\varepsilon_2-\varepsilon_1)$. Taking this into account, one finds from Equation (21) that $\tau(\eta)=\frac{\eta^2+k_2^2}{\varepsilon_2-\varepsilon_1}$ which gives $\tau(0)=1$, $\tau(h)=\frac{\varepsilon_2-\varepsilon_3}{\varepsilon_2-\varepsilon_1}$.

At this stage, the latter formula gives $\tau(h)>0$ for $\varepsilon_2>\varepsilon_1$ or $\varepsilon_2<\varepsilon_3$.

4.3 Remark 2

The linear case is very important for both linear and nonlinear theories. For this reason, the solvability of this case will be considered in detail (see Section 5).

4.4 Remark 3

The condition $C=0$ implies $\alpha Y^2(0)=-2(\varepsilon_2-\varepsilon_1)$ Since this condition imposes serious restrictions on the parameters of the problem, then the case covered by Equation (28) seems to be very special. Indeed, a slight change of the parameters destroys the latter condition, and

we are faced with the necessity of solving one of the other cases in Statement 1. For this reason, this case is omitted.

5. Dispersion Equations

In this section, dispersion equations are derived for each of the cases indicated in Statement 1.

5.1 Cases Covered by Equations (23), (24), and (25)

The eigenvalues of the problem $P(\bar{\alpha})$ are determined as roots of the so-called dispersion equation, which has the form [25, 26]

$$\Phi(\gamma;n)\equiv\int_{-k_3}^{k_1}\frac{ds}{w(s;\gamma)}+n\int_{-\infty}^{+\infty}\frac{ds}{w(s;\gamma)}=h\,,$$

$$n=0,1,2,\ldots \tag{38}$$

It should be noted that the left-hand side of Equation (38) does not depend on h. Equation (38) is the dispersion equation, which is true for any positive finite h. In fact, Equation (38) is a family (but not a system) of equations for different n. One must solve this with respect to γ for each of the equations. To be more precise, the following result takes place.

5.1.1 Theorem 1 (of Equivalence)

The value $\hat{\gamma}$ is an eigenvalue of the problem $P(\bar{\alpha})$ if and only if there is an integer $n=\hat{n}\geqslant 0$ such that $\gamma=\hat{\gamma}$ is a solution to $\Phi(\gamma;\hat{n})=h$.

The corresponding eigenfunction $y(x;\hat{\gamma})$ has exactly $\hat{n}$ (simple) zeros $x_1,\ldots,x_{\hat{n}}\in(0,h)$, where

$$x_i=\int_{-\infty}^{k_1}\frac{ds}{w(s;\hat{\gamma})}+(i-1)\int_{-\infty}^{+\infty}\frac{ds}{w(s;\hat{\gamma})}\,. \tag{39}$$

5.1.2 Proof

Since $\eta'=-w<0$, then the function $\eta(x)$ monotonically decreases for $x\in[0,h]$. It is supposed that the function η can have discontinuities inside the interval $(0,h)$. To be exact, let the function η have n breakpoints $x_1,\ldots,x_n\in(0,h)$. If $n=0$, then the function $\eta(x)$ is continuous on the interval $(0,h)$. We later discuss whether at these points $\tau(x_i)=0$ or $\lim_{x\to x_i}\tau(x)=+\infty$.

Since $\eta=\eta(x)$ monotonically decreases, then

$$\eta(x_i-0)=-\infty\,, \tag{40}$$

$$\eta(x_i+0)=+\infty\,,\ \text{where}\ \ i=\overline{1,n}\,.$$

Taking all this into account, solutions to the second equation in Equations (20) are sought on each of the (semi) intervals $[0,x_1)$, (x_1,x_2), …, $(x_n,h]$. Integrating $\eta'=-w$, one finds

$$\begin{cases}\displaystyle\int_{\eta(x)}^{\eta(x_1-0)}\frac{ds}{w(s)}=x+c_0, & 0\leqslant x<x_1;\\ \displaystyle-\int_{\eta(x_i+0)}^{\eta(x)}\frac{ds}{w(s)}=x+c_i, & x_i<x<x_{i+1},\ i=\overline{0,n-1};\\ \displaystyle-\int_{\eta(x_n+0)}^{\eta(x)}\frac{ds}{w(s)}=x+c_n, & x_n<x\leqslant h.\end{cases} \tag{41}$$

Substituting $x=0$, $x=x_{i+1}-0$, $x=h$ into, respectively, the first, second, and third equations of Equation (41), one determines constants $c_0,c_1,\ldots,c_n$:

$$\begin{cases}c_0=\displaystyle\int_{\eta(0)}^{\eta(x_1-0)}\frac{ds}{w(s)};\\ c_i=\displaystyle-\int_{\eta(x_i+0)}^{\eta(x_{i+1}-0)}\frac{ds}{w(s)}-x_{i+1},\ \ i=\overline{1,n-1};\\ c_n=\displaystyle-\int_{\eta(x_n+0)}^{\eta(h)}\frac{ds}{w(s)}-h.\end{cases} \tag{42}$$

With a glance at Equation (42), one can rewrite Equations (41) in the form

$$\begin{cases}\displaystyle\int_{\eta(x)}^{\eta(x_1-0)}\frac{ds}{w(s)}=x+\int_{\eta(0)}^{\eta(x_1-0)}\frac{ds}{w(s)}, & 0\leqslant x<x_1;\\ \displaystyle-\int_{\eta(x_i+0)}^{\eta(x)}\frac{ds}{w(s)}=x-\int_{\eta(x_i+0)}^{\eta(x_{i+1}-0)}\frac{ds}{w(s)}-x_{i+1}, & x_i<x<x_{i+1},\ i=\overline{1,n-1};\\ \displaystyle-\int_{\eta(x_n+0)}^{\eta(x)}\frac{ds}{w(s)}=x-\int_{\eta(x_n+0)}^{\eta(h)}\frac{ds}{w(s)}-h, & x_n<x\leqslant h.\end{cases} \tag{43}$$

Substituting $x = x_1 - 0$, $x = x_i + 0$, $x = x_n + 0$ into, respectively, the first, second, and third equations of Equation (43), one obtains

$$\begin{cases} 0 = x_1 + \int\limits_{\eta(0)}^{\eta(x_1-0)} \dfrac{ds}{w(s)}, \\ 0 = x_i - \int\limits_{\eta(x_i+0)}^{\eta(x_{i+1}-0)} \dfrac{ds}{w(s)} - x_{i+1}, \quad i = \overline{1, n-1}; \\ 0 = x_n - \int\limits_{\eta(x_n+0)}^{\eta(h)} \dfrac{ds}{w(s)} - h. \end{cases} \tag{44}$$

Taking into account Equations (19) and (40), one finds from Equation (44) that

$$\begin{cases} 0 < x_1 = \int\limits_{-\infty}^{k_1} \dfrac{ds}{w(s)}, \\ 0 < x_{i+1} - x_i = \int\limits_{-\infty}^{+\infty} \dfrac{ds}{w(s)}, \quad i = \overline{1, n-1}; \\ 0 < h - x_n = \int\limits_{-k_3}^{+\infty} \dfrac{ds}{w(s)}. \end{cases} \tag{45}$$

Equation (45) gives explicit expressions for the distances between the zeros of the function y; Equation (39) is easily derived from Equation (45). It also follows from Equation (45) that the improper integrals on the right-hand sides converge.

Further, summing up all the terms in Equation (45), one gets

$$x_1 + x_2 - x_1 + x_3 - x_2 + \ldots + x_{n-1}$$

$$- x_{n-2} + x_n - x_{n-1} + h - x_n$$

$$= \int\limits_{-\infty}^{k_1} \frac{ds}{w(s)} + (n-1) \int\limits_{-\infty}^{+\infty} \frac{ds}{w(s)} + \int\limits_{-k_3}^{+\infty} \frac{ds}{w(s)}.$$

This formula can easily be transformed into the dispersion equation of Equation (38).

In fact, we have proven that if $\gamma = \hat{\gamma}$ is an eigenvalue of the problem $P(\alpha)$, then $\gamma = \hat{\gamma}$ satisfies the equation $\Phi(\gamma; n) = h$ with $n = \hat{n}$. To complete the proof, one must prove that if $\gamma = \hat{\gamma}$ is a solution to the dispersion equation of Equation (38), then $\hat{\gamma}$ is an eigenvalue of the problem $P(\alpha)$.

Indeed, let $\gamma = \hat{\gamma}$ be a solution to the dispersion equation of Equation (38) with $n = \hat{n}$. Taking into account the classical results of ordinary differential-equation theory and Equation (17), there exists a unique solution $y \equiv y(x; \hat{\gamma})$ to the Cauchy problem for Equation (14) with initial data $y(0) = 1 \neq 0$, $y'(0) = k_1$. At this step, we do not assert that the condition $y'(h; \hat{\gamma}) / y(h; \hat{\gamma}) = -k_3$ is fulfilled. Using the solution $y \equiv y(x; \hat{\gamma})$, we construct the functions $\tau = y^2$ and $\eta = y'/y$. It is clear that $\tau(0) = 1$, $\eta(0) = k_1$. Let us suppose that $\eta(h) = y'(h)/y(h) \neq -k_3$; for certainty, let $\eta(h)$ be equal to $-a < -k_3$.

On the one hand, deriving Equation (38) for the functions τ and η, one obtains

$$\int\limits_{-a}^{k_1} \frac{ds}{w(s)} + \hat{n} \int\limits_{-\infty}^{+\infty} \frac{ds}{w(s)} = h. \tag{46}$$

On the other hand, $\gamma = \hat{\gamma}$ satisfies Equation (38). It should be noted that in Equations (46) and (38), the integrands are the same and positive. Subtracting Equation (38) from Equation (46), one finds

$$\int\limits_{-a}^{-k_3} \frac{ds}{w(s)} = 0. \tag{47}$$

By virtue of the obvious estimation

$$\int\limits_{-\infty}^{+\infty} \frac{ds}{w(s)} > \int\limits_{-a}^{-k_3} \frac{ds}{w(s)} > 0,$$

one finds that Equation (47) is fulfilled only for $a = k_3$. This means that $\hat{\gamma}$ is an eigenvalue of the problem $P(\alpha)$.

The assumption that the function η has n breakpoints results in the statement about n zeros of an eigenfunction $y(x; \hat{\gamma})$.

In the cases covered by Equations (23), (24), in which $\bar{\alpha} C > 0$, there are no additional restrictions on γ; in these cases, $\gamma^2 \in (\varepsilon_1, +\infty)$. The case covered by Equation (25), in which $\bar{\alpha} C < 0$, must be studied more carefully. Indeed, in this case, the function w^2 can be rewritten in the following way:

$$w^2 = \left[\eta^2 + \left(\varepsilon_2 - \gamma^2 - \sqrt{-2\bar{\alpha} C} \right) \right]$$

$$\left[\eta^2 + \left(\varepsilon_2 - \gamma^2 + \sqrt{-2\bar{\alpha} C} \right) \right].$$

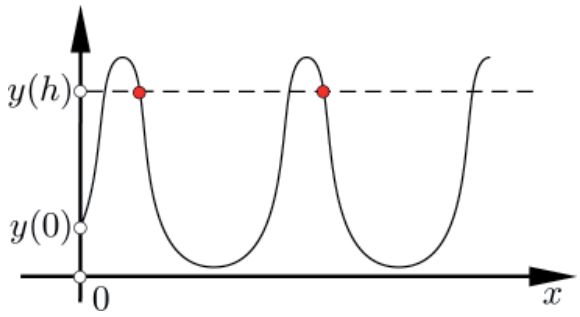

Figure 2a. A schematic view of an eigenfunction.

Taking into account that the radicand in w must be nonnegative for all possible η, one finds that the condition $\gamma^2 < \varepsilon_2 - \sqrt{-2\bar{\alpha}C}$ must be fulfilled. Taking into account the condition of Equation (13), one obtains from the previous inequality the following necessary condition:

$$\varepsilon_1 < \gamma^2 < \varepsilon_2 - \sqrt{-2\bar{\alpha}C}. \qquad (48)$$

This also implies $\varepsilon_2 > \varepsilon_1$, which agrees with Equation (25). From Equation (48), one finds $\varepsilon_1 < \varepsilon_2 - \sqrt{-2\bar{\alpha}C}$; this inequality is easily transformed into $\left(\varepsilon_2 - \varepsilon_1 + \bar{\alpha}\right)^2 > 0$. The latter is always fulfilled with the exception of the point $\bar{\alpha} = -\left(\varepsilon_2 - \varepsilon_1\right)$, which we excluded from the case covered by Equation (25) in Statement 1.

5.2 Cases Covered by Equations (22) and (26)

The function w^2 can be written in the form

$$w^2 = \left(a_-^2 - \eta^2\right)\left(a_+^2 - \eta^2\right),$$

where

$$a_\pm^2 = \gamma^2 - \varepsilon_2 \pm \sqrt{-2\bar{\alpha}C}$$

and

$$-a_+ < -a_- < -k_3 < 0 < +k_1 < +a_- < +a_+ .$$

At first, we are going to consider the case covered by Equation (22). As is known from Section 4, in this case, η must not possess an infinite value, that is, y does not take zero value. Since $\eta' = w > 0$, then the function η increases. However, Equation (19) shows that if η is continuous, then η must change its sign.

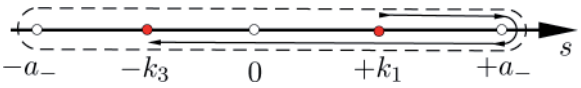

Figure 2b. The route of integration for the case covered by Equation (22).

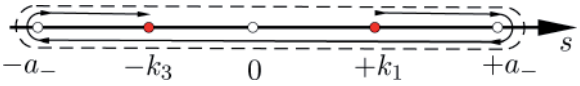

Figure 2c. The route of integration for the case covered by Equation (26).

Taking into account that the function w has branch points on the real axis, it is clear that in integrating the equation $\eta' = w$, one must not go directly from $\eta(0)$ to $\eta(h)$. As is shown in Figures 2b and 2c, starting from $\eta(0) = +k_1$, there are two ways to reach $\eta(h) = -k_3$.

Let us consider Figure 2b. Going one time over the route shown with a solid curve and then starting from the point $-k_3$ and going clockwise n times over the route shown with a dashed curve, one obtains

$$\int_{+k_1}^{+a_-} \frac{ds}{w(s;\gamma)} + \int_{+a_-}^{-k_3} \frac{ds}{-w(s;\gamma)} + 2n\int_{-a_-}^{+a_-} \frac{ds}{w(s;\gamma)} = h,$$

where $n = 0,1,2,\ldots$ After simple algebra, one finally arrives at the dispersion equation in the form

$$\int_{+k_1}^{+k_3} \frac{ds}{w(s;\gamma)} + (2n+1)\int_{-a_-}^{+a_-} \frac{ds}{w(s;\gamma)} = h.$$

Let us consider Figure 2c. Going one time over the route shown with a solid curve and then starting from the point $-k_3$ and going clockwise n times over the route shown with a dashed curve, one obtains:

$$\int_{+k_1}^{+a_-} \frac{ds}{w(s;\gamma)} + \int_{+a_-}^{-a_-} \frac{ds}{-w(s;\gamma)}$$

$$+ \int_{-a_-}^{-k_3} \frac{ds}{w(s;\gamma)} + 2n\int_{-a_-}^{+a_-} \frac{ds}{w(s;\gamma)} = h,$$

where $n = 0,1,2,\ldots$ After simple algebra, one finally arrives at the dispersion equation in the form

$$-\int_{-k_3}^{+k_1} \frac{ds}{w(s;\gamma)} + (2n+2)\int_{-a_-}^{+a_-} \frac{ds}{w(s;\gamma)} = h.$$

Let us pass to the case covered by Equation (26). As is known from Section 4, in this case, η must not possess an infinite value, that is y does not take zero value. Since $\eta' = -w < 0$, then the function η decreases. At first glance, Equation (19) does not contradict the behavior of η. However, taking into account Figure 2a, it is clear that if η is continuous, then η must change its sign.

In this case, it is also true that in integrating the equation $\eta' = -w$, one must not go directly from the point $\eta(0)$ to $\eta(h)$. As is shown in Figures 2b and 2c, starting from $\eta(0) = +k_1$, there are two ways to reach $\eta(h) = -k_3$.

Let us consider Figure 2b. Going one time around the route shown with a solid curve and then starting from the point $-k_3$ and going counterclockwise n times around the route shown with a dashed curve, one obtains

$$\int_{+k_1}^{+a_-} \frac{ds}{-w(s;\gamma)} + \int_{+a_-}^{-k_3} \frac{ds}{w(s;\gamma)} + 2n \int_{-a_-}^{+a_-} \frac{ds}{w(s;\gamma)} = h,$$

where $n = 1, 2, 3, \ldots$ After simple algebra, one finally arrives at the dispersion equation in the form

$$-\int_{+k_1}^{+k_3} \frac{ds}{w(s;\gamma)} + (2n-1) \int_{-a_-}^{+a_-} \frac{ds}{w(s;\gamma)} = h.$$

Let us consider Figure 2c. Going one time along the route shown with a solid curve and then starting from the point $-k_3$ and going counterclockwise n times along the route shown with a dashed curve, one obtains

$$\int_{+k_1}^{+a_-} \frac{ds}{-w(s;\gamma)} + \int_{+a_-}^{-a_-} \frac{ds}{w(s;\gamma)}$$

$$+ \int_{-a_-}^{-k_3} \frac{ds}{-w(s;\gamma)} + 2n \int_{-a_-}^{+a_-} \frac{ds}{w(s;\gamma)} = h,$$

where $n = 1, 2, 3, \ldots$ After simple algebra, one finally arrives at the dispersion equation in the form

$$\int_{-k_3}^{+k_1} \frac{ds}{w(s;\gamma)} + (2n-2) \int_{-a_-}^{+a_-} \frac{ds}{w(s;\gamma)} = h.$$

The classical theory in [58, 59] clarifies the derived formulas. A theorem of equivalence (similar to Theorem 1) can be proven for these two dispersion equations, as well.

5.3 Linear Case

If $\alpha = 0$, the problem $P(\alpha)$ becomes linear. We call it $P(0)$: see Equation (27).

Taking into account Statement 1 (Section 4) and Theorem 1 (this section), one obtains the dispersion equation of Equation (38) in the form

$$\Phi_0(\gamma; n) \equiv \int_{-k_3}^{k_1} \frac{d\eta}{k_2^2 + \eta^2} + n \int_{-\infty}^{+\infty} \frac{d\eta}{k_2^2 + \eta^2} = h, \qquad (49)$$

where $n \geqslant 0$ is an integer. After calculating the integrals and simplifying, one obtains

$$\Phi_0(\gamma; n) := \frac{1}{k_2} \arctan \frac{k_1 + k_3}{k_2^2 - k_1 k_3} + n\pi = h. \qquad (50)$$

Finally, taking the tangent of Equation (50), one arrives at

$$\tan k_2 h = \frac{k_1 + k_3}{k_2^2 - k_1 k_3}. \qquad (51)$$

This equation is usually derived using explicit solutions to the linear equation $Y'' = -k_2^2 Y$ and Equation (15); however, Equations (49) and (50) are more informative.

Equation (51) is a classical equation in electromagnetics [22, 27, 28]. The roots of this equation are propagation constants of an electromagnetic TE wave propagating along the surface of the dielectric layer Σ with constant permittivity.

Simple analysis of Equation (49) (or Equation (50), or Equation (51)) allows one to formulate the following:

5.3.1 Statement 2

If $\varepsilon_2 > \varepsilon_1$ and

$$h > h_{\min}^{\text{lin}} = \frac{1}{\sqrt{\varepsilon_2 - \varepsilon_1}} \arctan \frac{\sqrt{\varepsilon_1 - \varepsilon_3}}{\sqrt{\varepsilon_2 - \varepsilon_1}} > 0,$$

then the problem $P(0)$ has a finite number (not less than one) of positive eigenvalues $\tilde{\gamma}_1 < \tilde{\gamma}_2 < \ldots < \tilde{\gamma}_p$ (each of multiplicity one). For any $\tilde{\gamma}_i$, it is true that $\tilde{\gamma}_i^2 \in (\varepsilon_1, \varepsilon_2)$, $i = \overline{1, p}$. If $\varepsilon_1 = \varepsilon_3$, then $h_{\min}^{\text{lin}} = 0$.

If $\varepsilon_2 \leqslant \varepsilon_1$, then the problem $P(0)$ has no solutions.

The boundary value, $Y(h)=B$, of an eigenfunction $Y(x)$ is determined from the equation $B^2=\frac{\varepsilon_2-\varepsilon_1}{\varepsilon_2-\varepsilon_3}A^2$ (see Sections 3 and 4). The sign of $Y(h)$ is conditionally defined based on the number of zeros of the eigenfunction $Y(x)$: if $Y(x)$ has an even number of zeros, then $Y(h)>0$ if $Y(x)$ has an odd number of zeros, then $Y(h)<0$ (see Theorem 1; we take into account that $A>0$).

5.3.2 Remark 4

In the linear case, there are no periodic solutions that do not take zero value. Indeed, the explicit form of the eigenfunctions is $y=C_1\sin k_2x+C_2\cos k_2x$, where C_1 and C_2 are determined using Equation (15). If this linear combination does not take zero values, then it cannot be periodic.

In each of the cases considered (nonlinear and linear), an explicit formula for the period of the eigenfunctions can easily be extracted from the derived dispersion equations. To be more precise, if an eigenfunction $y(x;\hat{\gamma})$ is periodic, then its real period is equal to $2\int_{-\infty}^{+\infty}\frac{ds}{w(s;\hat{\gamma})}$ for the cases covered by Equations (23) [25, 26], (24), and (25); is equal to $2\int_{-a_-}^{+a_-}\frac{ds}{w(s;\hat{\gamma})}$ for the cases covered by Equations (22) and (26); and is equal to $\frac{2\pi}{\sqrt{\varepsilon_2-\hat{\gamma}^2}}$ for the linear case.

5.3.3 Remark 5

Obviously, an eigenfunction y in each of the cases considered achieves its maximum value inside the interval $(0,h)$. Since in this point $y'=0$, then the maximum is explicitly determined using Equation (17): for further details, see Section 4. If an eigenfunction y achieves its minimum value inside the interval $(0,h)$, then the minimum is also explicitly determined using Equation (17).

In the next section, we present complete results about the solvability of the problem $P(\bar{\alpha})$ for each of the studied cases. It is convenient to gather all the results in one place in the order as they given in Statement 1.

The dispersion equation of the problem $P(\bar{\alpha})$ has the following form:

$$\Phi_i(\gamma;n)=h,\quad \text{where } i=\overline{\text{I,V}}. \tag{52}$$

The function Φ_i has one of the following forms:

Case I

$$\Phi_{\text{I}}(\gamma;n)$$

$$\equiv\begin{cases}-\int_{-k_3}^{+k_1}\frac{ds}{w(s;\gamma)}+(2n+2)\int_{-a_-}^{+a_-}\frac{ds}{w(s;\gamma)}, & n=0,1,2,\ldots,\\ \int_{+k_1}^{+k_3}\frac{ds}{w(s;\gamma)}+(2n+1)\int_{-a_-}^{+a_-}\frac{ds}{w(s;\gamma)}, & n=0,1,2,\ldots,\end{cases} \tag{53}$$

where $\bar{\alpha}\in(0,\bar{\alpha}_-)$, $\gamma^2>\varepsilon_1\geqslant\varepsilon_3>\varepsilon_2$, ($\bar{\alpha}>0$, $C<0$);

Case II

$$\Phi_{\text{II}}(\gamma;n)\equiv\int_{-k_3}^{+k_1}\frac{ds}{w(s;\gamma)}+n\int_{-\infty}^{+\infty}\frac{ds}{w(s;\gamma)},\quad n=0,1,2,\ldots, \tag{54}$$

where $\bar{\alpha}\in(0,+\infty)$, $\varepsilon_2>\varepsilon_1\geqslant\varepsilon_3$, $\gamma^2>\varepsilon_1$ ($\bar{\alpha}>0$, $C>0$);

Case III

$$\Phi_{\text{III}}(\gamma;n)\equiv\int_{-k_3}^{+k_1}\frac{ds}{w(s;\gamma)}+n\int_{-\infty}^{+\infty}\frac{ds}{w(s;\gamma)},\quad n=0,1,2,\ldots, \tag{55}$$

where $\bar{\alpha}\in\left[2(\varepsilon_1-\varepsilon_2),+\infty\right]$, $\varepsilon_1>\varepsilon_2$, $\gamma^2>\varepsilon_1\geqslant\varepsilon_3$ ($\bar{\alpha}>0$, $C>0$);

Case IV

$$\Phi_{\text{IV}}(\gamma;n)\equiv\int_{-k_3}^{+k_1}\frac{ds}{w(s;\gamma)}+n\int_{-\infty}^{+\infty}\frac{ds}{w(s;\gamma)},\quad n=0,1,2,\ldots, \tag{56}$$

where $\bar{\alpha}\in\left[-(\varepsilon_2-\varepsilon_1),0\right]$, $\varepsilon_2>\varepsilon_1\geqslant\varepsilon_3$, $\varepsilon_1<\gamma^2<\varepsilon_2-\sqrt{-2\bar{\alpha}C}$ ($\bar{\alpha}<0$, $C>0$);

Case V

$$\Phi_{\text{V}}(\gamma;n)$$

$$\equiv\begin{cases}\int_{-k_3}^{+k_1}\frac{ds}{w(s;\gamma)}+(2n-2)\int_{-a_-}^{+a_-}\frac{ds}{w(s;\gamma)}, & n=1,2,3,\ldots,\\ -\int_{+k_1}^{+k_3}\frac{ds}{w(s;\gamma)}+(2n-1)\int_{-a_-}^{+a_-}\frac{ds}{w(s;\gamma)}, & n=1,2,3,\ldots,\end{cases} \tag{57}$$

where $\bar{\alpha} \in \left[\bar{\alpha}_+, 2(\varepsilon_1 - \varepsilon_2)\right]$, $\gamma^2 > \varepsilon_1 \geqslant \varepsilon_3 > \varepsilon_2$ ($\bar{\alpha} > 0$ $C < 0$).

The following notations are used:

$$w(s;\gamma) = \sqrt{\left(s^2 + k_2^2\right)^2 + 2\bar{\alpha}C},$$

$$k_1^2 = \gamma^2 - \varepsilon_1,$$

$$k_2^2 = \varepsilon_2 - \gamma^2,$$

$$k_3^2 = \gamma^2 - \varepsilon_3,$$

$$a_-^2 = \gamma^2 - \varepsilon_2 - \sqrt{-2\bar{\alpha}C},$$

and

$$\bar{\alpha}_\pm = -(\varepsilon_2 - \varepsilon_1) \pm \sqrt{(\varepsilon_2 - \varepsilon_1)^2 - (\varepsilon_2 - \varepsilon_3)^2}.$$

6. Main Results

In this section we present the main theoretical results (proofs are given in the next section). After each theorem, we also give a numerical example that partly illustrates the content of the theorem and, we hope, helps in better understanding the theoretical results. For each case, the dispersion curves (DCs) and eigenfunctions are plotted.

6.1 Remark 6

We should stress that all the results of this section apply for any frequency ω : see Equation (8). However, we do not assert that the Kerr law is valid for any frequency.

Below, two notations are used for the eigenvalues, $\hat{\gamma}$, of the problem $P(\bar{\alpha})$: $\hat{\gamma}_i$ means that all eigenvalues are arranged in their order of magnitude; $\hat{\gamma}(m)$ means that this eigenvalue is a solution to the dispersion equation $\Phi_i(\gamma; m) = h$.

6.2 Case I

6.2.1 Theorem 2 (Case I)

Let $\varepsilon_1 \geqslant \varepsilon_3 \geqslant \varepsilon_0 > 0$, $\varepsilon_2 < \varepsilon_3$, and $\bar{\alpha} \in (0, \bar{\alpha}_-)$. For any $h > 0$, the problem $P(\bar{\alpha})$ then has an infinite number of positive eigenvalues $\hat{\gamma}_i \left(> \sqrt{\varepsilon_1}\right)$ with an accumulation point at infinity.

For big γ and arbitrary fixed $\Delta > 0$, the following asymptotic two-sided inequality,

$$(1-\Delta)\gamma_\bullet(n) \leqslant \hat{\gamma}(n) \leqslant (1+\Delta)\gamma_\bullet(n+1/2)$$

is valid, where $\gamma_\bullet^2(n) = \varepsilon_2 - \sqrt{-2\bar{\alpha}C} + \left[f^{-1}\left(\frac{h}{4n+2}\right)\right]^2$, and f^{-1} is the inversion of $f(t) = t^{-1}\ln t$.

If $\hat{\gamma}_i \to \infty$, then $\max_{x\in(0,h)} \left|y(x;\hat{\gamma}_i)\right| \to \infty$.

6.2.2 Remark 7

Using first the integral of Equation (17), one finds that for any eigenfunction $y(x;\hat{\gamma})$, it is true that

$$\max_{x\in[0,h]} y(x;\hat{\gamma}) = \sqrt{\frac{-k_2^2 + \sqrt{k_2^4 + 2\bar{\alpha}C}}{\bar{\alpha}}},$$

$$\min_{x\in[0,h]} y(x;\hat{\gamma}) = \sqrt{\frac{-k_2^2 - \sqrt{k_2^4 + 2\bar{\alpha}C}}{\bar{\alpha}}}.$$

Obviously,

$$\lim_{\gamma\to+\infty} \max y(x;\hat{\gamma}) = +\infty,$$

$$\lim_{\gamma\to+\infty} \min y(x;\hat{\gamma}) = +0.$$

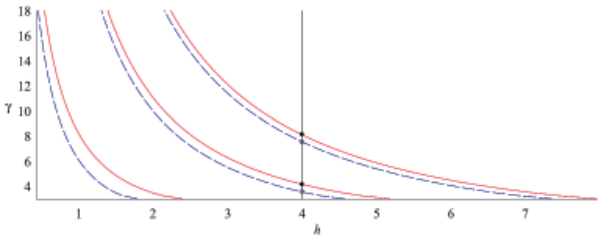

Figure 3. Case I: Dispersion curves. Only the first six dispersion curves are shown (for $n = 0,1,2$). The dispersion curves start from the point $\gamma = \sqrt{\varepsilon_1} = 3$, which is the lower bound for the spectral parameter. The vertical solid line corresponds to $h = 4$; points of intersections of this line with the dispersion curves are eigenvalues (empty and filled circles). The long-dashed curves correspond to the second row in Equation (53); the solid curves correspond to the first row in Equation (53).

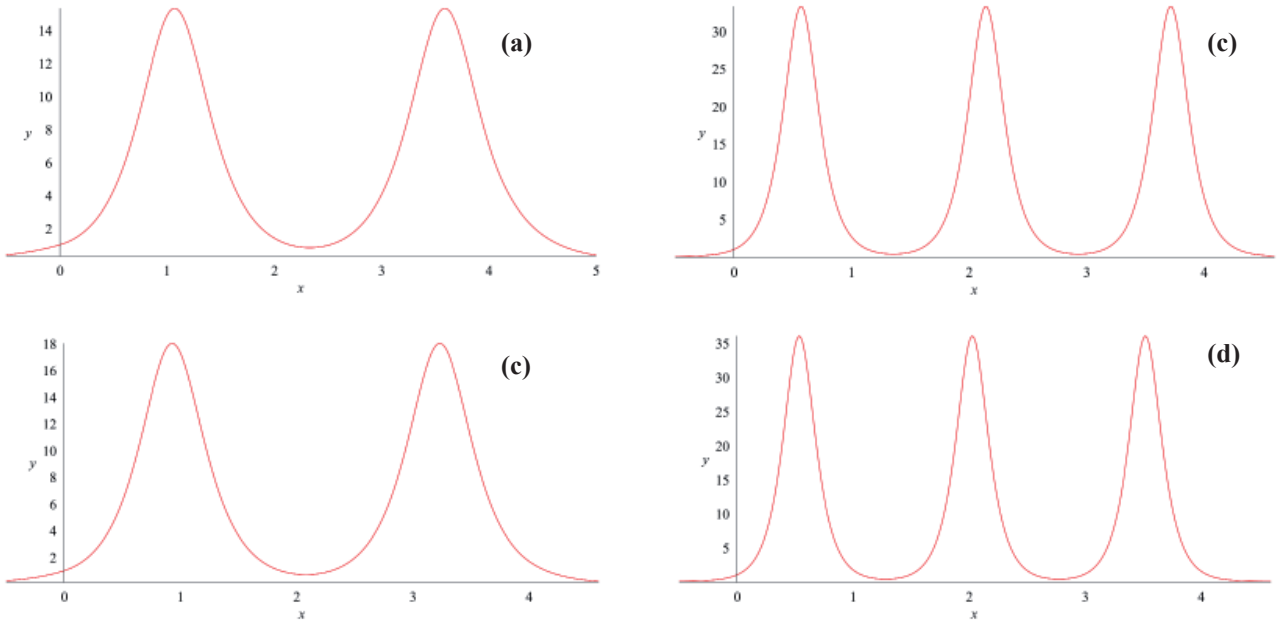

Figure 4. Case I: eigenfunctions for the eigenvalues marked in the previous figure: (a) $\hat{\gamma}_1 \approx 3.575$**, (b)** $\hat{\gamma}_3 \approx 7.521$ **(c)** $\hat{\gamma}_2 \approx 4.151$**, (d)** $\hat{\gamma}_4 \approx 8.137$**.**

The expression for the minimum is true if $y(x;\hat{\gamma})$ has more than one max for $x \in (0,h)$ (see Figure 2).

In Figures 3 and 4, the following parameters were used: $\varepsilon_1 = 9$, $\varepsilon_2 = 1$, $\varepsilon_3 = 4$, $\bar{\alpha} = 0.1$; the other parameters are specified in the captions.

6.3 Case II

6.3.1 Theorem 3 (Case II)

Let $\varepsilon_2 > \varepsilon_1 \geqslant \varepsilon_3 \geqslant \varepsilon_0 > 0$ and $\bar{\alpha} \in (0,+\infty)$. For any $h > 0$, the problem $P(\bar{\alpha})$ then has an infinite number of positive eigenvalues $\hat{\gamma}_i \left(> \sqrt{\varepsilon_1}\right)$ with an accumulation point at infinity.

If the problem $P(0)$ has p solutions $\tilde{\gamma}_1 < \tilde{\gamma}_2 < \ldots < \tilde{\gamma}_p$ then there exists $\bar{\alpha}_0 > 0$ such that for any $\bar{\alpha} = \bar{\alpha}' < \bar{\alpha}_0$ it is true that

$$\hat{\gamma}_1^2, \hat{\gamma}_2^2, \ldots, \hat{\gamma}_p^2 \in \left[\max(\varepsilon_1, \varepsilon_3), \varepsilon_2\right]$$

and

$$\lim_{\bar{\alpha}' \to 0} \hat{\gamma}_i = \tilde{\gamma}_i, \quad i = \overline{1,p},$$

where $\hat{\gamma}_1 < \hat{\gamma}_2 < \ldots < \hat{\gamma}_p$ are the first p solutions of the problem $P(\bar{\alpha}')$. If $q > p$, then $\lim_{\bar{\alpha}' \to +0} \hat{\gamma}_q^2 = +\infty$.

For big γ and arbitrary fixed $\Delta > 0$, the following asymptotic two-sided inequality,

$$(1-\Delta)\gamma_\bullet(n) \leqslant \hat{\gamma}(n) \leqslant (1+\Delta)\gamma_\bullet\left[\sqrt{2}(n+1)\right]$$

is valid, where $\gamma_\bullet^2(n) = \varepsilon_2 + \left[f^{-1}\left(\frac{h}{4n}\right)\right]^2$, and f^{-1} is the inversion of $f(t) = t^{-1}\ln t$.

If $\hat{\gamma}_i \to \infty$, then $\max_{x \in (0,h)} \left| y(x;\hat{\gamma}_i) \right| \to \infty$.

6.3.2 Remark 8

Using first the integral Equation (17), one finds that for any eigenfunction $y(x;\hat{\gamma})$, it is true that

$$\max_{x \in [0,h]} y(x;\hat{\gamma}) = +\sqrt{\frac{-k_2^2 + \sqrt{k_2^4 + 2\bar{\alpha}C}}{\bar{\alpha}}},$$

$$\min_{x \in [0,h]} y(x;\hat{\gamma}) = -\sqrt{\frac{-k_2^2 + \sqrt{k_2^4 + 2\bar{\alpha}C}}{\bar{\alpha}}}.$$

Obviously,

$$\lim_{\gamma \to +\infty} \max y(x;\hat{\gamma}) = +\infty, \quad \lim_{\gamma \to +\infty} \min y(x;\hat{\gamma}) = -\infty$$

In Figures 5 and 6, the following parameters were used: $\varepsilon_1 = \varepsilon_3 = 1$, $\varepsilon_2 = 4$, $\bar{\alpha} = 0.1$.

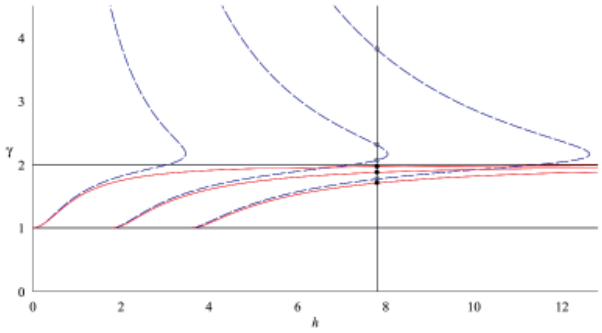

Figure 5. Case II: dispersion curves. Only the first three dispersion curves for the nonlinear case with $\bar{\alpha}=0.1$ and for the linear case with $\bar{\alpha}=0$ are shown. The long-dashed curves correspond to Equation (54) for $n=0,1,2$; the solid curves correspond to the solutions to the dispersion equation, Equation (51), for $n=0,1,2$. The horizontal solid line $\gamma=\sqrt{\varepsilon_1}=1$ is the lower bound for the spectral parameter; the horizontal solid line $\gamma=\sqrt{\varepsilon_2}=2$ is the asymptote for the linear case. The vertical solid line corresponds to $h=7.8$; points of intersections of this line with the dispersion curves are eigenvalues (empty circles for the nonlinear case and filled circles for the linear case).

6.4 Case III

6.4.1 Theorem 4 (Case III)

Let $\varepsilon_1 \geqslant \varepsilon_3 \geqslant \varepsilon_0 > 0$, $\varepsilon_1 > \varepsilon_2$, and $\bar{\alpha} \in \left[2(\varepsilon_1-\varepsilon_2),+\infty\right]$. For any $h>0$, the problem $P(\bar{\alpha})$ then has an infinite number of positive eigenvalues $\hat{\gamma}_i \left(>\sqrt{\varepsilon_1}\right)$ with an accumulation point at infinity.

For big γ and arbitrary fixed $\Delta>0$, the following asymptotic two-sided inequality

$$(1-\Delta)\gamma_\bullet(n) \leqslant \hat{\gamma}(n) \leqslant (1+\Delta)\gamma_\bullet\left[\sqrt{2}(n+1)\right]$$

is valid, where $\gamma_\bullet^2(n)=\varepsilon_2+\left[f^{-1}\left(\frac{h}{4n}\right)\right]^2$, and f^{-1} is the inversion of $f(t)=t^{-1}\ln t$.

If $\hat{\gamma}_i \to \infty$, then $\max_{x\in(0,h)}\left|y\left(x;\hat{\gamma}_i\right)\right| \to \infty$.

For the maximum and minimum values of an eigenfunction in this case, see Remark 8.

In Figures 7 and 8, the following parameters were used: $\varepsilon_1=\varepsilon_3=2$, $\varepsilon_2=1$, $\bar{\alpha}=2.5$.

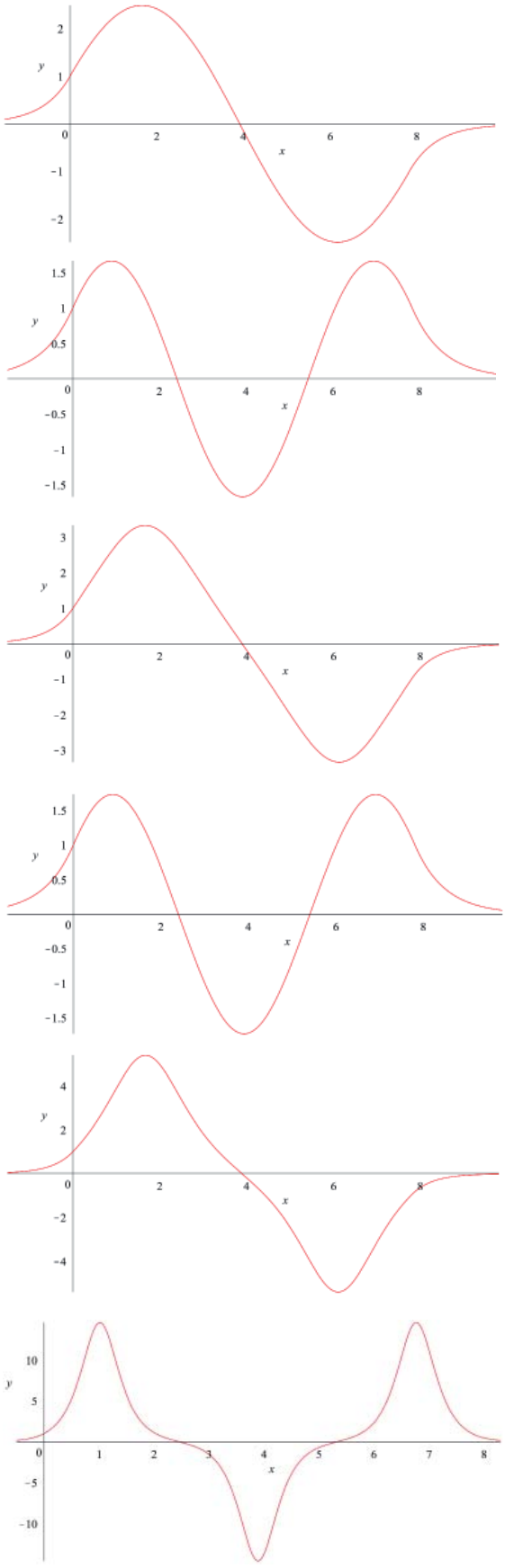

Figure 6. Case II: eigenfunctions for the eigenvalues marked in the previous figure: (a) $\tilde{\gamma}(1)\approx 1.8746$, (b) $\tilde{\gamma}(2)\approx 1.7089$, (c) $\hat{\gamma}_4\approx 2.0692$, (d) $\hat{\gamma}_3\approx 1.7691$, (e) $\hat{\gamma}_5\approx 2.3147$, (f) $\hat{\gamma}_6\approx 3.8216$.

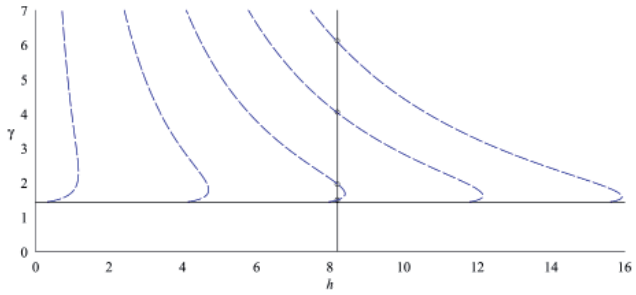

Figure 7. Case III: dispersion curves. Only the first five dispersion curves are shown (for $n = 0,1,2,3,4$). The dispersion curves start from the point $\gamma = \sqrt{\varepsilon_1} = \sqrt{2}$, which is the lower bound for the spectral parameter. The vertical solid line corresponds to $h = 8.2$; points of intersections of this line with the dispersion curves are eigenvalues (empty circles). The long-dashed curves correspond to Equation (55).

6.5 Case IV

6.5.1 Theorem 5 (Case IV)

Let $\varepsilon_2 > \varepsilon_1 \geqslant \varepsilon_3 \geqslant \varepsilon_0 > 0$ and $\bar{\alpha} \in \left[-(\varepsilon_2 - \varepsilon_1), 0\right]$. For any $h > \Phi_{\mathrm{IV}}(\varepsilon_1; 0) \geqslant 0$, the problem $P(\bar{\alpha})$ then has a finite number of positive eigenvalues $\hat{\gamma}_i$. It is true that $\hat{\gamma}_i^2 \in \left[\varepsilon_1, \varepsilon_2 - \sqrt{-2\bar{\alpha}(\varepsilon_2 - \varepsilon_1 + 0.5\bar{\alpha})}\right]$.

If the problem $P(\bar{\alpha})$ has p solutions $\hat{\gamma}_1 < \hat{\gamma}_2 < \ldots < \hat{\gamma}_p$ the problem $P(0)$ then has at least p solutions $\tilde{\gamma}_1 < \tilde{\gamma}_2 < \ldots < \tilde{\gamma}_p$. It is true that $\lim_{\bar{\alpha} \to 0} \hat{\gamma}_i = \tilde{\gamma}_i$ for $i = \overline{1, p}$.

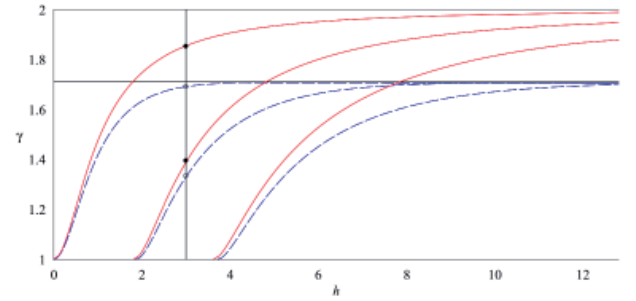

Figure 9. Case IV: dispersion curves. Only the first three dispersion curves for the nonlinear case with $\bar{\alpha} = -0.2$ and for the linear case with $\bar{\alpha} = 0$ are shown. The long-dashed curves correspond to Equation (56) for $n = 0,1,2$; the solid curves correspond to the solutions to dispersion equation in Equation (51) for $n = 0,1,2$. The horizontal solid line $\gamma = \sqrt{\varepsilon_1} = 1$ is the lower bound for the spectral parameter. The horizontal solid line $\gamma = \sqrt{4 - \sqrt{1.16}} \approx 1.709$ is the asymptote for the nonlinear case (see Equation (48)). The horizontal solid line $\gamma = \sqrt{\varepsilon_2} = 2$ is the asymptote for the linear case. The vertical solid line corresponds to $h = 3$; points of intersections of this line with the dispersion curves are eigenvalues (empty circles for the nonlinear case and filled circles for the linear case).

For the maximum and minimum values of an eigenfunction in this case, see Remark 8.

In Figures 9 and 10, the following parameters were used: $\varepsilon_1 = \varepsilon_3 = 1$, $\varepsilon_2 = 4$, $\bar{\alpha} = -0.2$.

6.6 Case V

Theorem 6 (Case V)

Let $\varepsilon_1 \geqslant \varepsilon_3 \geqslant \varepsilon_0 > 0$, $\varepsilon_2 < \varepsilon_3$, and $\bar{\alpha} \in \left[\bar{\alpha}_+, 2(\varepsilon_1 - \varepsilon_2)\right]$. For any $h > 0$, the problem $P(\bar{\alpha})$ then has an infinite number of positive eigenvalues $\hat{\gamma}_i \left(> \sqrt{\varepsilon_1}\right)$ with an accumulation point at infinity.

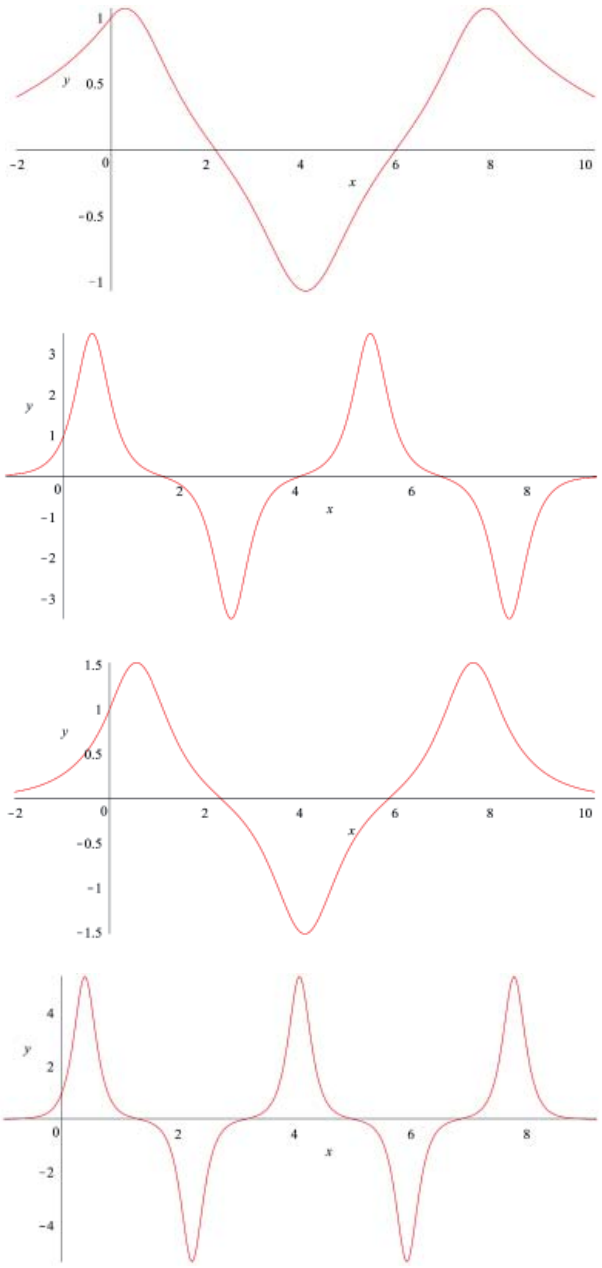

Figure 8. Case III: eigenfunctions for the eigenvalues marked in the previous figure: (a) $\hat{\gamma}_1 \approx 1.487$, (b) $\hat{\gamma}_3 \approx 4.035$ (c) $\hat{\gamma}_2 \approx 1.944$, (d) $\hat{\gamma}_4 \approx 6.099$.

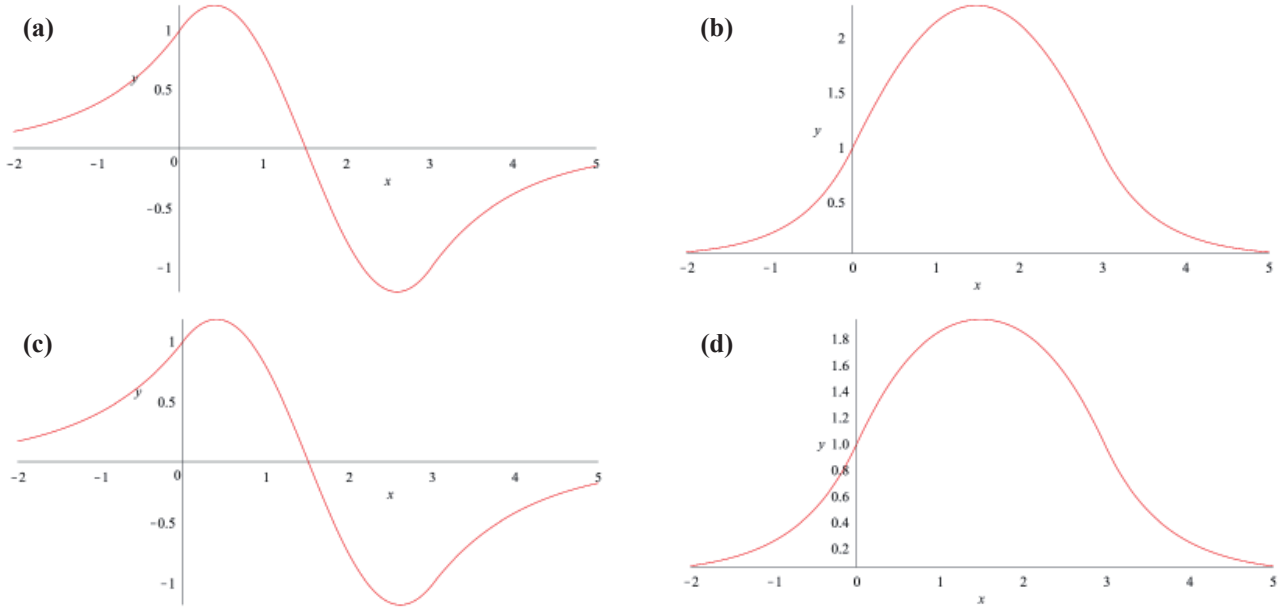

Figure 10. Case IV: eigenfunctions for the eigenvalues marked in the previous figure: (a) $\tilde{\gamma}_1 \approx 1.394$, (b) $\tilde{\gamma}_2 \approx 1.852$ (c) $\hat{\gamma}_1 \approx 1.333$, (d) $\hat{\gamma}_2 \approx 1.690$.

For big γ and arbitrary fixed $\Delta > 0$, the following asymptotic two-sided inequality,

$$(1-\Delta)\gamma_\bullet(n) \leqslant \hat{\gamma}(n) \leqslant (1+\Delta)\gamma_\bullet(n+1/2)$$

is valid, where $\gamma_\bullet^2(n) = \varepsilon_2 - \sqrt{-2\bar{\alpha}C} + \left[f^{-1}\left(\frac{h}{4n}\right)\right]^2$. f^{-1} is the inversion of $f(t) = t^{-1}\ln t$.

If $\hat{\gamma}_i \to \infty$, then $\max_{x\in(0,h)} \left| y\left(x;\hat{\gamma}_i\right)\right| \to \infty$.

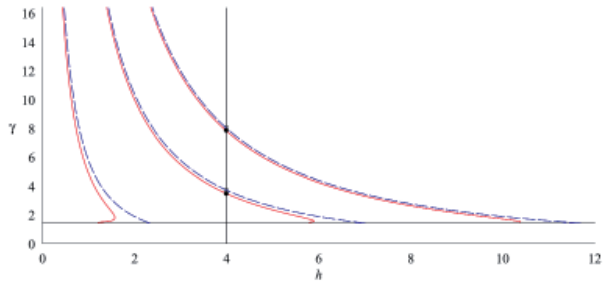

Figure 11. Case V: dispersion curves. Only the first six dispersion curves are shown (for $n = 1,2,3$). The dispersion curves start from the point $\gamma = \sqrt{\varepsilon_1} = \sqrt{3}$, which is the lower bound for the spectral parameter. The vertical solid line corresponds to $h = 4$; points of intersections of this line with the dispersion curves are eigenvalues (empty and filled circles). The long-dashed curves correspond to the second row in Equation (57); the solid curves correspond to the first row in Equation (57)

For the maximum and minimum values of an eigenfunction in this case, see Remark 7.

In Figures 11 and 12, the following parameters were used: $\varepsilon_1 = \varepsilon_3 = 2$, $\varepsilon_2 = 1$, $\bar{\alpha} = 1.5$.

7. Proofs

All the proofs are based on the estimations of the integrals, which the dispersion equations contain.

7.1 Proof of Case I

It is clear that (see Equations (52) and (53))

$$(2n+1)T \leqslant \Phi_1(\gamma;n) \leqslant (2n+2)T, \qquad (58)$$

where $n = 0,1,2,\ldots$ and

$$T = \int_{-a_-}^{+a_-} \frac{ds}{\sqrt{\left(k_2^2+s^2\right)^2 + 2\bar{\alpha}C}}$$

$$= 2\int_0^{+a_-} \frac{ds}{\sqrt{\left(k_2^2+s^2\right)^2 + 2\bar{\alpha}C}}.$$

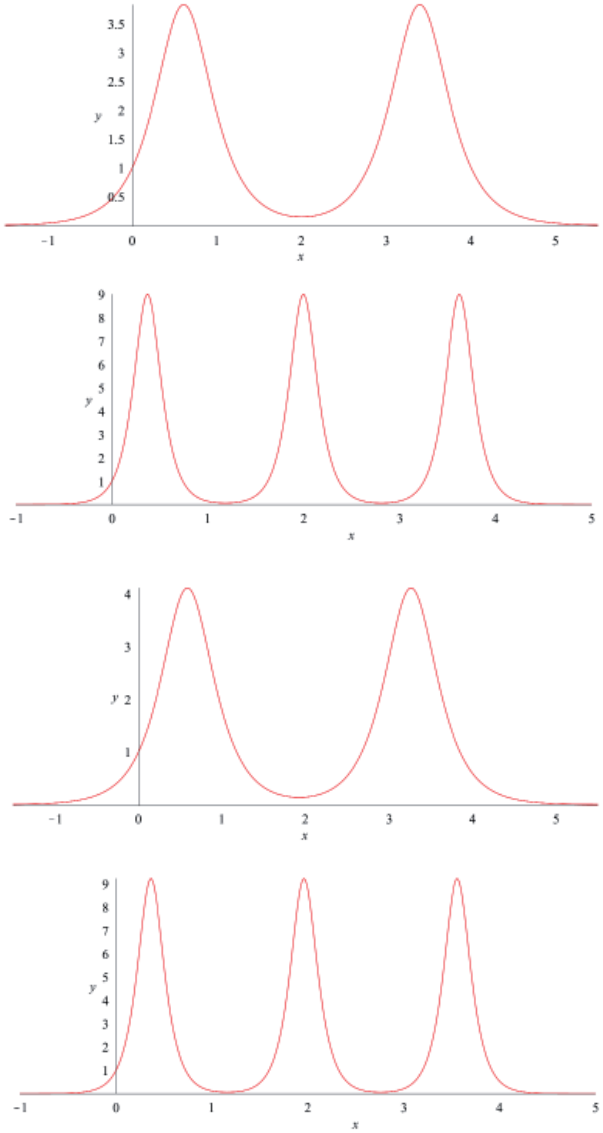

Figure 12. Case V: eigenfunctions for the eigenvalues marked in the previous figure: (a) $\hat{\gamma}_1 \approx 3.471$, (b) $\hat{\gamma}_3 \approx 7.859$, (c) $\hat{\gamma}_2 \approx 3.706$, (d) $\hat{\gamma}_4 \approx 8.066$.

The function $w^2 = \left(k_2^2 + s^2\right)^2 + 2\bar{\alpha}C$ can be rewritten in the form $w^2 = \left(a_-^2 - s^2\right)\left(a_+^2 - s^2\right)$, where $a_\pm^2 = \gamma^2 - \varepsilon_2 \pm \sqrt{-2\bar{\alpha}C} > 0$.

The integral T is transformed into

$$T = 2\int_0^{+a_-} \frac{ds}{\sqrt{\left(a_-^2 - s^2\right)\left(a_+^2 - s^2\right)}}$$

$$= \frac{2}{a_+}\int_0^1 \frac{dt}{\sqrt{\left(1-t^2\right)\left(1+k^2t^2\right)}}$$

$$= \frac{2}{a_+}\mathbf{K},$$

where $k^2 = a_-^2/a_+^2$, and $\mathbf{K}$ is the complete elliptic integral of the first kind. It is known [60] that

$$\mathbf{K} = \ln\frac{4}{k'} + O\left(k'^2 \ln k'\right) \text{ as } k' \to 0,$$

where $k'^2 = 1 - k^2 = 2\sqrt{-2\bar{\alpha}C}/a_+^2$.

Taking into account the latter formula, one finds

$$T = \frac{2}{a_+}\left[\ln\frac{4a_+}{\sqrt{2\sqrt{-2\bar{\alpha}C}}} + O\left(\frac{2\sqrt{-2\bar{\alpha}C}}{a_+^2}\ln\frac{a_+}{\sqrt{2\sqrt{-2\bar{\alpha}C}}}\right)\right]$$

as $\bar{\alpha} \to 0$ or $\gamma^2 \to \infty$.

For fixed $\bar{\alpha}$, one finds that $\lim_{\gamma\to\infty} T = 0$. This proves that for any $h > 0$, there exists an infinite number of eigenvalues.

Further, for fixed $\bar{\alpha}$ and big γ, one obtains the asymptotic formula $T \sim 2\frac{\ln a_+}{a_+}$. Using this formula and Equation (58), one finds that for arbitrarily small $\Delta > 0$, the following asymptotic formula,

$$(1-\Delta)\gamma_\bullet(n) \leqslant \hat{\gamma}(n) \leqslant (1+\Delta)\gamma_\bullet(n+1/2)$$

is true, where

$$\gamma_\bullet^2(n) = \varepsilon_2 - \sqrt{-2\bar{\alpha}C} + \left[f^{-1}\left(\frac{h}{4n+2}\right)\right]^2,$$

and f^{-1} is the inversion of $f(t) = t^{-1}\ln t$.

Multiplying Equation (14) by y and integrating from $x = 0$ to $x = h$, one then obtains

$$k_3 y^2(h) + k_1 + \int_0^h y'^2 dx - k_2^2\int_0^h y^2 dx = \bar{\alpha}\int_0^h y^4 dx.$$

The left-hand side of this formula is positive for all possible $\hat{\gamma}_i$, and so is the right-hand side. As the left-hand side tends to infinity as $\hat{\gamma}_i \to \infty$, one then finds that

$$\lim_{\hat{\gamma}_i \to +\infty} \int_0^h y^4(x;\hat{\gamma})\,dx = +\infty .$$

The previous formula results in

$$\lim_{\hat{\gamma}_i \to \infty} \max_{x\in(0,h)} \left| y(x;\hat{\gamma}_i) \right| \to \infty .$$

7.2 Proof of Case II

It is clear that (see Equations (52) and (54))

$$nT < \Phi_{\mathrm{II}}(\gamma;n) < (n+1)T, \qquad (59)$$

where $n \geqslant 0$ and

$$T = \int_{-\infty}^{+\infty} \frac{d\eta}{\sqrt{\left(k_2^2+\eta^2\right)^2 + 2\bar{\alpha}C}}$$

$$= 2\int_0^{+\infty} \frac{d\eta}{\sqrt{\left(k_2^2+\eta^2\right)^2 + 2\bar{\alpha}C}} .$$

For further analysis, the following easily checked inequalities are used:

$$\frac{1}{a+b} \leqslant \frac{1}{\sqrt{a^2+b^2}} \leqslant \frac{\sqrt{2}}{a+b}, \text{ where } a \geqslant 0, b > 0.$$

The inequality above implies the following estimations:

$$T^* \leqslant T \leqslant \sqrt{2}T^*, \qquad (60)$$

where $T^* := 2\int_0^{+\infty} \frac{d\eta}{\left|k_2^2+\eta^2\right| + \sqrt{2\bar{\alpha}C}}$. It therefore follows from Equations (59) and (60) that

$$nT^* \leqslant nT < \Phi_{\mathrm{II}}(\gamma;n) < (n+1)T \leqslant \sqrt{2}(n+1)T^*. \qquad (61)$$

For the integral T^*, there are three cases:

(a) If $\gamma^2 < \varepsilon_2$, then one obtains

$$T^* = 2\int_0^{+\infty} \frac{d\eta}{\left|k_2^2+\eta^2\right| + \sqrt{2\bar{\alpha}C}}$$

$$= 2\int_0^{+\infty} \frac{d\eta}{\eta^2 + k_2^2 + \sqrt{2\bar{\alpha}C}}$$

$$= \frac{\pi}{\sqrt{k_2^2 + \sqrt{2\bar{\alpha}C}}} ;$$

(b) If $\varepsilon_2 \leqslant \gamma^2 < \varepsilon_2 + \sqrt{2\bar{\alpha}C}$, then one obtains

$$T^* = 2\int_0^{+\infty} \frac{d\eta}{\left|k_2^2+\eta^2\right| + \sqrt{2\bar{\alpha}C}}$$

$$= -2\int_0^{\sqrt{|k_2^2|}} \frac{d\eta}{\eta^2 - \left(\left|k_2^2\right| + \sqrt{2\bar{\alpha}C}\right)} + 2\int_{\sqrt{|k_2^2|}}^{+\infty} \frac{d\eta}{\eta^2 + \left(-\left|k_2^2\right| + \sqrt{2\bar{\alpha}C}\right)}$$

$$= -\frac{1}{\sqrt{\left|k_2^2\right| + \sqrt{2\bar{\alpha}C}}} \ln \frac{\sqrt{2\bar{\alpha}C}}{\left(\sqrt{\left|k_2^2\right|} + \sqrt{\left|\left|k_2^2\right| + \sqrt{2\bar{\alpha}C}\right.}\right)^2}$$

$$+ \frac{2}{\sqrt{-\left|k_2^2\right| + \sqrt{2\bar{\alpha}C}}} \left(\frac{\pi}{2} - \arctan \frac{\sqrt{\left|k_2^2\right|}}{\sqrt{-\left|k_2^2\right| + \sqrt{2\bar{\alpha}C}}} \right);$$

(c) if $\gamma^2 \geqslant \varepsilon_2 + \sqrt{2\bar{\alpha}C}$, then one obtains

$$T^* = 2\int_0^{+\infty} \frac{d\eta}{\left|k_2^2+\eta^2\right| + \sqrt{2\bar{\alpha}C}}$$

$$= -2\int_0^{\sqrt{|k_2^2|}} \frac{d\eta}{\eta^2 - \left(\left|k_2^2\right| + \sqrt{2\bar{\alpha}C}\right)} + 2\int_{\sqrt{|k_2^2|}}^{+\infty} \frac{d\eta}{\eta^2 - \left(\left|k_2^2\right| - \sqrt{2\bar{\alpha}C}\right)}$$

$$= -\frac{1}{\sqrt{\left|k_2^2\right| + \sqrt{2\bar{\alpha}C}}} \ln \frac{\sqrt{2\bar{\alpha}C}}{\left(\sqrt{\left|k_2^2\right|} + \sqrt{\left|k_2^2\right| + \sqrt{2\bar{\alpha}C}}\right)^2}$$

$$-\frac{1}{\sqrt{\left|k_2^2\right| - \sqrt{2\bar{\alpha}C}}} \ln \frac{\sqrt{2\bar{\alpha}C}}{\left(\sqrt{\left|k_2^2\right|} + \sqrt{\left|k_2^2\right| - \sqrt{2\bar{\alpha}C}}\right)^2}.$$

It can be checked that for all possible γ, the integral T^* depends continuously on γ.

It follows from case (c) that $\lim_{\gamma \to +\infty} T^* = 0$. This formula implies that for any $h > 0$, there exists an infinite number of positive eigenvalues $\hat{\gamma}_i$.

The equations for cases (a) and (b) imply the link between linear and nonlinear solutions. The formula for case (c) implies that $\lim_{\bar{\alpha} \to +0} \hat{\gamma}_q^2 = +\infty$.

The asymptotic behavior of the eigenvalues results from the formula of case (c). Indeed, the asymptotic formula $T^* \sim 4\frac{\ln|k_2|}{|k_2|}$ occurs.

This formula easily results in two-sided inequality from the theorem.

An additional statement of the theorem is proven in the same way as was done in the proof of Case I.

7.3 Proof of Case III

This proof is based on the proof of Theorem 3. We are going to estimate $\Phi_{\mathrm{III}}(\gamma; n)$ for which the inequality $nT < \Phi_{\mathrm{III}}(\gamma; n) < (n+1)T$ occurs. The estimations of Equations (60) and (61) are valid with the same T^*. For the integral T^*, there are two cases:

(a) if $\gamma^2 < \varepsilon_2 + \sqrt{2\bar{\alpha}C}$, one obtains

$$T^* = -\frac{1}{\sqrt{\sqrt{2\bar{\alpha}C} + \left|k_2^2\right|}} \ln \frac{\sqrt{2\bar{\alpha}C}}{\left(\sqrt{\left|k_2^2\right|} + \sqrt{\sqrt{2\bar{\alpha}C} + \left|k_2^2\right|}\right)^2}$$

$$+\frac{2}{\sqrt{\sqrt{2\bar{\alpha}C} - \left|k_2^2\right|}} \left(\frac{\pi}{2} - \arctan \frac{\sqrt{\left|k_2^2\right|}}{\sqrt{\sqrt{2\bar{\alpha}C} - \left|k_2^2\right|}}\right);$$

(b) if $\gamma^2 \geqslant \varepsilon_2 + \sqrt{2\bar{\alpha}C}$, one obtain

$$T^* = -\frac{1}{\sqrt{\left|k_2^2\right| + \sqrt{2\bar{\alpha}C}}} \ln \frac{\sqrt{2\bar{\alpha}C}}{\left(\sqrt{\left|k_2^2\right|} + \sqrt{\left|k_2^2\right| + \sqrt{2\bar{\alpha}C}}\right)^2}$$

$$-\frac{1}{\sqrt{\left|k_2^2\right| - \sqrt{2\bar{\alpha}C}}} \ln \frac{\sqrt{2\bar{\alpha}C}}{\left(\sqrt{\left|k_2^2\right|} + \sqrt{\left|k_2^2\right| - \sqrt{2\bar{\alpha}C}}\right)^2}.$$

The calculations are the same as for cases (b) and (c) in the previous proof. It can be checked that for all possible γ, the integral T^* depends continuously on γ.

All the properties given in Theorem 4 are proven by word-for-word repetition of the reasoning used in the proof of Theorem 3.

7.4 Proof of Case IV

The function $w^2 = \left(k_2^2 + s^2\right)^2 + 2\bar{\alpha}C$ can be rewritten in the form $w^2 = \left(s^2 + b_-^2\right)\left(s^2 + b_+^2\right)$, where $b_-^2 = \varepsilon_2 - \sqrt{-2\bar{\alpha}C} - \gamma^2 > 0$, $b_+^2 = \varepsilon_2 + \sqrt{-2\bar{\alpha}C} - \gamma^2 > 0$.

Obviously, if $\gamma^2 \to \varepsilon_2 - \sqrt{-2\bar{\alpha}C}$, then $b_-^2 \to 0$ and, therefore,

$$\lim_{b_-^2 \to 0} \int_{-k_1}^{+k_1} \frac{ds}{w(s;\gamma)} = \infty$$

and

$$\lim_{b_-^2 \to 0} \int_{-\infty}^{+\infty} \frac{ds}{w(s;\gamma)} = \infty.$$

This means that the line $\gamma^2 = \varepsilon_2 - \sqrt{-2\bar{\alpha}C}$ is an asymptote for the dispersion curves: all dispersion curves lie below this line. This proves that $\varepsilon_1 < \hat{\gamma}_i^2 < \varepsilon_2 - \sqrt{-2\bar{\alpha}C}$.

Since the function $\Phi_{\mathrm{IV}}(\gamma; n)$ is an analytic function with respect to γ, then on any finite interval, there are not more than a finite number of zeros of the equation $\Phi_{\mathrm{IV}}(\gamma; n) = h$.

It is clear that for any $h > h_{\min} = \Phi_{\mathrm{IV}}(\varepsilon_1; 0)$, the problem $P(\bar{\alpha})$ has at least one solution. It follows from the easy checked inequa

$$\frac{1}{k_2^2 + s^2} < \frac{1}{\sqrt{\left(k_2^2 + s^2\right)^2 + 2\bar{\alpha}C}},$$

that $h_{\min} \geqslant h_{\min}^{\mathrm{lin}} \geqslant 0$. This proves an additional statement of the theorem.

7.5 Proof of Case V

This case is similar to Case I. However, the inequality of Equation (58) is replaced with

$$2nT \leqslant \Phi_V(\gamma; n) \leqslant (2n+1)T,$$

where $n = 0,1,2,\ldots$ with the other notation the same. This proof is now completely based on the proof of Case I.

8. Discussion and Conclusion

Here, we give an in-depth analysis of the problem, and present the results that help to understand the origin of the newly discovered waves. We hope that this work will draw attention to the novel guided regimes, or at least stimulate a discussion about the physical meaning of these results.

Since it is (physically) assumed that the nonlinearity coefficient, α, in the Kerr law is sufficiently small (see, for example, [1, 2]), then only Cases I, II, and IV seem to be of importance (obviously, in only these cases can α be chosen as small as necessary).

It is interesting to note that an infinite number of propagation constants arises if and only if $\alpha > 0$, that is, in the focusing case (Cases I to III, V). In the only case with negative α (Case IV), there always exists not more than a finite number of propagation constants. The focusing ($\alpha > 0$) and defocusing ($\alpha < 0$) cases thus produce qualitatively different results.

The regime that arises in Case II was studied in [25], where there is additional information. The regime that arises in Cases I and V seem to be even more interesting. There is no analogy between this regime and any linear regime, as the linearized problem has no periodic solutions that do not take zero value (see Statement 2 and the remark thereafter). Moreover, it is easy to understand that if one considers a dielectric waveguide (with nonlinear permittivity), shielded with one or both sides (at the points $x = 0$ or/and $x = h$) with perfectly conducting walls, then there will not be such solutions. This means that the regime found in Cases I and V exists only in an open waveguide.

It is also important that in each of the cases studied, the constant part, ε_2, of the permittivity in the layer can be positive. In other words, all the parameters in these cases are achievable, which gives promise to turn these theoretical results into experimental results. The most interesting and important thing is whether or not these novel regimes can be detected in an experiment. Of course, it is hardly reasonable to expect the existence of purely nonlinear waves for each propagation constant from an infinite set. However, it is possible that for some first purely nonlinear propagation constants, the corresponding purely nonlinear waves can be observed in an experiment. For the rest of the propagation constants, the value $\max_{x\in(0,h)}\left|y\left(x;\hat{\gamma}_i\right)\right|$ is so high that the Kerr law is no longer satisfied.

The Kerr law is described by an unbounded function, and this very fact results in the existence of infinitely many eigenvalues. For many types of nonlinear permittivities that take into account the saturation effect, e.g., $\varepsilon = \varepsilon_2 + \dfrac{\alpha|\mathbf{E}|^2}{1+\beta|\mathbf{E}|^2}$ or $\varepsilon = \varepsilon_2 + \alpha\left(1 - e^{\beta|\mathbf{E}|^2}\right)$, where $\alpha, \beta > 0$, there arise not more than a finite number of eigenvalues (see [61] for the former, [62, 63] for the latter, and [64] for the general case). In these cases, some new eigenvalues arise as well; however, all of them tend to linear solutions as $\alpha \to 0$. The fact that the Kerr and saturable nonlinearities give qualitatively different results can be used to verify in experiments what kind of nonlinearities are closer to real laws describing nonlinear materials.

It is worth noticing that in for Case II, purely nonlinear parts of the dispersion curves were previously numerically calculated [31, 32]; however, the dispersion equations found in these papers were not properly studied.

9. Acknowledgments

The author very much thanks the anonymous reviewers for their comments, which helped to make the text clearer. This study was supported by the Russian Foundation for Basic Research (grant no. 15-01-00206), the Russian Federation President Grant (project no. MK-4684.2016.1), and the Ministry of Education and Science of the Russian Federation (agreement no. 1.894.2017/Project Part).

10. References

1. A. G. Astill, "Material Figures of Merit for Non-Linear Optics," *Thin Solid Films*, **204**, 1, 1991, pp. 1-17.

2. R. W. Hellwarth, "Third-Order Optical Susceptibilities of Liquids and Solids," *Progress in Quantum Electronics*, **5**, 1977, pp. 1-68.

3. S. K. Srivatsa, G. S. Ranganath, "New Nonlinear Optical Processes in Liquid Crystals," *Optics Communications*, **180**, 4-6, 2000, pp. 349-359.

4. I. C. Khoo, "Nonlinear Optics of Liquid Crystalline Materials," *Physics Reports*, **471**, 5-6, 2009, pp. 221-267.

5. I. C. Khoo, "Nonlinear Optics, Active Plasmonics and Metamaterials with Liquid Crystals," *Progress in Quantum Electronics*, **38**, 2, 2014, pp. 77-117.

6. Y. R. Shen, *The Principles of Nonlinear Optics*, New York, John Wiley and Sons, 1984.

7. B. N. Delone, *Basics of Interaction of Laser Radiation with Matter*, Editions Frontiéres, 1993.

8. S. Kielich, *Molekularna Optyka Nieliniowa* (*Molecular Nonlinear Optics*), Warszawa, PWN (in Polish), 1977.

9. N. N. Akhmediev and A. Ankevich, *Solitons, Nonlinear Pulses and Beams*, London, Chapman and Hall, 1997.

10. W. Man, S. Fardad, Z. Zhang, J. Prakash, M. Lau, P. Zhang, M. Heinrich, D. N. Christodoulides, and Z. Chen, "Optical Nonlinearities and Enhanced Light Transmission in Soft-Matter Systems with Tunable Polarizabilities," *Physical Review Letters*, **111**, 21, 2013, p. 218302(5).

11. V. Besse, G. Boudebs, and H. Leblond, "Determination of the Third- and Fifth-Order Optical Nonlinearities: The General Case," *Applied Physics B*, **116**, 4, 2014, pp. 911-917.

12. A. Pasquazi, M. Peccianti, M. Clerici, C. Conti, and R. Morandotti, "Collapse Arrest in Instantaneous Kerr Media via Parametric Interactions," *Phys. Rev. Lett.*, **113**, 9, 2014, pp. 133901.

13. A. D. Boardman, P. Egan, F. Lederer, U. Langbein, and D. Mihalache, "Third-Order Nonlinear Electromagnetic TE and TM Guided Waves," Amsterdam, Elsevier Sci. Publ. North-Holland, 1991, reprinted from H.-E. Ponath and G. I. Stegeman (eds.), *Nonlinear Surface Electromagnetic Phenomena*.

14. U. Langbein, F. Lederer, H.-E. Ponath, and U. Trutschel, "Analysis of the Dispersion Relations of Nonlinear Slab-Guided Waves," *Applied Physics B*, **36**, 4, 1985, pp. 187-193.

15. N. N. Akhmediev, "Novel Class of Nonlinear Surface Waves: Asymmetric Modes in a Symmetric Layered Structure, *JETP*, **56**, 2, 1982, pp. 299-303.

16. D. Mihalache and V. K. Fedyanin, "P-Polarized Nonlinear Surface and Bounded (Guided) Waves in Layered Structures," *Theoretical and Mathematical Physics*, **54**, 3, 1983, pp. 289-297.

17. D. Mihalache, R. G. Nazmitdinov, and V. K. Fedyanin, "Nonlinear Optical Waves in Layered Structures," *Physics of Elementary Particles and Atomic Nuclei*, **20**, 1, 1989, pp. 198-253, (http://www1.jinr.ru/Archive/Pepan/1989-v20/v-20-1/5.htm; in Russian).

18. D. Mihalache, R. G. Nazmitdinov, V. K. Fedyanin, and R. P. Wang, "Nonlinear Guided Waves in Planar Structures," *Physics of Elementary Particles and Atomic Nuclei*, **23**, 1, 1992, pp. 122-173, (http://www1.jinr.ru/Archive/Pepan/1992-v23/v-23-1/4.htm; in Russian).

19. H. W. Schürmann, "Travelling-Wave Solutions of the Cubic-Quintic Nonlinear Schrödinger Equation," *Phys. Rev. E*, **54**, 4-B, 1996, pp. 4312-4320.

20. H. W. Schürmann, V. S. Serov, and Yu. V. Shestopalov, "Solutions to the Helmholtz Equation for TE-Guided Waves in a Three-Layer Structure with Kerr-Type Nonlinearity," *J. Phys. A: Math. Gen.*, **35**, 2002, pp. 10789-10801.

21. H. W. Schürmann, V. S. Serov, and Yu. V. Shestopalov, "TE-Polarized Waves Guided by a Lossless Nonlinear Three-Layer Structure," *Phys. Rev. E*, **58**, 1, 1998, pp. 1040-1050.

22. Yu. G. Smirnov and D. V. Valovik, *Electromagnetic Wave Propagation in Nonlinear Layered Waveguide Structures*, Penza, Russia, Penza State University Press, 2011.

23. H. K. Chiang, R. P. Kenan, and C. J. Summers, "Spurious Roots in Nonlinear Waveguide Calculations and a New Format for Nonlinear Waveguide Dispersion Equations," *IEEE Journal of Quantum Electronics*, **28**, 8, 1992, pp. 1756-1760.

24. Y.-F. Li and K. Iizuka, "Unified Nonlinear Waveguide Dispersion Equations Without Spurious Roots," *IEEE Journal of Quantum Electronics*, **31**, 5, 1995, pp. 791-794.

25. Yu. G. Smirnov and D. V. Valovik, "Guided Electromagnetic Waves Propagating in a Plane Dielectric Waveguide with Nonlinear Permittivity," *Physical Review A*, **91**, 1, 2015, pp. 013840, 6 pages.

26. D. V. Valovik, "Integral Dispersion Equation Method to Solve a Nonlinear Boundary Eigenvalue Problem," *Nonlinear Analysis: Real World Applications*, **20**, 12, 2014, pp. 52-58, doi: 10.1016/j.nonrwa.2014.04.007.

27. M. J. Adams, *An Introduction to Optical Waveguides*, Chichester, UK, John Wiley & Sons, 1981.

28. L. A. Vainstein, *Electromagnetic Waves*, Moscow, Radio i Svyaz, 1988 (in Russian).

29. D. V. Valovik, "Novel Propagation Regimes for TE Waves Guided by a Waveguide Filled with Kerr Medium," *Journal of Nonlinear Optical Physics & Materials*, **25**, 4, 2016, p. 1650051 (17 pages).

30. S. Okafuji, "Analysis of Nonlinear TE Waves in a Three-Layer Slab Waveguide with Self-Focusing Nonlinear Film and Substrate Layers," *Electronics and Communications in Japan*, **74**, 3, 1991, pp. 25-33.

31. A. D. Boardman and P. Egan, "Optically Nonlinear Waves in Thin Films," *IEEE Journal of Quantum Electronics*, **QE-22**, 2, 1986, pp. 319-324.

32. H. W. Schürmann, "On the Theory of TE-Polarized Waves Guided by a Nonlinear Three-Layer Structure," *Zeitschrift für Physik*, **B 97**, 4, 1995, pp. 515-522.

33. Yu. G. Smirnov and D. V. Valovik, "On the Infinitely Many Nonperturbative Solutions in a Transmission Eigenvalue Problem for Maxwell's Equations with Cubic Nonlinearity," *Journal of Mathematical Physics*, **57**, 10, 2016, p. 103504 (15 pages).

34. J. A. Stratton, *Electromagnetic Theory*, New York, McGraw Hill, 1941.

35. P. N. Eleonskii, L. G. Oganes'yants, and V. P. Silin, "Cylindrical Nonlinear Waveguides," *Soviet Physics JETP*, **35**, 1, 1972, pp. 44-47.

36. P. N. Eleonskii, L. G. Oganes'yants, and V. P. Silin, "Structure of Three-Component Vector Fields in Self-Focusing Waveguides," *Soviet Physics JETP*, **36**, 2, 1973, pp. 282-285.

37. P. N. Eleonskii, L. G. Oganes'yants, and V. P. Silin, "Vector Structure of Electromagnetic Field in Self-Focused Waveguides," *Sov. Phys. Usp.*, **15**, 4, 1972, pp. 524-525.

38. A. Zakery and S. R. Elliott, "Optical Nonlinearities in Chalcogenide Glasses and Their Applications," *Springer Series in Optical Sciences, Vol. 135*, Berlin, Springer-Verlag, 2007.

39. C. Schnebelin, C. Cassagne, C. B. de Araújo, and G. Boudebs, "Measurements of the Third- and Fifth-Order Optical Nonlinearities of Water at 532 and 1064 nm Using the d4σ Method," *Optics Letters*, **39**, 17, 2014, pp. 5046-5049.

40. A. A. Said, C. Wamsley, D. J. Hagan, E. W. Van Stryland, B. A. Reinhardt, P. Roderer, and A. G. Dillard, "Third- and Fifth-Order Optical Nonlinearities in Organic Materials," *Chemical Physics Letters*, **228**, 6, 1994, pp. 646-650.

41. Chuanlang Zhan, Deqing Zhang, and Daoben Zhu, "Third- and Fifth-Order Optical Nonlinearities in a New Stilbazolium Derivative," *Journal of the Optical Society of America B*, **19**, 3, 2002, pp. 369-375.

42. R. A. Ganeev, M. Baba, M. Morita, A. I. Ryasnyansky, M. Suzuki, M. Turu, and H. Kuroda, "Fifth-Order Optical Nonlinearity of Pseudoisocyanine Solution at 529 nm," *Journal of Optics A: Pure and Applied Optics*, **6**, 2, 2004, pp. 282-287.

43. Yi-Fan Chen, K. Beckwitt, F. W. Wise, B. G. Aitken, J. S. Sanghera, and I. D. Aggarwal, "Measurement of Fifth- and Seventh-Order Nonlinearities of Glasses," *Journal of the Optical Society of America B*, **23**, 2, 2006, pp. 347-352.

44. D. L. Weerawarne, X. Gao, A. L. Gaeta, and B. Shim, "Higher-Order Nonlinearities Revisited and their Effect on Harmonic Generation," *Physical Review Letters*, **114**, 9, 2015, p. 093901(5).

45. A. S. Reyna and C. B. de Araújo, "Spatial Phase Modulation Due to Quintic and Septic Nonlinearities in Metal Colloids," *Optics Express*, **22**, 19, 2014, pp. 22456-22469.

46. A. S. Reyna, K. C. Jorge, C. B. de Araújo, "Two-Dimensional Solitons in a Quintic-Septimal Medium," *Physical Review A*, **90**, 6, 2014, p. 063835(5).

47. H. W. Schürmann and V. S. Serov, "Theory of TE-Polarized Waves in a Lossless Cubic-Quintic Nonlinear Planar Waveguide," *Physical Review A*, **93**, 6, 2016, p. 063802(8).

48. F. Azzouzi, H. Triki, K. Mezghiche, and A. El Akrmi, "Solitary Wave Solutions for High Dispersive Cubic-Quintic Nonlinear Schrödinger Equation," *Chaos, Solitons and Fractals*, **39**, 3, 2009, pp. 1304-1307.

49. K. Y. Kolossovski, A. V. Buryak, V. V. Steblina, A. R. Champneys, and R. A. Sammut, "Higher-Order Nonlinear Modes and Bifurcation Phenomena Due to Degenerate Parametric Four-Wave Mixing," *Physical Review E*, **62**, 3, 2000, pp. 4309-4317.

50. J. Soneson and A. Peleg, "Effect of Quintic Nonlinearity on Soliton Collisions in Optical Fibers," *Physica D: Nonlinear Phenomena*, **195**, 1-2, 2004, pp. 123-140.

51. Yongan Xie and Shengqiang Tang, "New Exact Solutions for High Dispersive Cubic-Quintic Nonlinear Schrödinger Equation," *Journal of Applied Mathematics*, 2014, p. 826746(7).

52. Li-Chen Zhao, Chong Liu, and Zhan-Ying Yang, "The Rogue Waves with Quintic Nonlinearity and Nonlinear Dispersion Effects in Nonlinear Optical Fibers," *Communications in Nonlinear Science and Numerical Simulation*, **20**, 1, 2015, pp. 9-13.

53. M. Kerbouche, Y. Hamaizi, A. El-Akrmi, and H. Triki, "Solitary Wave Solutions of the Cubic-Quintic-Septic Nonlinear Schrödinger Equation in Fiber Bragg Gratings," *Optik – International Journal for Light and Electron Optics*, **127**, 20, 2016, pp. 9562-9570.

54. A. Choudhuri and K. Porsezian, "Impact of Dispersion and Non-Kerr Nonlinearity on the Modulational Instability of the Higher-Order Nonlinear Schrödinger Equation," *Physical Review A*, **85**, 3, 2012, p. 033820(6).

55. Zhonghao Li, Lu Li, Huiping Tian, and Guosheng Zhou, "New Types of Solitary Wave Solutions for the

Higher Order Nonlinear Schrödinger Equation," *Physical Review Letters*, **84**, 18, 2000, pp. 4096-4099.

56. Hang-Yu Ruan and Hui-Jun Li, "Optical Solitary Waves in the Generalized Higher Order Nonlinear Schrödinger Equation," *Journal of the Physical Society of Japan*, **74**, 2, 2005, pp. 543-546.

57. L. D. Landau, E. M. Lifshitz, and L. P. Pitaevskii, *Course of Theoretical Physics, Vol. 8, Electrodynamics of Continuous Media*, Oxford, Butterworth-Heinemann, 1993.

58. C. Hermite, *Cours de M. Hermite, Quatrieme Edition, Revue et Augmentee Edition*, Paris, Libraire Scientifique A. Hermann, 1891.

59. E. Goursat, *Cours D'Analyse Mathematique, Cinquieme Edition, Vol. II*, Paris, Gauthier – Villars.

60. H. Bateman and A. Erdelyi, *Higher Transcendental Functions, Vol. 3*, New York, McGraw Hill Book Company, Inc., 1955.

61. D. V. Valovik, "Propagation of Electromagnetic TE Waves in a Nonlinear Medium with Saturation," *J. Comm. Tech. Electron.*, **56**, 11, 2011, pp. 1311-1316.

62. V. Yu. Kurseeva and D. V. Valovik, "Propagation of TE Waves in a Plane Dielectric Waveguide with Nonlinear Permittivity, Proceedings of the International Conference Days on Diffraction 2014, Saint-Petersburg, 2014, pp. 177-180.

63. D. V. Valovik and V. Yu. Kurseeva, "On the Eigenvalues of a Nonlinear Spectral Problem," *Differential Equations*, **52**, 2, 2016, pp. 149-156.

64. D. V. Valovik, "Nonlinear Coupled Electromagnetic Wave Propagation: Saturable Nonlinearities," *Wave Motion*, **60**, 2016, pp. 166-180.

Sum-Frequency and Second-Harmonic Generation from Plasmonic Nonlinear Nanoantennas

Xiaoyan Y. Z. Xiong[1], Li Jun Jiang[1], Wei E. I. Sha[1], Yat Hei Lo[1], and Weng Cho Chew[1,2]

[1]Dept. of Electrical and Electronic Engineering
The University of Hong Kong, Hong Kong
E-mail: xyxiong@eee.hku.hk, jianglj@hku.hk, shawei@eee.hku.hk, yathei36@gmail.com

[2]Dept. of Electrical and Computer Engineering University of Illinois at Urbana-Champaign
Urbana, USA
E-mail: w-chew@uiuc.edu

Abstract

Plasmonic nanostructures that support surface plasmon (SP) resonance potentially provide a route for the development of nanoengineered nonlinear optical devices. In this work, second-order nonlinear light scattering – specifically, sum-frequency generation (SFG) and second-harmonic generation (SHG) – from plasmonic nanoantennas is modeled by the Boundary-Element Method (BEM). Far-field scattering patterns are compared with the results calculated by the Mie theory to validate the accuracy of the developed nonlinear solver. The sum-frequency generation from a multi-resonant nanoantenna (MR-NA) and the second-harmonic generation from a particle-in-cavity nanoantenna (PIC-NA) are analyzed by using the developed method. Enhancements of the scattering signals due to double-resonance of the multi-resonant nanoantenna and gap plasmonic mode of the particle-in-cavity nanoantenna are observed. Unidirectional nonlinear radiation for the particle-in-cavity nanoantenna is realized. Moreover, the emission direction of this radiation can be controlled by the location of the nanosphere. This work provides new theoretical tools and design guidelines for plasmonic nonlinear nanoantennas.

1. Introduction

Plasmonic nanoantennas made from nanostructured metals have attracted significant attention in nonlinear optics, due to their unique properties [1]. One such property is their ability to concentrate light in nanoscale volumes, and to subsequently boost the intensity of local fields near particle surfaces due to surface plasmon resonance (SPR) [2]. The surface-plasmon-resonance-enhanced near fields allow weak nonlinear processes – which depend superlinearly on the local fields – to be significantly amplified, giving rise to a promising research area called nonlinear plasmonics. The second-order nonlinear processes, e.g., sum-frequency generation (SFG) and second-harmonic generation (SHG), are significantly dependent on the symmetry of both the material being used and the structure being studied [3]. They are forbidden in the bulk of centrosymmetric media under the electric dipole approximation. However, the breaking of inversion symmetry at surfaces results in surface nonlinear scattering [4, 5]. The combination of nonlinear surface sensitive and strong near-field enhancement associated with surface plasmon resonance provides a unique tool for ultra-sensitive shape characterization [6, 7], super-resolution imaging, sensing and microscopy [8, 10], on-chip optical-frequency conversion, switching and modulation [11], etc.

Efficient nonlinear scattering requires the presence of strong nonlinear polarization sources at the surface of nanostructures, as well as efficient scattering of the signal into the far field. Analogous to classical antennas, the objective of nonlinear nanoantenna design is the optimization and control of the spatial distribution of scattered light. Several strategies have been applied to enhance the scattered nonlinear signals, including engineering near-field-coupled nanoparticle clusters associated with Fano resonances [12, 13], enhancing the electric fields using nanogaps [14], etc. However, tailoring the radiation pattern of nonlinear nanoantennas has great challenges. First, nonlinear radiation exhibits complex

multi-polar interactions [15, 16]. Second, currently, few tools are available for efficient and rigorous analyses of surface nonlinear scattering processes in complex structures. The volume-discretization-based full-wave methods, e.g., the Finite-Difference Time-Domain (FDTD) and the Finite-Element Method (FEM), are inefficient and inaccurate for solving surface nonlinear problems. Third, the relationship among plasmon resonances, particle geometry, and associated local-field distributions is very complicated [17]. Physical principles and design rules for nonlinear nanoantennas have not yet been explored.

In this work, a numerical solution based on the Boundary-Element Method (BEM) is proposed for the second-order surface nonlinear scattering problems. The proposed method is efficient with a surface discretization, and it can directly employ experimentally tabulated material parameters. The developed solver was utilized to systematically analyze the sum-frequency generation from a multi-resonant nanoantenna (MR-NA), and second-harmonic generation from a novel particle-in-cavity nanoantenna (PIC-NA) with strong surface plasmon resonance.

The remainder of this article is organized as follows. In the next section, we describe the Boundary-Element Method used in our study. Section 3 contains the main results. We first validate the accuracy of the developed solver by comparing the far-field scattering patterns with Mie-theory results. The sum-frequency generation from multi-resonant nanoantenna and the second-harmonic generation from particle-in-cavity nanoantenna are then analyzed. Finally, in the last section, we summarize the main conclusions of our work.

2. Methods

The second-order surface nonlinear problem, under the *undepleted-pump approximation*, can be described by the following driven wave equation, with the nonlinear polarization of the medium as a source term [18]:

$$\nabla^2\mathbf{E}^{(\nu)}+k^{(\nu)2}\mathbf{E}^{(\nu)}=-\frac{\nu^2}{\varepsilon_0 c^2}\mathbf{P}^{(\nu)}, \tag{1}$$

where $k^{(\nu)}$ is the wave number at frequency ν, and $\mathbf{P}^{(\nu)}$ is the surface nonlinear polarization at frequency ν. This has the form, $\mathbf{P}^{(\nu)}=\varepsilon_0\overline{\overline{\chi}}^{(2)}:\mathbf{E}_1^{(\omega_1)}\mathbf{E}_2^{(\omega_2)}$ and $\nu=\omega_1+\omega_2$ for sum-frequency generation. The second-harmonic generation process is a special case of sum-frequency generation with $\omega_1=\omega_2$ and $\nu=2\omega_1$. $\overline{\overline{\chi}}^{(2)}$ is the surface second-order nonlinear susceptibility tensor. $\mathbf{E}_1^{(\omega_1)}$ and $\mathbf{E}_2^{(\omega_2)}$ denote the fundamental fields at frequencies ω_1 and ω_2, respectively. The symbol ":" is a tensor operator that functions as

$$P_i^{(\nu)}=\sum\nolimits_{j,k}\chi_{ijk}^{(2)}E_{1j}^{(\omega_1)}E_{2k}^{(\omega_2)}.$$

Metals are centrosymmetric materials. The surface of metal nanoparticles has an isotropic symmetry with a mirror plane perpendicular to it. The surface susceptibility tensor has only three non-vanishing and independent elements:

$$\mathbf{P}^{(\nu)}=\varepsilon_0\hat{n}\left[\chi_{\perp\perp\perp}^{(2)}\mathbf{E}_{1\hat{n}}\mathbf{E}_{2\hat{n}}+\chi_{\perp\parallel\parallel}^{(2)}\left(\mathbf{E}_{1\hat{t}_1}\mathbf{E}_{2\hat{t}_1}+\mathbf{E}_{1\hat{t}_2}\mathbf{E}_{2\hat{t}_2}\right)\right]$$

$$+\hat{t}_1\chi_{\parallel\perp\parallel}^{(2)}\mathbf{E}_{1\hat{n}}\mathbf{E}_{2\hat{t}_1}+\hat{t}_2\chi_{\parallel\perp\parallel}^{(2)}\mathbf{E}_{1\hat{n}}\mathbf{E}_{2\hat{t}_2}, \tag{2}$$

where $\perp$ and $\parallel$ refer to the orthogonal and tangential components to the nanoparticle surface. $\left(\hat{t}_1,\hat{t}_2,\hat{n}\right)$ is a system of three orthogonal vectors, locally defined on the particle surface. The contributions of tangential and normal components of the surface nonlinear polarization are taken into account by the nonlinear surface electric and magnetic current sources:

$$\mathbf{J}_0^{(\nu)}=-i\nu\mathbf{P}_t^{(\nu)}, \tag{3}$$

$$\mathbf{M}_0^{(\nu)}=\frac{1}{\varepsilon'}\hat{n}\times\nabla_S P_n^{(\nu)}, \tag{4}$$

where $\mathbf{P}_t^{(\nu)}$ and $P_n^{(\nu)}$ are the tangential and normal components of $\mathbf{P}^{\nu}$. The Boundary-Element Method is applied to solve the driven wave equation by invoking Love's Equivalence Principle. The domain of the electromagnetic field is divided into the interior of the metal domain, V_i, the exterior medium, V_e, and the interface, S. The object is illuminated by the plane-wave source, $\mathbf{E}^{inc}$. The equivalent currents, $\mathbf{J}_e^{(\nu)},\mathbf{M}_e^{(\nu)}$, positioned on the external page, S^+ produce the scattered field in the region V_e, and a null field in the region V_i. The equivalent currents, $\mathbf{J}_i^{(\nu)},\mathbf{M}_i^{(\nu)}$ defined on the internal side, S^-, produce the total field in the region V_i, and a null field in the region V_e.

$$\left.\begin{array}{l}\mathbf{r}\in V_\ell,\mathbf{E}_\ell^{(\nu)}(\mathbf{r})\\ \mathbf{r}\notin V_\ell,0\end{array}\right\}=\begin{array}{l}i\nu\mu_\ell\int_S\overline{\mathbf{G}}^{(\nu)}(\mathbf{r},\mathbf{r}')\cdot\mathbf{J}_\ell^{(\nu)}(\mathbf{r}')d\mathbf{r}'\\ \quad-\int_S\nabla\times\overline{\mathbf{G}}^{(\nu)}(\mathbf{r},\mathbf{r}')\cdot\mathbf{M}_\ell^{(\nu)}(\mathbf{r}')d\mathbf{r}'\end{array} \tag{5}$$

where $\overline{\mathbf{G}}^{(\nu)}(\mathbf{r},\mathbf{r}')=\left[\bar{\mathbf{I}}+k^{(\nu)-2}\nabla\nabla\right]\exp\left[ik^{(\nu)}R\right]/4\pi R$ is the dyadic Green's function at frequency ν. Here,

$R = |\mathbf{r} - \mathbf{r}'|$. $\ell = e,i$ denote the exterior and interior regions of the object, respectively. The magnetic field has a similar representation. The equivalent currents satisfy

$$\mathbf{J}_i^{(\nu)} + \mathbf{J}_e^{(\nu)} = \mathbf{J}_0^{(\nu)}, \tag{6}$$

$$\mathbf{M}_i^{(\nu)} + \mathbf{M}_e^{(\nu)} = \mathbf{M}_0^{(\nu)}. \tag{7}$$

The surfaces of the nanostructures are discretized with a triangular mesh. The equivalent currents are expanded with Rao-Wilton-Glisson (RWG) basis functions [19]. A matrix system is then constructed by exploiting the Galerkin testing procedure. A modified Poggio-Miller-Chang-Harrington-Wu-Tsai (PMCHWT) formulation [20] is used to ensure accurate solutions, even at resonant conditions. The PMCHWT matrix equation can be written as

$$\overline{\mathbf{C}}^{(\nu)} \bullet \mathbf{X}^{(\nu)} = \mathbf{Y}^{(\nu)}. \tag{8}$$

The impedance matrix, $\overline{\mathbf{C}}^{(\nu)}$, is

$$\overline{\mathbf{C}}^{(\nu)} = \begin{bmatrix} \mathcal{L}_e^{(\nu)} & \mathcal{K}_e'^{(\nu)} & -\mathcal{L}_i^{(\nu)} & -\mathcal{K}_i'^{(\nu)} \\ -\mathcal{K}_e'^{(\nu)} & \eta_e^{-2}\mathcal{L}_e^{(\nu)} & \mathcal{K}_i'^{(\nu)} & -\eta_i^{-2}\mathcal{L}_i^{(\nu)} \\ \mathcal{I} & 0 & \mathcal{I} & 0 \\ 0 & \mathcal{I} & 0 & \mathcal{I} \end{bmatrix},$$

where $\mathcal{L}_\ell^{(\nu)} = i\nu\mu_\ell \overline{\mathbf{G}}^{(\nu)}$, and $\mathcal{K}_\ell'^{(\nu)}$ is the principal value part of the $\mathcal{K}_\ell^{(\nu)}$ operator with $\mathcal{K}_\ell^{(\nu)} = -\nabla \times \overline{\mathbf{G}}^{(\nu)}$. $\eta_\ell = \sqrt{\mu_\ell / \varepsilon_\ell}$ with $\ell = e,i$. The vector of unknowns $\mathbf{X}^{(\nu)}$ and the excitation $\mathbf{Y}^{(\nu)}$ are

$$\mathbf{X}^{(\nu)} = \begin{bmatrix} \mathbf{J}_e^{(\nu)} \\ \mathbf{M}_e^{(\nu)} \\ \mathbf{J}_i^{(\nu)} \\ \mathbf{M}_i^{(\nu)} \end{bmatrix},$$

$$\mathbf{Y}^{(\nu)} = \begin{bmatrix} \frac{1}{2}\hat{n} \times \mathbf{M}_0^{(\nu)} \\ -\frac{1}{2}\hat{n} \times \mathbf{J}_0^{(\nu)} \\ \mathbf{J}_0^{(\nu)} \\ \mathbf{M}_0^{(\nu)} \end{bmatrix}.$$

Equation (8) can be used to solve for the fundamental fields as well, by setting $\nu = \omega_\alpha$, with $\alpha = 1,2$ for frequencies ω_1 and ω_2, respectively. The driven source is now the incident excitation

$$\mathbf{J}_0^{(\omega_\alpha)} = \hat{n} \times \mathbf{H}^{(\omega_\alpha, inc)}, \tag{9}$$

$$\mathbf{M}_0^{(\omega_\alpha)} = -\hat{n} \times \mathbf{E}^{(\omega_\alpha, inc)}. \tag{10}$$

The Boundary-Element Method formulation can efficiently model the nonlinear scattering from arbitrarily shaped particles since it only requires surface discretization. In addition, measured material parameters can directly be used. In this work, $\chi_{\perp\perp\perp}^{(2)} = 1.59 \times 10^{-18}\,\mathrm{m}^2/\mathrm{V}$, and only the normal component, $\chi_{\perp\perp\perp}^{(2)}$, of the surface susceptibility tensor was considered, since it is the dominant term of the surface response of metallic nanoparticles. Note that other components are theoretically allowed, but they weakly contribute to the total second-harmonic response.

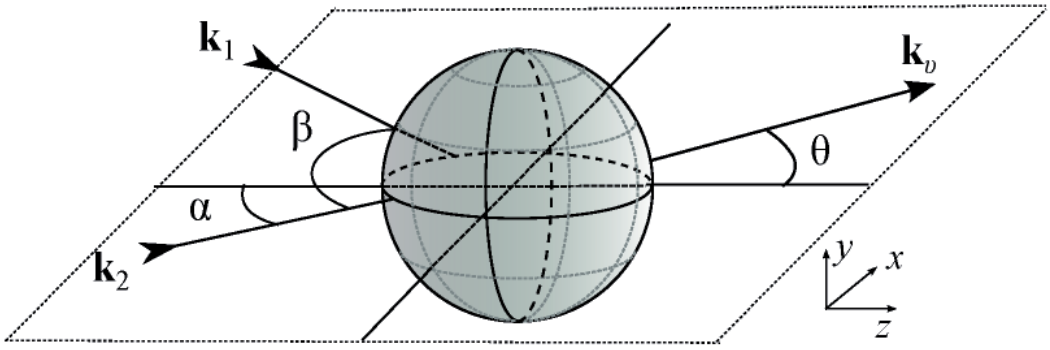

Figure 1. An overview of the relevant parameters in the model: The sum-frequency and source waves had wave vectors $\mathbf{k}_\nu$, $\mathbf{k}_1$, and $\mathbf{k}_2$, in order of decreasing frequency. The angle between the propagation direction of the lowest-frequency wave and the positive z axis was α; the opening angle between source waves was β. The sum-frequency scattering pattern was parameterized using the scattering angle θ [22].

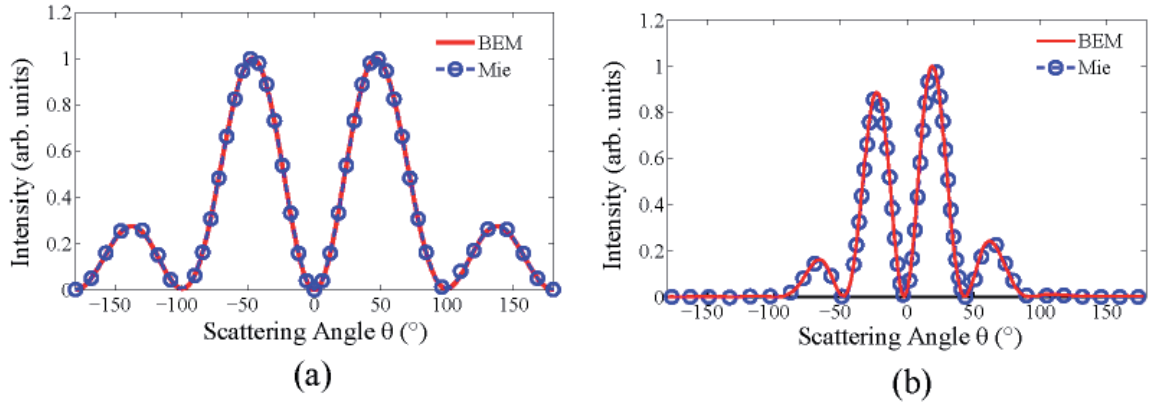

Figure 2. Comparisons of sum-frequency and second-harmonic scattering patterns with the nonlinear Mie solutions: (a) The sum-frequency scattering pattern. The simulation parameters were $R = 500$ nm ; $\lambda_1 = 800$ nm and $\lambda_2 = 3447$ nm ; $\beta = 15^\circ$. (b) The second-harmonic scattering pattern. The simulation parameters were $R = 50$ nm ; $\lambda_1 = 520$ nm .

3. Numerical Results

3.1 Verification of the Algorithm

We first validated the Boundary-Element Method algorithm by comparing the sum-frequency (SF) and second-harmonic (SH) scattering patterns of spherical nanoparticles with the nonlinear Mie solutions [21, 22]. For sum-frequency generation, two incident plane waves propagating at different angles with different frequencies were superposed, as shown in Figure 1. The polarization angles (defined as the angle between $-\hat{\theta}$ and $\mathbf{E}$) were set to zero for both incident waves. Figure 2a shows the comparison of the sum-frequency scattering patterns. Very good agreement was observed. Here, the radius of the sphere was $R = 500$ nm . The wavelengths of the incident waves were $\lambda_1 = 800$ nm and $\lambda_2 = 3447$ nm , respectively. The opening angle between the source waves was $\beta = 15°$, and the index of refraction was set to unity for all wavelengths. The asymmetry in the sum-frequency scattering pattern was due to the nonzero opening angle between source beams. For second-harmonic generation, a single electromagnetic field was taken as the source. A gold sphere with a radius of $R = 50$ nm was excited by a plane wave propagating along the positive direction of the z axis, and linearly polarized along x . The exciting wavelength, $\lambda = 520$ nm , corresponded to the plasmon resonance of the gold spherical particle. The dielectric constant for gold was taken from experimental data [23]. We could see that the second-harmonic scattering pattern calculated by the Boundary-Element Method agreed well with the nonlinear Mie-theory result.

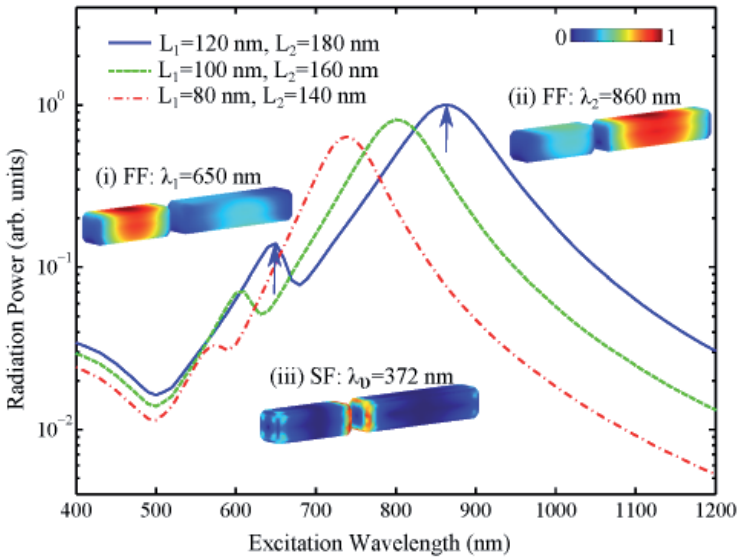

Figure 3. The radiation power of the multi-resonant nanoantenna as a function of the incident wavelength with different arm lengths. The arrows denote the resonant peaks of the multi-resonant nanoantenna with arm lengths $L_1 = 120$ nm and $L_2 = 180$ nm . The inset shows the distribution of fundamental and sum-frequency equivalent electric currents on the surface of the multi-resonant nanoantenna.

3.2 Sum-Frequency Generation from Multi-Resonant Nanoantenna

The multi-resonant nanoantenna consisted of two gold arms of different lengths, L_1 and L_2 ($L_1 < L_2$). The separation between the two arms was fixed at 20 nm. The width and height of the antenna arms were 40 nm. The lengths of the metal arms corresponded to two resonant frequencies, ω_1 and ω_2, respectively. Figure 3 shows the radiation power as a function of the incident wavelength with different arm lengths. Due to the asymmetry of the antenna design, two resonant peaks were observed, and they were red-shifted with the increase in the arm lengths. The insets in Figure 3 show the distribution of fundamental frequency and sum-frequency equivalent electric currents on the surface of the multi-resonant nanoantenna. The resonant peak at $\lambda_1 = 650$ nm corresponded to the half-wave resonance of the short arm, as presented in inset (i). Similarly, the resonant peak at $\lambda_2 = 860$ nm corresponded to the long arm's resonance, as presented in inset (ii). The nonlinear equivalent currents at the sum-frequency with $\lambda_\nu = 372$ nm were concentrated near the gap and corners of the arms.

3.3 Second-Harmonic Generation from Particle-in-Cavity Nanoantenna

The configuration of the investigated particle-in-cavity nanoantenna is depicted in Figure 4a. A gold nanosphere with a diameter of $D = 40$ nm was located inside a gold rounded-edge nanocup cavity, separated by a small gap of $g = 5$ nm. The nanocup cavity used was a truncated hemispherical nanoshell with external and inner radii of $R_1 = 120$ nm and $R_2 = 160$ nm, respectively. Depending on the angle between the center of the nanosphere and the symmetry axis of the nanocup, the nanoantenna possessed symmetric ($\beta = 0°$) or asymmetric ($\beta = 30°$) geometry. The particle-in-cavity nanoantenna was illuminated by a y-polarized plane wave at normal incidence from the top side. The linear and nonlinear responses of the particle-in-cavity nanoantenna were numerically simulated by the Boundary-Element Method.

Placing a metallic nanoparticle inside a cavity produced extremely strong field enhancements at the particle-cavity gap when one of the cavity modes was

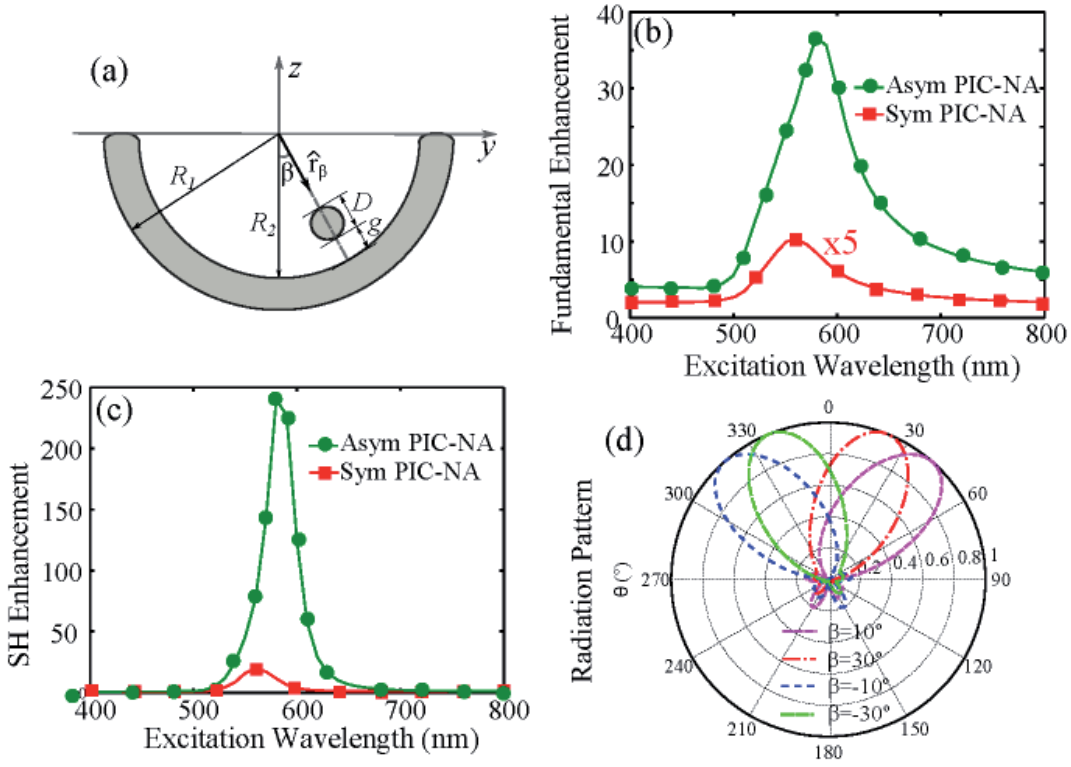

Figure 4. (a) A schematic drawing of the particle-in-cavity nanoantenna (yoz plane). A nanosphere (diameter D) was inside a nanocup cavity (external and inner radii being R_1 and R_2) separated by a gap, g. The angle between the center of the nanosphere and the symmetry axis of the nanocup was β. (b) The fundamental and (c) second-harmonic enhancement spectra of the symmetric and asymmetric particle-in-cavity nanoantenna. (d) The steering of the main beam of the radiation pattern (yoz plane) at the resonant wavelength by manipulating the position of the particle.

resonant with the cavity-dressed nanoparticle mode. The fundamental field enhancement was investigated at a fixed point (the center of the gap). The enhancement factor is defined as the ratio of the magnitude of the scattered field at the center of the gap to the magnitude of the incident field. Figure 4b shows the calculated fundamental field-enhancement spectra of the particle-in-cavity nanoantenna. Enhancement factors of roughly 2 at $\lambda = 560$ nm and 37 at $\lambda = 580$ nm were found for the symmetric and asymmetric cases, respectively. Because the second-harmonic field increased as the square of the fundamental field, a strong near-field at the fundamental frequency was particularly important for efficient second-harmonic generation enhancement.

The second-harmonic enhancement factor is defined as the ratio of the second-harmonic intensity of the particle-in-cavity nanoantenna to the summation of the second-harmonic intensities of the single nanosphere and nanocup. Figure 4c shows the second-harmonic enhancement factor. The correlation between the fundamental field-enhancement spectra (Figure 4b) and the second-harmonic intensity spectra (Figure 4c) demonstrated that the second-harmonic generation from the particle-in-cavity nanoantenna was boosted by the enhanced field intensity arising from the gap plasmonic mode. The radiation pattern of the particle-in-cavity nanoantenna is shown in Figure 4d. Unidirectional radiation was observed. This important feature further enhanced the second-harmonic generation in the far field, and facilitated the detection of the generated second-harmonic waves. Moreover, beam-steering feature was achieved by changing the position of the nanosphere.

4. Conclusion

In summary, the Boundary-Element Method was developed for modeling surface nonlinear scattering from plasmonic nonlinear nanoantennas. The method was validated by comparing far-field sum-frequency and second-harmonic scattering patterns with Mie theory solutions. The sum-frequency generation from the multi-resonant nanoantenna, where two incident frequencies corresponded to the fundamental resonances of the two arms, was analyzed by the developed method. The second-harmonic generation from the particle-in-cavity nanoantenna was also modeled by the developed method. Unidirectional radiation of asymmetric particle-in-cavity nanoantenna was realized, and the radiation direction could be controlled by the position of the nanoparticle. The directional beam steering offered by the proposed particle-in-cavity nanoantenna has promising applications, such as nonlinear sensing, spectroscopy, and frequency generation.

5. Acknowledgement

This work was supported in part by the Research Grants Council of Hong Kong (GRF 17207114 and GRF 17210815), NSFC 61271158, Hong Kong UGC AoE/P–04/08, and by the US NSF 1218552 and NSF 1609195.

6. References

1. M. Kauranen and A. V. Zayats, "Nonlinear Plasmonics," *Nature Photonics,* **6**, 2012, pp. 737-748.

2. S. A. Maier, *Plasmonics: Fundamentals and Applications*, New York, Springer, 2007.

3. Y. R. Shen, *The Principle of Nonlinear Optics*, New York, John Wiley & Sons, Inc., 1984.

4. J. E. Sipe, V. C. Y. So, M. Fukui, and G. I. Stegeman, "Analysis of Second-Harmonic Generation at Metal Surfaces," *Physical Review B*, **21**, 1980, pp. 4389-4395.

5. C. Ciraci, E. Poutrina, M. Scalora, and D. R. Smith, "Origin of Second-Harmonic Generation Enhancement in Optical Split-Ring Resonators," *Physical Review B*, **85**, 2012, p. 201403.

6. J. Butet, K. Thyagarajan, and O. J. F. Martin, "Ultrasensitive Optical Shape Characterization of Gold Nanoantennas Using Second Harmonic Generation," *Nano Letters*, **13**, 2013, pp. 1787-1792.

7. V. K. Valev, "Characterization of Nanostructured Plasmonic Surfaces with Second Harmonic Generation," *Langmuir*, **28**, 2012, pp. 15454-15471.

8. J. Butet, I. Russier-Antoine, C. Jonin, N. Lascoux, E. Benichou, and P.-F. Brevet, "Sensing with Multipolar Second Harmonic Generation from Spherical Metallic Nanoparticles," *Nano Letters*, **12**, 2012, pp. 1697-1701.

9. G. Bautista, M. J. Huttunen, J. Makitalo, J. M. Kontio, J. Simonen, and M. Kauranen, "Second-Harmonic Generation Imaging of Metal Nano-Objects with Cylindrical Vector Beams," *Nano Letters*, **12**, 2012, pp. 3207-3212.

10. H. Harutyunyan, S. Palomba, J. Renger, R. Quidant, and L. Novotny, "Nonlinear Dark-Field Microscopy," *Nano Letters*, **10**, December 2010, pp. 5076-5079.

11. G. Sartorello, N. Olivier, J. Zhang, W. Yue, D. J. Gosztola, G. P. Wiederrecht, G. Wurtz, and A. V. Zayats, "Ultrafast Optical Modulation of Second- and Third-Harmonic Generation from Cut-Disk-Based Metasurfaces" *ACS Photonics*, **3**, 2016, pp. 1517-1522.

12. G. F. Walsh and L. Dal Negro, "Enhanced Second Harmonic Generation by Photonic-Plasmonic Fano-Type Coupling in Nanoplasmonic Arrays," *Nano Letters*, **13**, 2013, pp. 3111-3117.

13. K. Thyagarajan, J. Butet, and O. J. F. Martin, "Augmenting Second Harmonic Generation Using Fano Resonances in Plasmonic Systems," *Nano Letters*, **13**, 2013, pp. 1847-1851.

14. K. Thyagarajan, S. Rivier, A. Lovera, and O. J. F. Martin, "Enhanced Second-Harmonic Generation from Double Resonant Plasmonic Antennae," *Optics Express*, **20**, June 2012, pp. 12860-12865.

15. X. Y. Z. Xiong, L. J. Jiang, W. E. I. Sha, Y. H. Lo, and W. C. Chew, "Compact Nonlinear Yagi-Uda Nanoantennas," *Scientific Reports*, **6**, January 2016, p. 18872.

16. X. Y. Z. Xiong, L. J. Jiang, W. E. I. Sha, Y. H. Lo, M. Fang, W. C. Chew, and C. H. Choy, "Strongly Enhanced and Directionally Tunable Second-Harmonic Radiation by a Plasmonic Particle-in-Cavity Nanoantenna," *Physical Review A*, **94**, November 2016, p. 053825.

17. R. Czaplicki, J. Makitalo, R. Siikanen, H. Husu, J. Lehtolahti, M. Kuittinen, and M. Kauranen, "Second-Harmonic Generation from Metal Nanoparticles: Resonance Enhancement Versus Particle Geometry," *Nano Letters*, **15**, 2015, pp. 530-534.

18. R. W. Boyd, *Nonlinear Optics*, New York, Academic Press, 1992.

19. S. M. Rao, G. R. Wilton, and A. W. Glisson, "Electromagnetic Scattering by Surfaces of Arbitrary Shape," *IEEE Transactions on Antennas and Propagation*, **AP-30**, 3, May 1982, pp. 409-418.

20. L. N. Medgyesi-Mitschang, J. M. Putnam, and M. B. Gedera, "Generalized Method of Moments for Three-Dimensional Penetrable Scatterers," *Journal of the Optical Society of America A*, **11**, April 1994, pp. 1383-1398.

21. J. I. Dadap, J. Shan, and T. F. Heinz, "Theory of Optical Second-Harmonic Generation from a Sphere of Centrosymmetric Material: Small Particle Limit," *Journal of the Optical Society of America B*, **21**, 2004, pp. 1328-1347.

22. A. G. F. de Beer and S. Roke, "Nonlinear Mie Theory for Second-Harmonic and Sum-Frequency Scattering," *Physical Review B*, **79**, 2009, p. 155420.

23. P. B. Johnson and R. W. Christy, "Optical Constants of Noble Metals," *Physical Review B*, **6**, 1972, pp. 4370-4379.

Hornet Biological Radar for Detection, Tracking, Direction Finding, and Long Distance Communication: Is This Possible?

J. Gavan and M. Haridim

HIT-Holon Institute of Technology
Faculty of Engineering
Holon 58102, Israel
E-mail: mharidim@hit.ac.il

Abstract

The late, great entomologist, Prof. Jacob S. Ishay, from the faculty of medicine in Tel-Aviv University, dedicated his life to hornet research. He found that the hornet's body produces a considerable amount of electrical energy by means of photovoltaic and piezoelectric effects. Using an electronic microscope, Prof. Ishay showed to the authors the existence of two-dimensional arrays of very short spikes on the body skin of hornets, not unlike antenna arrays for radar and wireless communication systems. Later, Prof. Ishay and his team also found that the hornet's two antennas produce electricity and include spikes. These three radiation sources enable direction finding – even at great distances – from cooperative targets by wireless communication, allowing a new hypothesis of triangulation and an inverse GPS property for hornets.

In this paper, a hypothetical biological radar for hornets is presented. In particular, we present a hypothesis regarding short spikes that may act as three phased arrays with extremely short monopole antenna elements. Due to their tiny physical dimensions, the frequency range of the antennas was estimated to be beyond 250 GHz, in the THz band. A comparison with other biological radar and direction-finding wireless communication systems is also provided.

1. Introduction

The current progress in wireless positioning systems was set off by recent great improvements in the precision, reliability, and timing of modern Global Positioning Systems (GPS), Digital Signal Processing (DSP), and other technologies. These resulted in a host of innovative military and civilian applications, as well as significant life-saving capabilities. However, on our Earth there exist a number of creatures, mammals, and insects that possess extremely sophisticated and accurate capabilities, the perfection of which Mother Nature has been "working on" for millions of years, and which they use to locate and position their friends and foes. For instance, it is well known that bats have developed superior ultrasonic acoustic radio-detection and ranging (radar) around 20 kHz to detect, locate, and hunt their prey. Elephants, dolphins, whales, and other mammals also have very-low-frequency acoustic wireless systems for radar, communication, and positioning. There are several small insects, such as moths, which possess detection and localization systems for mating and other purposes at very high frequencies, up to the THz range, due to their small physical dimensions. Scientists also study these biological systems today for improving man-made positioning systems, and other purposes.

The late, great entomologist, Prof. Jacob S. Ishay, from the faculty of medicine at Tel-Aviv University, dedicated his life to hornet research. Prof. Ishay installed hornet nests near the window of his laboratory, on the fifth floor of the medicine faculty building of the Tel Aviv university. This was not highly appreciated by his neighbors, although nobody was stung. Several theories have been developed so far in trying to explain how hornets can hunt their prey, easily localize their nests at distances of up to a few kilometer, and how male hornets track and fertilize queens belonging to other nests. Prof. Ishay found that the hornet's body produces a considerable amount of electrical energy by means of photovoltaic and piezoelectric processes [1]. He also identified that hornets cannot operate in darkness, since they use photovoltaic cells as their energy source.

The authors had the privilege of knowing Prof. Ishay as a friend and colleague. He was a true scientist of honor and integrity. Through an electronic microscope, Prof. Ishay and the authors have observed a multitude of very short spikes with three different lengths, located on the center body skin of local oriental hornets. Photos of these

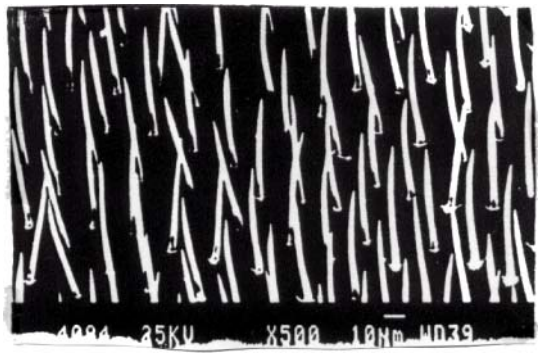

Figure 1a. A photo of the densest hornet phased array ($n = 1$). The spikes were about $L_{s1} = 55$ μm long, spaced 20 μm to 25 μm from each other.

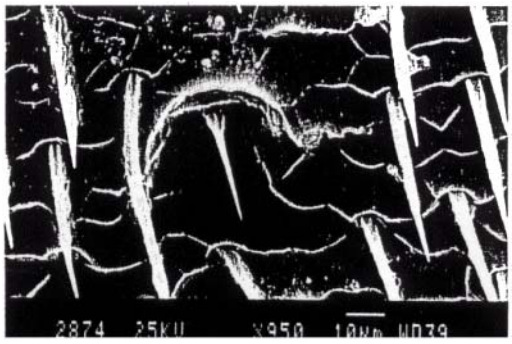

Figure 1b. A photo of the intermediately dense hornet phased array ($n = 2$) (from the same area as Figure 1a). The spikes were about $L_{s2} = 30$ μm long.

spikes are shown in Figure 1 [2]. Prof. Ishay and his team measured the dimensions of the spikes in order to estimate the frequency ranges, considering the estimated length of the spike as a quarter wavelength [3] for optimal radiation. The extremely short length of the hornet's spikes (dielectric antennas) implies extremely high operational frequencies of 100s of GHz, THz, and higher.

Based on our previous experience in radar, radio communications, RFI, direction finding (DF), GPS systems, and the findings of Prof. Ishay, we have arrived at some interesting conclusions [2-4]. The short spikes may act as phased-array dielectric antennas, with extremely short monopole elements transmitting and receiving radio or acoustic signals [5-7]. This is analogous to the well-known acoustic radar tracking and location systems of bats, operating at ultrasonic frequencies from 20 kHz to 200 kHz [8, 9]. However using spike antennas at extremely high frequencies with limited mechanical energy, it is more probable that the signals propagated are carried by EM waves, instead of longitudinal acoustic waves.

The hypothesis developed in this paper assumes that the significant electrical energy in the hornet's body, found and measured by Prof. Ishay [1, 4], is partly converted to EM waves to operate biological radar and direction-finding systems in the THz frequency bands. Calculations show that the hornet's THz radar operating range for detecting and positioning their prey is limited to 10s of meters, which is similar to the operating range of predator bats. Such radar and direction-finding systems are perhaps less developed for honey bees. The bees are more similar to fruit-eating bats that possess less-sophisticated and shorter-distance location systems than those for the insect-eating predator bats [8, 9].

The significantly higher operating ranges required for localizing the hornet's nests can be explained by the operation of the hornet-nest sentinels. The hornet-nest sentinels continuously transmit signals during the daytime that may be received by remote hornets. The remote hornets, even far from their nest, receive the transmitted signals, which help them to localize the exact position of the nest [3, 4]. This can be explained and computed using the Friis line-of-sight (LOS) radio-communication model, rather than the radar equation [10]. The hornet's remote-positioning system can be precisely explained by a triangulation process, similar to an inverse GPS, modeled by a transmitting antenna from the nest sentinels or the queen hornets [3, 11], and three receivers located on the hornet's body and the hornet's two antennas, as will be explained in Sections 3 and 4.

In this paper, we present the hypothetical biological radar of hornets. Our hypothesis suggests that the three different spike lengths represent three transmitting and receiving phased arrays, each operating at a different sub-millimeter wavelength, as implied by the short physical dimensions of the spikes [2, 5]. This hypothesis is supported by the existence of a natural photovoltaic, thermoelectric, and piezoelectric internal generation of energy in the hornet's body, which provides the radio-frequency (RF)

Table 1. The frequency range, wavelengths, spike lengths, atmospheric losses, and dispersion losses at a distance of 10 m from oriental hornet workers [2].

	L_{sn} (μm)	λ_{sn} (μm)	f_{sn} (GHz)	$2A_d$ (dB)	$2A_{at}$ max (dB)
1. Denser phased array	55	220	1365	230	6.0
2. Intermediate phased array	30	120	2500	240	8.0
3. Sparser phased array	140	560	535	215	2.0

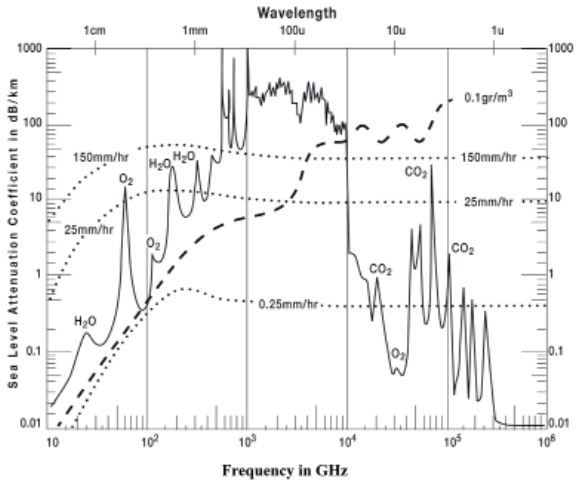

Figure 2. The sea-level atmospheric attenuation coefficient [dB/km] as a function of frequency (lower horizontal axis) for: a gaseous atmosphere (solid line, for 20° C and a water-vapor density of 7.5 g/m^3, clouds, or fog (dashed curve for water droplets 0.1 g/m^3), and various rainfall rates (dotted curves) [10].

energy required for the operation of such a biological radar system [3]. This novel hypothesis could replace those related to the terrestrial magnetic field or pheromone scent trails [4].

2. The Hornet's Biological Radar Tracking: Analysis and Operating Range Computation

Table 1 presents estimated values for the important parameters of the hornet's three phased arrays: the operational wavelength, the frequency ranges, and the propagation-loss limits [3]. The two-way radar free-space line-of-sight dispersion losses, $2A_d$, of the transmitted navigation signal are given in decibels (dB) [6, 10].

In Table 1, L_{sn} is the length of the spikes (belonging to array n), and λ_{sn} is the estimated wavelength. From the basic relation

$$f_{sn} = \frac{c}{\lambda_{sn}}, \qquad (1)$$

where $c \approx 3\times10^8$ m/s is the velocity of light, and the approximate optimal radiated wavelengths are around $\lambda_{sn} \approx 4L_{sn}$.

The estimated three influential frequency ranges, f_{sn} of the oriental hornet workers are thus around 535 GHz, 1365 GHz, and 2500 GHz: all in the THz frequency band [12]. The dispersion losses, A_d, in the far-field region are given by

$$A_d = 20\log\frac{4\pi d}{\lambda}\ \text{(dB)}. \qquad (2)$$

For instance, for the sparse phased-array-radar space (wavelength λ_{s3}), the dispersion losses at a line-of-sight distance of $d = 10$ m from the hornet are $A_d = 107$ dB for one-way and $A_d = 215$ dB for two-way operation. Obviously, the high loss levels require highly sensitive receivers and high gain of the (spike) array antennas in order to achieve high detection probability of targets for distances exceeding 10 meters [4, 11].

At millimeter and sub-millimeter wavelengths, the atmosphere contributes additional losses due to molecular frequency resonances and air moisture. The measured mean and maximum atmospheric loss factor α [dB/m] was obtained from the International Telecommunication Union Radio (ITU-R) [10] and Jet Propulsion Lab (JPL) statistical measurement results [11]. The atmospheric losses, $2A_{at}$, at a distance of $d = 10$ m from an oriental hornet at sea level under maximum heavy status cloud humidity conditions, are also presented in Table 1 for the three estimated frequency ranges [3].

For instance, at a distance of 10 m from the hornet under atmospheric conditions, the maximum two-way atmospheric losses for the medium-density phased-array radar would be around 8 dB, and for the sparse phased-array (535 GHz) would be less than 2 dB, as shown in Table 1 and Figure 2. It is thus possible to neglect the atmospheric-propagation loss in most cases, because the inherent line-of-sight propagation dispersion losses exceeding 200 dB dominate [11, 13]. During nighttime, heavy cloud, or rain, hornets are not active, due to the lack of solar and photoelectrical energy, which is mandatory for the operation of their radar system [1, 14].

The estimated sub-millimeter-wavelength range of $120 < \lambda_{sn} \le 560$ for worker hornets is far lower (by at least one order-of-magnitude) than the classical infrared (IR) wavelength of NdYag (1.06 μm) and CO_2 (10.6 μm) lasers [15, 16]. The hornets' far-IR operating wavelengths are thus not yet common, except in radio astronomy. This may be one of the reasons that our hypothesis has not been validated to date.

The operational distance of the hornets' biological radar localization and tracking system depends on the transmitted power level, frequency, weather, and also on the propagation losses.

The hornet's radar operating range, d_{max}, can be computed using the following classical radar equation [11]:

$$d_{max} = \sqrt[4]{\frac{P_t G_t A_e \sigma}{(4\pi)^2 S_{min}}}, \qquad (3)$$

where the estimated values are [1, 3, 4, 17] as follows. The radiated power is $P_t = 20$ μW. This is due to the significant photovoltaic power developed by the hornets from the electric energy harvested from the sun, and based on the recent paper of M. Plotkin (the last PhD student of Prof. Ishay) [17]. (The paper shows that the I/V measurements for the oriental hornet gave an I_{sc} of 0.858 mA/cm^2 and a V_{oc} of 0.56 V. For an effective area of 0.5 cm^2 and a fill factor of 50%, the dc power could thus reach more than 120 μW. Assuming a low dc-to-THz conversion efficiency of 20%, an estimated RF power of 20 μW is quite possible. For larger males, queens, German, and destructive Asian hornets, the RF generated power would be enhanced.

The antenna gain is $G_t = 10^3$ (30 dBi), due to the high number of spikes (dielectric antenna elements) in the arrays. The minimum detectable signal is $S_{min} = 10^{-13}$ W. The receiving antenna's effective area is $A_e = 2\times10^{-14}$ m^2 The radar cross-sectional (RCS) area for an insect is $\sigma \simeq 10^{-4}$ m^2 (for an adult person, it is $\sigma \approx 1$ m^2). For frequency bands up to 4 THz at room temperature, the system's thermal noise, P_n, is still dominant over the quantum noise, and limits the minimum detectable signal [6, 14]:

$$P_n = FkTB\,, \qquad (4)$$

where $k = 1.38\times10^{-23}$ J/°K is the thermo-dynamical Boltzmann constant at the ambient temperature $T = 300K$ B is the frequency bandwidth (estimated to be less than 1 MHz), and $F \approx 10$ is the noise figure. This gives $P_n \simeq 4\times10^{-14}$ W.

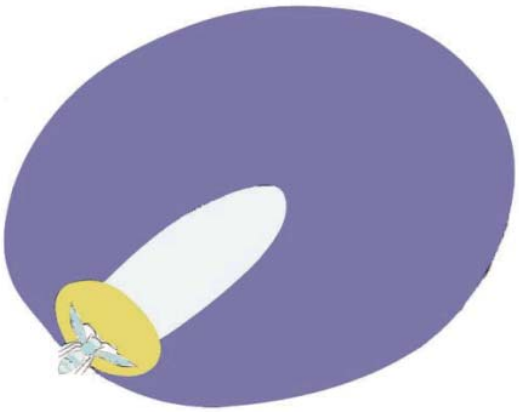

Figure 3. The three-mode tracking mechanism of the hornet's natural radar systems.

Substituting these realistic estimated values into Equation (3), we obtain

$$d_{max} = \sqrt[4]{\frac{2\times10^{-5}\ 10^3\ 2\times10^{-4}\sigma}{(4\pi)^2\,10^{-13}}} \approx 23\sqrt[4]{\sigma}\ \text{m} \qquad (5)$$

The biological radar operational range for a flying hornet to detect and track an adult person is thus about $d = 23$ m, and for a small insect, about 2.3 m. This range is extended because the hornet's cerebral control system may perform a signal-processing pulse-integration process, similar to the case of bats [8, 9]. For an adequate probability of detection and a low false-alarm rate, the operational radar range can be enhanced up to three times to

Table 2. The important antenna parameters of the various spike arrays present on the oriental hornet workers and males [4].

A. Worker's (dielectric antennas) spikes

Types	Length (μm)	Wavelength Range (μm)	Frequency Range (GHz)	Base Diameter (μm)	Tip Diameter (μm)	Relative Number**
Trichoid	22.6	89.4	3340	2.4	Spine-like	100
Placoid	24.7	98.8	3035	4.6*	–	20
Campaniform	11.9	47.6	6300	7	3.3	5
Agmon	8.9	35.6	8430	3.7	Spine-like	2

B. Male's (dielectric antennas) spikes

Types	Length (μm)	Wavelength Range (μm)	Frequency Range (GHz)	Base Diameter (μm)	Tip Diameter (μm)	Relative Number**
Trichoid	20	80	3750	3.5	Spine-like	100
Placoid	27.1	108.4	2770	8.8	3.6	5
Campaniform	11.7	46.8	6400	3.4*	–	20
Agmon	8.2	32.8	9150	3.3	Spine-like	2
Tyloid	253.6	1014.4	295	72.3*	–	1*

*Width, **on a relative scale of 1 to 100

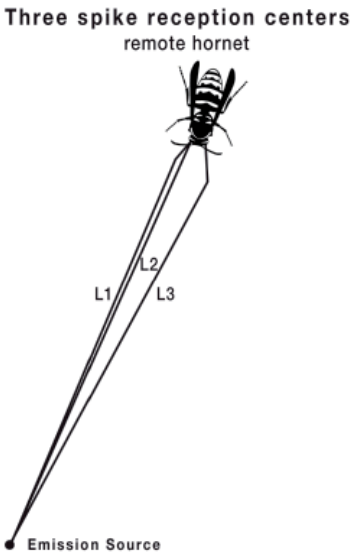

Figure 4. The hornet's communication-based direction-finding technique, with three reception centers, L1, L2, and L3, for remote cooperative target detection, nest localization, or mating queens by the males.

$$7 \text{ m} < d_{max} < 70 \text{ m}. \quad (6)$$

For comparison, it is known that for bats, the operational range of their navigational system extends from a few cm up to 30 m [8, 9]. The extremely-high-frequency (EHF) radio emissions of hornets depend on the weather and light intensity. Under good sunny conditions, significantly higher probabilities of prey detection and tracking accuracy can be obtained [14].

For a radar using a biological switching multimode operation, it is logical that an array with the lowest frequency range, and lower antenna directivity and dispersion losses, is operated first when starting the detection and localization process [13, 16]. Later, when the target is very close and the reflected signal exceeds a higher-threshold power level, the biological radar system would switch to the most-accurate tracking mode, with the highest frequency range and the smallest operation range, as presented in Figure 3.

However, the provided radar analysis and computational results cannot explain the higher detection and localization ranges at which worker hornets can track and reach their nest, or at which male (drone) hornets can join a queen from distances up to a few kilometers.

3. Hornet Communication-Based Direction-Finder Investigation (General Concepts)

It was later shown by a young student of Prof. Ishay, Yafit Agmon, that the two antennas of hornets are also densely covered by numerous short spikes of different lengths [14]. Prof. Ishay therefore named the shorter spikes on the hornet's antennas Agmon (see Table 2). Measurements have shown that the electric voltage, current, and power of the two hornet antennas are significantly high, similar to their body cuticle. In addition, piezo-electrical energy can be generated in the antennas during flight times. The hornet's two antennas and the cuticle thus together provide three different sources of wireless transmission and reception for detection, localization, and tracking of cooperative target echoes, as shown in Figure 4 [4].

The measured spike dimensions are presented in Table 2, including four spike species for hornet workers, as presented in Figure 5, and five species for drones (males), as presented in Figure 6. Table 2 shows the average length, L_{sn}, of the spike species and the estimated frequency ranges obtained for simple monopole spike antennas, where

$$\lambda_{sn} \approx 4L_{sn}, \quad (7)$$

and

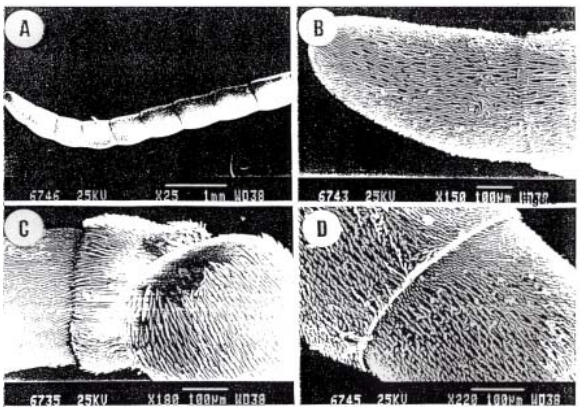

Figure 5. Worker hornet spike arrays: pictures taken in the laboratory of Prof. Ishay using an electronic microscope [4].

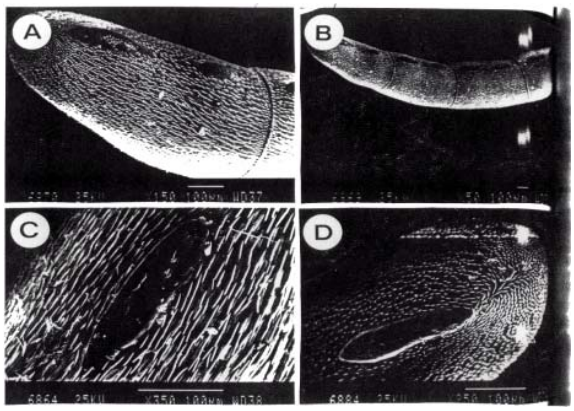

Figure 6. Drone (male) hornet spike arrays: pictures taken with an electronic microscope.

$$f_{sn} \approx \frac{3\times10^5}{4L_{sn}} \text{ GHz.} \quad (8)$$

Table 2 also provides the spike elements' base and tip diameters, and the relative number of spike elements in a scale of one to 100 units.

The photoreceptor elements are not considered here, because of their scarcity and the difficulty in measuring the permittivity and the operational frequency ranges of this stripline configuration. Table 2 shows that the frequency bands of the oriental worker hornets' phased-array antennas may extend from 3035 GHz to 8430 GHz, in the THz band. Most of the spike elements belong to the two lower frequency bands, providing the highest operational range because of the lowest dispersion losses. The scarcer spikes of the two antennas provide the two higher-frequency ranges required for the maximum accuracy for the shorter-distance ranges from the target (the last mile, or more accurately, the last meters). The frequency operating band of the oriental male hornets' antenna phased-arrays may extend from 295 GHz to 9150 GHz. The array operating at 295 GHz, with the lowest density of spikes, provides the longest operational range, due to the lower dispersion losses. However, its directivity is too low, and it can be useful only for initiating the orientation process to detect, track, and mate with the queen hornets.

The highest number of spikes and maximum phased-array directivity are obtained at the highest frequency band of 9150 GHz, where the phased array can provide the highest accuracy for the final tracking steps [14].

It has been previously shown that the radar detection and tracking operational ranges are limited to tens of meters, due to the extremely high losses, which increase at an exponential rate as d^n, where $n \geq 4$. However, the fixed distances between the hornet's two radiating antennas and the cuticle radiation and detection sources suggest a new hypothesis of a radio-communication direction-finding technique [17]. The radio-communication direction-finding technique allows a precise and fast localization and tracking of hornet cooperative targets from the net sentinels or the queen, which may transmit up to THz frequency signals. In these cases, the operational range is therefore extended up to a few kilometers using wireless communication instead of an ordinary radar system. The space dispersion losses increase as d^2 under line-of-sight conditions, compared to the sharper rate of d^4 for radars [14, 18].

This new direction-finding hypothesis, shown in Figure 4, could explain the hornets' ability for tracking over large ranges of up to a few kilometers. This high operational range is computed by simulation, as presented in Section 4.

The hypothesis of an insect's radio-communication system using microwave or IR wavelengths is not new. It was published in a few papers, such as [19, 20], concerning night-flying moths that locate mating partners via a natural far-IR radio-communication link. However, the hypothesis of sub-millimeter radar detecting, tracking, and radio-communication links using direction-finding techniques applied to hornets is new. It should be noted that the military combat aircraft (F18) called the Hornet, and the new Boeing and Northrop Grumman advanced Super Hornet aircraft and radars [21], have no direct relationships to this new hypothesis.

Nowadays, the most popular and useful manmade direction-finding technique is the Global Positioning Satellite (GPS) system. Using the triangulation technique, GPS provides very precise and fast three-dimensional positioning by simultaneously receiving microwave (MW) signals from at least three orbiting transmitting satellite sources [22]. For hornets, the direction-finding technique differs by using millimeter or sub-millimeter signals simultaneously received by three different distant phased-array sources located on the searching hornet's cuticle body, and on its two antennas at fixed distances between themselves. This special biological inverse GPS thus includes one transmitting source from the common operation of several flying hornet sentinels operating in daytime around the nest, and three receiving sources located on a remote hornet, providing indications on the way to reach its nest. We can apply the analogy of a lighthouse beacon illuminating a target in order to attract it. Similar triangulation direction-finding processes can also occur between queen and male hornets.

4. Hornet's Direction Finder: Computation and Simulations

The direction-finding communication-based hypothesis enables us to also explain how males from remote nests can track and localize queen hornets for mating purposes. The direction-finding operational range can be computed using the Friis line-of-sight free-space equation, considering that for the extremely short waves transmitted by the hornets, more than 60% of the first Fresnel ellipsoid of the link is generally free of obstacles [6]:

$$P_r = P_t G_t G_r \left(\frac{\lambda}{4\pi d}\right)^2, \quad (9)$$

or

$$\frac{P_r}{P_t} = \frac{G_t G_r c^2}{16\pi^2 f^2 d^2}, \quad (10)$$

where P_r and P_t (watt) are the power at the receiver antennas' inputs (male) and the power radiated by the transmitter antennas (queen), respectively. G_t and G_r are the transmitter and the receiver antennas' array gains,

respectively. f is the operational frequency in GHz, and d is the estimated operational distance (in meters).

From Equation (10) we obtain

$$d = \sqrt{\frac{P_t G_t G_r 9 \times 10^{-2}}{160 P_r f^2}} . \qquad (11)$$

The maximum operational range is obtained from the nondirective minimum frequency band of 295 GHz, shown in Table 2 for initial detection of the queen's position by the males. The following typical realistic values were used in the simulations: $P_t = 2 \times 10^{-5}$ W, $P_r = 4 \times 10^{-14}$ W, as shown previously for clear atmospheric conditions; G_t and G_r were each around 1000 (30 dBi); and we found $d \approx 1150$ m.

The direction-finding hypothesis can also explain the localization and the return to their nest of distant hornet workers. Using the former natural radar detection and tracking techniques, the maximum hornet operational range is limited to only a few tens of meters, as previously shown using Equation (5). However, it is also well known that hornets can directly find their way to their nest up to a distance of several kilometers. To enable detecting and tracking the location of the nest from these far distances, several sentinel worker hornets simultaneously ventilate their wings as a group near the nest [4] to generate radio energy during the daytime, and radiate their sub-millimeter signals in a similar fashion, as in the case of a lighthouse beacon.

The emission from multiple identical radiation sources can be received by the three phased arrays of a remote hornet. These phased arrays are located at fixed mutual distances on the hornet, and enable the direction-finding system to localize and track the nest by a triangulation process [11, 17].

The maximum distance of direction-finding communication, d, of remote hornets from their nest can also be computed using Equation (11). It was shown that the most efficient radiation was at the worker hornet's lowest frequency range of 535 GHz (Table 1). Assuming $P_t = 2 \times 10^{-5}$ W, $P_r = 4 \times 10^{-14}$ W, and $G_t = G_r = 1000$ (30 dBi), we obtained $d_{max} \approx 650$ m. For the oriental hornets, d_{max} is slightly reduced, due to the additional atmospheric losses for a distance of 1 km at 535 GHz[3, 10, 17]. However, the diversity technique achieved using the common sub-millimeter radiation from several transmitting hornets and integration of pulse transmissions can still enhance the operational range by about a factor of three or even more [14]. Using the same equations for the bigger German hornets, operating at lower frequencies, results in a significantly higher d_{max} under line-of-sight propagation conditions.

5. Preliminary Experiment, Test Results, and Discussion

The validation of the proposed novel hypothesis of natural radar tracking and communication-based direction-finding systems affecting the flight of hornets was very complex in the past. This was due to the rarity and high price of measurement equipment, radio sources and detectors, operating at frequency ranges exceeding 100 GHz (sub-millimeter waves). As shown in Tables 1 and 2, the estimated radiation and detection frequencies for oriental hornet workers were from 535 GHz to 8430 GHz, and for males (drones) they were from 295 GHz to 9150 GHz [4, 14].

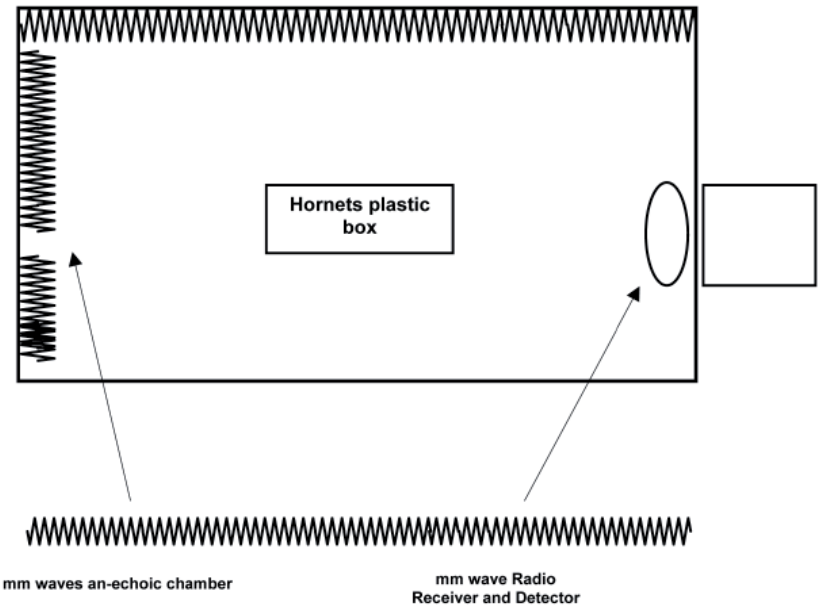

Figure 7. A schematic diagram of the hornet radiation experiment [3, 4].

Prof. Ishay also investigated the German hornets (wasps) Paravespula Germanica. For the (German) European wasps, the maximum length of the spikes is close to 0.5 mm, which corresponds to a minimum estimated frequency range of around 150 GHz. The existence of these longer spikes can be attributed to the high rainfall, cloud, and foliage conditions in central Europe. These long spike lengths enable satisfactorily higher radar distance tracking and communication direction-finding systems at millimeter rather than sub-millimeter wavelengths.

In 2002, Prof. Ishay and the authors tried to test the first hypothesis regarding hornets in a best qualified laboratory state-of-the-art start-up R&D company at the Technion research center campus in Haifa (Israel). The laboratory facilities included a millimeter-wave anechoic chamber, and two bulky, sensitive, and accurate measurement receivers, operating at fixed frequencies of 140 GHz and 220 GHz. Prof. Ishay built an experimental setup with two glass-covered boxes. The first one included about 50 German hornets, and the second had tens of the Oriental type of workers, and six male hornets. A schematic diagram of the hornet radiation experiment is shown in Figure 7 [3, 4].

Following a long calibration process separately for each hornet box, when held in a dark anechoic chamber, the boxes were illuminated by a strong projector light for a period of a few minutes, in order to enable the hornets to better radiate. When the hornets are flying, it may be that they develop additional electric energy from the piezo-electric effect, which is partially converted to more RF emission in the THz frequency range.

In all the experiments with the German hornet box, the 140 GHz receiver systematically showed an increase of about 1% in the ratio of the received to the background radiation intensities under illumination, when compared to the dark conditions. However, in several cases with the 220 GHz receiver, the intensity ratio decreased under illuminated conditions. These results were correlated to the estimated German wasp minimum radiation frequency of 150 GHz, which was far from the 220 GHz range. By comparison, the ratio intensity measurement results with the Oriental hornets showed contradictory results for both the 140 GHz and 220 GHz receiver cases. This may have been due to the significant frequency difference within the expected oriental hornet radiation frequency bands.

Our main conclusions from the preliminary experimental results were:

1. The partially affirmative results obtained with the German wasps at 140 GHz were encouraging, but not sufficient for a conclusive proof of our hypothesis.

2. The hornets must be flying in order to supply additional piezo-electric energy, besides the mandatory illumination conditions for optimal radiation. This can be achieved by producing waves of appropriate frequency (using a horn, for instance) in order to stimulate the tested hornets to fly, and/or by allowing some of them to be free outside of the box in the anechoic chamber.

3. At least a frequency sweeper with a range of 140 GHz to 220 GHz is required, to detect the reception of the peak radiation of the German hornets at the precise main frequency. This may be sufficient to prove the hypothesis of millimeter-wave radar tracking for the German wasps, but not enough for the investigated Oriental hornets operating at significantly higher frequency ranges, where very rare and expensive sub-millimeter-wave sources, chambers, and detectors existed at this time.

4. Prof. Ishay suggested testing hornets held away from their nests by affecting their spike location system, which may prevent them from finding their nest. Unfortunately, he could not complete these experiments and his laboratory was closed following his death.

6. Collaboration Required to Prove and Benefit from Our Hornet Hypothesis

The future measurements and experiments to completely confirm our hornet hypothesis and usefully utilize the results would require a tight collaboration between:

1. Expert entomologists in hornets (or in the worst case, in bees, which may be less performing than hornets), with a leading, well-equipped laboratory, similar to the laboratory of the late Prof. Ishay.

2. Wireless communication or/and radar experts also working in the THz frequency ranges using up-to-date equipment in the field [23-25].

There are two kinds of tests required to prove our hypothesis: positive and negative tests.

The positive tests would be similar to those we have done as described in Section 5. However, they would require the use of sophisticated, sensitive, and accurate variable-frequency receivers or spectrum analyzers in the THz ranges to detect the hornets' emissions, especially when they are flying. This required novel equipment was not yet available when we performed our experiments. It is now available in several laboratories. It may also be possible to expose the hornets to modern THz variable-frequency transmitters or signal generators and to test their reactions.

The negative experiments, of damaging the spikes of the hornets and observing if they are affected and hence unable to find their required direction, were suggested by the late Prof. Ishay. However, they were not done because he became ill. It is also suggested to use different electrical shielding materials between some hornets and their nest,

and to test if they loose their direction in the case of strong shielding. These negative experiments are easier to do, but are less important and conclusive than the positive experiments described.

7. Final Conclusions

Experiments have been conducted to investigate the functions of the spikes on the body skin and antennas of hornets. These were observed by the late, great entomologist, Prof. Jacob S. Ishay, using an electronic microscope. These have led to the new hypothesis of a natural complex radar navigation system, referring also to Prof. Ishay's discovery of a large amount of electric energy produced in the bodies and antennas of the hornets, partly from biological photo-voltaic cells [1-3, 17, 26].

Our computational results show that the radar tracking and detection operational ranges are limited to tens of meter, even for large radar cross sectional areas. The hypothesis of the hornet males tracking the queens and workers, localizing their nests at distances of up to a few kilometers, were developed, using the concept of direction-finding and inverse-GPS technique based on radio communication, instead of a radar-based system. The possibility of sub-millimeter wave radiation transmission towards three transmitting and receiving wireless communication radiation and detection centers, included on a single remote hornet, were also suggested. This may enable direction-finding radio-communication localization and tracking of cooperative hornet targets up to an operational range of a few kilometers [4, 14].

Our fascinating hypothetical hornet radar and direction-finding wireless communication systems may explain their short-range hunting radar and astonishing three-dimensional long-range guidance and localization abilities. However, these have yet to be confirmed by precise measurement results that correlate with the parameters of the sub-millimeter-wave radiated power sources. The estimated natural hornet's radar-system wavelength bands are far beyond the usable longer radio microwave and millimeter-wave bands, and shorter than the infrared bands. The likelihood of detecting the hornet's radiation in the THz frequency band to date has therefore been very small, as the development of equipment was in its infancy [12]. However nowadays, with the huge progress, developments, new applications, and the availability of accurate and sensitive measurement equipment in the THz bands, it easier and more probable to prove our hypothesis [23-25]. Cooperation with entomological experts in hornets and bees is required to validate our hypothesis and to replace the actual hypotheses on hornet performance of long-distance detection and direction finding due to the terrestrial magnetic fields or pheromone scent trails [17, 26]. Validation of our proposed hypothesis may open new horizons for the existence of other similar three-dimensional insect or bird radar and direction-finding systems. Furthermore, it could also be useful for research on flying insects and birds, and on novel improved sub-millimeter-wave improved wireless systems for new applications.

It has also been published in scientific and popular reviews that honey bees can be used for detecting explosives and drugs [28]. However, the predator hornets are more skilled for these applications than bees, whose main functions are to provide honey and to pollinate the flora. It is also very interesting to investigate the possibilities of applying nanotechnology circuitry on cyborg hornets for influencing them to fulfill similar tasks, such as what has been implemented by DARPA and other R&D institutions with bats and insects for intelligence and other remote-sensing missions [29].

Recently, huge hornets from the far east invaded France, Italy, and neighboring countries in Europe. They are exterminating honey bees, the contribution to nature and agriculture of which is tremendous [30]. Expert use of hornets' advanced tracking and localization systems may also help in protecting the bees, which may also be affected from polluted radiation by the numerous new wireless systems operating at increased frequency ranges, such as cellular phones. The recent threats to honey bees from the big Asian yellow-legged hornets could be reduced or solved using cyborg hornets and the results of the natural radar and wireless-communication materials developed in this paper and in the references [29-31].

8. References

1. J. S. Ishay, O. Goldstein, E. Rosenzweig, D. Kalicharan, and W. L. Jongebloed, "Hornet Yellow Cuticle Microstructure: A Photovoltaic System," *Phys. Chem. & Physics and Med. NMR*, **9**, 1, 1997, pp. 71-93.

2. J. S. Ishay and J. Gavan, "Hypothesis Stipulating that a Natural radar Navigational System Guides Hornet Flight," *Journal of Electromagnetic Waves and Applications*, **13**, 1999, pp. 1611-1625.

3. J. Gavan and J. S. Ishay, "Hypothesis of Natural radar Detection and Navigation Systems Guiding Hornets Flight," *International Journal of Infrared and Millimeter Waves*, **21**, 2, February 2000, pp. 309-320.

4. J. Gavan and J. S. Ishay, "Hypothesis of Natural Radar Tracking and Communication Direction Finding Systems Affecting Hornets Flight," Progress in Electromagnetics Research PIER 2002.

5. A. J. Fenn, *Adaptive Antennas and Phased Array for radar and Communications*, Norwood, MA, Artech. House, 2007.

6. J. Gavan and R. Perez (eds.), *Electromagnetic Compatibility Handbook*, New York, Academic Press, 1995, Chapter 19, pp. 715-745.

7. J. Gavan and J. S. Ishay, "*Hypothesis of Natural Radar Detection and Navigation Systems Guiding hornets flight*," 24th International Symposium of IR and mm Waves, Monterey, California, September 1999, pp. FB3 (1-2).

8. D. R. Griffin, *Listening in the Dark*, Bellevue, WA, Yale University Press, 1958, pp. 150-166.

9. M. Geva-Sagiv, L. Las, Y. Yovel, and N. Ulanovsky, "Spatial Cognition in Bats and Rats: From Sensory Acquisition to Multi Scale Maps and Navigation," *Nature Review/Neuro Science*, **16**, 2, February 2015, pp. 93-108.

10. CCIR, *Propagation in Non Ionized Media*, Recommendations and Report of the CCIR, Dusseldorf, International Telecommunication Union Publication, Geneva 1990.

11. *Reference Data for Radio Engineers*, New York, McGraw Hill, 2002, Chapters 35-37.

12. C. M. Snowden, "*Towards Terahertz Semiconductor Technology*," in W. R. Stone (ed.) *Reviews of Radio Science, 1996-1999*, Oxford, Oxford University Press, pp. 327-346.

13. J. Gavan and M. Haridim, "Tri- Mode LADAR/Radar Transponder Systems for Tracking Long Range Cooperative Targets," *International Journal of IR and mm Waves*, **17**, 4, 1996, pp. 721-734.

14. J. Gavan and J. S. Ishay, "Hypothesis of Natural Radar Detection, Navigation and Direction Finding Tracking Systems Guiding Hornets Flight," IEEE International Conference Israel, May 2000, pp. 134-137

15. J. Gavan, "Optimal Radio Beams for Detection and Localization of underground Passive Transponders," *Journal of Electromagnetic Waves and Applications*, **6**, 8, August 1992, pp. 1069-1082.

16. J. Gavan, "LADAR/Radar Dual Mode Operation System for Enhancing Tracking Range and Accuracy," *International Journal of IR and mm Waves*, **15**, 1, 1995 pp. 145-153.

17. M. Plotkin, et al., "Solar Energy Harvesting in the Epicuticle of the Oriental Hornet," *Naturwissenchaften*, **97**, 2010, pp. 67-76.

18. F. Demmel, W. Genal, and U. Unselt, "Digital Scanning Direction Finder," *News from Rhode & Schwarz*, **158**, 1998, pp. 21-23.

19. P. S. Callahan, "Far-Infrared Emission and Detection by Night-Flying Moths," *Nature*, 1965, pp. 1175-1183.

20. H. S. Hsia and C. Susskind, "Infrared and Microwave Communication by Moths," *IEEE Spectrum*, March 1970, pp. 69-76.

21. Goggle, searching of the expression "Hornet Radar and Direction Finding."

22. C. Tristram and S. Biver, "Has GPS Lost Its Way?," *Technology Review*, July/August 1999, pp. 71-74.

23. C. M. Armstrong, "The Truth About Terahertz," *IEEE Spectrum*, August 2012, p.17.

24. I. F. Akylddiz, J. M. Jornet, and C. Han, "Terahertz Band: Next Frontier for Wireless Communications," *Physical Communication*, Elsevier, **12**, September 2014, pp. 16-32.

25. C. Williams, "Terahertz Breakthrough Allows for Ultrafast Wireless Communications," *Extreme Tech. Newsletter*, September 21, 2015.

26. S. Volynchik, M. Plotkin, D. J. Bergman, and J. S. Ishay, "Hornet Flight Activities and its Correlation with UVB Radiation, Temperature and Relative Humidity," *Photochemistry and Photobiology*, **84**, 1, 2008, pp. 81-85.

27. J. Gavan and A. Peled, "Optimized LADAR/Radar Systems for Detection and Tracking," 16th International Symposium of IR and mm Waves, Lausanne, 12, 1994, pp. 1035-1142.

28. R. Menzel, et al., "Honey Bees Navigate According to a Map Like Spatial Memory," *Proc. National Academy Science USA*, **102**, 2005, pp. 3040-3045.

29. A. Bozkurt, R. F. Gilmour, Amit, Lal., "Balloon-Assisted Flight of Radio-Controlled Insect Biobot," *IEEE Transactions on Biomedical Engineering*, **56**, 9, 2009, pp. 2304-2307.

30. E. Marck, "Insecticide Packing Drone Takes out Hornet Nets," *Drone Volt*, June 12, 2016.

31. D. Milanesio, M. Saccani, R. Maggiora, D. Laurino, and M. Poporato, "Design of an Harmonic Radar for the Tracking of the Asian Yellow-Legged Hornet," *Ecol. Evol.*, April 2016, pp. 2170-2178.

Foreword to Radio Science for Humanity: URSI-France 2017 Workshop

Tullio Joseph Tanzi[1] and Joël Hamelin[2]

[1]Institut Mines-Telecom – Telecom ParisTech France
E-mail: tullio.tanzi@telecom-paristech.fr

[2]Past Secretary General of URSI-France

1. Background

Evaluation, anticipation, communication, observation, care, measurement, detection, localization: These are some of the missions for which the science of electromagnetism can provide concrete answers in daily life and during crises or disasters. These were the themes of the URSI-France 2017 workshop under the title "Les radiosciences au service de l'humanité" (Radio Science for Humanity). This workshop was remarkable in that it ran over three days (February 1-3) in Sophia Antipolis, near Nice. It included a joint special session of URSI-ISPRS on disaster management, testifying to the tight collaboration between these two organizations. It also included a special session dedicated to François Lefeuvre, in tribute to his major contributions to space science and activities within URSI, and to the international community of radio science, itself.

This 2017 workshop was also marked by a wide European and international participation. It had nine invited speakers introducing sessions and the presence of representatives of European URSI committees. It had scientific communications from more than 14 countries, mainly Europeans, but also from North America and other countries.

During the gala dinner, at "Auberge du Rédier," in Colomars (a small village on the hills around Nice), the CNFRS Medal was awarded to Prof. Omar El Mazria by astronomer Albert Bijaoui, who represented the French Academy of Sciences. (CNFRS is the Comité National Français de Radioélectricité Scientifique: the French National Committee of URSI.)

A selection of papers nominated by the Scientific Committee will be proposed for publication in either an issue of *Comptes rendus Physique de l'Académie des sciences*, in the journal *Revue de l'électricité et de l'électronique* (*REE*) (in French), or in the *Radio Science Bulletin* in special issues in March and June 2017, depending on each paper's intended audience.

2. URSI Student Prize

During this workshop, an URSI Student Prize of €500 was awarded to honor the best paper presented by a PhD student. This year, the Scientific Committee was unable to decide between two equally accomplished finalists, and it awarded the prize to the two winners *ex-aequo*. The awards were presented by Prof. Peter Van Daele, URSI Assistant Secretary General.

The first student, François Mercier (Météo-France, Toulouse, France), presented an approach intending to improve the estimation of water resources: "For a Better Estimation of Water Resources: Measurement of Rain by Merger of Satellite Data and Rainfall Fields."

> Rainfall is complex, and highly variable in time and space. An accurate measure of the amount of precipitation is an issue important for society, particularly during extreme weather or for management of water resources. The networks of developed countries are dense, and allow a fairly accurate measurement due to the combination of data from both radar and rain gauges. In areas not covered by radar, measurements are fragmented, and algorithms of restitution are imperfect.
>
> In his research, François Mercier offered a method for estimating precipitation using two types of data from gauges and Earth-satellite TV links. These electromagnetic connections can estimate attenuation due to rain on trips of 5 km to 6 km. The measurement was therefore performed on an existing satellite network. Both sets of data were combined via a 4D-Var assimilation algorithm and a model of advection to

render maps of precipitation measurements. In the case of realistic sensors and a dense urban network, this method will decrease the cost of providing rainfall maps for flood alerts and the management of water resources.

The second student awarded, Denys Nikolayev (Bohemia University, Czech Republic), presented a miniature antenna for in-body applications: "In-Body Antenna for Miniature Biotelemetry Capsules: Increase the Robustness and Efficiency of Antenna Radiation."

In his contribution, D. Nikolayev offered an efficient, versatile miniature antenna for in-body applications. The operating frequency was in the ISM 434 MHz band. The antenna was synthesized using a hybrid analytical-numerical method, and optimized to work in a biocompatible ceramic capsule 17 mm × 7 mm in size. The narrow-band microstrip antenna was charged by a high-permittivity superstrate. In this manner, the antenna-body coupling was significantly reduced. This allowed for the improvement of the robustness in terms of adaptation, and the effectiveness of the radiation of the antenna. The designed antenna proved well adapted ($S_{11} < -10$ dB) for a wide range of tissues. The gain was −22.4 dBi, and the radiation effectiveness was 0.4%. The bandwidth of 17 MHz, or 4% relative value, was sufficient for operation as a capsule antenna or antenna implant.

3. In this Issue of the *Radio Science Bulletin*

This issue includes the following:

A report describing the URSI-France 2017 workshop.

A paper entitled "François Lefeuvre: A Long Way Among Waves." This paper reminisces on the many contributions of François, both in space science and in the service of URSI.

An article by Michel Parrot, a close collaborator of François Lefeuvre, on the results of the DEMETER mission: "Events Linked to the Lithosphere-Atmosphere-Ionosphere Coupling Observed by DEMETER"

It has been statistically shown that before their occurrence, earthquakes induce perturbations in the ionosphere. Models taking into account the global electric circuit between the ground and the bottom of the ionosphere can explain these perturbations. To validate these models, the aim of this paper is to show that the signature of various events occurring at the Earth's surface or in the atmosphere can be detected in the ionosphere. These events include the old natural nuclear reactor located at Oklo (Gabon), sandstorms in the Sahara, volcanic activity, thunderstorms, and hurricanes.

The paper of François Mercier on the assessment of water resources.

URSI France 2017 Workshop on Radio Science for Humanity

Journées scientifiques URSI-France 2017 Radiosciences au service de l'humanité

Tullio Joseph Tanzi

Institut Mines-Telecom – Telecom ParisTech France
E-mail: tullio.tanzi@telecom-paristech.fr

1. Introduction

The annual Journées Scientifiques (JS) workshop of URSI-France (the French National Committee of URSI) took place this year from February 1-3, 2017. It was held in Sophia Antipolis (Alpes-Maritimes) on Campus SophiaTech, a center dedicated to science, education, and new communication and information technologies. The overlying theme was "Radio science to the service of humanity." This was a very broad subject that the Scientific Committee managed to cover with nine invited lectures and 65 selected presentations in eight main sessions. The three-day workshop had a very dense program (Figure 1 shows the call for papers).

Figure 1. The call for papers for the URSI France 2017 workshop, Radio Science for Humanity.

The session in tribute to François Lefeuvre was chaired by Smail Tedjini, Président of URSI-France. This session was an opportunity to retrace both the scientific contributions and the roles of François Lefeuvre in URSI, including serving as President of URSI-France (1996-1999), Vice President of URSI, and finally President of URSI (2005-2008 and 2009-2011). It was obviously impossible to describe all his activities within the 45 minutes allocated (which was, in fact exceeded), as presented by Michel

Figure 2. Ms. Guilaine Debras, Mayor of Biot.

Parrot (LPC2E/CNRS, France), Orhan Altan (ISPRS and University of Istanbul, Turkey), Madhu Chandra (University of Chemnitz, Germany), Paul Lagasse (Secretary General of URSI and University of Ghent, Belgium), Guy Perrin (Observatoire de Paris and CNRS-INSU, France), and Joël Hamelin (past Secretary General of URSI-France). Since François Lefeuvre was unable to be among us to receive the commissioned glass sculpture created by master glassblower Christophe Saba of Biot, Michel Parrot was asked to deliver the sculpture to François Lefeuvre.

Sophia Antipolis is located in the community of Biot. In her welcoming speech, Ms. Guilaine Debras, Mayor of Biot, perfectly described SophiaTech Campus's greatest scientific and industrial missions: competence, teaching, research, and development.

2. Sessions

The URSI-France 2017 Workshop, under the sponsorship of the French Academy of Sciences, was co-organized by the Institute Mines Telecom – Telecom ParisTech and Université Nice Sophia Antipolis. The Scientific Committee of the Workshop received contributions from more than 14 countries, in the form of nine keynote speeches and 65 contributions.

2.1 Wireless Solutions for Distributed Communications: Internet of Things

The presentations described the operating principles and applications of various wireless systems for communication, supervision, and control:

- G. Privat (Orange Labs, France): "The Web of Things, Beyond Networked Devices"
- E. Calvanese (CEA-LETI, France): "Computation Caching: A New Frontier for Mobile Edge Cloud"
- D. Quaglia (University of Verona, Italy): "Network Synthesis for Internet of Things"
- C. Pham (University of Pau, France): "Why the Internet-of-Things is Becoming Reality?"
- J-B Agnani and E. Conil (ANFR, France): "Compteurs communicants et exposition aux ondes"
- R. d'Errico (CEA-LETI, France): "Channel Modeling and Emulation for Unconventional Scenarios and 5G and IoT Deployment"
- Claude Tetelin, (Centre National RFID, France), "Avancées et applications récentes de la RFID, au-delà de l'identification"
- D. Velev (Sofia University, Bulgaria) gave an overview of the many effects of these techniques on everyday life in his presentation, "Societal Look at the Contribution of Radiosciences," following along the lines of the ITU report, "Measuring the Information Society" (International Telecommunications Day took place on May 17, 2017).

The organizers were able to resist following the rising trend towards using only IMT 2020, alias 5G (as defined in IUT CMR-19 item 1.13). While important, we must not forget the numerous other technologies relevant to radio science. The mission of JS'17 was promoted through the presentation of the range of applications of radio science in the service of humanity.

2.2 Radiation for Imaging and Biomedical Applications

Three presentations illustrated the diverse usage:

- J. Fröhler and L. Vietzorreck (University Munich, Germany): "Planar Leaky-Wave Antenna with Tunability"
- Iliopoulos et al. (IETR/CNRS, France): "Penetration Depth Enhancement in Breast Cancer Detection at High Frequency"
- D. Nikolayev et al. (University Pilsen & Rennes, Czech Republic and France): "Antenne in-body pour capsules biotélémétriques miniatures: augmentation de la robustesse et de l'efficacité de rayonnement"

Several contributions presented used the ISM (industrial, scientific, and medical) band. Apart from the exception of radio astronomy for historical reasons, the ISM bands are contained within a very limited subset of the spectrum, with telecommunications in the strict sense of the term under the auspices of the UIT being given the "lion's share" (cf. Rapport UIT-R SM. 2180 (09/2010): Does this situation not merit reflection?)

2.3 Observations of Earth, Climate, and Societal Effects

A central mission of the spatial component of terrestrial observation was presented by two invited speeches. One was from the Copernicus program, given by G. Duchaussois, "Copernicus, a Major European Cooperation Program: From the Early Concept to Operational Services." The other was on the potential of measurements using satellite navigation systems, by M. Zribi (CNRS/CESBIO, France), "Analysis of the Potential of GNSS Measurement for the Monitoring of Continental Surface Conditions."

Figure 3. François Lefeuvre: Directeur de recherche émérite, Laboratoire de physique et chimie de l'environnement et de l'espace (LPC2E), Orléans. François Lefeuvre: Emeritus Director of Research, Laboratory of Physics and Chemistry of Environment and Space (LPC2E), Orléans.

The presentation on land-moisture assessment, "Towards a New Climate Record of Soil Moisture," was given by N. Rodriguez-Fernandez et al. (CESBIO, INRIA, ESA, France and The Netherlands). A talk on the estimation of moisture in the boundary layer by R. Hallali and J. Parent du Châtelet (Météo-France) presented research on progress in the domain of meteorology, and consequently to the benefit of the prediction of the performance of radio systems, especially radars.

2.4 Disaster Relief: URSI-ISPRS Collaboration

Prof. Orhan Altan easily convinced the participants of the complementary nature of the activities of these two international unions for the benefit of disaster management. Drones are finding an increasingly important place as well for the deployment of emergency networks, as presented by D. Plets et al. (University of Ghent, Belgium), and for the search for new remote-sensing methods, as presented by Prof. Chandra (University of Chemnitz, Germany). A joint session was scheduled for the 2017 GASS in Montreal.

2.5 URSI Working Group F1 "Education and Training"

Among the Working Groups established during the 2014 General Assembly (Beijing) of URSI for 2014-2017, one of them was named "Remote Sensing and Related Aspects of Propagation/Next Generation Radar Remote Sensing." The JS'17 workshop was a unique opportunity to present new techniques in remote sensing. Prof. Madhu Chandra, who was in charge of this working group, certainly discussed the subject in his guest lecture, "Advanced Radars

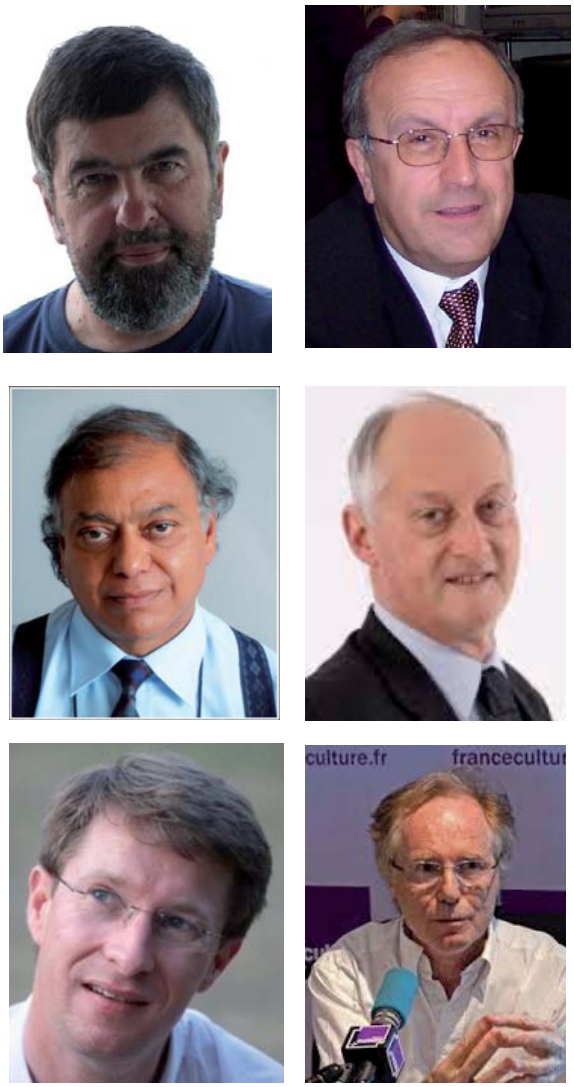

Figure 4. The speakers in the session held in tribute to François Lefeuvre: (a) Prof. Michel Parrot (LPC2E/CNRS Orléans, France); (b) Prof. Orhan Altan (ITU Civil Engineering Faculty Division of Photogrammetry, Istanbul, Turkey ISPRS); (c) Prof. Madhu Chandra (Chemnitz TU, Germany; URSI Germany); (d) Prof. Paul Lagasse (URSI; Ghent University, Belgium); (e) Guy Perrin (DAS A&A CNRS-INSU, France); (f) Joël Hamelin (URSI France).

for Societal Needs." In this, he underlined the need to revisit the physical laws on which radar systems are based.

2.6 Poster Session

The diversity of the posters makes a complete summary practically impossible. Instead, we note three subjects especially well presented by their authors:

- X. Wu and S. Salous (University of Durham, United Kingdom): "Micro-Doppler Signature of Rotating Targets in SAR-GMTI System Using CSI Technique"

Figure 5. The session held in tribute to François Lefeuvre.

- R. Rousseau et al. (INSA Lyon, France): "Analysis of an Energy Harvesting Circuit Behavior in the Presence of Complex Waveforms"

- J-P Damiano (CNRS/LEAT, France): "Protection of the Scientific Potential and Technology of the Nation: Utopia or Reality to Find the Right Balance, Foster Innovation, Protect Knowledge." This interesting subject deserved an oral presentation. The author clearly explained the conflict between disinterested research, on the one hand, and the financing of disinterested research, on the other. This can only be achieved by the duly protected benefits of its applications. The importance of the subject is well known, but the urgency to find an answer is very recent. This question is attached to the broad question regarding the quality of work in the growing flow of publications.

2.7 Space Meteorology

The final day of this workshop was particularly original and interesting. The keynote speaker, F. Kamalabadi (ECE Illinois, USA), gave a synopsis of the subject in his paper, "Space Weather Effects in the Earth's Ionosphere and Below: An Overview of the NASA ICON Mission and Recent Insights on Geomagnetic Disturbances."

Several speakers then discussed the detection of ionospheric storms and the resulting difficulties for radio links:

- M. Parrot (LPC2E/CNRS, France): "Evénements liés au couplage lithosphère-atmosphère-ionosphère observés par DEMETER"

- K.-L. Klein et al. (Observatoire de Paris-Meudon, France): "Radioastronomie solaire et météorologie de l'espace,"

- P. Gallagher (University Dublin, Ireland): "Solar Radio Bursts and Their Space Weather Impacts"

- R. Ilie (University of Michigan, USA): "Multi-Physics Large-Scale Simulations of the Terrestrial Magnetosphere and Geomagnetic Storm Studies"

- Rolland (*Université* de la Côte d'Azur, France): "Tsunami Monitoring from Space Using Ionosphere Seismology"

3. Session Dedicated to François Lefeuvre

A session was held in tribute to François Lefeuvre (Figure 3). The speakers in the session are shown in Figures 4 and 5. A glass sculpture (Figure 6) was commissioned to be created by master glassblower Christophe Saba of Biot to honor François. Since Dr. Lefeuvre was unable to attend due to illness, Michel Parrot was asked to deliver it to him.

Figure 6. The original glass sculpture specially crafted by Christophe Saba, master glassblower of Val de Pome, Biot.

François's first research position began at the Ionospheric Research Group (GRI) in Saint-Maur des Fossés in 1969, under the direction of Owen Storey, dealing with propagation of electromagnetic waves in the ionosphere. He continued his work in 1971 at the University of Sheffield, studying ELF/VLF emissions in the magnetosphere.

Back in the Saint Maur laboratory, he was appointed Research Associate and then Director of Research. In 1979/1980, he joined the Radio Science Group of Stanford University for one year, under a CNRS/NSF fellowship agreement. He was the principal investigator and co-investigator of numerous space projects, including probes and scientific satellites in various regions of our magnetosphere:

- S3OO on GEOS 1 and 2 (launched in 1977 and 1978)
- ARCAD-3 on the Franco-Russian AUREOL-3 satellite (1981)
- MEMO on the auroral probe of the Russian project INTERBALL (1996)
- STAFF on the four satellites CLUSTER of the ESA (2000)
- IMSC on the CNES DEMETER microsatellite (2004), during which LPC2E also designed and managed the scientific mission center

To study the transient light phenomena observed above storm clouds, he also participated in the design of another microsatellite, TARANIS, which should be launched in 2018. He was the Director of LPCE from 1994 to 2002, and was a member of Section 17 of the CNRS National Committee for the 2004-2008 term. Since 2009, he has been Emeritus Director of Research at LPC2E.

François Lefeuvre served extensively in URSI for 21 years, both at the national (URSI-France) and international levels. His contributions to URSI include multiple leadership positions and enduring collaboration projects. He was elected Deputy Chair of Commission G (Ionospheric Radioelectricity and Space Meteorology) of URSI in 1990. He became President in 1993 for three years. He next assumed the Presidency of URSI-France (CNFRS) from 1996 to 1999. In 2002, he was elected Vice President of URSI (2002-2005), and then President in 2005 (2005 -2008). He became Past President in 2008. In 2009, Gert Brussaard, elected President of URSI in 2008, resigned due to illness. François was then asked to replace him. He served as President again from 2009 to 2011, and then again became Past President from 2011 to 2014.

After the 2008 URSI General Assembly in Chicago, François Lefeuvre was interested in the contribution of radio science to disaster management. He forged a connection with the International Society for Photogrammetry and Remote Sensing (ISPRS). This extensive joint effort between these two distinguished societies was formed mainly by their two Presidents, François Lefeuvre and Orhan Altan. Since 2009, URSI and ISPRS have been organizing joint workshops on "disaster management." These joint sessions were organized in Antalya in 2010 (GI4DM), Istanbul in 2011 (URSI GASS), and Melbourne in 2012 (ISPRS GA), all contributing to the document VALID (The Value of Geo-Information for Disaster and Risk Management VALID): Benefit Analysis and Stakeholder Assessment), published in 2013 by Prof. Ohran Altan. As a continuation of this work, at a joint URSI-ISPRS "Disaster and Risk Management" session held at the ISPRS 2016 General Assembly in Prague, a working group was formed for long-term collaboration between ISPRS and URSI.

4. CNFRS Medal and Gala Dinner

An event such as the JS'17 workshop had to be marked by a gala dinner. The organizers thus invited the participants to a dinner in Nice at the Auberge du Redier, in the hills of the heath. In this tranquil ambience, the traditional medal of URSI-France was awarded to Prof. Omar El Mazria (Figure 7) (University of Lorraine, Nancy) by Albert Bijaoui from the Academy of Science in the presence of Madame I. Bres, Mayor of Colomars, and Madame G. Debras, Mayor of Biot. The latter had invited all of the participants to a nocturnal visit of her city the previous night.

The CNFRS medal, awarded under the auspices of the Academy of Science, is intended to honor a scientist who contributes or has contributed in at least the past six years to remarkable advances in the field of radio science, and has been involved in the scientific growth of the French and international communities. This contribution may relate to progress in the field of knowledge and/or the contribution of radio science to the socioeconomic world,

Figure 7. Prof. Omar El Mazria, recipient of the CNFRS medal (Ecole Supérieure de Sciences et Technologies de l'Ingénieur de Nancy (ESSTIN), Institut Jean Lamour, UMR 7198, Nancy Université – CNRS; E-mail: omar.elmazria@ijl.nancy-universite.fr).

Figure 8. Prof. Peter Van Daele viewing the URSI Student Prize winners.

and/or the development of the radio science community, young scientists, or the general public.

Omar El Mazria is a professor at the Université de Lorraine (UL) within the Institut Jean Lamour (IJL) for research and Ecole Supérieure de Sciences et Technologies de l'Ingénieur de Nancy (ESSTIN – Polytech Nancy) for teaching. Born in 1968 in Casablanca, he received his MS in Industrial Computer Science and Opto-electronics conjointly from the Universities of Metz, Nancy I, and the National Polytechnic Institute of Lorraine, in 1993, and his PhD in Electronics (evaluation and prediction of irradiation effects on semiconductor devices) in 1996 from Metz University, France. In 1997, he joined the University of Nancy I (now Université de Lorraine) as Associate Professor of Electronic and Communication systems, and as a full Professor, respectively, in 1997 and 2003. He is also a member of the IUF (Institut Universitaire de France), and was a guest professor at Simon Fraser University (British Colombia, Canada), Institute of Acoustics of the Chinese Academy of Sciences, and University of Central Florida, respectively, in 2009, 2011, and 2013.

Figure 9. Denys Nikolayev (Pilsen University, Czech Republic), URSI Student Prize Winner, presenting "Antenne in-body pour capsules biotélémétriques miniatures: augmentation de la robustesse et de l'efficacité de rayonnement."

Figure 10. François Mercier (Météo-France, Toulouse, France), URSI Student Prize Winner, presenting "Pour une meilleure estimation de la ressource en eau: mesure des champs de pluie par fusion de données satellite et pluviométrique."

He was the head of the Micro and Nanosystems Group and the leader of the Callot Project (an interdisciplinary project in the field of nanoscience and nanodevices) within the Institut Jean Lamour. His current research focuses on surface acoustic wave (SAW) devices for communication systems and sensing applications. SAW filters and resonators based on layered structures including diamond, AlN, ZnO, developed for high-frequency applications (in the 3 GHz to 10 GHz range), and original SAW sensors for temperature, pressure, and the magnetic field, have demonstrated advantages of being passive (battery-less), wireless, and/or package-less. These promising sensors present the best solutions in various fields such as monitoring in harsh environments or in biomedical applications. Prof. El Mazria is currently the coordinator of the ANR SALSA project, aimed at the development of passive and wireless sensors for the steel industry, operating up to 1000°C. He also manages several projects funded by ANR, DGA, ISITE (Loraine Université d'Excellence), SATT GE for the development of wireless sensors for biomedical applications. His currently manages a budget of approximately two million euros of external research contracts and grants. He is the author or coauthor of more than 160 international scientific articles, four issued international patents, and more than 120

Figure 11. Prof. Paul Lagasse at the closing session.

Figure 12. The logos of the entities who provided support for the workshop.

communications in international conferences. He has been a co-chair of the Technical Program Committee (TPC) Group 4 of the IEEE International Ultrasonics Symposium. He was co-chair of the IEEE IECMI (International Conference on Electronic and Measurement Instruments), and a member of the technical or organization committees of several other international conferences.

The CNFRS Medal was awarded to Omar El Mazria by Albert Bijaoui from the Academy of Sciences.

5. Closing Session and URSI Student Prize

In closing the JS'17 workshop and forging a link to the future scientists of URSI, Prof. Peter Van Daele (Figure 8) (University of Ghent, Belgium), Assistant Secretary General of URSI, presented the URSI student prize. This was shared equally between two candidates: D. Nikolyev (Figure 9) (University of Pilsen, Czech Republic) and F. Mercier (Figure 10) (Météo-France). Prof. Van Daele congratulated them on the originality of their thesis projects and the clarity of their presentations.

Lastly, Smaïl Tedjini thanked all the participants, especially the members of URSI-Germany, and the Secretary Generals Paul Lagasse and Peter Van Daele. He thanked the organizing committees dedicated to the success of this JS'17 workshop, in particular Tullio Tanzi, Jean-Pierre Damiano, and Joël Hamelin.

We hope to see you all again at next year's workshop Journées scientifiques JS'18.

6. Acknowledgements

The URSI-France workshop Journées scientifiques (JS'17) was held on the SophiaTech campus, in Sophia Antipolis, from February 1-3 2017. It was organized under the patronage of the Academy of Sciences, and devoted to "Radiosciences in the service of humanity." The workshop was jointly organized by Institut Mines Télécom/Telecom ParisTech and Nice Sophia Antipolis University.

This year, the workshop received remarkable international contributions, notably through the participation of several European speakers and from our colleagues from other URSI national committees. These meetings allowed a fundamental dialogue between scientists from international and national laboratories, doctoral students, researchers and engineers, academics and industrialists, who joined us on campus. We were grateful to all participants for their hard work on their publications, presentations, fruitful scientific exchanges, and discussions on the future of radio science.

We would like to express our sincere thanks to URSI-Germany, who actively participated in the presentations at the various sessions. Prof. Paul Lagasse (URSI Secretary General) took the floor at the special session dedicated to François Lefeuvre, and participated in our General Assembly. Prof. Peter Van Daele (URSI Assistant Secretary General) awarded the URSI prize to the young doctoral students.

A scientific event is a success when all the participants actively work towards the same goal. We would like to thank the institutions, the laboratories, the exhibitors, etc. (Figure 12), for their financial and logistical support, without forgetting, of course, all of the organizers who were diligently involved in the preparation and success of this event.

7. Reference

The Proceedings (articles, lectures, and most oral presentations) and all information regarding the URSI-France 2017 workshop are available on the URSI-France Web site: www.ursi-france.org

Contact informatiln: Comité National Français de Radioélectricité Scientifique, Union Radio Scientifique Internationale: Main Office: Académie des Sciences, 23 quai de Conti, Paris 6ème . France; Web site: http://ursi-france.mines-telecom.fr. Mailing address: Alain Sibille, Secrétaire général d'URSI-France, Télécom ParisTech, 46 rue Barrault, 75634 Paris Cedex 13; Tel: +33 (0)1 45 81 70 60; e-mail: ursi-france@mines-telecom.fr.

François Lefeuvre: A Long Way Among Waves

Tullio Joseph Tanzi[1] and Joël Hamelin[2]

[1]Institut Mines-Telecom – Telecom ParisTech France
E-mail: tullio.tanzi@telecom-paristech.fr

[2]Past Secretary General of URSI-France

1. History

François's first research work in 1969, within the Groupe de Recherche Ionosphérique (GRI: Ionospheric Research Group) at Saint-Maur des Fossés, under the direction of Owen Storey, focused on the propagation of electromagnetic waves in the ionosphere. He continued this work in 1971 at the University of Sheffield, studying in particular ELF/VLF (extremely low frequency, 3 Hz to 30 Hz, and very low frequency, 3 kHz to 30 kHz) emissions in the magnetosphere. Having rejoined the laboratory of Saint Maur, he was appointed Researcher and then Director of Research. In 1979-1980, he joined the Radio Science Group of Stanford University for one year, under a CNRS/NSF fellowship agreement.

Since his thesis, François Lefeuvre was interested in waves in plasmas. He developed the concept of a wave-distribution function, because there were no tools for the study of waves simultaneously propagating in different directions. Existing methods were limited to a single direction of propagation. He thus could solve this inverse problem where the nuclei were obtained from Maxwell's equations, and the data were contained in a spectral matrix formed by the auto-spectra and cross-spectra of the six electromagnetic field components measured onboard a satellite. He successfully applied his method of the wave-distribution function to the data collected by the GEOS-1 satellite (1977). In 1978, GEOS-2, which was on a geostationary orbit, confirmed its results. This was followed by major publications in 1981 and 1982 in the *Journal of Geophysical Research* [1, 2].

He was also highly interested in the VLR (TBF: très basses fréquences, in French), powerful transmitters that participate in the precipitation of particles in the radiation belts. The OREOL-3 launch at the end of 1981 by the Soviets led to further action, but at a lower altitude in the ionosphere. It was at this time that a Russian-Japanese team published a surprising article on observations of changes in intensity of the waves before earthquakes. As data were available in France, François Lefeuvre correlated seismic phenomena with VLR (TBF) recorded by GEOS. This led to publications in *Annales Geophysicae* in 1985 [3, 4].

François Lefeuvre attracted many foreign visitors to the laboratory. In 1981, he welcomed the Masashi Hayakawa from Japan for one year (see Figures 1 and 2, showing pictures taken at a dinner). This led to many common publications and student exchanges in the years that followed.

Figure 1. (l-r) Jean-Louis Rauch, François Lefeuvre, Claudine Parrot, and Pierrette Décreau.

Figure 2. (l-r) Roland Debrie, Michel Parrot, Youssef Marouan, Masashi Hayakawa, and Claude Delannoy.

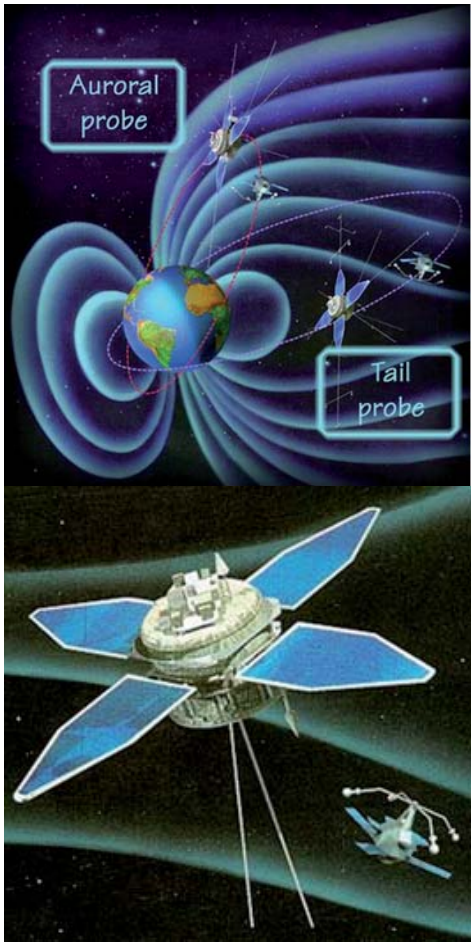

Figure 3. The MEMO Experience, on INTERBALL-2, launched August 29, 1996.

François was Principal Investigator (PI) of the MEMO experience on the auroral probe of the Russian INTERBALL project, launched in 1996 (Figure 3). This allowed applying the wave-distribution function method to kilometric radiation observed in the auroral zones. Many publications were written about these observations and their interpretations [5-8].

Figure 4. The INTERBALL Project, 1996: (l-r) Bernard Poirier, Michel Parrot, François Lefeuvre, with Micha Mogilevski from behind.

These collaborations led François Lefeuvre to perform several missions in Russia. Figure 4 shows him in the "*datcha*" of a Russian colleague, during the preparation phase of the INTERBALL mission.

François was co-investigator of the STAFF experience on the four ESA CLUSTER satellites. The launch of these satellites in 1996 failed (see Figure 5), but they were rebuilt and resumed with success four years later. They still currently operate. François strongly contributed to characterizing turbulence in space plasmas by using the four measuring points [9] of CLUSTER.

François Lefeuvre was Director of the LPCE (Laboratoire de Physique et Chimie de l'Environnement: Laboratory of Physics and Chemistry of the Environment) from 1994 to 2002. He was a member of Section 17 of the national committee of the CNRS for the 2004-2008 mandate. Since 2009, he has been Research Director Emeritus at the LPC2E (Laboratoire de Physique et Chimie de l'Environnement et de l'Espace: Laboratory of Physics and Chemistry of the Environment and Space, LPCE transformation in 2008).

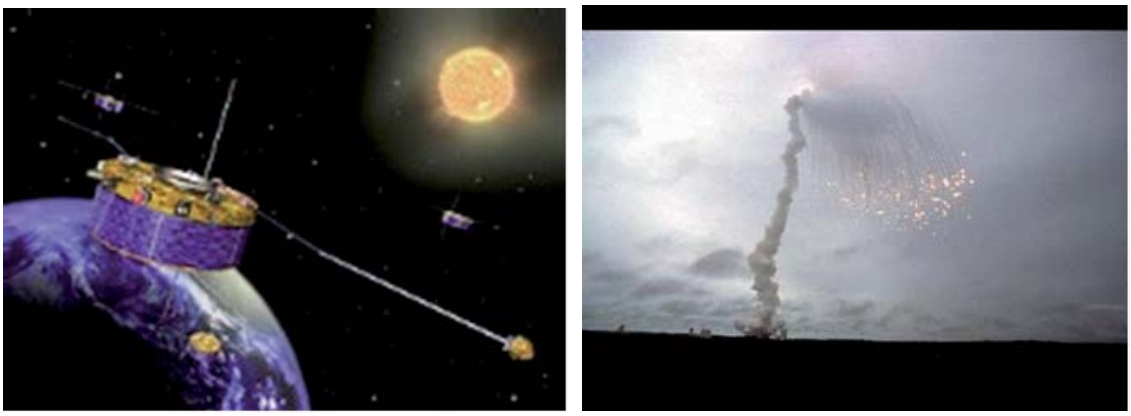

Figure 5. The CLUSTER satellites.

Figure 6. The 40th anniversary of Franco-Russian space cooperation: François Lefeuvre (l) and Jean-Jacques Berthelier.

Figure 8. A meeting in Moscow at the Institute of Physics of the Earth, October 2006: (l-r) Jean-Jacques Berthelier, Jean-Louis Rauch, François Lefeuvre, and Michel Parrot.

In October 2006, the 40th anniversary of the Franco-Russian space cooperation was celebrated. François Lefeuvre was present, and, as always, with his URSI tie (Figure 6). It was an opportunity to meet cosmonauts (Figure 7), and to discuss the seismo-electromagnetic effects with colleagues from the Institute of Physics of the Earth (Figure 8).

François Lefeuvre was co-investigator of the IMSC experience on the CNES (Centre National d'Etudes Spatiales: French Space Agency) DEMETER microsatellite (Figure 9). IMSC was the Instrument Magnetometer Search Coil. It measured the three components of the magnetic field in the 10 Hz to 18 kHz range, with three magnetic sensors attached to the end of a deployable arm. The LPC2E also designed and managed onboard electronics that interfaced sensors and telemetry, as well as the scientific mission center that processed and distributed data to users. For six years, between 2004 and 2010, DEMETER allowed the study of ionospheric disturbances based on seismic activity [10-12] and human activity, including TBF emitters [14].

At the second international DEMETER symposium in Paris, in October 2011, many foreign scientists (Russians, Chinese, Japanese, Americans...) responded to present their results (Figure 10).

With Elisabeth Blanc, François was at the origin of the CEA (Commissariat à l'énergie atomique et aux énergies alternatives: French Alternative Energies and Atomic Energy Commission) for the design of the TARANIS microsatellite. It was designed to study transient light phenomena observed above storm clouds [13]. Selected by CNES, TARANIS may be launched in 2018 (Figure 11).

Since 2009, François Lefeuvre, Emeritus Research Director at the LPC2E, has played a major role in the definition and design of space missions and instruments of space missions. He contributed to the fame of the LPC2E at both the national and international levels.

2. François Lefeuvre and URSI

François Lefeuvre spent 21 years in the service of URSI, both at the national (URSI France) and international levels. His contributions to URSI include multiple leadership positions and enduring collaboration projects.

Figure 7. The 40th anniversary of Franco-Russian space cooperation: Russian Cosmonauts posing with Jean-Loup Chrétien.

Figure 9. The DEMETER CNES microsatellite: 2004-2010.

He was elected Deputy Chair of Commission G (Ionospheric Radioelectricity and Space Meteorology) of URSI in 1990. He became Chair in 1993, for three years. He held the Presidency of URSI-France (CNFRS: Comité National Français de Radioélectricité Scientifique, the URSI French Committee) from 1996 to 1999.

In 2002, he was elected as one of the four Vice Presidents of URSI. In 2005, he was elected President of URSI for the 2005-2008 triennium. He became Past President for three years in 2008. However, in 2009, Gert Brussard, François's successor to the URSI Presidency, became very seriously ill and resigned. The URSI Board asked François to take the office of the President, and François accepted, despite the weight of the office. He assumed a new Presidency from 2009 to 2011, and then again became Past President for the 2011-2014 triennium.

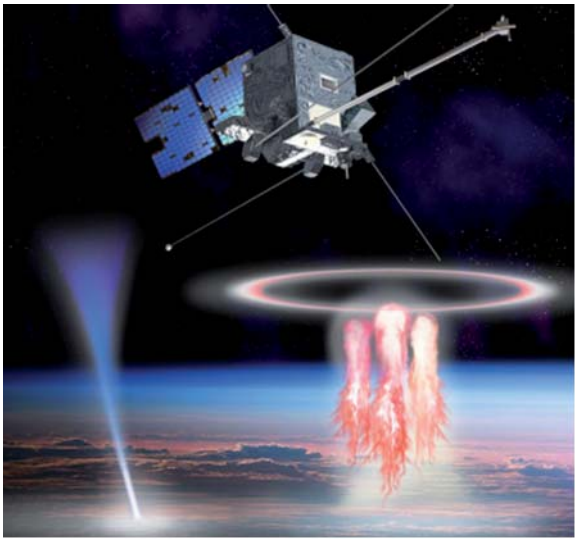

Figure 11. The future: the microsatellite TARANIS, to be launched in 2018.

Figure 10. The Second International DEMETER Workshop at CNES headquarters, Paris, in October 2011 (François Lefeuvre is at the top right).

In the recent history of URSI, François was the only person to have completed nearly two full terms as President and to have been a member of the URSI Board for 12 years.

As early as the 2008 URSI General Assembly in Chicago, François Lefeuvre focused on the contribution of radio science to disaster management. He made a connection with the International Society for Photogrammetry and Remote Sensing (ISPRS). A long joint collaboration between the two societies began, driven mainly by their two respective Presidents: François Lefeuvre and Orhan Altan.

3. URSI-ISPRS Common Work on Disaster Management

François Lefeuvre and Orhan Altan met for the first time in 2006 in Rome, at a meeting of the International Council of Scientific Unions (now the International Council for Science, ICSU), where they represented their respective unions. In October 2008, at the ICSU General Assembly

Figure 12. The tribute to François Lefeuvre.

in Maputo, Mozambique, they subsequently happened to be on the same plane, but their flight was cancelled. This cancellation allowed them to discuss their respective societies and to identify common interests, mainly on topics such as microwaves, remote sensing, etc., as well as a common interest in disaster management. After this exchange of views, François joined Orhan Altan at his hotel, and they put down on paper the beginnings of a long collaboration. From 2009, URSI and ISPRS began organizing joint workshops on disaster management [15, 16].

4. Session Dedicated to François Lefeuvre

During the annual scientific workshop of URSI-France (in Sophia Antipolis, February 1-3, 2017), a special session dedicated to François Lefeuvre was held to honor him for his scientific work and his actions for years within URSI. It was obviously impossible to describe all his activities within the 45 minutes allocated (which was in fact exceeded). Presentations were made by Michel Parrot (LPC2E/CNRS, France); Orhan Altan (ISPRS and University of Istanbul, Turkey); Madhu Chandra (University of Chemnitz, Germany); Paul Lagasse (Secretary General of URSI and University of Ghent, Belgium); Guy Perrin (Observatoire de Paris and CNRS-INSU, France); and Joël Hamelin (past Secretary General of URSI-France).

Since François Lefeuvre was unable to be among us to receive the commissioned glass sculpture, created by master glassblower Christophe Saba of Biot, Michel Parrot was asked to deliver it to François (see Figure 12).

5. Acknowledgements

I would like to thank all the colleagues who participated in the JS'17 workshop. They all responded in a friendly manner to our solicitation, and, for some, traveled from far to come in Sophia Antipolis. This overview of the many activities and innovations due to François could not have been achieved without the support and advice as well as the writings of all of the participants in this event. A large number of the photos illustrating this article came from the oral presentation of Michel Parrot (available on the JS'17 Web site).

6. References

1. F. Lefeuvre, M. Parrot, and C. Delannoy, "Wave Distribution Functions Estimation of VLF Electromagnetic Waves Observed Onboard GEOS-1," *Journal of Geophysical Research*, **86**, A4, 1981.

2. F. Lefeuvre, T. Neubert, and M. Parrot, "Wave Normal Direction and Wave Distribution Function for Ground-Based Transmitter Signals Observed on GEOS-1," *Journal of Geophysical Research*, **87**, A8, 1982.

3. M. Parrot, F. Lefeuvre, Y. Corcuff, and P. Godefroy, "Observations of VLF Emissions at the Time of Earthquakes in the Kerguelen Islands," *Annales Geophysicae*, **3**, 6, 1985.

4. M. Parrot and F. Lefeuvre, "Correlation Between GEOS VLF Emissions and Earthquakes," *Annales Geophysicae*, **3**, 6, 1985.

5. F. Lefeuvre, M. Parrot, J. L. Rauch, B. Poirier, A. Masson, and M. Mogilevsky, "Preliminary Results from the MEMO Multicomponent Measurement of Waves On-Board INTERBALL 2," *Annales Geophysicae*, **16**, 1998, pp. 1117-1136.

6. F. Lefeuvre, M. Parrot, J. L. Rauch, B. Poirier, Z. Y. Zhao, M. Mogilevsky, S. Perraut, and J. Hanasz, "On the INTERBALL 2 Measurements of Auroral Kilometric Emissions and Associated Phenomena," *Journal of Technical Physics*, **40**, 2, 1999, pp. 121-134.

7. O. Santolik, F. Lefeuvre, M. Parrot, and J. L. Rauch, "Propagation of Z-Mode and Whistler-Mode Emissions Observed by Interball 2 in the Nightside Auroral Region," *Journal of Geophysical Research*, **106**, 21, 2001, pp. 137-21,146.

8. M. Parrot, F. Lefeuvre, J. L. Rauch, O. Santolik, and M. M. Mogilevsky, "Propagation Characteristics of AKR Observed by the MEMO Experiment Onboard INTERBALL 2," *Journal of Geophysical Research*, **106**, 2001, pp. 315-325.

9. J. L. Pinçon and F. Lefeuvre, "Local Characterization of Homogeneous Turbulence in a Space Plasma from Simultaneous Measurements of Field Components at Several Points in Space," *Journal of Geophysical Research: Space Physics*, **96**, A2, 1991, pp. 1789-1802.

10. F. Elie, M. Hayakawa, M. Parrot, J. L. Pinçon, and F. Lefeuvre, "Neural Network System for the Analysis of Transient Phenomena Onboard the DEMETER Micro-Satellite," *Journal of IEICE*, **E82-A**, 8, 1999, pp. 1575-1581.

11. O. Molchanov, A. Rozhnoi, M. Solovieva, O. Akentieva, J. J. Berthelier, M. Parrot, F. Lefeuvre, P. F. Biagi, L. Castellana, and M. Hayakawa, "Global Diagnostics of the Ionospheric Perturbations Related to the Seismic Activity Using the VLF Radio Signals Collected on the DEMETER Satellite," *Natural Hazards and Earth System Sciences*, **6**, 2006, pp. 745-753.

12. A. Rozhnoi, O. Molchanov, M. Solovieva, V. Gladyshev, O. Akentieva, J. J. Berthelier, M. Parrot, F. Lefeuvre, M. Hayakawa, L. Castellana, and P. F. Biagi, "Pos-

sible Seismo-Ionosphere Perturbations Revealed by VLF Signals Collected on Ground and On a Satellite," *Natural Hazards and Earth System Sciences*, **7**, 2007, pp. 617-624.

13. F. Lefeuvre, R. Marshall, J. L. Pinçon, U. S. Inan, D. Lagoutte, M. Parrot, and J. J. Berthelier, "On Remote Sensing of Transient Luminous Events' Parent Lightning Discharges by ELF/VLF Wave Measurements On Board a Satellite," *Journal of Geophysical Research*, **114**, A09303, 2009, doi:10.1029/2009JA014154.

14. F. Lefeuvre, J. L. Pinçon, and M. Parrot, "Midlatitude Propagation of VLF to MF Waves Through Nighttime Ionosphere Above Powerful VLF Transmitters," *Journal of Geophysical Research: Space Physics*, **118**, 2013, doi:10.1002/jgra.50177.

15. T. J. Tanzi and F. Lefeuvre, "Radio Sciences and Disaster Management," *Comptes Rendus Physique*, **11**, 2010, pp. 114-124.

16. T. J. Tanzi and F. Lefeuvre, "L'apport des radios sciences à la gestion des catastrophes," in Journées scientifiques 2009 d'URSI-France: Propagation et Télédétection, 2009.

Events Linked to the Lithosphere-Atmosphere-Ionosphere Coupling Observed by DEMETER

Michel Parrot

Université d'Orléans
LPC2E/CNRS
France
E-mail: mparrot@cnrs-orleans.fr

Abstract

It has been statistically shown that earthquakes induce perturbations in the ionosphere before their occurrence. Models taking into account the global electric circuit between the ground and the bottom of the ionosphere can explain these perturbations. To validate these models, the aim of this paper is to show in the ionosphere the signature of various events occurring at the Earth's surface or in the atmosphere. This includes the old natural nuclear reactor located at Oklo (Gabon), sandstorms in the Sahara, volcanic activity, thunderstorm activity, and hurricanes.

Il a été statistiquement démontré que les tremblements de Terre induisent des perturbations dans l'ionosphère avant leur apparition. Des modèles tenant compte du circuit électrique global entre la surface de la Terre et le bas de l'ionosphère peuvent expliquer ces perturbations. Pour valider ces modèles, le but de ce papier est de montrer dans l'ionosphère les signatures de divers événements ayant lieu à la surface de la Terre ou dans l'atmosphère. Cela concerne: l'ancien réacteur nucléaire naturel situé à Oklo (Gabon), les tempêtes de sable au Sahara, l'activité volcanique, l'activité orageuse, et les typhons.

1. Introduction

Many ionospheric changes have been statistically observed in the past prior to earthquakes [1-6]. These perturbations can be considered as short-term precursors (between a few hours and some days before the shock). Mechanisms that can trigger these ionospheric events are much debated. However, there are several models of lithosphere-atmosphere-ionosphere-magnetosphere (LAIM) coupling to explain ionospheric perturbations that can be observed prior to earthquakes [7-9]. These mostly

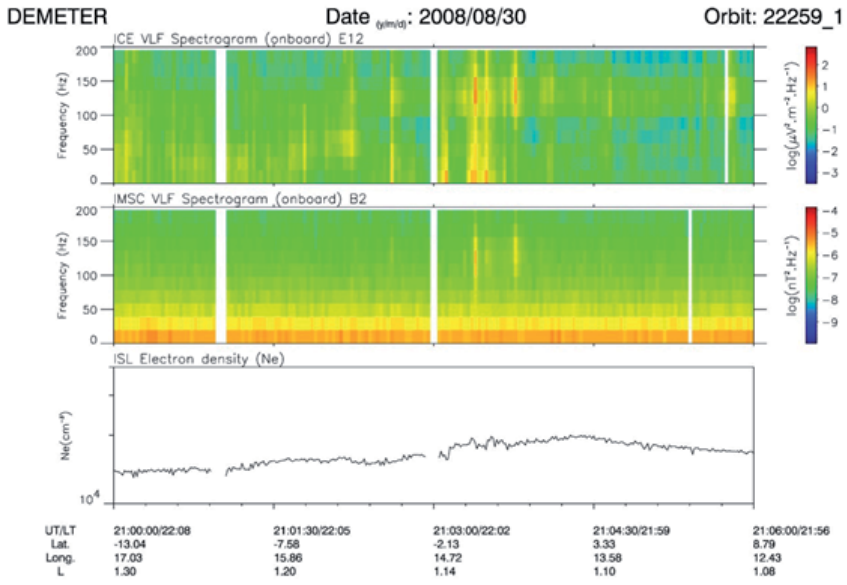

Figure 1. DEMETER data recorded on August 30, 2008, between 21:00 and 21:06 UT. (top panel) A spectrogram of one component of the electric field up to 200 Hz. (middle panel) A spectrogram of one component of the magnetic field up to 200 Hz. The intensities of the spectrograms are color-coded according to the color scale on the right. (bottom panel) The variation of the electron density (logarithmic scale). The geographical latitude and longitude are indicated on the bottom.

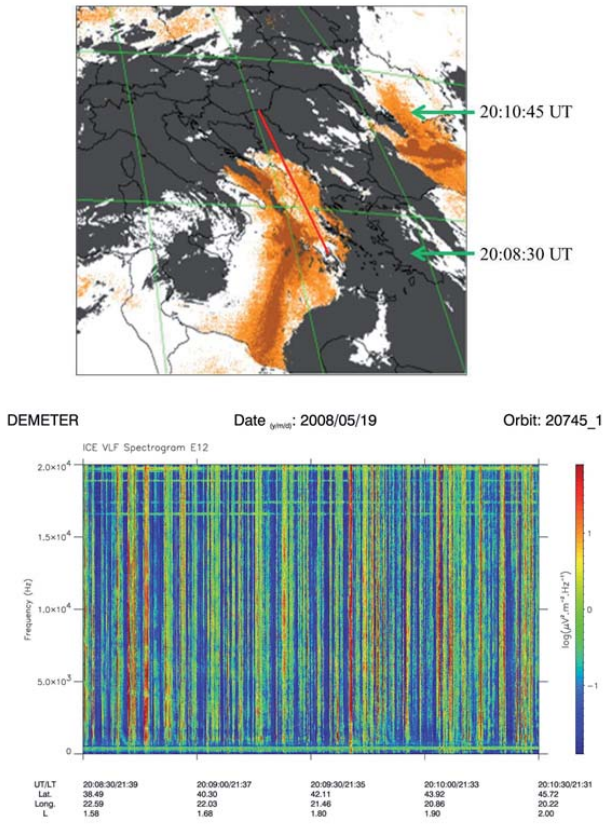

Figure 2. (top) A map of 20/05/2008 at 00:00 UT showing a RST (robust satellite technique) dust index [12]. This indicates the location of the sandstorm (courtesy of V. Tramutoli). A part of the DEMETER orbit on 19/05/2008 between 20:08:30 and 20:10:45 UT is plotted in red. (bottom) DEMETER data showing a spectrogram of one electric-field component up to 20 kHz.

involve the appearance of aerosols and gas, including radon, which can lead to the ionization of air molecules, and many different effects such as temperature and pressure anomalies, and the redistribution of electric charges in the global electric circuit that exists between the Earth's surface and the bottom of the ionosphere [10]. In the framework of this model's validation, several events have been studied with the DEMETER's satellite data.

DEMETER was an ionospheric micro-satellite in operation between June 2004 and December 2010. Its orbit was circular (660 km), polar, and nearly sun-synchronous (10.30 LT and 22.30 LT). Its payload measured electromagnetic waves in different frequency ranges from ULF to MF, and also plasma parameters (for example, the electron and ion densities). A description of the experiments can be found in [11]. The electric and magnetic spectrograms were always calculated onboard with a low time (2 s) and frequency (19 Hz) resolution all around the Earth, except in the auroral zone.

The events studied in this paper occurred in the atmosphere. They concerned the effects of (i) the ancient natural nuclear reactor located at Oklo (Gabon), (ii) sandstorms in the Sahara, (iii) volcanic activity, (iv) lightning activity, and (v) hurricanes. The main signatures of these events in the ionosphere will be shown.

2. The Oklo Nuclear Reactor

Two billion years ago, a natural nuclear reactor was active close to Oklo (Gabon) for hundreds of thousands of years. A survey was done to check if residual ionization could be detected when DEMETER was flying over the site, located at lat = 1°23′, long = 13°09′. The plots in Figure 1 show an example of variations of waves and plasma density when the orbit of the satellite was just above Oklo. One could see that the power spectral densities of electric and magnetic fields were enhanced. At the same time (just after 21:03 UT), fluctuations of the electron density were observed. This is typical of electrostatic turbulence induced by plasma density fluctuations at the altitude of the satellite.

3. Sandstorms in the Sahara

The DEMETER data was checked when the satellite was above sandstorms, in order to detect possible changes in the ionosphere.

In the top panel of Figure 2, a novel technique was used to detect the presence of sand in the atmosphere. At the same time, the wave activity was recorded by DEMETER. In the bottom of Figure 2, one could notice a lot of whistlers (vertical lines) that corresponded to lightning strokes in the atmosphere. This two-minute spectrogram showed very unusual lightning activity, because there were a huge number of lightning strokes, not especially intense, but very close in time. This could perhaps be attributed to electrostatic discharges in the sandstorm.

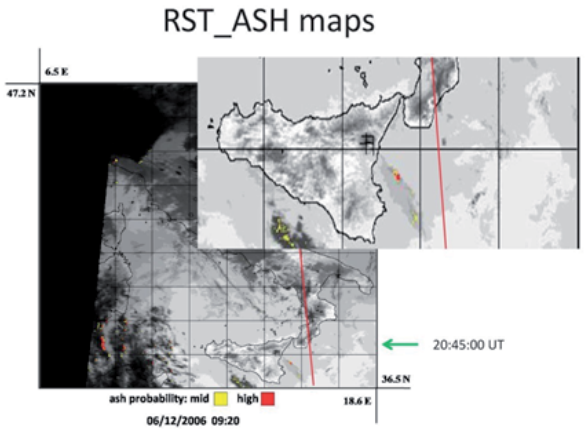

Figure 3. The hotspot detection of ashes during an eruption of Mt. Etna (courtesy of V. Tramutoli). The red line indicates the orbit of DEMETER.

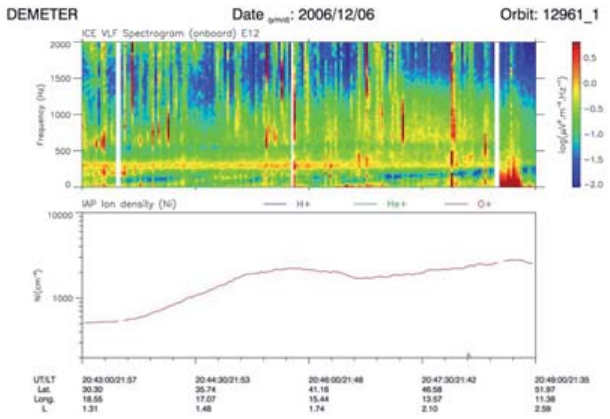

Figure 4. This corresponds to DEMETER data recorded along the part of the orbit shown in Figure 3. The top panel represents a spectrogram of an electric component up to 2 kHz, and the bottom panel is related to the variation of the density of the ion O+.

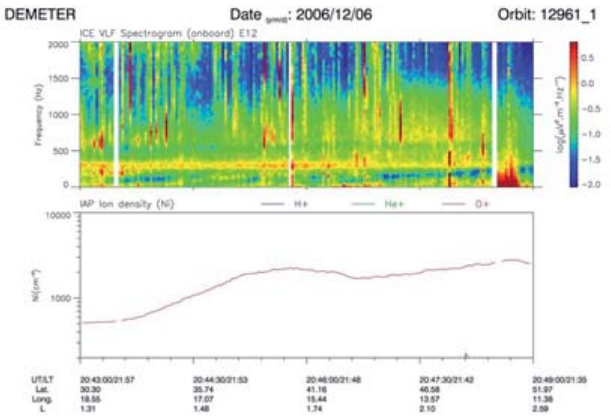

Figure 5. (top panel) A spectrogram of an electric-field component up to 20 kHz, recorded on January 7, 2006. The intensity is color-coded on the right color scale. (bottom panel) The variation of the O+ ion density (adapted from [15]).

4. Volcanic Activity

Ashes in volcanic plumes are likely to produce electrostatic discharges in the atmosphere, and to then induce disturbances in the ionosphere. This was discussed in [13], where some examples were given. Here, we intend to simultaneously show the atmospheric perturbation and the induced ionospheric change. During an eruption of Etna, Figure 3 displays hotspot detection of ashes, with an RST (robust satellite techniques) approach optimized by a long-term time-domain analysis performed on several satellite records, covering the Mt. Etna area and applied both to NOAA-AVHRR and EOS-MODIS data [14].

In Figure 4, one can see some lightning activities (vertical lines in the spectrogram) but, above all, an increase of the ion density when the satellite was at the latitude of Mt. Etna (around 20:45 UT).

5. Lightning Activity

The thunderstorm activity in the atmosphere triggers waves called whistlers in a large frequency range. These waves, which propagate in the Earth-ionosphere waveguide, can escape into the ionosphere and the magnetosphere. They induce precipitation of the particles that are in the radiation belts. This particle precipitation produces an additional ionization at the altitude of the satellite.

Figure 5 displays data registered when DEMETER was above a thunderstorm. The top panel shows the spectrogram of an electric-field component up to 20 kHz, where intense whistlers were observed (vertical lines), just after 12:03 UT. At the time when the number of whistlers increased together with their intensities, one could see, in the bottom panel, an increase of the O+ ion density.

6. The Hurricanes

Investigations were done when the satellite was above atmospheric events with large pressure modifications, such as hurricanes. Figure 6 displays the location of hurricane Dean on August 17, 2007. At that time, the wind speed was 145 mph. The red line corresponds to a part of the DEMETER half-orbit during that day. Hours are indicated. Figure 7 is related to the DEMETER data recorded along this half-orbit. One noticed the large number of whistlers (vertical lines) in the top panel that were mainly located at

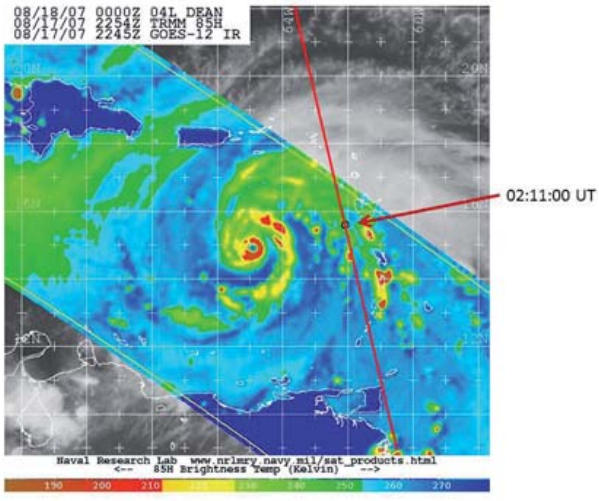

Figure 6. Passive microwave imagery from the NASA TRMM satellite, depicting the eyewall replacement cycle in Hurricane Dean on August 17, 2007, at 2254 UTC. All images are from the 85 GHz channel, in which ice scattering reveals areas of deep convection displayed in the red shades (image courtesy of the Naval Research Laboratory, NRL).

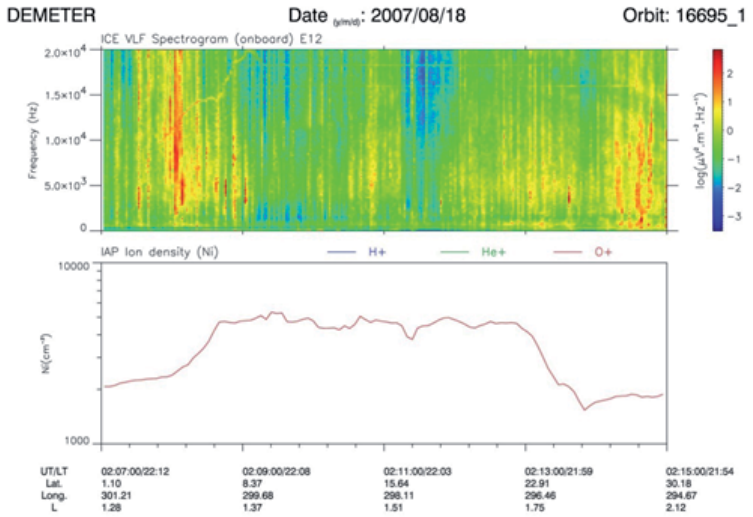

Figure 7. DEMETER data recorded along the half-orbit shown in Figure 6. The top panel displays the spectrogram of an electric-field component up to 20 kHz, and the bottom panel is related to the O+ ion density.

the edges of the hurricane. A large increase of the density was observed in the bottom panel at the closest approach of the hurricane.

7. Discussion and Conclusion

Various sets of events occurring at the Earth's surface or in the atmosphere have been studied with the DEMETER data. These events were related to radioactivity, electrostatic discharges of different intensities, and temperature and pressure changes. It was shown that they all induced variations in the ionosphere at the altitude of the satellite. These phenomena involve mechanisms that are put forward to explain ionospheric perturbations induced by earthquakes prior to their occurrence. The DEMETER observations then pointed out that the different steps described in the LAIM coupling models [7, 9] were possible.

8. Acknowledgements

This study was issued from an ISSI team led by S. Pulinets (RU) and D. Ouzounov (US), started in 2013 to work with the following aim: Multi-Instrument Space-Borne Observations and Validation of the Physical Model of the LAIM Coupling (see http://www.issibern.ch/teams/spaceborneobserve/). They are deeply acknowledged, together with the contributions of K. Hattori, Tiger J. Y. Liu, A. Namgaladze, and V. Tramutoli.

9. References

1. F. Němec, O. Santolík, and M. Parrot, "Decrease of Intensity of ELF/VLF Waves Observed in the Upper Ionosphere Close to Earthquakes: A Statistical Study," *Journal of Geophysical Research*, **114**, A04303, 2009, doi:10.1029/2008JA013972.

2. Y. He, D. Yang, J. Qian, and M. Parrot, "Response of the Ionospheric Electron Density to Different Types of Seismic Events," *Natural Hazards and Earth System Sciences*, **11**, doi:10.5194/nhess-11-2173-2011, 2011, pp. 2173-2180.

3. M. Li and M. Parrot, "'Real Time Analysis' of the Ion Density Measured by the Satellite DEMETER in Relation with the Seismic Activity," *Natural Hazards and Earth System Sciences*, **12**, doi:10.5194/nhess-12-2957-2012, 2012, pp. 2957-2963.

4. M. Li and M. Parrot, "Statistical Analysis of an Ionospheric Parameter as a Base for Earthquake Prediction," *Journal of Geophysical Research: Space Physics*, **118**, 2013, pp. 3731-3739, doi:10.1002/jgra.50313.

5. D. Piša, F. Němec, O. Santolik, M. Parrot, and M. Rycroft, "Additional Attenuation of Natural VLF Electromagnetic Waves Observed by the DEMETER Spacecraft Resulting from Preseismic Activity," *Journal of Geophysical Research: Space Physics*, **118**, 2013, doi:10.1002/jgra.50469.

6. K. Ryu, E. Lee, J. S. Chae, M. Parrot, and S. Pulinets, "Seismo-Ionospheric Coupling Appearing as Equatorial Electron Density Enhancements Observed via DEMETER Electron Density Measurements," *Journal of Geophysical Research: Space Physics*, **119**, 2014, pp. 8524–8542, doi:10.1002/2014JA020284.

7. S. Pulinets and D. Ouzounov, "Lithosphere-Atmosphere-Ionosphere Coupling (LAIC) Model – A Unified Concept for Earthquake Precursors Validation," *Journal of Asian Earth Sciences*, **41**, June 2011, pp. 371-382.

8. S. Pulinets, "Low-Latitude Atmosphere-Ionosphere Effects Initiated by Strong Earthquakes Preparation Process," *International Journal of Geophysics*, 2012, Article ID 131842, 14 pages.

9. S. Pulinets and D. Davidenko, "Ionospheric Precursors of Earthquakes and Global Electric Circuit," *Advances in Space Research*, **53**, 5, March 2014, pp. 709-723.

10. R. G. Harrison, K. L. Aplin, and M. J. Rycroft, "Atmospheric Electricity Coupling Between Earthquake Regions and the Ionosphere," *Journal of Atmospheric and Solar Terrestrial Physics*, **72**, April 2010, pp. 376- 381.

11. M. Parrot, "First Results of the DEMETER Micro-Satellite," *Planetary and Space Science*, **54**, 5, 2006, pp. 411-558.

12. F. Sannazzaro, C. Filizzola, F. Marchese, R. Corrado, R. Paciello, G. Mazzeo, N. Pergola, and V. Tramutoli, "Identification of Dust Outbreaks on Infrared MSG-SEVIRI Data by Using a Robust Satellite Technique (RST)," *Acta Astronautica*, **93**, 2014, pp. 64-70.

13. J. Zlotnicki, Feng Li, and M. Parrot, "Signals Recorded by DEMETER Satellite Over Active Volcanoes During the Period 2004 August - 2007 December," *Geophysical Journal International*, **183**, 3, 2010, pp. 1332-1347.

14. N. Pergola, V. Tramutoli, F. Marchese, I. Scaffidi, and T. Lacava, "Improving Volcanic Ash Cloud Detection by a Robust Satellite Technique," *Remote Sensing of Environment*, **90**, 1, 2004, pp. 1-22.

15. M. Parrot, J. A. Sauvaud, S. Soula, J. L. Pinçon, and O. van der Velde, "Ionospheric Density Perturbations Recorded by DEMETER Above Intense Thunderstorms," *Journal of Geophysical Research: Space Physics*, **118**, 2013, doi:10.1002/jgra.50460.

Fine-Scale Evaluation of Rainfall from TV-Sats: A New Method for Water Monitoring and Flash Flood Prevention

François Mercier[1,2], Nawal Akrour[1], Laurent Barthès[1], Cécile Mallet[1], and Ruben Hallali[1,3]

[1]Laboratoire Atmosphères, Milieux, Observations Spatiales

[2]Now: Centre National de Recherches Météorologiques, France

[3]Now: Direction des Systèmes d'Observation, Météo France, France
E-mail: francois.mercier@meteo.fr, nawal.akrour@latmos.ipsl.fr
laurent.barthes@latmos.ipsl.fr cecile.mallet@latmos.ipsl.fr
ruben.hallali@meteo.fr

Abstract

In this paper we present a method for rebuilding rainfall maps at high resolution (500 m × 500 m, 1 min). This method is based on the assimilation of opportunistic measurements of the attenuation that affects the signals coming from TV satellites in a model of spatiotemporal advection of rainfall fields. At the frequencies used (Ku band), the attenuation affecting the signals in the atmosphere is mainly due to rain. We set a sensor (field analyzer) on the ground, and then measured the mean rainfall over the link. This method was applied to a simulated network of sensors. These simulated sensors were realistically set over the Paris area, on a zone assumed to be typical of an area with high socio-economic issues (flood prevention, water resources management). We compared the simulated rainfall maps with the maps rebuilt by our algorithm. We then showed the feasibility of our approach for measuring the rainfall in urban areas with high resolution.

1. Introduction

This paper presents a new method for retrieving rain maps (namely, two-dimensional fields of rainfall rates on the ground, in mm/h, at successive time steps) at fine spatiotemporal resolution (typically 500 m × 500 m and 1 min). This method uses the measurement of the attenuation due to rain affecting electromagnetic waves emitted in the Ku band by geosynchronous TV satellites.

Traditionally, these rain maps are produced from rain-gauge records or weather-radar data, or from a combination of both types of measurements. However, both of these instruments have weaknesses. Rain gauges only provide point measurements. The very high spatiotemporal variability of rain implies having a very dense rain-gauge network to correctly estimate fine-scale rain maps (as well as the total amount of rain over an area, for instance, for hydrological purposes). The deployment of such a dense network implies significant maintenance costs, so that there are now fewer and fewer rain gauges available [1]. Furthermore, radars are blocked by mountains (inter alia), and are very expensive to buy, to sustain, and to use. Mountainous areas as well as developing countries are consequently generally not covered by operational networks. The use of radars in hydrology also raises questions [2].

The use of the attenuation affecting microwave electromagnetic signals as a new way for measuring rain has received increasing attention in the scientific community for about 20 years. Most of the studies on this topic focused on the attenuation of telecommunications microwave signals [1, 3-6]. However, some of them already measured the attenuation of waves coming from geosynchronous TV satellites on the ground [7, 8]. By nature, all these measurements provide information about rainfall that is indirect and integrated in space. Firstly, it is indirect because we measure attenuations, and so we need a way (actually, a power law, see [7] and Section 2 of this paper) to convert these attenuations into rain rates. Secondly, they are integrated because we measure the mean attenuation over an emitter/receiver pathway. These pathways are typically a few kilometers long, whether this is for the telecommunication links or the satellite/Earth links (the attenuation only occurs in rain, so the pathway is restricted to the segment from the base of the clouds or from the freezing level to the ground; see Section 2). Consequently, for retrieving rain maps at fine spatiotemporal resolution (around 1 km or below), we need to couple the raw measurements with a retrieval algorithm.

The first studies on this topic generally restricted the links to their center points, and have used kriging or tomography algorithms to retrieve rain maps [9]. In these algorithms, the measurements at successive time steps are regarded as independent (they do not use a propagation model to explicitly link the successive data). Several studies using very dense measuring networks (and/or data at low time sampling) also proceeded in this way (for instance, [1] produced rainfall maps over the entire Netherlands using telecommunications data and a kriging algorithm).

Reference [5] first used the mathematical framework of data assimilation to post-process telecommunications measurements. Data assimilation roughly consists in using a propagation model (typically, a model that moves the rain fields according to the wind) to link the measurements recorded at successive time steps. The unknown of such a model is the rain map at a given initial time, t_0. We then look for the rain map at t_0 that once propagated by the model best explains the measurements (the attenuations) recorded over a time period. This approach allows working with less-dense networks. The good temporal sampling of the data is used (via the model) to increase the spatial resolution.

The study presented in this paper used attenuations measured from TV satellites emitting in the Ku band (around 12 GHz). It combined these data together with a four-dimensional-variational assimilation algorithm. This approach was applied to real rain case studies recorded in the department of Ardèche, in the southeast of France, during the HyMeX campaign (Hydrological Cycle in the Mediterranean Experiment, [10]). These results were published [11]. We then extended the approach – for now, only on simulated data – to a more-dense and realistic network of attenuation sensors simulating an urban area.

Section 2 of this paper gives more information about the measuring system and the retrieval algorithm. In Section 3 we then present the results obtained with this simulated network.

2. Methodology

2.1 Measuring Device

The Ku frequency band (around 12 GHz) is mainly attenuated in the atmosphere by liquid raindrops [7]. This attenuation consequently mainly occurs in rain (under the clouds or under the freezing level).

The idea is to set sensors on the ground in order to measure the attenuation of microwave signals coming from geosynchronous TV satellites. Figure 1 schematically represents this situation for one sensor. We can see that the recorded attenuation is integrated over Earth/satellite segments a few kilometers long. A precise description of the sensor and of the first post-processing treatment applied to the very raw data (temporal averaging to get a 10 s sampling, with the algorithm able to distinguish the part of the attenuation due to rain from the (small) part due to clouds and other effects) was provided in [7]. We can just notice that these sensors can theoretically be connected to dedicated antennas or to personal antennas, already installed. We then consider in this study that our "raw" data are the attenuations (in decibels, dB) along these Earth/satellite links with a 10 s sampling.

These attenuations are linked to the mean rainfall rate over the link (R, in mm/h) by the power law [7]

$$K = aR^b,$$

with a and b being two coefficients that notably depend on frequency, polarization, and on the drop-size distribution (typically, at 12 GHz, a is around 0.024 and b around 1.1 to 1.2).

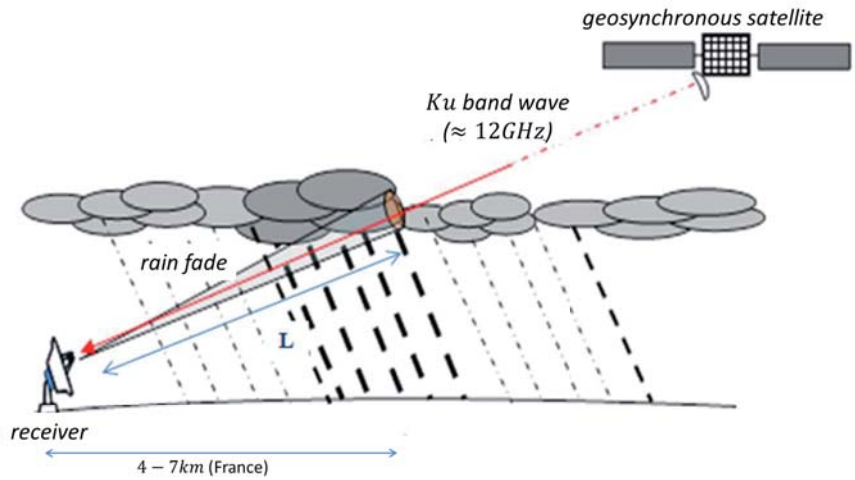

Figure 1. A description of the system that allows measuring the attenuation of satellite signals and that was used in this study ("Ku link").

The purpose of this study was to retrieve rainfall maps by combining such measurements (recorded at successive time steps by several sensors) with a model able to simulate the propagation of the rain fields. Because we wanted to avoid the use of the power law during the execution of the data-assimilation algorithm, we worked with linear attenuations (in dB/km) during the entire process, and converted these linear attenuations into rain rates offline, at the very end of the algorithm. We will nevertheless generally present visual results in terms of rainfall rates.

2.2 Retrieval Algorithm

The 4D-VAR data-assimilation algorithm (see, for instance, [12]) consists in coupling time-distributed observations with a numerical model able to propagate information through time, in order to retrieve values compatible both with the observations (then allowing to fuse them) and with the dynamics included in the model. Consequently, we first have to define a model (typically, the discretization of partial differential equations, PDEs) able to simulate the dynamics of the rainfall fields (or, similarly, of the attenuation fields).

2.2.1 Propagation Model

In this study, we used a simple advection model at constant speed. Let $K(t,x,y)$ be an attenuation field at any time t and any point (x,y) on a plane (we restrict the problem to a plane by assuming that the rain is homogeneous on the vertical columns). Let u and v be the advection speeds to the north and to the east. The partial differential equation driving the propagation of the of the attenuation field is then

$$\frac{\partial K}{\partial t} = u\frac{\partial K}{\partial x} + v\frac{\partial K}{\partial y}.$$

We can note that the assumptions made here are the same as in [11]. We also note that this model, which assumes that rain fields move without any distortion and assumes homogeneous and constant winds, will only be workable, for the spatial resolution considered here, over short time periods (typically, 30 min to 1 h, depending on the topography of the area studied). It could be possible to use a more-complex model (for instance, with non-constant winds), but we would need a dense network of attenuation sensors to estimate its parameters. Such a network was not available in our first study [11], but could be considered for future developments. About the wind parameters (u and v), we showed in [11] that if two sensors are available and wisely set up, the wind parameters can be directly estimated from the time series of attenuations (using a cross-correlation technique). We then assume that these parameters are fully known.

The partial-differential-equation problem is well-posed only if we also define boundary and initial conditions. About the boundary conditions, we assume that no rain enters the considered area during the time period (the inflow is zero). If we retrieve the initial condition $K(0,x,y)$, we would thus be able to estimate the attenuation field at any time and location. This is the goal of the 4D-VAR data-assimilation algorithm.

We finally note that we also have to discretize the partial differential equation for running it. To do so, we use an anti-diffusive scheme proposed by [13]. The discretization steps are 500 m and 1 s.

2.2.2 Data-Assimilation Algorithm

We have defined the dynamics governing the evolution of the attenuation fields, so we can now introduce the 4D-VAR data-assimilation algorithm used to retrieve the initial attenuation field, $K(0,x,y)$, which is the only unknown of the problem. An introduction to data assimilation was provided, for instance, in [12]. This algorithm roughly consists in minimizing a cost function, J, which sums two parts which estimate:

> The gap between the observations available and the initial (unknown) field propagated through the model until the time steps corresponding to the observation records.

There are possibly other terms bringing information about a priori knowledge of the unknown field (the gap between the unknown field and a predefined field, or more general information, for instance, regularization terms).

In this study, we used the following cost function:

$$\mathbf{J}\left(\mathbf{K}^0\right) = \alpha\left\|\mathbf{K}^0 - \mathbf{m}\left(\mathbf{K}^0\right)\right\|^2 + \sum_n \left\|\mathbf{y}^n - \mathbf{H}^n\mathbf{K}^n\right\|^2$$

$\mathbf{K}^0$ is the two-dimensional attenuation field at $t=0$ rewritten under a vector form. $\mathbf{K}^n$ is the attenuation field at time t_n (also under a vector form). $\mathbf{K}^n$ is just the propagation of $\mathbf{K}^0$ until t_n using the discretization of the advection model, called $\mathbf{M}^n$. $\mathbf{H}^n$ is the operator of observations that allows converting the linear attenuations at every grid point into attenuations integrated over the Ku Earth/satellite pathways. For a given Ku link, this operator is a linear combination of the linear attenuations in the grid points "crossed" by the link. The $\mathbf{y}^n$ are the observations at time t_n (the attenuations). $\mathbf{m}\left(\mathbf{K}^0\right)$ is the local average of $\mathbf{K}^0$ (calculated over the nine grid points directly connected to the considered point). Finally, the first part of $\mathbf{J}\left(\mathbf{K}^0\right)$ is a regularization term, while the second one is a term estimating the gap to the observations. For a more detailed

description of this cost function, we can refer to [11]. For minimizing this cost function and so estimating $\mathbf{K}^0$, we have to calculate its gradient. This calculation is made using the adjoint operators (transpose of the linear tangent) of the operator of observations, $\mathbf{H}^n$, and of the model, $\mathbf{M}^n$.

In order to facilitate all these developments, we used the YAO tool, developed at the LOCEAN laboratory (Laboratoire d'Océanographie et du Climat), and described, for instance, in [14]. This tool, written in *C++*, eases the development of 4D-VAR algorithms by writing their components (operator of observations, nonlinear model, etc.) under the form of basic components (analytic operations performed at every grid point and time step). These basic components are linked by a graph describing their connections (for the concept of a modular graph, see [14]). The minimization part of this process is done with the quasi-Newton m1qn3 algorithm developed in [15].

We now have defined the 4D-VAR algorithm that retrieves the attenuation map at the initial time, $\mathbf{K}^0$. Using the model $\mathbf{M}^n$, we can deduce $\mathbf{K}^n$, the attenuation maps at every time. Using the power law linking rain rate and attenuation, we can estimate the rain maps at every time.

3. Results from Simulated Data for an Urban Area

This retrieval algorithm was successfully tested on real but sparse data (one ground receiver measuring the attenuation of the waves coming from four different satellites). The goal of this paper is to evaluate the retrieval algorithm for a denser network of sensors, corresponding to a realistic urban-area situation. Because we did not have experimental data for such an area (it would imply the use of many sensors), we worked with simulated sensors and simulated rain maps. In this section, we first introduce the method employed to simulate all the data needed, and we then present our results.

3.1 Method Employed to Generate the Simulated Data

To run a data-assimilation experiment on simulated data, we successively have to:

1. Choose an area of interest.
2. Define locations for the Ku sensors, in a realistic way.
3. Simulate "true" rain maps, which are the maps we will then try to retrieve with our assimilation algorithm.
4. Simulate a wind (advection speed determined by parameters u and v) to run the advection model.
5. Simulate observations. To do so, from the "true" rain maps, we will use the advection model and the operator of observations. These observations are the attenuations along the links defined at point 2, plus possible instrumental noise.

These five steps allowed simulating what could be measured by a real system for maps of different sizes and

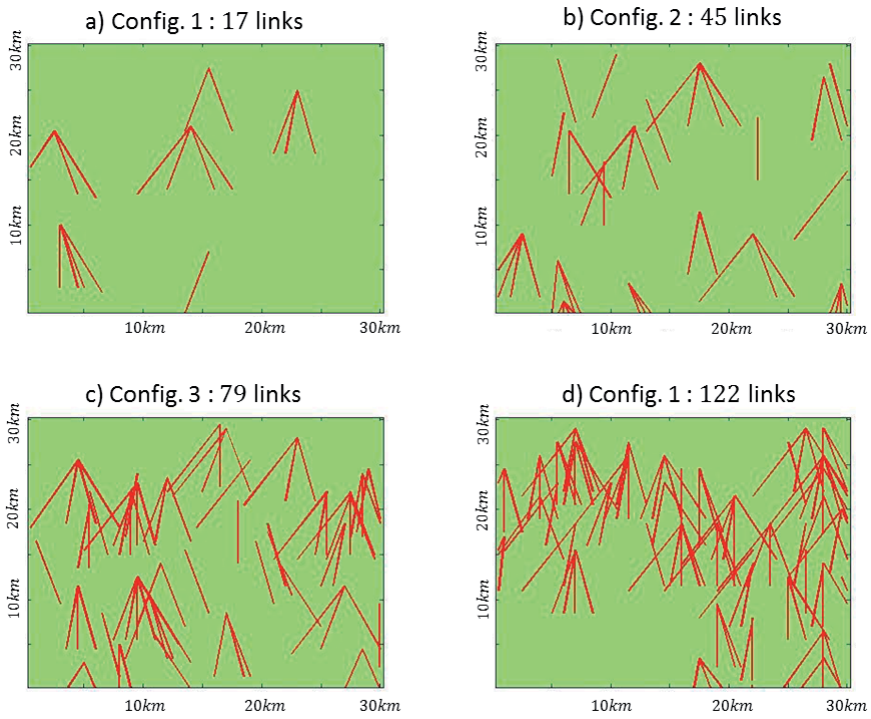

Figure 2. The Ku links used for configurations 1 to 4 in the area of interest.

for different network configurations. We then applied our retrieval algorithm to the simulated observations (created at point 4), and studied the ability of the algorithm to retrieve the rain maps (created at point 3) from these observations. Just before going through the results, we will give some details about these five points.

1. The area studied was located in the Paris area, France. More specifically, it covered a part of the French department of Yvelines, on an area of approximately 30 km × 30 km, centered over the city of Trappes (48.78N, 1.98E). This area is a densely populated area, but the spread of the population is not really homogeneous, with both urban communities and agricultural areas. We could therefore expect areas with dense Ku-sensor networks, and others with almost no sensors available. Moreover, there are different socio-economic impacts of rain in this area. First, the urban areas can be affected by floods caused by the river Seine. Second, water-resource management is important, for both the inhabitants' needs and for agriculture.

2. We then had to define locations for the Ku sensors. Figure 2 shows four configurations tested in this study. In any case, the Ku sensors were set up according to the population density on the considered grid point. All the links were also directed to real satellites available around Paris ([11] listed some of these satellites). We can also note that all the links pointed mainly to the south, because the satellites are geosynchronous, and so located above the equator. From one configuration to another one, we changed the number of available sensors (17, 45, 79, and 122 for configurations 1 to 4). These configurations were thus realistic configurations, depending on the investments made in terms of number of installed sensors.

3. For the rainfall maps, we simulated the map at the initial time, t_0, and we then used the advection model to generate the other maps. To create this individual first map, we used a method developed by [16] that allows simulating realistic two-dimensional rainfall maps. In this study, we worked with the map that is shown in Figure 3. On this map, it was raining over 37% of the grid points, with an average rain rate of 1.1 mm/h and a maximum of 38 mm/h.

4. Concerning the advection parameters, we supposed that the rain cells moved eastward at a speed of 10 m/s, realistic for the Paris area. We therefore had $u = 0$ and $v = 10$ m/s.

5. All the needed parameters of the problem were now defined. We used the wind defined at point 4 in the advection model to move the rain rate of Figure 3 and to get the rain maps at any time. We then transformed these rain maps into linear attenuation maps (power law), and we used the operator of observations to simulate the attenuations along the different links defined in Figure 2. We then possibly added instrumental noise to these data. We thus had observations ready to be used as input to the assimilation algorithm.

We can nevertheless note that in this procedure, we assumed that the numerical model of advection was perfect. We used the same advection model with the same parameters ($u = 0$, $v = 10$ m/s) for both simulating the observations and for running the assimilation model from these observations. The results that follow therefore were representative of cases for which the model was "sufficiently" realistic. This question (what does "sufficiently" mean?) was already asked in our first study on real data [11]. We then showed that we were able to treat four rain events over eight. This value nevertheless depends on the topography, meteorological conditions, and sensor network design, and needs to be carefully studied in any future real data study. An improvement of the model's performance (by using non-constant winds) can also be considered.

We were now ready to run the assimilation model and to compare its output (the rain map at t_0) with the true map of Figure 3.

3.2 Results

3.2.1 Non-Noisy Data: Results According to the Density of Sensors

First, we chose to not add instrumental noise to the simulated data. We also assumed that our observations were

Table 1. The statistical errors produced by the assimilation algorithm compared to the true initial rain map for the experiments shown in Figure 4.

	Entire Map		Rainy Areas		Dry Areas	
	RMSE (mm/h)	Bias (mm/h $\frac{mm}{h}$)	RMSE (mm/h)	Bias (mm/h)	RMSE ($\frac{mm}{h}$ mm/h)	Bias (mm/h)
Config. 1	0.88	–0.09	1.95	–0.75	0.16	+1.16
Config. 2	0.82	–0.10	1.71	–0.24	0.18	+0.18
Config. 3	0.40	+0.01	0.99	–0.98	0.07	+0.07
Config. 4	0.37	–0.01	0.93	–0.11	0.10	+0.10

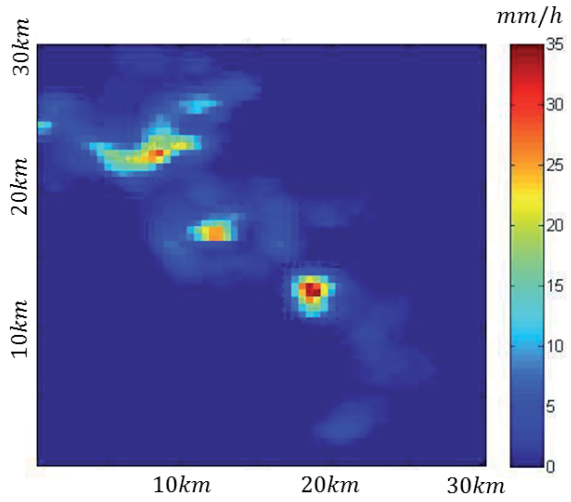

Figure 3. The simulated rain map considered as the true rain map in this study.

sampled at 10 s (as were the real data in [11]). We then tested our algorithm's performance on the four configurations shown in Figure 2, from the sparsest (configuration 1, Figure 2a) to the densest (configuration 4, Figure 2d).

Figure 4 shows the initial true rain map (a) and the four maps retrieved by our algorithm (b to e) for each of these configurations. Table 1 gives several statistical results concerning the errors that our algorithm implied in terms of bias and RMSE (root mean square error) compared to the true map. In Table 1, we also distinguished the areas of the true rain map that were dry from the rainy areas.

Several results could be deduced from these visual and numerical results:

- We noted that only configurations 3 and 4 were able to correctly retrieve the three main rain cells that appeared on the true map (Figure 4). Both configurations 1 and 2 missed the southern rain cell. This was not an unexpected result, because during its eastward advection, this cell only crossed areas with a very low density of population. These areas were consequently not covered (or very sparsely covered) by Ku sensors (Figure 2).

- In any case, the total amount of water that fell over the area was very well retrieved (biases in the third column of Table 1). This was especially true for configurations 3 and 4, when the sensors gave a very good coverage of the entire area. Again, we noted that the bias was slightly negative for configurations 1 and 2 because a part of the rain could not be seen by any sensor.

- The root mean square error decreased when we added links (from configuration 1 to configuration 4). Nevertheless, it remained quite strong from 0.4 mm/h up to 0.8 mm/h for an average rain rate of 1.1 mm/h. However, this could be produced by noise (oscillations) on the initial map as a result of the assimilation algorithm. These oscillations would then be quickly smoothed during the advection (numerical diffusion phenomenon), and so they would not add an important cost in the assimilation cost function. We could again calculate these root mean square errors using the rain maps at any time, instead of only for the initial case. However, the regularization term of the cost function was specifically added in order to limit this effect, so we kept the values calculated from the initial rain maps as an indicator.

- We can note overall (and especially for configurations 3 and 4) that the features (intensity, size, and location) of the true rain maps were very well reproduced by the assimilation-retrieval algorithm.

- Finally, we noted (Table 1) that this algorithm tended to underestimate the rain in rainy areas, and to slightly overestimate the rain in dry areas (we retrieved rain in areas where it did not rain). This is due to the fact that our retrieved maps were smoother than the true map.

In summary, the assimilation algorithm was able to retrieve the true map's features only if there were enough sensors to cover the entire area considered (we retrieved only what was seen). We could nevertheless note that the areas in which the rain rates were poorly retrieved in this study corresponded to sparsely populated areas.

3.2.2 Results on Noisy Observations and Impact of the Time Sampling of Observations

We then studied two phenomena that could decrease the performance of the retrieval algorithm. The first was instrumental noise. The second was the time sampling of the observations. To this end, we added to our simulated observations noise of 0.5 dB, which corresponded to the typical noise affecting the sensor used in [7, 11]. We then performed assimilation experiments with successive time samplings of 10 s (the same as in the previous paragraph), 1 min, and 5 min. In all these tests, we used configuration 3 for the sensor network. This configuration allowed covering all the area studied with as few sensors as possible.

For these experiments, Figure 5 and Table 2 show the same results as the previous Figure 4 and Table 1 (rain maps, biases, root mean square error).

We noted (Figure 5b compared to Figure 4d and Table 2) that if we added noise to the observations, it also added noise to the assimilation outputs. This nevertheless did not affect the good overall retrieval of the features of the true map (for instance, we still retrieved the main rain-cell locations very well). This did not affect the overall bias (+0.05 mm/h with noise, +0.01 mm/h without noise). However, when we added noise, this tended to produce very localized and strong fake rain areas, possibly far from the real rain cells. During the assimilation process, the initial

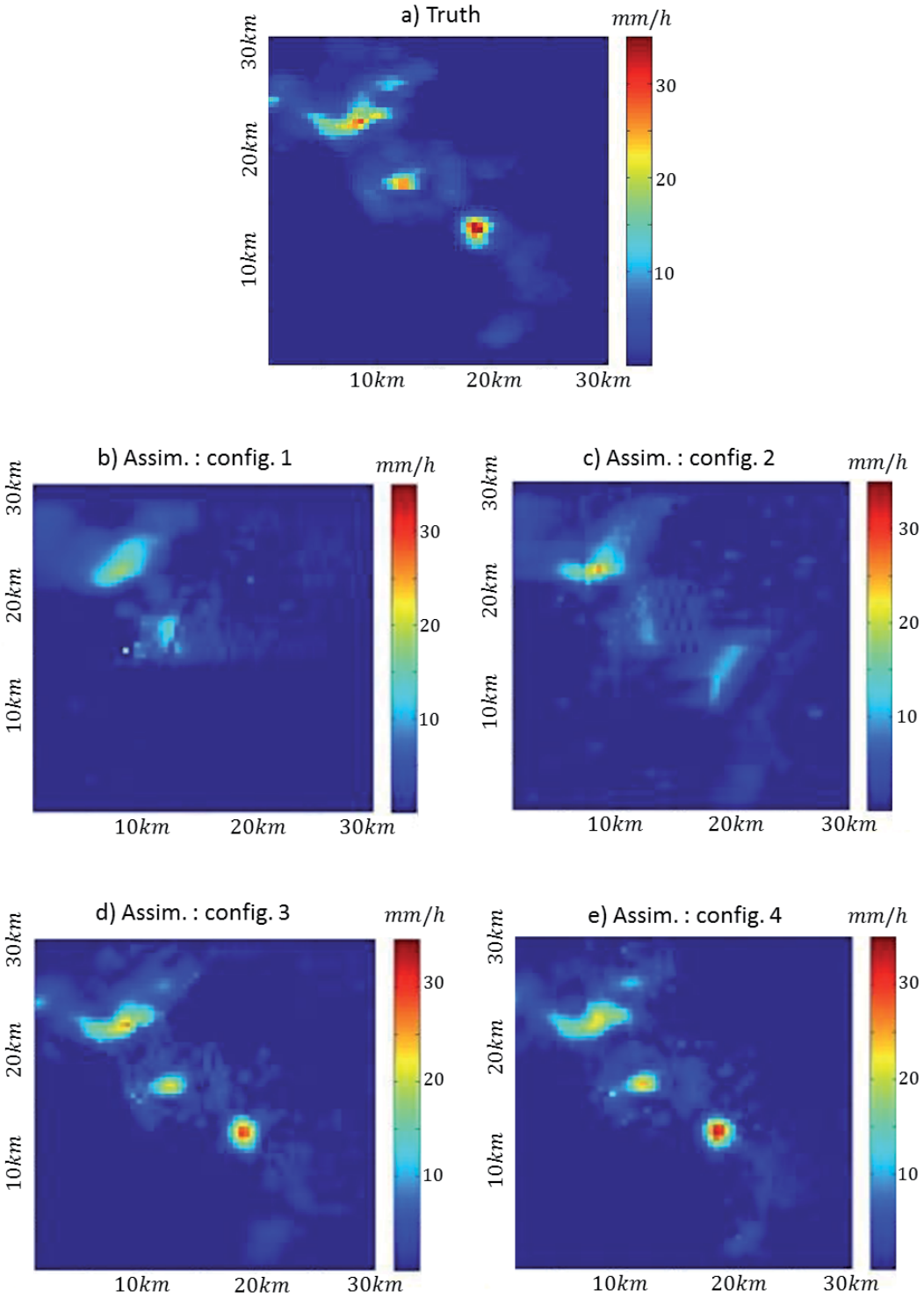

Figure 4. (a) The initial true rain map. (b)-(e) The initial rain maps produced by the assimilation algorithm, for observations with a sampling of 10 s and the four configurations shown in Figure 2.

rain map is advected by the numerical model before being compared to the observations in the cost function. The numerical model immediately (meaning, in a few time steps) smoothes the strong rain gradients appearing on the initial map. Finally, these localized strong gradients will be almost transparent, both in the cost function and in the bias statements.

Now, when we decreased the time sampling (Figures 5c, 5d, and the two last lines of Table 2), we could see that the performance of the algorithm significantly decreased. For instance, the root mean square errors were quite strong (1.52 mm/h for a 5 min time sampling). We also remark that several fake strong rain retrievals (Figure 5d) occurred.

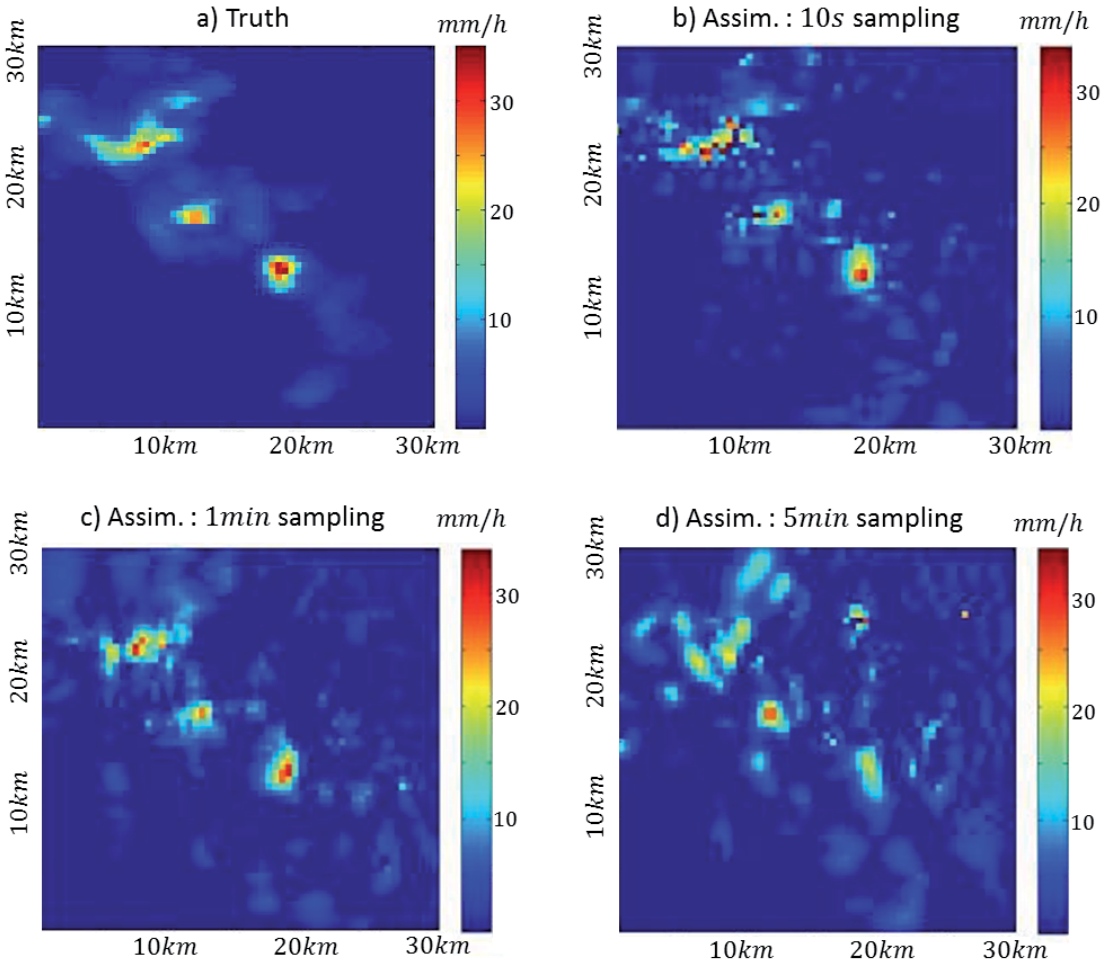

Figure 5. (a) The true initial rain map. (b)-(d) The initial rain maps produced by the assimilation for noisy observations for configuration 3 of Figure 2, with time samplings from 10 s to 5 min for the observations.

To conclude, we noted that 0.5 dB noise in the observations was not troublesome for the algorithm retrievals. The statistical results were almost the same (for instance, we still got low biases). The initial retrieved rain map was noisier, but this noise was very quickly smoothed during the advection process by the model (numerical diffusion). We rather noted that we needed a time sampling better than 1 min (ideally, 10 s if it is possible). If it was 1 min or worse, the quality of the retrievals largely decreased. This was not an unexpected result: one of the main principles of this technique is to use the good time sampling of the measurements to produce (via the model) maps with high spatial resolution. If we do not have this good time sampling, the algorithm fails. These simulations have shown the ability of the method to produce rain maps with very good spatiotemporal resolution. As the sensors used are not expensive, they could be deployed in areas that are not already covered by traditional rain measurement systems (rain gauges, radars), or in areas subject to strong rain impacts (for flash flood prevention, for instance).

Table 2. The statistical errors produced by the assimilation algorithm compared to the true initial rain map for the experiments shown in Figure 5.

	Entire Map		Rainy Areas		Dry Areas	
	RMSE (mm/h)	Bias (mm/h)	RMSE (mm/h)	Bias (mm/h)	RMSE (mm/h)	Bias (mm/h)
Sampling 10 s	0.84	+0.05	2.19	–0.04	0.24	–0.07
Sampling 1 min	1.03	+0.18	2.17	–0.18	0.39	+0.39
Sampling 5 min	1.52	+0.46	2.99	+0.07	0.69	+0.66

4. Conclusions

In this paper, we have introduced a new technique for retrieving rainfall maps at high spatiotemporal resolution. This method uses measurements of the attenuation affecting microwaves from TV satellites during their crossing of the atmosphere. These attenuation measurements – related by a power law to the mean rainfall rates over the Earth-satellite links and made by sensors located on the ground – are combined in a data-assimilation algorithm by a simple advection numerical model to propagate the rain fields through time. This technique allows retrieving the rainfall map at an initial time step that once propagated by the model is able to explain the observations recorded at different times.

This method was already successfully tested on real data sets recorded over a small area [11]. These encouraging results convinced us to go through larger areas, covered by many sensors.

In this paper, we showed results for simulated data on a realistic urban area. We proved the ability of our algorithm to deal with many sensors, and so to successfully retrieve rain maps over a quite larger area (30 km × 30 km). We have shown that this algorithm is able to deal with realistic instrumental noise, but that it needs observations with a very good time sampling (less than 1 min) to be run.

The next step in these developments consists in deploying a real system in an urban area, in order to validate the approach on real data over a city. The envisaged prototype would use 20 to 25 sensors and would be deployed over a medium-sized town, ideally subject to intense flash-flood events. This prototype experiment could be a first step before deploying this system in areas where no other classical and costly system is available.

5. References

1. A. Overeem, H. Leijnse and R. Uijlenhoet, "Country-Wide Rainfall Maps from Cellular Communication Networks," Proceedings of the National Academy of Sciences, **110**, 2013, pp. 2741-2745.

2. A. Berne and W. F. Krajewski, "Radar for Hydrology: Unfulfilled Promise or Unrecognized Potential?," *Advances in Water Resources*, **51**, 2013, pp. 357-366.

3. C. Chwala, A. Gmeiner, W. Qiu, S. Hipp, D. Nienaber, U. Siart, T. Eibert, M. Pohl, J. Seltmann, J. Fritz, and H. Kunstmann, "Precipitation Observation Using Microwave Backhaul Links in the Alpine and Pre-Alpine Region of Southern Germany," *Hydrology & Earth System Sciences*, **16**, 2012.

4. A. Doumounia, M. Gosset, F. Cazenave, M. Kacou, and F. Zougmore, "Rainfall Monitoring Based on Microwave Links from Cellular Telecommunication Networks: First Results from a West African Test Bed," *Geophysical Research Letters*, **41**, 2014, pp. 6016-6022.

5. A. Zinevich, H. Messer, and P. Alpert, "Frontal Rainfall Observation by a Commercial Microwave Communication Network," *Journal of Applied Meteorology and Climatology*, **48**, 2009, pp. 1317-1334.

6. M. Schleiss and A. Berne, "Identification of Dry and Rainy Periods Using Telecommunication Microwave Links," *IEEE Geoscience and Remote Sensing Letters*, **7**, 2010, pp. 611-615.

7. L. Barthès and C. Mallet, "Rainfall Measurement from the Opportunistic Use of an Earth-Space Link in the Ku Band," *Atmospheric Measurement Techniques*, **6**, 2013, pp. 2181-2193.

8. A. Maitra and K. Chakravarty, "Ku-Band Rain Attenuation Observations on an Earth-Space Path in the Indian Region," Proceedings of the URSI General Assembly, 2005.

9. D. Giuli, L. Facheris and S. Tanelli, "Microwave Tomographic Inversion Technique Based on Stochastic Approach for Rainfall Fields Monitoring," *IEEE Transactions on Geoscience and Remote Sensing*, **37**, 1999, pp. 2536-2555.

10. O. Bousquet, A. Berne, J. Delanoë, Y. Dufournet, J. Gourley, J. Van-Baelen, C. Augros, L. Besson, B. Boudevillain, O. Caumont et al., "Multifrequency Radar Observations Collected in Southern France During Hymex-sop1," *Bulletin of the American Meteorological Society*, **96**, 2015, pp. 267-282.

11. F. Mercier, L. Barthès and C. Mallet, "Estimation of Finescale Rainfall Fields Using Broadcast TV Satellite Links and a 4DVAR Assimilation Method," *Journal of Atmospheric and Oceanic Technology*, **32**, 2015, pp. 1709-1728.

12. E. Kalnay, *Atmospheric Modeling, Data Assimilation, and Predictability*, Cambridge, Cambridge University Press, 2003.

13. P. K. Smolarkiewicz, "A Simple Positive Definite Advection Scheme with Small Implicit Diffusion," *Monthly Weather Review*, **111**, 1983, pp. 479-486.

14. L. Nardi, C. Sorror, F. Badran and S. Thiria, "YAO: A Software for Variational Data Assimilation Using Numerical Models," Computational Science and Its Applications-ICCSA 2009, 2009, pp. 621-636.

15. J. C. Gilbert and C. Lemaréchal, "The Module m1qn3," INRIA Rocquencourt & Rhone-Alpes, 2006.

16. N. Akrour, A. Chazottes, S. Verrier, C. Mallet and L. Barthes, "Simulation of Yearly Rainfall Time Series at Microscale Resolution with Actual Properties: Intermittency, Scale Invariance, and Rainfall Distribution," *Water Resources Research*, **51**, 2015, pp. 7417-7435.

Call for Papers

2nd URSI Atlantic Radio Science Conference (URSI AT-RASC)

May 28 - June 1, 2018

ExpoMeloneras Convention Centre, Gran Canaria

Important deadlines

Paper submission
January 10, 2018

Notification
February 21, 2018

Early bird registration
March 24, 2018

Conference start
May 28, 2018

Please consult **www.at-rasc.org** for the latest information

The triennial URSI Atlantic Radio Science Conference (URSI AT-RASC) is one of the URSI flagship conferences besides the URSI General Assembly and Scientific Symposium and the AP-RASC conference (Asia-Pacific Radio Science Conference).

This 2nd URSI AT-RASC will have a series of convened and open sessions within the domains covered by all ten Commissions of URSI:

Commission A:	Electromagnetic Metrology	Commission F:	Wave Propagation and Remote Sensing
Commission B:	Fields and Waves		
Commission C:	Radiocommunication and Signal Processing Systems	Commission G:	Ionospheric Radio and Propagation
Commission D:	Electronics and Photonics	Commission H:	Waves in Plasmas
Commission E:	Electromagnetic Environment	Commission J:	Radio Astronomy
		Commission K:	Electromagnetics in Biology and Medicine

Paper submission deadline: January 10, 2018

Detailed information on paper submission as well as travel information will become available through the website: www.at-rasc.org. Papers presented at this 2nd URSI AT-RASC will be submitted for posting to IEEE Xplore. In addition, there will be special programs for young scientists, a student paper competition and programs for accompanying persons.

Technical Programme Committee

Chair:	Prof. P.L.E. Uslenghi
European Liaison :	Prof. O. Santolik, Prof. A. Sihvola, Prof. J. Wiart
AP-RASC Liaison :	Prof. K. Kobayashi
Publication Chair:	Dr. W.R. Stone
Organizing Committee:	
Chair:	Prof. P. Van Daele
Vice-Chair:	Prof. P. Lagasse

URSI Awards 2017

The URSI Board of Officers decided,upon the recommendations of the Awards Panel, to give the 2017 URSI awards to the following distinguished scientists

Balthasar van der Pol Gold Medal

The Balthasar van der Pol Gold Medal was awarded to **Prof. Lluis M. Mir** with the citation,

For leadership in Pulsed Electric Fields Applications in Biology and Medicine: fundamentals of cell electroporation in vitro and in vivo, and development of anti-tumour electro-chemotherapy, from inception to clinical use.

Appleton Prize

The Appleton Prize was awarded to **Prof. Yoshiharu Omura** with the citation,

For significant contributions to nonlinear wave-particle interaction theory, simulations of chorus and ion cyclotron emissions and the associated acceleration and precipitation of relativistic electrons in the radiation belts.

John Howard Dellinger Gold Medal

The John Howard Dellinger Gold Medal was awarded to **Prof. Sir John Pendry** with the citation,

For outstanding advances in electromagnetic and optical metamaterials, the design of the perfect lens and transformation optics.

Booker Gold Medal

The Booker Gold Medal was awarded to **Prof. Lotfollah Shafai** with the citation,

For outstanding contributions to antenna miniaturization by electromagnetics and numerical techniques, small satellite terminals, planar antennas, invention of virtual reflectors, low loss Engineered conductors and dielectric film components and antennas.

The URSI awards were presented to the awardees during the Opening Ceremony of the XXXIIth General Assembly and Scientific Symposium at Palais des congrès Montreal, Canada, on August 20, 2017.

Karl Rawer Award

The Rawer Gold Medal is a new URSI Award and honours the work and life of Professor Karl Rawer who was father of the International Reference Ionosphere (IRI), chairing the COSPAR/URSI Inter-Union IRI Working Group from 1968 to 1976 and the Vice-Chair and Chair of what is now Commission G between 1966 and 1972. The Medal is awarded for outstanding contributions in any discipline of direct interest to URSI.

The award is for career achievements of scientists who have worked for and within URSI and have fostered international cooperation across political borders and cultures.

The Rawer Gold Medal was awarded to **Dr. Dieter Bilitza** with the citation,

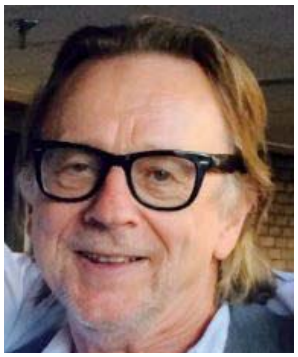

For leading the development of the empirical International Reference Ionosphere (IRI) climatology model and making it the international ISO standard, and for advancing the Real-Time Assimilative IRI model.

Issac Koga Gold Medal

The Issac Koga Gold Medal was awarded to **Assistant Prof. Li Yue** with the citation,

For contributions to the development of electromagnetic metamaterial circuits and antenna designs in mobile communication systems.

President's Award

The President's Award is a new URSI award, which is awarded at the discretion of the President of URSI on the occasion of the General Assembly and Scientific Symposium of URSI.

The Award honours outstanding contributions to the work and mission of URSI.

The President's Award was awarded to **Dr. W. Ross Stone** with the citation,

For his leadership as the Assistant Secretary General for Publications, his editorship of the Reviews of Radio Science and the Radio Science Bulletin, and for his pivotal roles in the organisation of many GASS.

Santimay Basu Prize

The Santimay Basu Prize was awarded to **Associate Prof. Jamesina Simpson** with the citation,

For advancing three-dimensional finite-difference time-domain (FDTD) solutions of electromagnetic wave propagation within the global Earth-ionosphere waveguide applied to space weather, remote-sensing, and very low-frequency propagation.

In Memoriam: Richard L. Dowden

Richard ("Dick") Dowden died in Dunedin, New Zealand, on December 15, 2016, after a short illness.

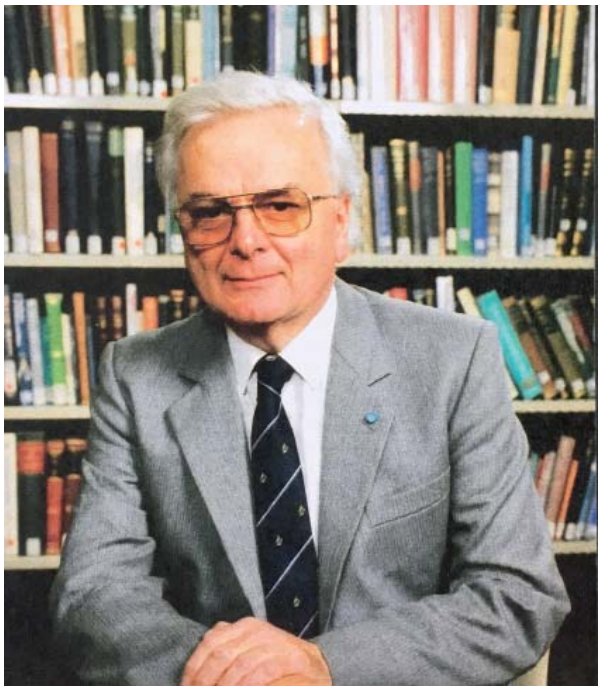

Dick originally graduated from the University of Sydney School of Physics. He spent a few months with the Radiophysics Division of CSIRO, then on the Sydney campus. He worked for a year in the sub-Antarctic on Macquarie Island in 1955-56, just before the International Geophysics Year, and then started graduate research while employed in Tasmania. In those eight years, he acquired an MSc, a PhD, and later a DSc. From 1957-1963, he served as a Physicist in the Ionospheric Prediction Service, based in Hobart, before working at the University of Tasmania as Lecturer and Senior Lecturer from 1963-1966. In 1966, he was appointed Professor at the University of Otago in New Zealand, retiring to become an Emeritus Professor in 1998.

Through his long career, he worked on multiple different scientific topics, spanning all the electromagnetic frequency range from ULF to HF. Dick made a number of fundamental contributions in several fields of planetary and geophysics, mostly using electromagnetic theory and techniques. He was involved in fundamental theory, the understanding and interpretation of electromagnetic signals, and the design and construction of hardware.

One of his earliest significant discoveries was the deduction of the polarity and longitude of the dipole axis of the magnetic field of Jupiter from 10 MHz radio bursts. This was in 1963, more than a 10 years before Pioneer 10 arrived at Jupiter. It relied upon state-of-the-art ground-based observations and detailed radio science knowledge. We believe that Dick was the first to interpret the radio emissions from Jupiter in a way to deduce physical parameters.

Another ground-breaking example was the first correct theory put forward to explain the generation of VLF emissions ("whistler-mode chorus") generated by radiation-belt electrons through anomalous Doppler-shifted resonance. He also provided an explanation of the dynamic spectral (frequency-time plane) shape of "hooks," "risers," etc., in terms of a phase bunch of electrons traveling along a geomagnetic field line. He verified that short-range echoes observed on HF ionospheric sounders located near the sea were caused by coherent backscatter from sea waves, which led him to suggest sea-scatter radar as an oceanographic tool. He undertook the first recordings of whistler-mode signals remote from the conjugate of a VLF transmitter, reception on the ground of non-ducted whistlers, VLF generation by modulation of the auroral electrojet by an ionospheric heater, identification of phase perturbations ("phase Trimpis") in association with whistlers, identification and interpretation of VLF perturbations caused by red sprites, and the first ground observation and video capture of red sprites outside the USA.

National research funding bodies are recent developments in New Zealand and Australia. In addition to being an experimentalist and theoretician, Dowden thus had to design and (usually) make his research equipment himself. For VLF dynamic spectra, he devised the "Dynagraph," which used a tape recorder with a device to give repeated (about 500 times) sampling of every portion of tape. Other inventions were the Jupiter polarimeter, which suppressed man-made transmissions near 10 MHz, and the RF heating beam-scanning system used at the Max-Planck-Institut fur Aeronomie's Ionospheric Heating facility at Tromsø in Norway (although designed and built in Dunedin, New Zealand). From the late eighties, the "OMSK" and later the "OmniPAL" VLF receivers, used for Trimpi studies, were also designed and built by Dowden and his students.

Prof. Dowden was an active member of the international scientific community. He was a member of the American Geophysical Union since 1966, a Fellow of the Institute of Physics (UK) from 1968, a Fellow of the Royal Society of New Zealand since 1983, and a Fellow of the American Geophysical Union from 2003. He served as

Vice President of the International Union of Radio Science (URSI) from 1987-1993. In addition, Dick was the Beverly Professor of Physics and Michaelis Medal recipient of the University of Otago, a former President of the New Zealand Institute of Physics, Commission Chair and Editor-in-Chief of the URSI *Radioscientist*, Member of the International Astronautical Academy, Sidey Medal recipient of the Royal Society of New Zealand, Australian Antarctic Division Medal recipient, Member Otago Polytechnic Council, Member Otago Museum Trust Board, and Founding Director of Low Frequency Electromagnetic Research Ltd.

Richard Dowden was one of the foremost geophysicists in the Oceania region. As such, he was strongly involved in the organization of international meetings held inside this region. He served as the regional editor of the *Journal of Atmospheric and Solar Terrestrial Physics* (1990-1998). After retiring from the University of Otago in New Zealand in 1998, he remained scientifically active for more than a decade. In that period, he developed the idea behind the "TOGA technique," which is at the heart of the global real-time World Wide Lightning Location Network (WWLLN).

As an academic for many years, Dick was an active teacher, lecturing students in all levels of undergraduate and graduate courses. He also supervised many postgraduate students, including both of the authors of this memoriam, who remember his innovative ideas, his boundless enthusiasm, and his inspiring encouragement. Since his death, the Otago University Physics Department has been contacted by former students who remember him as a very enthusiastic lecturer.

His funeral was held in Dunedin on Saturday, December 17, 2016. Later that day, a memorial service occurred at the Staff Club of the University of Otago. Dick is survived by his wife, Eleanor, their eight children, and 11 grandchildren.

Craig J. Rodger
Professor and Head of the Physics Department,
University of Otago
E-mail: craig.rodger@otago.ac.nz

Neil R. Thomson
Associate Professor of Physics, University of Otago,
President of the NZ URSI Member Committee
E-mail: n_thomson@physics.otago.ac.nz

14th International Workshop on Finite Elements for Microwave Engineering
FEM2018

The International Workshop on Finite Elements for Microwave Engineering is a highly-focused biannual event. It provides an ideal meeting place for researchers and practitioners active in the theory and application of the Finite-Element Method in RF and microwave engineering.

September 10-14, 2018 Cartagena De Indias, Colombia
Jointly held with 20th ICEAA

Jointly organized by

the Colorado State University and the University of Florence.

Scope Topics will include, but are not limited to: • Advanced FEM Techniques • Optimization Techniques, Model Order Reduction • Multigrid and Domain Decomposition Methods • Discontinuous Galerkin Methods • FEM for Multiphysics Problems • FEM for Metamaterials and Nanophotonics • Time Domain FEM • Adaptive methods • Hybrid Methods • FEM Modeling and Applications • CAD / Meshing Advances and Tools • Parallel Computation on Multi- and Many-Core Computers • Adaptive methods • Integral Equation Methods • Hybrid Methods.

Publication Workshop abstracts will appear on IEEE Xplore. Selected workshop contributions will be published in a Special Issue of journal Electromagnetics.

General Chairs

Branislav Notaros, Colorado State University (USA)
Stefano Selleri, University of Florence (IT)

Scientific Committee

A. Boag, Tel Aviv University, (IL); • A. C. Cangellaris, University of Illinois Urbana-Champaign (USA); • D. B. Davidson, University of Stellenbosch, (ZA); • R. Dyczij-Edlinger, Universität des Saarlandes (DE); • T. Eibert, Technische Universität München (DE); • G. Ghione, Politecnico di Torino, (IT); • R. D. Graglia, Politecnico di Torino, (IT); • J. Jin, University of Illinois, Urbana-Champaign (USA); • L. Kempel, Michigan State University (USA); • J.-F. Lee, Ohio State University (USA); • R. Lee, Ohio State University (USA); • Z. Nie, University of Electronic Science and Technology of China (CN); • B. M. Notaros, Colorado State University (USA); • G. Pelosi, University of Florence (IT); • A. F. Peterson, Georgia Institute of Technology (USA); • M. Salazar-Palma, Universidad Carlos III de Madrid (ES); • C.J. Reddy, EMSS (USA); • S. Selleri, University of Florence (IT); • B. Shanker, Michigan State University (USA) • A. Toscano, University of Roma Tre (IT); • J. L. Volakis, Ohio State University (USA); • M. N. Vouvakis, University of Massachusetts (USA); • J. P. Webb, McGill University (CA); • A. Yilmaz, University of Texas at Austin (USA); • J. Zapata, Universidad Politécnica de Madrid (ES).

Young Researcher Award Starting with 14th edition a solid gold "Fiorino" coin will be awarded by the Department of Information Engineering of the University of Florence to the Best Paper by a Young Researcher.

Important Dates
Abstract submission: March 9, 2018
Notification of acceptance: April 9, 2018
Registration: June 8, 2018

notaros@colostate.edu
stefano.selleri@unifi.it

www.FEM2018.unifi.it

Colorado State University

IEEE

UNIVERSITÀ DEGLI STUDI FIRENZE
DINFO DIPARTIMENTO DI INGEGNERIA DELL'INFORMAZIONE

Giuseppe Pelosi
Department of Information Engineering
University of Florence
Via di S. Marta, 3, 50139 Florence, Italy
E-mail: giuseppe.pelosi@unifi.it

Foreword from the Associate Editor

EuCAP 2017, the European Conference on Antennas and Propagation, was held in Paris March 19-24, 2017 (http://www.eucap.org/). Although the conference was of course focused on recent advances in antennas and propagation, it did not overlook its past developments. In particular, there was a session on "A Century After Tesla: How Far Have We Come With Wireless Power Transfer." This explicitly referred to the history of wireless and, most importantly, a page on the Web site was dedicated to "A Parisian history of antennas and propagation." There, the achievements of Claude Chappe [December 25, 1763, Brûlon, France – January 23, 1805, Paris, France] were briefly outlined (Figure 1).

Chappe indeed managed to set up the first true telecommunications network, before the advent of the electrical telegraph, by devising and building chains of optical signaling towers. Since the Web page on the EuCAP Web site is brief and yet the topic is interesting, I asked Stefano Selleri (University of Florence), who has already published some studies on Chappe in an Italian book (F. Angotti and G. Pelosi (eds.), *Antonio Meucci e la città di Firenze – tra scienza, tecnica e ingegneria* [Antonio Meucci and the City of Florence – Science, Technique and Engineering], Firenze University Press, Florence, Italy, 2009) to write a short contribution for the readers of the *Radio Science Bulletin*.

Figure 1 – The page on "A Parisian history of antennas and propagation," on EuCAP 2017 site (http://www.eucap.org/paris-1/parisian-history)

Claude Chappe and the First Telecommunication Network (Without Electricity)

Stefano Selleri

Department of Information Engineering
University of Florence
Via di S. Marta,3, I-50139, Florence, Italy
E-mail: stefano.selleri@unifi.it

Abstract

This paper briefly reviews the essential stages of the telecommunication networks that have developed, mainly at the European level, before the discovery of electricity and the invention of the electric telegraph. In particular, it focuses on the most widespread of these, the only one that really deserves the name of "telecommunication network," the one implemented by Claude Chappe in France between the late 1700s and early 1800s.

1. Introduction

Nowadays, we are all able to instantly communicate with almost every other human being on the planet, thanks to the pervasive fixed and mobile telecommunication networks. This possibility, which now seems completely natural, was born with the creation of telegraphy by Carl Friedrich Gauss, Wilhelm Eduard Weber, William Fothergill Cooke, Charles Wheatstone, David Alter, and the ultimate commercial success of Samuel Morse's telegraph system (1837) [1]. Electric-based telecommunications rapidly flourished with the subsequent inventions of the telephone by Antonio Meucci in 1854 [2, 3], followed by Alexander Graham Bell's patents in 1876 and 1877 [4, 5], and, of the radio by Heinrich Rudolf Hertz in 1888 and Guglielmo Marconi in 1895 [6, 7].

Even if all these methods of communications are inextricably linked to electricity and electromagnetism, this does not mean that telecommunications were born with them. The need to communicate with people far away has characterized all civilizations and throughout history. Each sufficiently evolved centralized state tried to set up its own communication network. However, these networks were, with rare exceptions, postal networks, with the exchange of written messages at the top speed technologically available: pigeons and horses.

True telecommunications are instead something where *information*, rather than a physical, material object, is delivered. The earliest systems of true telecommunications were very rough. In the Persian Empire, the horse-change post stations also had a signaling beacon associated with them. This allowed the much faster sending of elementary messages (yes/no or on/off: a bit, in modern terms) by lighting the beacons in the chain. This beacon-based system remained for a long time the only form of telecommunication. Its usage was also testified to by bas-reliefs on Trajan's Column in Rome (113 A.D.), which shows the use of towers with fires on mobile poles. Polybius also described some more-complex systems based on multiple torches and synchronized clepsydrae [water clocks], but there is no evidence they were ever used in practice [8]. Much later, in the Renaissance, letter-based coding was introduced, conveyed via light flashes [9] or on a few reconfigurable symbols [10]. Regardless, these systems were somewhat awkward and never got through.

Figure 1. Claude Chappe [December 25, 1763, Brûlon, France – January 23, 1805, Paris, France] (from [11])

2. The Chappe System

The man who actually linked his name to the first modern telecommunication network is Claude Chappe (Figure 1). Chappe, born on December 25, 1763, was the grandson of a Baron. He was supposed to become a clergyman, but at the outcome of the French revolution (1789-1799), he switched to the career of inventor.

Toward the end of 1790, he devised a system based on synchronized clocks (Figure 2), similar to one of the many theoretically enunciated by Polybius. Transmitting and receiving clocks had a hand and numbers on their quadrants, and the hands were to be kept synchronized. When the hand at the transmitting side was on the number to be transmitted, a sound signal was issued. The same number was of course indicated by the synchronized clock on the receiving station, and the sound signal allowed people on the receiving side to take note of it. Figure 3 shows the description, written by Claude Chappe's brother, Ignace [11].

During an official demonstration on March 2, 1791, Chappe used a painted wooden sign, white on one side and black on the other, in place of sound signals (Figure 2 shows this panel). This allowed a distance of over 10 miles between the two stations.

Claude Chappe called this first device "tachygraphe" (ancient Greek: fast writer), and decided to propose it to the French Government for nation-wide employment. Chappe also very early changed the name of his invention from tachygraphe to télégraphe (ancient Greek: remote writer).

The system was not substantially different from one described by Polybius. It had his weak point in the need to have a series of perfectly synchronized clocks. Chappe himself was not too pleased with the pendulum system. After some other experimental communications, he designed a new transmitter that had a rectangular wooden structure with five sliding panels that could be shown individually or obscured by pulleys. The five panels gave birth to a binary code with 32 possible combinations, more than three times the symbols used in the previous system.

Figure 2. An engraving, based on suppositions and probably unauthentic, dating back to the XIX century, of the first telegraph devised by Claude Chappe (from [11]).

ses frères. La première correspondance télégraphique qu'ils eurent ensemble fut établie avec deux pendules à secondes, parfaitement en harmonie entre elles; le cadran étoit divisé en dix parties, dont chacune désignoit un chiffre de la numération ordinaire. Lorsque l'aiguille des secondes de l'un des cadrans passoit sur le chiffre qu'on vouloit indiquer, on faisoit entendre un son qui annonçoit au

8 *

124 HISTOIRE

poste correspondant que le chiffre sur lequel se trouvoit l'aiguille, au moment où le son étoit entendu, étoit significatif, et en appliquant successivement les chiffres aux mots d'un vocabulaire, on pouvoit rendre toutes les idées.

Figure 3. The text describing the first telegraph by Claude Chappe, written by his brother Ignace (from [12, pp. 123-124]). English translation: "The first telegraph communication which they (*the Chappe brothers*) performed together was established by two pendulum clocks, kept in perfect sync. The dials of the watches were divided into ten areas, each bearing a cardinal number. When the seconds hand went to the number you wish to transmit a sound was produced, that announced the recipient that the number that was indicated by the hand of his watch, at the instant in which the sound was heard, was significant. Compiling an appropriate dictionary associating numbers and words so as to convey every thought."

Nevertheless, the panels were not satisfactory for Chappe, who realized that elongated objects would be more visible from a distance with respect to the panels. The solution at which he arrived at the end was that of a vertical axis, at the top of which a mobile bar was hinged. To both ends of this bar were hinged two shorter bars, they also being mobile. Reciprocal rotations were controlled by a series of pulleys and cranks (Figure 4). The description of the development, also from a political point of view, we still find in the book by Ignace Chappe (Figure 5).

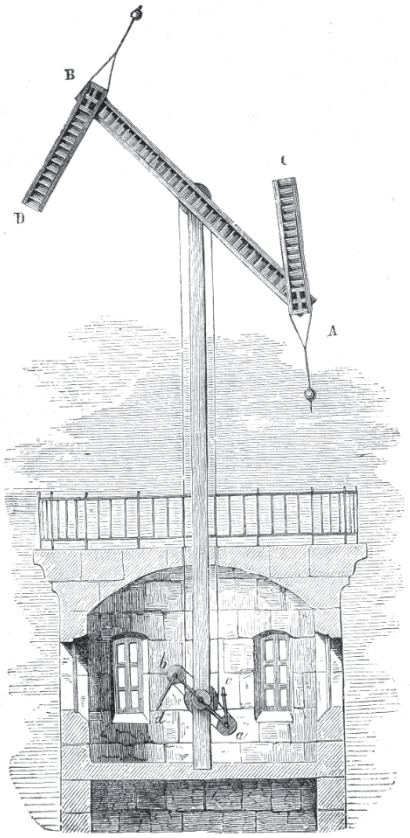

Figure 4. An engraving based on the actual design of the device devised by Claude Chappe for his telecommunication network (from [11]).

Claude Chappe established that the rotations of the three movable bars was to be made in 45° steps. This defined four positions for the main beam, and eight for each of the secondary beams (Figures 4 and 6), for a total of 256 different symbols. He called these devices "sémaphores" (ancient Greek: sign bearer).

Meanwhile, France was going through that stage of the revolution that eventually brought the downfall of the monarchy. Chappe's studies on the "sémaphores" system were well regarded by the Assembly but opposed by the people. In a riot, they destroyed the experimental installations in the park of Menil-Montant in 1792, believing them to be some odd monarchical device. Chappe thought it well to put his own equipment under the protection of the Assembly (September 11, 1972).

The Legislative Assembly was replaced on September 21, 1792, by the National Convention. Ignace Chappe, a member of the Assembly, was not confirmed to the Convention. This led to a stoppage of the telegraph development until April 1, 1793, when the Convention decided to fund the experiments. On July 12, 1793, the demonstration of the telegraph "sémaphores" in the presence of members of the Commission appointed by the Convention finally took place.

3. The Network

After the demonstration, things began to accelerate. On July 26, 1973, the Convention approved the establishment of the "Telegraphs of the French State." On August 4, 1793, the Convention passed a loan of 58,400 francs for the construction of the first line: fifteen stations, from Paris to Lille. On September 24, 1793, Chappe had *carte blanche* to use any tower or existing house, cutting down all interfering trees, to hire staff, and to roll out a regulation for the "French Telegraph." Chappe was also appointed "Telegraph Engineer," and was given a monthly salary of 600 francs for his services. In this context, Chappe

126 HISTOIRE

Leurs recherches ne discontinuèrent pas, et ils acquirent la certitude, quelque temps après, que les corps allongés étoient plus visibles que les trappes adoptées auparavant. La forme du télégraphe fut alors définitivement arrêtée, et la découverte fut présentée à l'Assemblée législative (dans la séance du jeudi soir, le 22 mars 1792); elle en renvoya l'examen à son comité d'instruction publique. Mais les événements qui survinrent quelque temps après, l'empêchèrent de s'en occuper, et le premier rapport qui fut fait sur cet objet n'eut lieu que le 4 avril 1793: ce rapport autorisoit Claude Chappe à faire construire trois postes d'essai; MM. Chappe les établirent à Ménil-Montant, Écouen et Saint-Martin-du-Tertre, distant de sept lieues de Paris. Ce com-

Figure 5. The text describing the development of the telegraph and its political issues, written by Ignace Chappe (from [12, pp. 126]). English translation: "Their research (*of the Chappe brothers*) has not stopped, and reached the consciousness, some time later, that the elongated bodies are more visible than the plates previously used. The telegraph form was then finalized, and the invention was presented to the Legislative Assembly (in the Thursday night session, March 22, 1792). The Assembly referred the matter to its Committee of Education. Subsequent events prevented the Committee from dealing with it and the first report was not written down before April 4, 1793. In this report Claude Chappe was authorized to build three test stations; the Chappes positioned them at Menil-Montant, at Écouen and at Saint-Martin-du-Tertre, seven leagues from Paris."

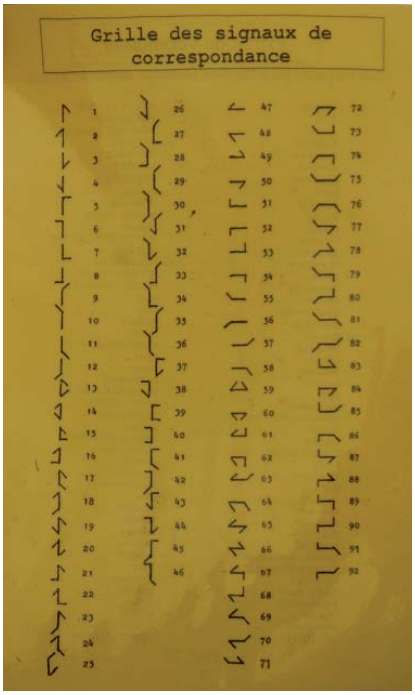

Figure 6. The final 92 beam positions of the Chappe code [Anne Goldenberg, Creative Commons License].

published the first manual containing signal coding for transmission on his telegraph lines. The manual contained 8464 different messages that could be transmitted, obtained by pairing individual symbols.

These were much less than the 256 × 256 possible pairs. However, Chappe had noticed difficulties during transmissions due to erroneous recognition of those signals corresponding to the perfect alignment, inward or outward,

Figure 7a. The French optical telecommunication network at its maximum extent, in France and Belgium [14].

Figure 7b. The French optical telecommunication network at its maximum extent in Italy [14].

of the two shortest beams. He hence had reduced the original 256 possible configurations to 98 the first time, and later to only 92 (Figure 6). Considering the signals in pairs, this led to 8464 possibilities.

On April 30, 1794, after only one year from the resolution of the Convention, the Paris-Lille line was completed, and tests were started. There were 18 stations, including two in Paris and one in Lille. On July 16, 1794, the line was officially opened. The towers were built at a distance of 10 km to 15 km from each other, and formed a line that extended along 190 km. At the beginning, the transmission occurred at the speed of a signal per minute.

Since then, growth was unstoppable (Figure 7, [12]):

1794	from Paris to Lille	190 km
1794	from Paris to Landau and Strasbourg	128 km
1798	from Lille to Dunkerque	64 km
1798	from Paris to Brest	210 km
1799	from Strasbourg to Hunigue	96 km
1803	from Lille to Brussels	96 km
1803	from Lille to Boulogne	80 km
1804	from Paris to Dijon and Lyon	370 km
1804	from Lyon to Turin	250 km
1804	from Turin to Milan	100 km
1805	from Lyon to Toulon	305 km

As one can note from the list, the development was given new impetus when Napoleon proclaimed himself emperor in 1804. He understood the enormous potential of the telegraph network.

Claude Chappe was not without his critics. Many attacked him claiming to have invented the telegraph before him, including Abraham-Louis Breguet, the renowned clockmaker who had collaborated with the construction of the Chappe "sémaphores" prototype. Other claims arrived from Agustin de Betancourt and other people who had unsuccessfully offered alternative schemes. In the last years of his life, Chappe particularly suffered from these criticisms, and fell into depression and committed suicide in 1805 [12].

4. The End of Optical Systems

For most of the nineteenth century, telecommunication networks based on optical signaling continued to expand, even after the death of Claude Chappe (1905) and the fall of Napoleon (1915). Only in France:

1809	Brussels to Antwerp	40 km
1809	Antwerp to Vlissingen	72 km
1810	Antwerp to Amsterdam	128 km
1810	Milan to Venice	241 km
1813	Metz to Mainz	225 km
1816	Lille to Calais	80 km
1821	Lyon to Toulon	305 km
1823	Paris to Bordeaux	507 km
1823	Bordeaux to Bayonne	160 km
1823	Avranches to Nantes	157 km
1825	Paris to Lille (expanded)	190 km
1828	Avignon to Perpignan	209 km
1833	Avranches to Cherbourg	108 km
1834	Bordeaux to Toulouse	205 km
1834	Toulouse to Narbonne	127 km
1834	Narbonne to Montpellier	84 km
1834	Montpellier to Avignon	80 km
1840	Boulogne to Calais	32 km
1840	Narbonne to Perpignan	54 km
1840	Calais to Boulogne	40 km
1840	Dijon to Besancon	72 km
1844	Bordeaux to Agen (replaced)	145 km
1845	Boulogne to Eu	100 km
1846	Bayonne to Behobie	30 km

The possibility of transmitting signals by means of electricity was yet in the air, starting with Gauss and Weber (1933). Morse devised in 1832, experienced in 1835, and protected with a caveat on September 28, 1837, a single-wire technique significantly cheaper than the other technique proposed. This technique came to fruition in 1844 to finally be tested over large distances and fully patented in 1849 [15].

With its optical systems, Europe resisted the introduction of the electrical telegraph, which indeed spread quickly in United States. The country that resisted the introduction of the electric telegraph most was, understandably, France. In 1864, there were still 24 optical stations, flanked by 174 electric stations. The optical stations were used where it was difficult to lay electric cables. Only in 1881 were the last three stations for optical signaling dismantled.

5. Conclusions

The most significant telecommunication network ever realized before the advent of the electrical telegraph was the network initially set up by Claude Chappe. At its apex, it encompassed several thousand kilometers. It connected the main cities of France and northern Italy, and was mimicked by similar systems in England, Germany, and Sweden. The development of the electric telegraph in the thirties of the nineteenth century marked the end of the short service life of the optical telegraph.

6. Bibliography

1. J. J. Fahie, *A History of Electric Telegraphy to the Year 1837*, London, E. & F. N. Spon, 1884.

2. B. Catania, *Antonio Meucci – L'Inventore e il suo Tempo - Da Firenze a L'Avana, Vol. 1*, [Antonio Meucci, the

Inventor and His Time – From Florence to Havana], Roma: Seat - Divisione STET, Editoria per la Comunicazione, 1994.

3. B. Catania , *Antonio Meucci – L'Inventore e il suo Tempo - New York 1850-1871, Vol. 2* [Antonio Meucci, the Inventor and His Time – New York 1850-1871, Volume 2], Torino, Seat - Divisione STET, 1996.

4. A. G. Bell, US Patent 174465, "Improvement in Telegraphy," February 14, 1876.

5. A. G. Bell, US Patent 186787, "Improvement in Electric Telegraphy," January 30, 1877.

6. G. S. Smith, "An Analysis of Hertz's Experimentum Crucis on Electromagnetic Waves," *IEEE Antennas and Propagation Magazine*, **58**, 5, October 2016, pp. 96-108.

7. G. Pelosi, S. Selleri, and B. Valotti, "From Poldhu to the Italian Station of Coltano: Marconi and the First Years of Transcontinental Wireless," *IEEE Antennas and Propagation Magazine*, **46**, 3, June 2004, pp. 47-54.

8. Polibio, *Histories, Book X, Cap. 44,45 (ca. 220-146 A.C.*), London, Macmillan, Trad. Ing. di Evelyn S. Shuckburgh,1889.

9. F. Kessler, *Unterschiedliche bisshero mehrern Theils Secreta oder Verborgene*, *Geheime Kunste* [Various and Up to Now Hidden, Secret Arts], Oppenheim (D), 1616.

10. R. Hooke, "Dr. Hook's Discourse to the Royal Society, May 21, 1684 Shewing a Way How to Communicate One's Mind at Great Distances," in *Philosophical Experiments and Observations of the Late Eminent Dr. Robert Hooke*, William Derham (ed.), London, W. and T. Innys, 1726, pp. 142-150.

11. L. Figuier, *L'Elettricità e le sue applicazioni* [Electricity and its Applications], Milan (I), F.lli Treves, 1884.

12. I. U. J. Chappe, *Histoire de la télégraphie [History of the Telegraph],* Paris, L'Imprimerie de Crapelet, 1824.

13. G. J. Holzmann and B. Pehrson, *The Early History of Data Networks*, Hoboken, NJ, John Wiley & Sons, 2003.

14. Multiple Authors, *La Télégraphie Chappe* [Chappe Telegraph], Fédération Nationale des Associations de Personnel des Postes et Télécommunications pour la Recherche Historique (FNARH) (ed.), Nancy, France, Éditions de l'Est, 1988.

15. S. F. B. Morse, *Improvement in Electric Telegraphs*, US Patent 6420, May 1, 1849.

Book Review

George Trichopoulos
Electrical, Computer & Energy Engineering ISTB4 555D
Arizona State University
781 E Terrace Road, Tempe, AZ, 85287 USA
Tel: +1 614 364 2090
E-mail: gtrichop@asu.edu

The Rise of Radio Astronomy in the Netherlands: The People and the Politics by Astrid Elbers, Springer International Publishing, 2017, 240 pages; ISBN 978-3-319-49078-6 (hardcover) €118.00; ISBN 978-3-319-49079-3 (eBook) €92.00.

It was 85 years ago that Jansky serendipitously detected "cosmic static," noise originating in the direction of the center of our Milky Way galaxy. Eighty years ago, Reber started to systematically observe the sky at radio wavelengths with his home-built paraboloidal reflector of 10 m diameter. Today, radio astronomy plays a major role in astronomical research. Astronomy has actually become an integrated field of research, where progress is achieved by combining data obtained by telescopes operating over the entire electromagnetic spectrum, from gamma rays to long radio waves. Astronomy has become "big science," both in terms of the size and cost of telescopes, and data handling.

Concurrently, an interest in the historical development of their science has grown among astronomers. This is exemplified by the Commission History of Astronomy in the International Astronomical Union, and by the *Journal of Astronomical History and Heritage*, established in 1998. The history of early radio astronomy up to 1950 was masterfully presented by Woodruff Sullivan in his 2009 book, "Cosmic Noise," which was reviewed in the *Radio Science Bulletin* No. 338 (September 2011).

The book under review here concentrates on the developments in just one small country, the Netherlands. It is limited to the period up to 1970, at which time the Westerbork Synthesis Radio Telescope commenced its astronomical observing program. The author is a historian, with special interests in the history and philosophy of science. The book is an outgrowth of the doctoral dissertation that she prepared while being employed by the Observatory of the University of Leiden. As the subtitle of the book indicates, the "people and politics" are the main protagonists, rather than the science and technology. We only find slight indications of the astronomical problems to be attacked and the technology developed for the telescopes. However, the organizational and political aspects of the rise of Dutch radio astronomy are dealt with in great and vivid detail, along with lively descriptions of the major personalities involved in the process. Extensive quotations from correspondence and meetings enliven the story. Many of these reappear as a footnote in the original Dutch language, a feature that will be appreciated by Dutch-speaking readers.

The story of radio astronomy in the Netherlands begins with Prof. Jan Oort reading Grote Reber's article, "Cosmic Static," in the *Astrophysical Journal* in December 1940. The journal had found its way to the Observatory in Leiden, despite the German occupation. Oort immediately saw a great advantage for radio astronomy. Not only could one observe all day, even in cloudy weather, but also the radio radiation would not be attenuated by the interstellar dust, as it is at optical wavelengths. This would allow a much deeper view of the Galaxy and its spatial structure. A spectral line in the radio regime would enable the study of the dynamical structure of the Galaxy much better than had been possible with optical observations. At Oort's instigation, a young astrophysicist, Henk van de Hulst, looked into the spectral-line aspect. In 1944 he presented his conclusion that the spin transition of atomic hydrogen emitted a photon at about 21 cm wavelength, and the abundance of hydrogen in space would render the detection of this line feasible.

From that moment, it was clear to Oort that the Netherlands would embark on the study of the Galaxy by means of radio observations. The war ended in May 1945, and before the end of the year, Oort had made contacts with industry (Philips Laboratory, PTT (postal service) and KNMI (weather service)) for help in the technical aspects. A proposal soon followed to the government for the construction of a radio telescope of some 20 m diameter.

Radio astronomy in Holland was initiated by astronomers who lacked technical expertise. In other countries (England, Australia, USA), radio astronomy emerged from the radar laboratories from engineers who did not know anything about astronomy. These different approaches and their consequences are well presented in Chapter 2.

In 1949, the Netherlands Foundation for Radio Astronomy (NFRA) was established. A "Würzburg Riese," a 7.5 m diameter radar antenna left behind by the Germans, was made available by the PTT. In the spring of 1951, the 21 cm spectral line of hydrogen was indeed detected, and radio astronomy became an important part of astronomical research in the Netherlands. Oort used this success for the proposal of a large parabolic antenna of 25 m diameter. The road to this instrument is the subject of Chapter 3. The power of Oort to achieve what he had in mind is well demonstrated, including his penchant to move well beyond the usual diplomatic customs of the Dutch government and its national research organization. It is interesting that in the proposal, meeting protocols, and correspondence, there is no mention of the simultaneously constructed, much larger Jodrell Bank telescope, and of the German 25 m antenna. At its dedication in April 1956, the Dwingeloo telescope was the largest fully steerable radio telescope in the world for about a year, when Jodrell Bank took over. It produced a wealth of data on the distribution of neutral hydrogen, and mapped the polarization of Galactic radiation. The significant modernization in the early seventies that extended the productive lifetime until the late nineties is not mentioned.

A well-written discussion of the role and status of engineers in the NFRA illuminates the big difference in character from the foreign groups. There, the engineers were the initiators; in Holland, they were the "servants," who were valued for their indispensable technical work, but remained "second class citizens." The author shortly describes the development of radio astronomy in other countries, in particular England and the USA. The relatively late ascent of radio astronomy in the USA is summarized and concluded with a mention of the NRAO 140-ft telescope, which came into operation only in 1965. However, the accompanying figure of this telescope shows the 100-m Green Bank Telescope of 2002!

Soon after the Dwingeloo telescope became fully operational, it became clear that other countries were planning significantly larger telescopes. The study of extragalactic radio sources became an important branch, which would require much better angular resolution. Prof. Oort did not long hesitate to propose a large telescope that would deliver a resolution of one arc minute. Although the policy in the Netherlands was still very much in favor of research, it was considered unlikely that the country would be able to meet the efforts of the larger countries, in particular the USA. Contact was therefore sought in 1958 with Belgium towards the realization of a joint radio-telescope project. The idea was to build a large "cross antenna," after an Australian example. The reaction from Belgium was positive, and the Benelux Cross Antenna Project (BCAP) was born. In Chapter 4, the author takes us on a tour along the different national and international (OECD) entities that were involved in the preparation for this plan. However, the large differences in science and technology policies between the two countries, along with the lukewarm interest of the Belgian astronomers, eventually led to the withdrawal of Belgium, effectively in 1963, and officially in 1966. This forced the Dutch to realign their plans to the reduced financial possibilities. The evolution of the BCAP Cross in 1957 to the final linear Westerbork Synthesis Radio Telescope (WSRT) in 1970 is the subject of Chapter 5. The original design was a cross configuration of cylindrical paraboloids to operate at 75 cm wavelength. A detailed design study indicated a cost that appeared prohibitive, and alternative solutions were sought. This took the form of a cross of some 400 parabolic dishes with a limited angular range. By 1961, the operational wavelength was changed to 21 cm, and the telescope was reduced to about 100 dishes in a cross configuration. This proposal still exceeded the financial limit. Fortunately, by this time, the concept of aperture synthesis had successfully been applied. It was extended to *Earth-rotation-synthesis* by using the rotation of the Earth to provide two-dimensional coverage of the sky with a linear array. An east-west array of about 30 dishes with full-sky coverage was thus proposed. The author offers an extensive account of the somewhat murky issue of the origin and originators of the aperture-synthesis concept, which reads like a criminal story. Under financial pressure, the final project was reduced to 10 fixed 25 m diameter antennas on an east-west baseline of 1300 m length, and two antennas on a 300 m long rail track. It was frozen in late 1963, and realized in the national forest near Westerbork, 25 km from Dwingeloo. It is known as the WSRT, and it commenced regular observations in 1970.

The chapter closes with a fascinating account of the growing tension between Prof. Oort and ZWO, the funding agency of the telescope, and the growing resistance – also among the staff of the observatories including the NFRA – against the patriarchal style of leadership. The author states that ultimately the WSRT, as with the Dwingeloo telescope, would not be used for the original science program for which it was intended, at least not entirely. I believe most astronomers would object to this statement. Both telescopes contributed significantly to radio astronomy, also in the areas that had been highlighted in the original proposals. The two beautiful pictures of the radio sources on page 220, not obtained with the WSRT, could better have been replaced by some of the fascinating WSRT observations of the spiral structure in nearby galaxies, or of the giant radio lobes of distant active radio galaxies.

This is a specialized book, restricted to the political and personality aspects of the rise of radio astronomy in the Netherlands. It is a book for what the Germans call "Kenner und Liebhaber" (knowledgeable devotees). To

this reviewer, the total lack of astronomical discussion, and the neglect of the technical difficulties and solutions in the areas of antenna construction and receiver electronics, is a missed chance to show the truly magnificent achievements of the Dutch under the powerful and visionary guidance of Jan Oort in developing radio astronomy in their country. Perhaps someone will fill this gap in due time. Finally, as also is the case with Sullivan's history, mentioned above, both books stop at the moment where it really becomes scientifically interesting. Still, all people who have some personal experience with the story told here will enjoy it, and all readers will experience an intimate and fascinating look at the people and the politics during the rise of radio astronomy in the Netherlands.

Jacob W. M. Baars
Guest scientist
Max-Planck-Institut für Radioastronomie
E-mail: jacobbaars@arcor.de

Et Cetera

Tayfun Akgül
Istanbul Technical University
Dept. of Electronics and Communications Engineering
Telecommunications Division
80626 Maslak Istanbul, Turkey
Tel: +90 212 285 3605; Fax: +90 212 285 3565
E-mail: tayfunakgul@itu.edu.tr.

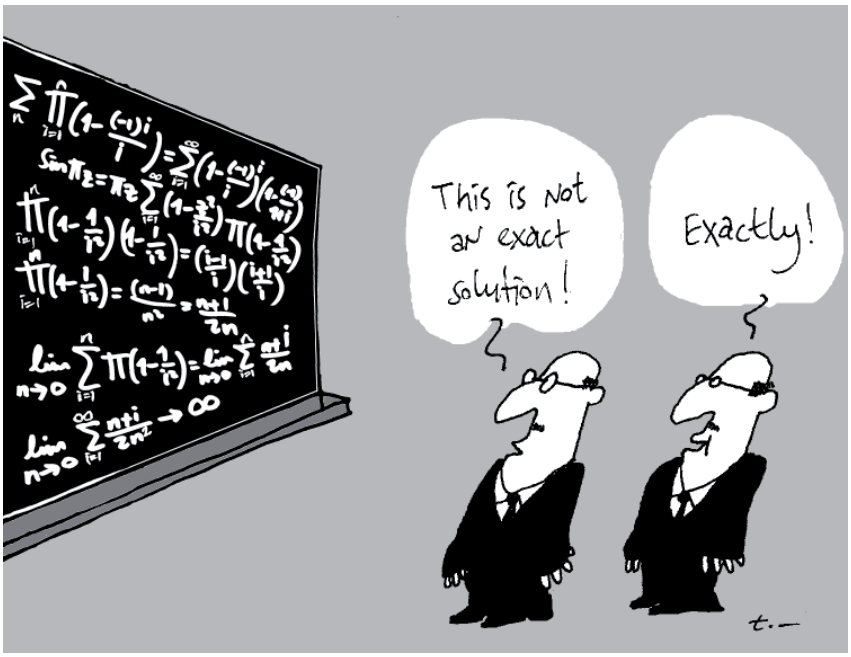

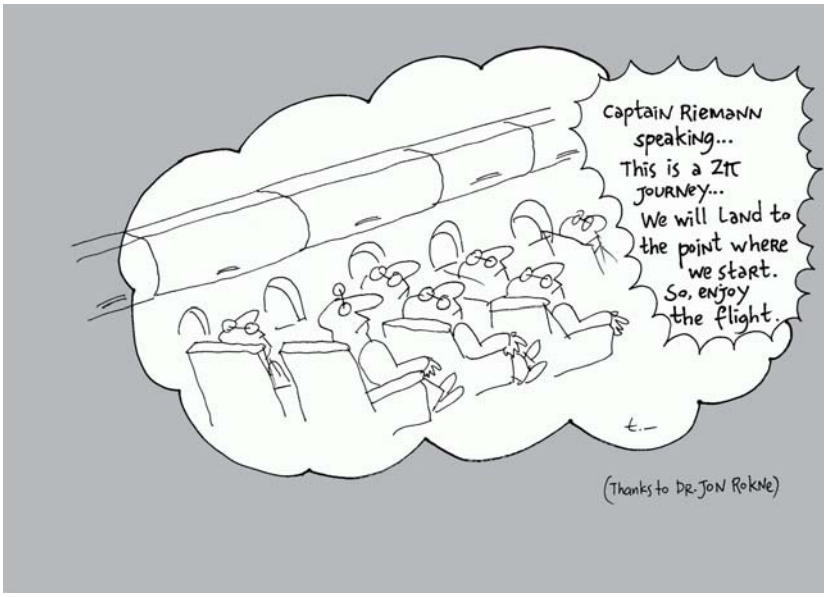

Randy L. Haupt
Colorado School of Mines
Brown Building 249
1510 Illinois Street, Golden, CO 80401 USA
Tel: +1 (303) 273 3721
E-mail: rhaupt@mines.edu

Amy J. Shockley
E-mail: aj4317@gmail.com

Ethical Directions

Randy L. Haupt and Amy J. Shockley

When I first started driving, getting from one place to another was completely different than it is today. I remember driving from Massachusetts with my wife to attend a friend's wedding in Pennsylvania in 1980. We used a map to get us from Massachusetts to the town in Pennsylvania; we then had written instructions to get from the town to the church where the wedding was to take place. Everything went fine until we did not find the church. The church was in the midst of many small farms, surrounded by a maze of back-country roads. We failed to find it before backtracking and trying again without success. We next resorted to stopping at businesses to ask for help. That approach failed as well, because there were no businesses close to the church. At that point, we were searching randomly, and were about to give up when we found our destination. The bride and groom were leaving the church amidst a shower of rice. Had I known about genetic algorithms at the time, I'm sure we would have found the optimum solution much sooner. It was obvious that we needed a better form of navigation.

In 1980, the American Automobile Association (AAA) provided TripTiks, which included maps and detailed instructions for driving from one place to another. You had to go to their office and wait in line before being rewarded with detailed maps and directions that were produced in real time. I thought it was a great advancement when you were able to request the directions via phone, and have them mailed to you a week or so later. Technology took a giant leap when AAA, MapQuest, etc., provided online maps that could be printed. I no longer had to wait, but instead was able to retrieve information in real time. I didn't think that it could get any better, until it did. We now use our smartphones, which not only provide us with near-instantaneous step-by-step directions, but also pinpoint gas stations, restaurants, and traffic jams. My first exposure to this new technology was driving to dinner in a car at the AP-S Symposium in Albuquerque, when one of the passengers had a new smartphone. I know that I am supposed to be a highly technical person – but I thought it was magic! Surely, we have reached the pinnacle of finding our way.

Not quite. A few years ago I was using my smartphone to navigate from the Boston airport, where I had rented a car, to my final destination. I pulled out of the parking lot, and was looking forward to jousting with the nice Boston drivers, when Google Girl lost her way. She started giving me very confusing directions, due to several elevated roads blocking the GPS signal. I ended up back at the terminal a few times before I resorted to my old-fashioned intuitive direction-finding skills.

Most of us like to have someone tell us where to go or what to do, so that we don't have to stress about making mistakes. However, directions are not always clear, even in our high-tech world. I was in the backseat of a car driven by a husband, with his wife in the passenger seat. They had a unique approach to car navigation that I had never before encountered. The husband used his Android phone to pull up directions, while his wife used her iPhone for navigation at the same time. When there was a discrepancy in directions,

they both believed that their respective phone was correct. On top of this, they also had a navigation system in their car: I could only assume that this was for settling any disputes between the Android device and the iPhone. We were driving from Dayton, Ohio, to Columbus, Ohio, while listening to three high-tech devices confidently spout out their assessment of which way to go. Front-seat arguments started whenever the devices had different opinions. I was amused with this advanced human-machine navigation system, which came to a climactic peak when we arrived at a particular intersection in Columbus. Android: "Turn left." iPhone: "Turn right." Car navigation system: "Go straight." There was a brief silence before pandemonium erupted. I couldn't stop laughing, and still chuckle today when I think about it. It turns out that all three devices found correct yet different ways to get to the same destination. This husband-wife intelligent-navigation system managed to drive from the east coast of the US to the west coast and back a few months later. I am happy to report that they are alive and well.

Your ethics are your driving directions through life. If you end up in the wrong place, you can use your guiding principles to get you out via the best route. If you miss some important events or relationships due to ethical lapses, other opportunities will arise as long as you recalibrate and abide by your ethical compass. It is easy to delegate your thinking and decisions in today's society. People and electronics will try to give you directions, and sometimes there may be multiple paths to the same goal, but ultimately, it is your decision. Let ethics be your guide.

Özgür Ergül
Department of Electrical and Electronics Engineering
Middle East Technical University
TR-06800, Ankara, Turkey
E-mail: ozgur.ergul@eee.metu.edu.tr

SOLBOX-06

Aşkın Altınoklu and Özgür Ergül

Department of Electrical and Electronics Engineering
Middle East Technical University
TR-06800, Ankara, Turkey
E-mail: altinokluaskin@gmail.com; ozergul@metu.edu.tr

1. Introduction

The topic of this issue is an optimization problem (SOLBOX-06), involving nanocubes at optical frequencies. This type of array arrangement (namely, a nanoarray) is useful for controlling and directing optical waves in numerous applications, such as optical links, sensing, and energy harvesting [1-6]. A particular aim in SOLBOX-06 is to maximize the scattering or radiation of a given array structure in desired directions. Despite the number of unknowns being relatively small, the main challenge is the size of the optimization space, which is grows exponentially with the number of nanocubes. In addition, the nanocubes are made of silver (Ag). They must therefore be modeled as penetrable objects with negative real permittivity, at optical frequencies. The sample solutions also included in this issue use genetic algorithms, combined with a solver based on surface integral equations, and the Multilevel Fast Multipole algorithm. Alternative solutions of the same problems with other solvers, possibly using different and more-efficient optimization tools (heuristic or gradient-based) and solution methods (e.g., volume integral equations, other types of acceleration algorithms, iterative solvers, and discretization techniques), are welcome. Please submit your solutions to ozergul@metu.edu.tr.

2. Problems

2.1 Problem SOLBOX-06 (by A. Altınoklu and Ö. Ergül)

A nanoarray involving a total of 30 identical Ag nanocubes that are linearly arranged is considered. The nanocubes have dimensions of 150 mm × 150 mm × 150 nm, and the center-to-center distance is fixed at 200 nm. Consequently, the full array, which is aligned in the x direction, is approximately 6 μm in length. A Hertzian dipole is located on one side of the array (the side with the smaller x value), at a distance of 150 nm from the center of the first nanocube. It is aligned in the z direction, with a unit dipole moment. The array and dipole are located in free space, and are investigated at 200 THz, i.e., when the wavelength is approximately 1.5 μm. At this frequency, the complex permittivity of Ag can be approximated as $-97+7.5\mathrm{i}$ (with negative real permittivity). With the given arrangement of the array and the location of the Hertzian dipole, the overall structure naturally produces large electromagnetic radiation in the x direction. On the other hand, it is desired to maximize the radiation in other selected directions (e.g., at $\phi = 60°$ and at $\phi = 300°$ due to symmetry in the following numerical examples) in the

far zone. Depending on the application, either the radiation of the overall structure, or secondary (scattered) fields due only to the excited nanocubes, can be optimized. The cost function can be selected as the amplitude of the electric-field intensity in the desired direction divided by the average field intensity on the investigated cut (*x*-*y* plane). In the optimizations, we are looking for which nanocubes should be extracted from the array. There are hence a total of 2^{30} possible cases, including the full array (keeping all nanocubes) and no array (extracting all nanocubes such that the Hertzian dipole radiates in empty space), which may not be tried one by one.

3. Solution to Problem SOLBOX-06

3.1 Solution Summary

Solver Type (e.g., noncommercial, commercial): Noncommercial research-based code developed at CEMMETU, Ankara, Turkey.

Solution core algorithm or method: Frequency-domain Multilevel Fast Multipole Algorithm (MLFMA).

Programming language or environment (if applicable): *MATLAB + MEX*

Computer properties and resources used:
2.5 GHz Intel Xeon E5-2680v3 processors, using six cores

Total time required to produce the results shown (categories: < 1 sec, < 10 sec, < 1 min, < 10 min, < 1 hour, < 10 hours, < 1 day, < 10 days, > 10 days):
< 10 hours (per optimization)

3.2 Short Description of the Numerical Solution

Problem SOLBOX-06 was solved by employing an efficient and integrated combination of genetic algorithms and an in-house implementation of the MLFMA in the frequency domain [7, 8]. The surfaces of the nanocubes were discretized with the Rao-Wilton-Glisson functions on triangles. The modified combined tangential formulation [9], which provides accurate and stable solutions for plasmonic objects, was used to formulate the problems. The number of unknowns for the full array was 2160. Genetic algorithms were employed using pools of 40 individuals, while each individual had a chromosome of length 30 bits to represent on/off (kept/extracted) nanocubes. Optimizations were carried out for 150 generations, leading to approximately

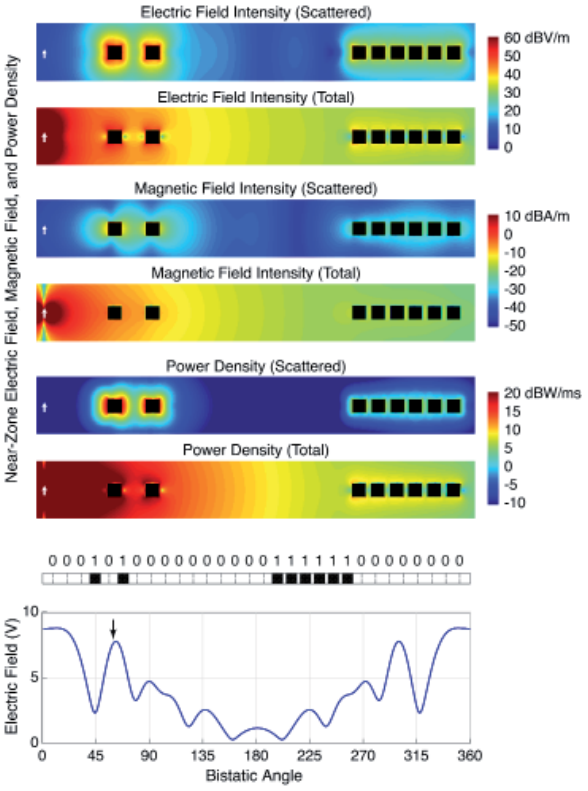

Figure 1. The optimization results when the electric field scattered from the nanoarray is maximized at $\phi = 60°$.

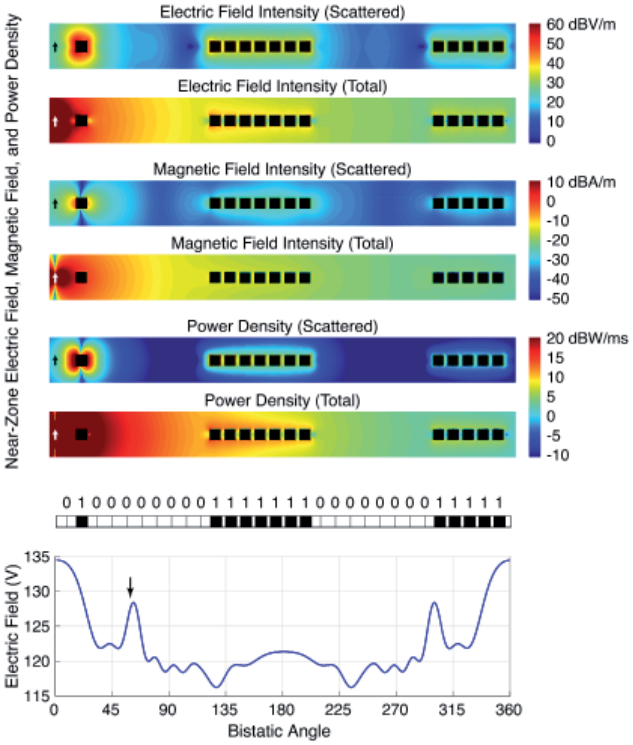

Figure 2. The optimization results when the electric field radiated from the overall structure (nanoarray and Hertzian dipole) is maximized at $\phi = 60°$.

6000 trials per optimization (identical and repeating individuals were not solved multiple times). In addition, each optimization was repeated for three times to check the stability. The cost function was selected as in the problem definition, i.e., the electric-field intensity in the optimization direction was normalized to the average electric-field intensity on the *x*-*y* plane. Each trial (individual) was solved as a full-wave computational problem using the MLFMA. Iterative solutions were accelerated via an inner-outer scheme (using GMRES and flexible GMRES), employing the MLFMA and its approximate forms (AMLFMA). The residual error for iterative convergence was set to 0.001. AMLFMA was also used for dynamic accuracy control to further accelerate optimizations [10]. In the case of the full MLFMA, all electromagnetic interactions were computed with a maximum 1% error, while some interactions were truncated without loss of accuracy [11]. In addition to far-zone results, near-zone electric-field intensity, magnetic-field intensity, and power-density values were computed to visualize the responses of the nanocubes.

3.3 Results

Figures 1 and 2 present the results of two kinds of optimizations, i.e., when the scattered electric field and the total radiation of the overall structure, respectively, were optimized. The optimization direction was selected as $\phi = 60°$ on the *x*-*y* plane, as in the problem definition. In both cases, we present the following:

- The scattered electric-field intensity (dBV/m) from the array in the near zone.
- The radiated electric-field intensity (dBV/m) from the overall structure (Hertzian dipole and array) in the near zone.
- The scattered magnetic-field intensity (dBA/m) from the array in the near zone.
- The radiated magnetic-field intensity (dBA/m) from the overall structure (Hertzian dipole and array) in the near zone.
- The scattered power density (dBW/ms) from the array in the near zone.
- The radiated power density (dBW/ms) from the overall structure (Hertzian dipole and array) in the near zone.
- The final structure of the optimized array (the best individual out of three optimization session). We note that the structure is also visible in the near-zone plots.
- The electric-field intensity (V) in the far zone.

As depicted in Figure 2, a successful optimization led to an array structure with two nanocubes on the left-hand side and six consecutive nanocubes on the right-hand side, while all other nanocubes were removed. The electric-field intensity in the far zone (scattered from the nanoarray) had large values at around $\phi = 0°$ (in the direction of the array), while the optimization led to similarly large values at around $\phi = 60°$, shown with an arrow. Due to the symmetry of the structure with respect to the *x* axis, the scattered electric field was symmetric with respect to 180°, so that maximization also occurred at $\phi = 300°$.

As shown in Figure 3, it was also possible to effectively maximize the total radiated field in the desired direction, $\phi = 60°$. We noted that the total radiation was dominated by the isotropic pattern of the Hertzian dipole, while peaks could be obtained at $\phi = 60°$ and $\phi = 300°$. The optimized structure involved an isolated nanocube on the left-hand side, followed by a block of seven nanocubes at the middle, and finally, five nanocubes located at the end of the array.

4. References

1. T. Kosako, Y. Kadoya, and H. F. Hofmann, "Directional Control of Light by a Nanooptical Yagi-Uda Antenna," *Nat. Photonics*, **4**, May 2010, pp. 312-315.

2. E. G. Mironov, A. Khaleque, L. Liu, I. S. Maksymov, and H. T. Hattori, "Enhancing Weak Optical Signals Using a Plasmonic Yagi-Uda Nanoantenna Array," *IEEE Photon. Technol. Lett.*, **26**, 22, August 2013, pp. 2236-2239.

3. M. Alavirad, L. Roy, and P. Berini, "Optimization of Plasmonic Nanodipole Antenna Arrays for Sensing Applications," *IEEE J. Sel. Top. Quantum Electron.*, **20**, 3, May/June 2014.

4. M. E. Mezeme and C. Brosseau, "Are Scaling Laws of Sub-Optical Wavelength Electric Field Confinement in Arrays of Metal Nanoparticles Related to Plasmonics or to Geometry," *Opt. Exp.*, **20**, 16, May 2012, pp. 17591-17599.

5. D. M. Solis, J. M. Taboada, F. Obelleiro, and L. Landesa, "Optimization of an Optical Wireless Nanolink Using Directive Nanoantennas," *Opt. Exp.*, **21**, 2, 2013, pp. 2369-2377.

6. H. Chen, A. M. Bhuiya, L. Runyu, D. M. Wasserman, and K. C. Toussaint, Jr., "Design, Fabrication, and Characterization of Near-IR Gold Bowtie Nanoantenna Arrays," *Phys. Chem. C*, **118**, 35, August 2014, pp. 20553-20558.

7. Ö. Ergül, "Solutions of Large-Scale Electromagnetics Problems Involving Dielectric Objects with the Parallel Multilevel Fast Multipole Algorithm," *J. Opt. Soc. Am. A.*, **28**, 11, November 2011, pp. 2261-2268.

8. B. Karaosmanoğlu, C. Önol, S. Güler, A. Altınoklu, and Ö. Ergül, "Full-Wave Electromagnetic Optimizations

Using Surface Integral Equations and the Multilevel Fast Multipole Algorithm," Proc. Progress in Electromagnetics Research Symp. (PIERS), 2016, pp. 262-266.

9. B. Karaosmanoğlu, A. Yılmaz, and Ö. Ergül, "On the Accuracy and Efficiency of Surface Formulations in Fast Analysis of Plasmonic Structures via MLFMA," Proc. Progress in Electromagnetics Research Symp. (PIERS), 2016, pp. 2629-2633.

10. C. Önol, B. Karaosmanoğlu, and Ö. Ergül, "Efficient and Accurate Electromagnetic Optimizations Based on Approximate Forms of the Multilevel Fast Multipole Algorithm," *IEEE Antennas Wireless Propag. Lett.*, **15**, April 2016, pp. 1113-1115.

11. B. Karaosmanoğlu, A. Yılmaz, U. M. Gür, and Ö. Ergül, "Solutions of Plasmonic Structures Using the Multilevel Fast Multipole Algorithm," *Int. J. RF Microwave Comput.-Aided. Eng.*, **26**, 4, May 2016, pp. 335-341.

James C. Lin
University of Illinois at Chicago
851 South Morgan Street, M/C 154
Chicago, IL 60607-7053 USA
E-mail: lin@uic.edu

Recent Research and Developments Focusing on Microwave Sensing and Monitoring in Biology and Medicine

On one of the coldest days of the season, seating in front of my laptop, I raised my head to look outside through a set of Frank Lloyd Wright prairie-style windows. A large flock of Canadian geese were resting, calmly and orderly, on ice over a frozen pound. Why didn't they fly away to some place with a more temperate climate, especially for this time of year? My thoughts drifted to San Francisco, California, in late spring or maybe early summer.

Ah, San Francisco, the city by the Bay: it is one of those exciting places on Earth that enjoys international renown for its beauty, culture, action, and innovation. It was a fitting venue for the 2016 IEEE International Microwave Symposium, held on May 22-27.

The exhilarating breadth of microwave technology and application was amply displayed during the week-long gathering of enthusiastic scientists, engineers, and technologists from around the world. What caught my eyes and ears most (not surprisingly, perhaps) was the wide range of exciting research and development activities surrounding microwave sensing and monitoring in biology and medicine: an area I pioneered some years ago, if I may humbly say so.

It stemmed from an appreciation that in sharp contrast to acoustic and optical radiations, which have been well-recognized as providing valuable diagnostic instruments and tools in biology and clinical medicine, the use of microwave instruments in biomedical laboratories and clinics deserved more attention.

The work began with an investigation on the sensing of respiratory movements in humans and animals using continuous-wave (CW) Doppler microwaves [1]. It then was extended to a wide range of sensing and monitoring applications for physiological movements and volume changes, including microwave apexcardiography (displacement measures of the precordium or chest wall overlying the apex of the heart, which echoes movements of the left ventricle and closely correlates with hemodynamic events within the left ventricle); apnea (cessation of respiratory activity) monitoring; vital sign (heart rate and respiration rate) detection; arterial pulse sensing; and monitoring of brain pressure and edema [2]. A Doppler microwave device for arterial pulse-wave sensing had demonstrated its clinical efficacy as an aid for assessing cardiovascular diseases using the technique [3-5].

A major advantage of microwave techniques is that it can provide a noninvasive and/or non-contacting (including remote) approach, without compromising the integrity of underlying physiological structure or function [6, 7]. A beam of microwave radiation is directed toward the biological target, and reflected microwaves are processed to yield information on the particular systems or organs of interest. In this case, the reflected microwave signals are modulated both in amplitude and phase by interfacial dielectric properties and other biological attributes.

Application scenarios include neonatal monitoring, burn-patient management, rescue operations involving hazardous materials, fitness training, home healthcare, safety and security surveillance, laboratory animal research, or field studies involving insects and birds. In fact, emerging technological innovations enabled by next-generation microwave sensors could help define the landscape for novel future applications in life sciences and healthcare.

The symposium in San Francisco was exceptionally informative, and I learned a lot about current activities. Presentations not only moved microwave sensing and monitoring in biology and medicine forward, but also showcased a wealth of leading-edge research in biomedical sensors, sensing technology, and applications of microwaves in ways that both fancied and excited the mind, at the same time.

There were about seven or more sessions and workshops that focused on applications of microwave technology in the life sciences [8]. In general, presented papers tended to emphasize microwave miniaturization of systems, enabling processing technologies and software algorithms. The following is a sampling of some presented papers:

A common complication for non-contact monitoring of vital signs is noise from unrelated body movements, such as during exercise. One paper reported on the use of a dual-self-injection-locking 2.4 GHz radar configuration to successfully reduce such artifacts by 85%.

A meta-material-based scanning leaky-wave antenna was developed for use as part of a 5.8 GHz spatial-scanning radar system to sense vital signs of subjects within a given scanning region.

To measure the tiny movements associated with the heart beats of small animals, such as laboratory rats, it was necessary to use a 60 GHz millimeter-wave radar. However, heart-beat detection in small animals by the millimeter-wave radar is corrupted by severe nonlinear effects from respiration-rate harmonics due to nonlinear phase demodulation. An adaptive harmonics comb notch digital filter was implemented to remove the respiration harmonics. Experimental results showed that even when the heart beat is totally overlapped by the respiration-rate harmonics, the heart-beat signal can be faithfully extracted.

Microwave sensing of speech-related movements of vocal cords has been previously reported. The subject of another presentation was on a portable 24 GHz radar for non-contacting speech sensing. It applied a pair of 4×4 arrays of antennas to measure the feeble vibrations produced in the neck by human vocal cords. Experiments under conditions of high background noise and voice interference yielded results that were comparable to microphone recordings. The novel 24 GHz array radar system was able to accurately acquire high-resolution time-varying speech information with good noise rejection, directional discrimination, and high sensitivity.

The above scenarios delimit the landscape of microwave sensing of physiological movements or signatures, where systems do not require any body-borne element or implant telemetry. There are obvious and distinct advantages from the point of view of signal integrity and source fidelity.

In contrast, a fascinating paper reported on the use of a dual-frequency (9.4 GHz/18.8 GHz) radar and a differential miniature harmonic transponder on a bee's body for bee searching. To help extend the detection range of the bee-searching radar, a thin (2.5 mm) foam substrate was inserted between the transponder and the bee's body to reduce body-related signal loss, and to enhance the transponder's omnidirectional operation. The differential transponder design for harmonic operation introduced a virtual ground plane and promoted antenna gain.

There also were a large number of papers reporting research on microwave sensors and detectors for biomedical applications. Below are some examples.

Noninvasive blood-glucose measurement would significantly improve the quality of diabetic patients' lives. Microwave sensors have the advantage over optical sensors because they have lower tissue scattering. Detection of physiological-range glucose in a multi-component aqueous solution was demonstrated through multivariate analysis of broadband dielectric spectra from 500 MHz to 50 GHz. The prediction error of glucose concentration was estimated at less than 73 mg/dL.

In a related project, a double-beam dielectric spectroscopic system, using integrated phase modulators, for glucose hydration sensing demonstrated accurate detection of glucose dielectric spectra for hydration analysis of glucose-water interaction in the sub-THz region (from 0.25 THz to 1.0 THz).

A complex permittivity sensor for microwave dielectric spectroscopy, integrated in 40-nm CMOS, utilized a single-ended patch as a near-field sensing element embedded in a double-balanced, fully-differential impedance bridge. A low-IF multi-harmonic down-conversion scheme was employed to extend the characterization frequency range and increase the measurement speed. The compact architecture offered accurate and fast measurements of liquids with an rms error of $< 1\%$ over a frequency range of 0.1 GHz to 12 GHz.

There was also a BICMOS microfluidic sensor for single-cell label-free (without dye staining) monitoring, but through inter-modulated microwaves.

A biological cell's dielectric properties are governed by its physiology and morphology. Cell dielectric

properties could indicate cellular pathological conditions. A microfluidic dielectrophoresis (DEP) cytometer to measure the dielectric properties of single biological cells while in flow over the 100 kHz to 400 MHz frequency range was reported. A microwave interferometer was used to detect DEP-induced translation of individual cells as they flowed over a multi-electrode sensing array, to measure the spectral response of Chinese hamster ovary (CHO) cells.

Another paper demonstrated the efficient use of microwave dielectric spectroscopy for single-cell irreversible electroporation monitoring. Experimental results showed a high correlation with accepted gold standards based on flow cytometry. The microwave approach featured several key advantages: marker-less, contact-less, and in-liquid cell monitoring. The microwave and microfluidic-based biosensor were able to detect increases in capacitance and conductance of single cells subjected to irreversible electroporation (cellular modification).

Common features of the papers itemized above were unique, noninvasive microwave sensors as tools for sensing cells or components of cells based on their dielectric or permittivity properties. They offered potentials for an emerging generation of biomedical-sensor innovations, enabled by microwave technology, which may help to define the landscape for future applications of life-changing biomedical sensors with specific functional advantages.

In summary, the papers presented at the symposium in San Francisco not only moved microwave sensing and monitoring in biology and medicine forward, but also showcased the research and development of sophisticated, leading-edge research in biomedical sensors, sensing technology, and applications of microwaves. They were spot-on examples of the symbiosis between contributing to and profiting from technologies enabled by miniaturization, microwave-device innovations, wireless mobility, ubiquitous networks, and computational intelligence for the enhancement of human lives.

References

1. J. C. Lin, "Noninvasive Microwave Measurement of Respiration," *Proceedings of the. IEEE*, **63**, October 1975, pp. 1530.

2. J. C. Lin, "Microwave Sensing of Physiological Movement and Volume Change," *Bioelectromagnetics*, **13**, December, 1992, pp 557-565.

3. J. Y. Lee and J. C. Lin, "Microprocessor Based Non-Invasive Pulse Wave Analyzer," *IEEE Trans. Biomed. Eng.*, **32**, June 1985, pp. 451-455.

4. K. H. Chan and J. C. Lin, "Microprocessor Based Cardiopulmonary Rate Monitor," *Med Biol. Eng. and Computing*, **25**, January 1987, pp. 41-44.

5. M. A. Papp, C. Hughes, J. C. Lin and J. M. Pouget, "Doppler Microwave: A Clinical Assessment of Its Efficacy as an Arterial Pulse Sensing Technique," *Invest. Radiol*, **22**, 1987, pp. 569-573.

6. J. C. Lin, "Microwave Propagation in Biological Dielectrics with Application to Cardiopulmonary Interrogation," in L. E. Larsen and J. H. Jacobi (eds.), *Medical Applications of Microwave Imaging*, New York, IEEE Press, 1986, pp. 47-58.

7. J. C. Lin, "Microwave Noninvasive Sensing of Physiological Signatures," in J. C. Lin (ed.), *Electromagnetic Interaction with Biological Systems*, New York, Plenum, 1989, pp. 3-25.

8. IEEE/IMS, "Gateway to the Wireless Future," MTT-S International Microwave Symposium, San Francisco, CA, May 22-27, 2016; http://www.ims2016.org/technical-program/virtual-proceedings.

Asta Pellinen-Wannberg
Umeå University, Department of Physics and
Swedish Institute of Space Physics
S-90187 Umeå, Sweden
Tel: +46 90 786 7492
E-mail: asta.pellinen-wannberg@umu.se

Introduction from the Associate Editor

I learned to know the name Hajduková a long time ago, when I started to read papers in meteor astronomy about the Halley comet, and what existed in interplanetary space. At my first Meteoroids conference, in Tatranská Lomnica in the Tatra Mountains in Slovakia in 1998, for the first time, I met the famous meteor family, Anton Hajduk, Mariá Hajduková, and Mariá Hajduková Jr. Father Anton was a professor at the Astronomical Institute of the Slovak Academy of Sciences, Department of Interplanetary Matter. Mother Maria was at the Faculty of Mathematics Physics and Informatics, Department of Astronomy, Physics of the Earth, and Meteorology, Comenius University, Bratislava.

During the following years, I sporadically met at least one them at different meetings, but in 2005, Anton passed away. After a while, the name again appeared more actively, and I understood that Anton's and Mariá's daughter was just following in the parents' footsteps.

It is interesting to note that this whole family has asteroids named after them:

- 9822 Hajdukova
- 11448 Miahajdukova
- 11657 Antonhajduk

Last spring at the Meteoroids conference (the sixth

Figure 1. Mariá Hajduková

Coffee, Cake and Comet Crumbs

Mariá Hajduková

Astronomical Institute of the
Slovak Academy of Sciences
Department of Interplanetary Matter
Dubravska cesta 9, 845 28 Bratislava, Slovakia
E-mail: Maria.Hajdukova@savba.sk

An interest in stars and space is of course essential for anyone wishing to become an astronomer. Indeed, we can take it for granted that most astronomers begin their careers by looking up at the stars and wondering. Then, given an ability in math, they follow their interest all the way to the hallowed halls of academia and the scientific community.

However, it is not sufficient to simply be interested in astronomical matters or to be good at the requisite sub-

skills. Other factors also play their role in the formation of an astronomer; this was especially so with myself. It is of some of them that I wish to speak.

My way to astronomy was exceptionally easy. I was born into a family of astronomers: two, to be precise, my mother and my father. It was not the night sky that made me become an astronomer, but rather discussions about it.

When I was young, I did not think astronomy was anything special or mysterious. I did not stand at night looking up at the darkened sky, imagining a world of Martians and spacemen and intergalactic disputes similar to the Cold War disputes that were then a daily part of life. No, to me, astronomy was something rather commonplace, which people talked about every day: meteors, comets, and the Big Bang were dinner-table talk. Post-prandial cake would be accompanied by discussions of celestial mechanics (well I remember the beauty of the formulas my mother would cover her blackboard with, using her special no-dust chalk). Science seemed to be something interesting, since my parents really enjoyed it. I remember my excited father waiting in front of the television with his old camera, waiting to snap a picture of Halley's comet from an Austrian news broadcast. I remember the oft-repeated story about my parents visiting their friend and colleague, Vladimír Porubčan, and together watching the first landing on the moon (which did not impress me half so much as his budgie sitting down on my father's shoulder, just when the moon landing was at its most exciting, and twittering into his right ear – a fortunate choice, as it was the only one he could hear with). I loved it when, for months on end, we had to navigate the piles and piles of paper that my parents had distributed around the whole living room because they were preparing the publication of the *Encyclopedia of Astronomy*. I loved being allowed to stay up unusually late, and watching the moon through our army-issue binoculars (I still can smell their distinctive odor) from our balcony above the dark forest.

That not every kid was similarly engaged only came to my notice when I started elementary school, and I discovered what their parents did for a living. I began to suspect that to be an astronomer was not totally normal, and so, whenever I was asked what my parents did, I felt ashamed to answer "astronomer," and would say "physicist," instead. It seemed much less *outre*.

However, there was one truly amazing thing about my parents' work, and that was its international dimension: they had friends from all over the world (even from Western imperialist countries). However, such international animosities did not extend to the world of science. Many of their friends visited us when they came to Slovakia to attend a conference. The pleasant times the whole family had with these amiable guests from abroad played their part in drawing me to the world of astronomy.

I remember very kind people, and I will here list a few of these memories:

- Bertil Lindblad with his family, enjoying my grandmother's cooking, after which he would always ask for a glass of milk.
- Bruce and Louise McIntosh, with their map almost larger than our living room, learning all of the Slovak castles.
- Peter Millman, who continued to send us his beautiful photographs for decades.
- My father picking up Tom Kaiser, whose car had overheated in the middle of nowhere, on his way to the High Tatras, and who, lacking distillated water, had used beer to eke out a few more kilometers.
- Lubor and Gitka Kresák, who liked to play bridge with my parents.
- Krzysztof Ziolkowski philosophizing with them about the infinity of the universe.
- The discussions with one of my parents' closest friends, Janko Štohl, about the very beginning of the universe.
- The many friendly visits of Iwan and Judy Williams.
- Giordano Cevolani with Maria Teresa, laughing loudly with my parents deep into the night.
- Prof. Hasegawa, together with his nine students, marveling at how big our small flat was.
- Jack Baggaley visiting with enthusiasm the Slovak Opera House (where I worked as an usherette when at university).
- One Russian colleague, who asked my father for help in buying some gold cotton (which it was not possible to buy in the Soviet Union), which he needed to embroider a priest's cassock back home.
- David Hughes' happiness with a few used bus tickets from Bratislava to enrich his ticket collection!

It was only years later that I realized that all these kind and normal people, with their varied interests, were well-known astronomers and recognized scientists.

It was thus that I grew up with two people who derived huge pleasure from scientific research, both in itself and from the people they came into contact with in the course of their work. Naturally, I gained a lot of knowledge just from being around them, of astronomy and of life. I accompanied my

parents to many conferences and loved them. Again there was that special relationship of highly intelligent people working together on various projects, exchanging ideas, enriching their scientific knowledge, and at the same time establishing friendships that would last, in some cases, until the end of their lives. I remember especially how much we laughed together at these events.

As yet, though, it was the social aspects of the scientific community and the atmosphere of intellectual discourse that attracted me more than the astronomy, per se. However, I went to Prague to study astronomy at Charles University. Of course, there were many members of the staff there to whom I still feel grateful for their generosity to me, even though I must surely have been somewhat of a disappointment to them in terms of my academic record. I especially remember the great moral support of Prof. Vanýsek and my course advisor, Marek Wolf. Mention should also go to Dr. Šolc, Dr. Mayer, and Dr. Šidlichovský.

The sad fact was that I was probably not quite mature enough to be a university student at that time – that, and I was too busy enjoying all the classical concerts, operas, and theatre that Prague had to offer. However, I was old enough to get excited by the Velvet Revolution of 1989. Understandably, I became more interested in attending the various street protests than in attending my lectures. Inevitably, all this had a deleterious effect on my studies, and I had to repeat one of the state exams.

After that, influenced by home's never-ending philosophical discussions about life, the universe, and everything, and by a desire to find my role amongst it all, I spent a few years at Ruprecht-Karls University in Heidelberg, studying theology. When, after several great years of the student life in Germany, I came back to Slovakia, I also came back to astronomy. I have not left it since.

I took my PhD at the Astronomical Institute. I started working on interstellar meteors, a topic I had worked on in my master's diploma work, when I was led by Lubor Kresák. He is one of the greatest scientists I have met (he was also cool, with his cigarette and enigmatic smile), and he provided me with the best foundation for my future work that I could possibly have had. I finished my PhD under the direction of my father. Although unusual, this enabled us to discuss my thesis for hours and hours, and allowed me to ask questions without any apprehension or fear.

Since receiving my PhD, I have worked at the Department of Interplanetary Matter of the Astronomical Institute, the same workplace with which I was so very familiar from my time going there as a little child. Even so, I only started working more seriously after my father died: I had to stand on my own two feet. I couldn't rely on him anymore. One example of this was continuing the work he had begun between our institute and the National Research Council of Italy. Several times, I visited the Bologna Institute of Atmospheric Sciences and Climate Institute, and worked with Giordano Cevolani. The research program was based on the radio observations of meteor showers by the Bologna-Lecce-Modra forward-scatter system. However, this has been my only experience with radio science. These days, I deal more with meteor observations by video techniques and their analyses.

The field of my current research is the dynamical evolution of the small bodies of the Solar System (led by my colleague, Luboš Neslušan). This has brought me into contact with the modeling of meteoroid streams, which, compared with observed meteors, provides very interesting outcomes for the understanding of the evolution and distribution of the whole meteoroid population. Analyzing meteoroid orbits, I also aim to call attention to the measurement and determination errors, and their impact on subsequent analyses.

I love my work now, but I know that I could have done much more if I had started taking it more seriously much earlier. In summary, this road to astronomy has been the way of a lazy daughter of two scientists.

One last thing: I was recently helping my eight-year-old daughter with her natural-sciences homework, and was explaining something to her when she interrupted me. "Oh, mum," she said, "Don't start again with the universe!" I had to laugh. For me, science has always been associated with that sound.

2018 IEEE International Symposium on Antennas and Propagation and USNC-URSI Radio Science Meeting
Boston, MA
July 8-14, 2018

The 2018 IEEE AP-S Symposium on Antennas and Propagation and USNC-URSI Radio Science Meeting will be held on July 8-14, 2018, at the Westin Boston Waterfront in Boston, Massachusetts. The combined symposium and meeting are co-sponsored by the IEEE Antennas and Propagation Society (AP-S) and the U.S. National Committee (USNC) of the International Union of Radio Science (URSI). The technical sessions, workshops, and short courses will be coordinated between the two organizations to provide a comprehensive and well-balanced program. This meeting is intended to provide an international forum for the exchange of information on state-of-the-art research in antennas, propagation, electromagnetic engineering, and radio science. The paper submission deadline is **January 15, 2018**.

The symposium Web site, **www.2018apsursi.org** has instructions for the preparation and submission of papers, the details for the Student Paper Competition and Student Design Contest, as well as the full Call for Papers. Information for potential exhibitors, special session proposals, and the contact person for those wishing to organize a short course or workshop are also included in the Call for Papers.

Questions should be directed to:

Steven Best – Chair
E-mail: Steve.Best@comcast.net

Mike Shields – co-Chair
E-mail: shields@LL.mit.edu

Alan Fenn – TPC Chair
E-mail: AJF@LL.mit.edu

www.2018apsursi.org

URSI Accounts 2016

In 2016, URSI continued its transformation towards offering more opportunities for radio scientists to meet and exchange information by organizing the yearly flagship meetings. After the successful first AT-RASC meeting in 2015 in Gran Canaria, the 2016 AP-RASC meeting organized in Seoul was again great success, with regard to the scientific content, the organization and the venue.

As can be seen from the accounts URSI is managing this transformation in a financially careful way. Although URSI has substantial reserves that allow us to invest in new initiatives, it is done in a way that reduces the losses to levels that are negligible compared to the reserves. This is only possible thanks to the work and dedication that a number of people volunteer for URSI. Those yearly flagship meetings have indeed very substantially increased the workload for the secretariat. The number of assistant secretary general had to be increased to four. I am most grateful to Peter Van Daele, Ross Stone , George Uslenghi and Kazuya Kobayashi who under the guidance of the URSI President Paul Cannon have made all of this possible. Often it is not realized and appreciated that an organization such as URSI can only function thanks to the unselfish commitment of a number of persons. Establishing a conference takes time, but the expectation is that as the success of the flagship meetings will increase, this will generate extra revenue that can be invested in the URSI Young Scientist and Student Paper Competition programs. Attracting young people to careers in radio science, helping them launch their career successfully, giving them the opportunity to present their work and facilitating their participation in a free exchange of scientific results in a worldwide community of radio scientists, is indeed in my view the most important aspect of the URSI mission.

Prof. Paul Lagasse
Secretary General of URSI

BALANCE SHEET: 31 DECEMBER 2015

	EURO	EURO
ASSETS		
Installations, Machines & Equipment		1,505.64
Dollars		
PNB Paribas	1,747.76	
		1,747.76
		547.30
Euros		
Banque Degroof	0.00	
BNP Paribas zichtrekening	80,105.18	
BNP Paribas spaarrekening	56,683.57	
BNP Paribas portefeuillerekening	84,442.35	
Paypal	5,42	
		221,236.52
Investments		
Degroof Bonds EMU (formerly Demeter Sicav Shares)	22,681.79	
Rorento Units	111,796.03	
Degroof Monetary Eur Cap (formerly Aqua Sicav)	63,785.56	
Bonds	400,000.00	
	598,263.38	
673 Rorento units on behalf of van der Pol Fund	12,033.19	
		610,296.57
Petty Cash		24.03

Total Assets		834,810.52
Less Creditors		
IUCAF	33,119.56	
ISES	5,053.53	
		(38,173.09)
Balthasar van der Pol Medal Fund		(12,033.19)
Paid Remuneration		6,697.97
NET TOTAL OF URSI ASSETS		**791,302.21**

The net URSI Assets are represented by:	EURO	EURO
Closure of Secretariat		
Provision for Closure of Secretariat		115,000.00
Scientific Activities Fund		
Scientific Activities in 2017	60,000.00	
Routine Meetings in 2017	15,000.00	
Publications/Website in 2017	40,000.00	
Young Scientists in 2017	0.00	
Administration Fund in 2017	105,000.00	
I.C.S.U. Dues in 2017	12,000.00	
		232,000.00
Flagship Meetings		
GASS 2017		210,000.00
AT-RASC - Gran Canaria (2018)		20,000.00
AP-RASC (2019)		10,000.00
Total allocated URSI Assets		587,000.00
Unallocated Reserve Fund		204,302.21
		791,302.21

Statement of Income and expenditure for the year ended 31 December 2016

I. INCOME		
Contributions from National Members (year -1)	24,519.00	
Contributions from National Members (year)	175,975.00	
Contributions from National Members (year +1)	37,097.50	
Income AT-RASC 2018	0.00	
Income AP-RASC 2019	0.00	
Sales of Publications, Royalties	0.00	
Bank Interest	191.96	
Other Income	4,779.41	
Total Income		**245,846.81**

II. EXPENDITURE		
A1) Scientific Activities		107,292.53
General Assembly 2008/2011/2014/2017	2,036.09	
Mid Term Meetings 2015	0.00	
AT-RASC	3,273.03	
AP-RASC	91,725.19	
Scientific Meetings: Symposia/Colloquia	9,400.00	
Representation at Scientific Meetings	858.22	
Other	0.00	

A2) Routine Meetings			18,768.75
Bureau/Executive committee		18,768.75	
Other		0.00	
A3) Publications			12,150.82
B) Other Activities			6,575.13
Contribution to ICSU		4,575.13	
Contribution to other ICSU bodies		2,000.00	
C) Administrative Expenses			115,919.05
Salaries, Related Charges		95,824.41	
General Office Expenses		2,604.82	
Travel and representation		0.00	
Insurances/Communication/Gifts		4,074.63	
Office Equipment		0.00	
Accountancy/Audit Fees		7,673.46	
Bank Charges/Taxes		4,236.55	
Depreciation		1,505.18	
Loss on Investments (realised/unrealised)			
Total Expenditure:			**260,706.28**
Excess of Expenditure over Income			(14,859.47)
Currency translation diff. (USD => EURO) - Bank Accounts			107.33
Currency translation diff. (USD => EURO) - Investments			0.00
Currency translation diff. (USD => EURO) - Others			0.00
Accumulated Balance at 1 January 2016			806,054.35
			791,302.21
Rates of exchange			
January 1, 2016	1 $ = 0.8940 EUR		
December 31, 2016	1 $ = 0.9490 EUR		
Balthasar van der Pol Fund			
663 Robeco Global (former Rorento Shares) : market value on December 31 (Aquisition Value: USD 12.476,17/EUR 12.033,19)			38,076.09
Book Value on December 31, 2016/2015/2014/2013/2012			12,033.19
Market Value of investments on December 31, 2015-2011			
Degroof Bonds EMU (formerly Demeter Sicav Shares)			94,409.70
Robeco Global (formerly Rorento Units) (1)			749,450.00
Aqua-Sicav (formerly Degroof Monetary Eur Cap)			89,768.79
Bonds			400,000.00
			1,333,628.49
Book Value on December 31, 2016/2015/2014/2013/2012			610,296.57

(1) Including the 663 Rorento Shares of v d Pol Fund

APPENDIX : Detail of Income and Expenditure

I. INCOME

Other Income		
Income General Assembly 2011	0.00	
Income General Assembly 2014	0.00	
Young scientist support (Japan)	0.00	
Income bonds	4,779.41	
Other	0.00	
		4,779.41

II . EXPENDITURE

General Assembly 2011		
Organisation	0.00	
Young scientists	0.00	
Expenses officials	0.00	
Support Commissions	0.00	
General Assembly 2014		
Organisation	0.00	
Vanderpol Medal	0.00	
Young Scientists	0.00	
Expenses officials	0.00	
Support Commissions	0.00	
General Assembly 2017		
Organisation	637.25	
Vanderpol Medal	0.00	
Young Scientists	0.00	
Expenses officials	1,398.84	
Support Commissions	0.00	
		2,036.09
AT-RASC		
Organisation	1,838.50	
Young Scientists	0.00	
Expenses Officials	1,434.53	
Support Commissions	0.00	
		3,273.03
AP-RASC		
Organisation	32,016.66	
Young Scientists	0.00	
Expenses Officials	46,519.12	
Support Commissions	0.00	
		91,725.19
Routine Meetings		
Board Meeting	18,768.75	
		18,768.75
Symposia/Colloquia/Working Groups		
Commission A	0.00	
Commission B	0.00	
Commission C	0.00	
Commission D	0.00	
Commission E	300.00	
Commission F	500.00	
Commission G	2,600.00	
Commission H	3.000.00	
Commission J	1.000.00	
Commission K	0.00	
Central Fund	0.00	
Central Fund (Student Award MC)	2,000.00	
		9,400.00
Contribution to other ICSU bodies		
IUCAF	2,000.00	
		2,000.00
Publications		
Publications/Website	12,150.82	
Printing ‘The Radio Science Bulletin’	0.00	
Mailing ‘The Radio Science Bulletin’	0.00	
		12,150.82

Rapport CROWNCOM 2016

La 11° conférence internationale on Cognitive Radio Oriented Networks and COMmunications (CROWNCOM), s'est tenue à Grenoble du 30 mai au 1 juin 2016. Avec IEEE DYSPAN, CROWNCOM est l'une des deux conférences mondiales spécialisées dans le domaine de la radio intelligente.

Cette année la conférence s'est focalisée sur le rôle de la radio intelligente dans la 5G, l'IoT et la gestion du spectre (http://crowncom.org/2016/show/ home). Cette édition a été un vrai succès, avec la participation de 125 conférenciers (Figure 1) issus de 17 pays.

A l'issue d'un processus de sélection impliquant 252 reviews, 63 papiers ont été acceptés pour présentation. Le programme (Figure 2) était réparti sur trois sessions parallèles: (présentation des papiers, trois tutoriaux, trois workshops), avec des temps fort en sessions plénières autour de keynote talks de niveau international:

- Douglas C. Sicker, Lord Endowed Professor and Department Head and Professor of Engineering and Public Policy and the School of Computer Science at Carnegie Mellon University
- Wassim Chourbaji, Vice President for Government Affairs Europe, Middle East and North Africa at Qualcomm
- Philippe Lefebvre, Head of the 5G Sector in the European Commission's DG CONNECT
- Honggang Zhang, Full Professor of College of Information Science and Electronic Engineering and Co-Director of York-Zhejiang Lab for Cognitive Radio and Green Communications at the Zhejiang University
- Walter Weigel, VP of the European Research Institute of Huawei

Figure 1. Les participants à CROWNCOM 2016.

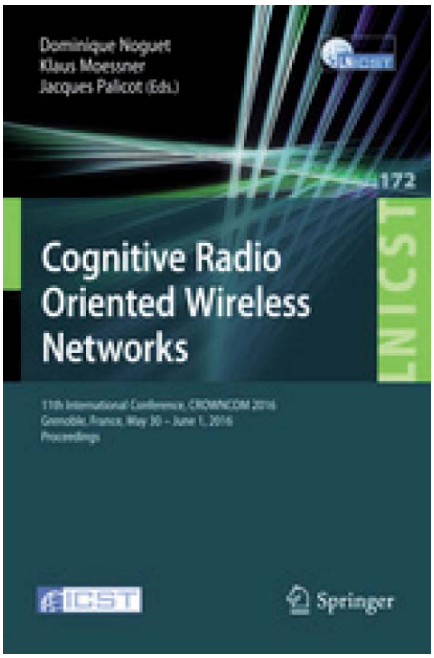

Figure 2. Les comptes rendus de CROWNCOM 2016.

- Christophe Fourtet, co-founder and CTO, Sigfox

Cette année, nous avons eu la volonté de mettre en avant des démonstrations technologiques dans un espace dédié. Huit démonstrateurs technologiques ont été sélectionnés et présentés ainsi que deux sponsors exhibits (Keysight Technologies et National Instrument) lors de l'évènement.

Un prix du meilleur papier, sponsorisé par Orange, a été décerné le dernier jour de la conférence. La qualité de la conférence a été saluée par les participants et par EAI.

La conférence a été soutenue par sept sponsors financiers: Keysight Technologies, Huawei, Nokia, Qualcomm, National Instrument, Orange, ForeMont; et un sponsor moral: URSI. Les actes sont publiés par Springer sous forme d'un livre co-édité par Dominique Noguet (CEA-Leti), Klaus Moessner (University of Surrey), et Jacques Palicot (CentraleSupélec, campus de Rennes).

Les meilleurs papiers de la conférence ont été invités à soumettre une version étendue à un numéro spécial d'Eurasip *Journal on Communications and Wireless Networking* sur le thème "Dynamic Spectrum Access and Cognitive techniques for 5G". Ce numéro spécial a été proposé spécifiquement en lien avec la conférence.

L'édition 2017 de la conférence est prévue au Portugal.

IEEE Radio and Antenna Days of the Indian Ocean 2016 (IEEE RADIO 2016)

Dr. Philippe Jean Pierre, President of the Regional Committee for Innovation of Reunion Island, officially opened the fourth edition of the Radio and Antenna Days of the Indian Ocean (IEEE RADIO 2016). This was held at Hotel Le Récif, Saint-Gilles Les Bains, Reunion Island, from October 10-13, 2016. The conference was organized by the Radio Society (Mauritius). It was jointly sponsored by the IEEE Antennas and Propagation Society (AP-S) and the Université de La Réunion. In addition, IEEE RADIO 2016 was technically cosponsored by the International Union of Radio Science (URSI), IEEE Region 8, and the IEEE France Section. The local organizing committee consisted of researchers from CentraleSupélec, France, Université de La Réunion, and the University of Mauritius.

IEEE RADIO 2016 is the fourth of a series of conferences covering the fields of antennas and propagation organized in the Indian Ocean region. The conference gathered participants from over twenty countries, coming from different regions of the world, including Africa, Asia, Europe, the Middle East, and North America. IEEE RADIO 2016 featured fourteen oral sessions on state-of-the-art research themes, including antenna design, bio-electromagnetics, computational electromagnetics, devices and circuits, metamaterials and applications, radio astronomy, remote sensing, and wireless sensor networks.

Invited talks were delivered by Prof. Tapan Sarkar from Syracuse University, USA; Prof. Qing Liu from Duke University, USA; and Prof. Monaï Kraikriksh from King Mongkut's Institute of Technology Ladkrabang, Thailand. A special session, organized by Dr. Eric Mokole, Vice Chair of the IEEE AP-S Special Interest Group on Humanitarian Technology (SIGHT), was dedicated to humanitarian activities and projects within the Indian Ocean region.

In line with the previous editions, the oral presentations of young scientists and students were evaluated by a jury. A cash prize of 300 Euros and a shield were awarded to the Best Young Scientist. Moreover, three cash prizes of 300 Euros, 200 Euros, and 100 Euros, as well as shields, were awarded to the first, second, and third Best Student Papers, respectively.

Following the successes of the four editions of the RADIO international conferences, the organizing committee will hold the next edition of the conference in Cape Town, South Africa, in 2017.

Vikass Monebhurrun
General Chair, IEEE RADIO 2016
E-mail: vikass.monebhurrun@centralesupelec.fr

Figure 1. The IEEE RADIO 2016 opening ceremony on Monday, October 10, 2016.

Report on ISAP2016

1. Introduction

The 2016 International Symposium on Antennas and Propagation (ISAP2016) was held at the Okinawa Convention Center on the waterfront of the East China Sea (Figure 1), Okinawa, Japan, from October 24 to 28, 2016. This symposium, the 21st ISAP, was organized and sponsored by the IEICE Communications Society (IEICE-CS). It was held in cooperation with the International Union of Radio Science (URSI); the IEEE Antennas and Propagation Society (IEEE/AP-S); the Institution of Engineering and Technology (IET); the European Association on Antennas and Propagation (EurAAP); the Institute of Antenna Engineers of Taiwan (IAET); the Korean Institute of Electromagnetic Engineering and Science (KIEES); the Antenna Society of the Chinese Institute of Electronics (AS-CIE); the Chinese Microwave Association (CMA); the Radio Electronics Association of Vietnam (REV); and the Electrical Engineering/Electronics, Computer, Communications and Information Technology Association of Thailand (ECTI).

The conference featured three plenary talks, six invited talks, six technical workshops, and 65 technical sessions including 26 organized sessions and two poster sessions. It was attended by 865 researchers and engineers, including 47 accompanying persons, and 143 exhibitors from 33 countries and regions. All of these numbers were the largest in the history of ISAP.

2. Conference History

The ISAP is intended to provide an international forum for the exchange of information on the progress of research and development in antennas, propagation, and electromagnetic wave theory. The first ISAP was held at Sendai, Japan, in 1971. The conference has been held nine times in Japan every four years until 2004. From 2005, the ISAP expanded the conference venues to the Asia and Pacific areas, and became an annual conference. The host cities from 2005 to 2015 were Seoul, Singapore, Niigata (Japan), Taipei, Bangkok, Macao, Jeju (Korea), Nagoya (Japan), Nanjing (China), Kaohsiung (Taiwan), and Hobart (Australia), respectively. This symposium is now recognized as one of the major conferences in this technical field.

3. Opening Ceremony and Plenary Talks

The symposium started with an opening address by the General Chair, Prof. Toru Uno, as shown in Figure 2. This was followed by brief complimentary addresses from the representatives of technical cosponsors: EurAAP, IEEE/AP-S, KIEES, AS-CIE, IAET, ECTI, and CMA.

Three plenary talks were organized following the opening ceremony. In the first plenary talk, Prof. Wei Hong from Southeast University in China (CIE), talked about "Millimeter-Wave Communications for 5G." In this talk, the current research status of China's 5G was briefly introduced, including the candidate frequency bands, goal and key technologies, etc. The research advances in millimeter-wave indoor and outdoor communications for 5G were then presented.

In the second plenary talk, Mr. Tomohiro Saito, from the Japanese broadcasting company NHK Science & Technology Research Laboratories, talked about "Wireless Transmission Technology for Ultra-High-Definition Television." In this talk, he reviewed individual technologies

Figure 1. The Okinawa Convention Center on the waterfront of the East China Sea.

Figure 2. The opening address from Prof. Toru Uno.

for camera, television, audio, recording, and wireless communications for 8K super-high-vision UHDTV under the background of digital broadcasting HDTV becoming popular in Japan.

In the third plenary talk, Mr. Jongsik Lee, from KT Telecom in Korea, talked about "5G Trial in 2018 PyeongChang Winter Olympics –Technical Challenges & Preparations." In this talk, he shared KT's view and vision on 5G, and also introduced what KT had done so far. He presented what KT was currently working on for launching 5G networks in collaboration with partners, mainly focusing on 5G pre-commercial specifications and corresponding service plans.

4. Invited Talks

Six speakers were invited for the first presentations in the sessions with each related topic:

1. Prof. Seong-Ook Park (KAIST), "Analysis of Low Loss Magneto-Dielectric Antenna for the Mobile Communication"

2. Prof. Qun Wu (Harbin Institute of Technology), "Functional Metamaterial Devices for Manipulation of Waves in Microwave Region Based on Transformation Optics"

3. Prof. Hao Xin (University of Arizona), "3D Printing Technology for RF and THz Antennas"

4. Prof. Monai Krairish (King Mongkut's Institute of Technology Ladkrabang), "Phased Array of Switched Beam Elements and Application"

5. Dr. Seiji Kawamura (National Institute of Information and Communications Technology), "Water Vapor Estimation Using the Propagation Delay of Digital Terrestrial Broadcasting Waves"

6. Prof. Jian Yang and Prof. Andres Alayon Glazunov (Chalmers University of Technology), "Design and Characterization of Cost-Effective Planar Antennas with Steerable Beams: Gap Waveguides, SMT, and Random LOS"

5. Technical Sessions

528 papers were presented during ISAP2016 from 30 countries and regions. In this symposium, the following topics were highlighted:

- Broadband, Multi-Frequency, and Small Antennas
- Characteristic Mode Analysis for Small Antennas
- Antennas for Mobile Communications
- Advanced Base Station Antennas
- MIMO Antennas and Decoupling Technologies
- 3D-Printed Lens and Antennas
- Reconfigurable and Tunable Antennas
- Metamaterial-Inspired Antennas
- Frequency Selective Surfaces and Metasurfaces
- Reflector, Reflectarray, and Array Antennas
- Millimeter-Wave and THz Antenna Technologies
- Antennas and Propagation for 5G Systems
- DOA Estimation
- Adaptive and Phased Arrays
- Radar and Remote Sensing and Applications
- Propagation Models
- Indoor and Outdoor, Tunnel Propagation
- Antenna Measurements
- Electromagnetic Wave Theory
- Advances in Computational Electromagnetics
- Wearable Devices and Human Body Interactions
- Wireless Power Transfer
- Filters and EMC

Figure 3. The technical sessions and workshops.

Figure 4. ISAP2016 General Chair Prof. Toru Uno (l) passed the ISAP flag to the next ISAP2017 General Chair, Prof. Monai Krairish.

In addition to the above topics, three special sessions were organized:

- EurAAP Session: Recent Advances in European Antennas and Propagation Research I-II
- Recent Advances in Antennas and Propagation in ASEAN countries I-II
- Next 50 Years of Antennas and Propagation Technologies in Japan (50-Year Anniversary of AP Committee in IEICE)

6. Technical Workshops

The following technical workshops on recent hot topics were organized free of charge for the attendees, as shown in Figure 3:

1. Prof. Ikmo Park (Ajou University), "Design of Antenna with Crossed Dipoles"

2. Prof. Fan Yang (Tsinghua University), "Reflectarray Antennas: Theory, Designs, and Applications"

3. Prof. Nozomu Ishii (Niigata University), "Fundamentals of Practical Antenna Measurement to Get More Accurate Data for Input Impedance and Pattern"

4. Prof. Raj Mittra (Pennsylvania State University/ University of Central Florida), "A New Look at Transformation Optics (TO) Approach for Designing Electromagnetic Devices Such as Flat Lenses and Cloaks"

5. Prof. John L. Volakis (The Ohio State University), "Ultra-Wideband Phased Arrays and Transceivers"

6. Mr. Lars J. Foged (Microwave Vision Group), "Multi-Probe Antenna Measurement Systems with Applications to Telecom, Space, and Defense"

7. Exhibition

32 exhibitors and nine technical seminars joined and demonstrated their works and products, such as electromagnetic simulators, measurement instruments, antennas and microwave components, and equipment, in the exhibition area.

8. Award

ISAP2016 established two awards: the Best Paper Award, chosen from all the papers, and the Student Paper Award, chosen from the student poster presentations. The following five papers received the Best Paper Award:

1. Luigi La Spada and Yang Hao (Queen Mary University of London, United Kingdom), 1A4-2, "Surface Wave Manipulation Based on Transformation Optics: From Design to Manufacturing"

2. Motoharu Sasaki, Minoru Inomata, Wataru Yamada, Naoki Kita, Takeshi Onizawa, Masashi Nakatsugawa (all from NTT Corporation, Japan), Koshiro Kitao, and Tetsuro Imai (both from NTT DOCOMO, Inc., Japan), 1D3-5, "Path Loss Characteristics Between Different Floors from 0.8 to 37 GHz in Indoor Office Environments"

3. Shogo Matsumoto, Hiroki Yamada, Hiroyuki Deguchi and Mikio Tsuji (Doshisha University, Japan), 3D3-5, "Reflectarray with Arbitrarily Shaped Elements for Linear-to-Circular Polarization"

4. Abbas Vosoogh, Per-Simon Kildal, Vessen Vassilev, Ashraf Uz Zaman (all from Chalmers University of Technology, Sweden), and Stefan Carlsson (Gapwaves, Sweden), POS1-10, "E-Band 3-D Metal Printed Wideband Planar Horn Array Antenna"

5. Seonho Lim, Woo Cheol Choi, Young Joong Yoon, and Chisang You (Yonsei University, Korea), POS1-36, "An Isolation Technique for Closely Stacked MIMO Antennas"

The following eight papers were awarded the Student Paper Award:

1. Wan Chin Wu (National Sun Yat-sen University, Taiwan), "Metal-Frame Inverted-F Antenna for the LTE Metal-Casing Smartphone"

2. Taihei Fujino (Tokyo Institute of Technology, Japan), "Design and Fabrication of a Dual-Polarized Corporate-Feed Waveguide 32 × 32-Slot Array Antenna with an Orthmode Transducer for 40 GHz Band"

3. Abbas Vosoogh (Chalmers University of Technology, Sweden), "E-Band 3-D Metal Printed Wideband Planar Horn Array Antenna"

4. Riho Suzuki (Yokohama National University, Japan), "Probe-Positioning Error Estimation for Planar Near-Field Phaseless Measurements"

5. Xin Xu (Tokyo Institute of Technology, Japan), "An E-Band Slotted Waveguide Monopulse Array Antenna with Corporate-feed Using Diffusion Bonding of Laminated Plates"

6. Masanori Gocho (Niigata University, Japan), "Verification of Simple Calibration Method for Multi-Baseline SAR Tomography"

7. Joonsuk Kim (Yonsei University, Korea), "Simulation of Passive Time-Reversal Surveillance System for Detection of Target Invasion Inside Forested Environment"

8. Shigeaki Okumura (Kyoto University, Japan), "Technique of Tracking Multiple Pedestrians Using Monostatic Ultra-Wideband Doppler Radar with Adaptive Doppler Spectrum Estimation"

9. ISAP-ISC Meeting

An ISAP International Steering Committee (ISAP-ISC) meeting was held during the symposium. The ISAP-ISC was organized by the researchers mainly of countries and regions in the Asia and Pacific areas that contributed to ISAP. The operation of the symposium was discussed, and future ISAP venues were decided in the meeting. In this meeting, the representatives from Australia, China (CIE), Hong Kong, India, Indonesia, Japan, Korea, Singapore, Taiwan, and Thailand attended. The ISAP-ISC decided that the venue of ISAP2019 will be Xi'an, China (CIE), following Phuket, Thailand, in 2017, and Busan, Korea, in 2018. The ISAP flag was passed from Prof. Uno to Prof. Monai, as shown in Figure 4.

10. Conclusion

The ISAP2016 steering committee thanked all attendees and related people for the contributions to organizing the ISAP2016. All the papers of past ISAP symposia can be referred at the Web page "ISAP archives" (http://ap-s.ei.tuat.ac.jp/isapx/) free of charge during the trial service. The papers of ISAP2016 have appeared in the ISAP archives starting in May, 2017. In addition, the papers of ISAP2016 have been included in IEEE Xplore. The symposium Web page of ISAP2017 is available (http://www.isap2017.org).

Toru Uno
General Chair, ISAP2016
Professor, Tokyo University of Agriculture and Technology, Japan
E-mail: uno@cc.tuat.ac.jp

IUCAF 2016 Annual Report

1. Introduction

The Scientific Committee on Frequency Allocations for Radio Astronomy and Space Science, IUCAF, was formed in 1960 by its adhering scientific Unions, IAU, URSI, and COSPAR. The IUCAF brief is to study and coordinate the requirements of radio frequency allocations for passive (i.e., non-emitting or receive-only) radio sciences, such as radio astronomy, space research, and remote sensing, in order to make these requirements known to the national administrations and international bodies that allocate and regulate the use of radio frequencies. IUCAF operates as a standing inter-disciplinary committee under the auspices of ICSU, the International Council for Science. IUCAF is a Sector Member of the International Telecommunication Union's Radiocommunication Sector (ITU-R).

2. Membership

There being no general assemblies of the adhering Unions or resignations, IUCAF membership was unchanged in 2016. At the end of 2016 the membership for IUCAF elected by the three adhering Unions was as shown in Table 1. Additionally, the Counselor for ITU-R Study Group 7 (Science Services), Vadim Nozdrin, is a member ex-officio by virtue of his position, as specified in IUCAF's Terms of Reference.

IUCAF also has an informal group of Correspondents, in order to improve its global geographic representation and for specific issues, for instance concerning astronomical observations in the optical and infrared domains.

3. IUCAF's Terms of Reference (2015)

A revision to the statement of IUCAF's composition, operating practices, and Terms of Reference (ToR), originally dating to 1972, was submitted to ICSU and approved by ICSU's Executive Board at its meeting in November 2015. The Terms of Reference may be viewed at http://www.iucaf.org/IUCAF_Terms_Of_Reference.pdf.

4. Spectrum Meetings

During the period January-December 2016, members participated in the regional and international meetings on behalf of IUCAF shown in Table 2. Additionally, IUCAF members participated in numerous national spectrum-management proceedings, working in their capacities as spectrum managers at their observatories.

5. Business Meetings

IUCAF held in-person business meetings immediately prior to each of the ITU-R sessions of Working Party 7D in Geneva listed in Table 2. During the year, IUCAF business is undertaken via e-mail as matters arise.

6. Finances

The IUCAF budget is managed by URSI.

As requested by IUCAF, sustaining contributions of €5,000, €2,000, and €1,000 were gratefully received from

Table 1. The membership of IUCAF at the end of 2016.

URSI	S. Ananthakrishnan (Com J)	India
	S. Reising (Com F)	USA
	I. Häggström (Com G)	Sweden
	A. Tzioumis (Com J)	Australia
	W. van Driel (Com J)	France
IAU	H. Chung	Korea (Republic of)
	H. S. Liszt (Chair)	USA
	M. Ohishi (Past Chair)	Japan
	A. Tiplady	South Africa
COSPAR	Y. Murata	Japan

Table 2. The regional and international meetings in which members participated on behalf of IUCAF in 2016.

April	ITU-R Working Party WP 7D	Geneva, Switzerland
May	US National Academy of Sciences Committee on Radio Frequencies (CORF)	Washington, DC, USA
May	ITU-R Task Group TG 5/1	Geneva
May-June	Committee on Radio Astronomy Frequencies (CRAF)	Helsinki, Finland
June	Space Frequency Coordination Group (SFCG)	Mainz, Germany
June	ITU-R Symposium on Satellite Interference	Geneva
October	RFI2016	Socorro, New Mexico, USA
October	WP 7D	Geneva
November	WP 5A, 5B, 5C	Geneva
November	WP 1A, 1B	Geneva

IAU, URSI, and COSPAR, respectively, for calendar year 2016. Expenses were €1876 ($2000) as a sponsor of the RFI2016 meeting in Socorro, New Mexico, during October 2016; €776 in support of IUCAF member attendance at ITU-R TG 5/1 in Geneva in May; and $1347 in support of member attendance at WP 5B and WP 1A in November, the latter to be charged to the balance sheet in 2017.

7. The IUCAF Role Protecting Passive Radio Science Services

IUCAF is the global forum where concerns of passive radio service in all ITU-R Regions are regularly addressed in a comprehensive manner. The group is expert in the underlying science, in the spectrum-management needs of the science, and in the workings of the spectrum-regulatory regime that allocates spectrum and makes the rules for spectrum use. IUCAF is the main contributor to the support of radio astronomy at the ITU-R in Geneva, and it provides the interface between radio astronomy and the space-science community. As such, IUCAF is a unique resource. It has a long record of contributions, the early history of which was recounted in some detail by a former IUCAF Chair: see "Frequency Allocation: The First Forty Years," by Brian Robinson, *Annual Reviews of Astronomy and Astrophysics*, 1999, **37**, pp. 65-96 (behind a pay wall).

8. Contact with ICSU, the Sponsoring Unions, and Other Organizations

IUCAF maintains regular contact with its adhering Unions and with the parent body, ICSU. These organizations play a strong supporting role for IUCAF, the members of which are greatly encouraged thereby. A summary annual report of IUCAF activities was requested by ICSU and completed in September, and thereafter circulated to IUCAF members and to the secretariats of the adhering Unions with the annual IUCAF request for financial support. While in Paris in December, the IUCAF Chair visited the IAU Secretariat at the Institut d'Astrophysique for fruitful discussions with Maria Rosaria D'Antonia and the IAU General Secretary, Piero Benvenuti. The Chair also passed much of a pleasant afternoon at ICSU headquarter in Paris's 16th arrondissement, visiting the Head of Scientific Programmes, Lucilla Spini. The discussions at ICSU led to further coordination between ICSU and a researcher at the University of Witwatersrand, who had discussed potential development of infrastructure for radio astronomy in Africa at RFI2016.

Pursuing its brief, IUCAF maintains strong links with other passive radio-science communities and with space science. One example is the Space Frequency Coordination Group, where IUCAF is an accredited observer and has encouraged coordination to eliminate illumination of radio-astronomy sites by high-power orbiting radars. IUCAF was invited to address the ITU-R's Symposium on Satellite Interference in Geneva in June 2016, where a session on protection of science services was shared between IUCAF and a speaker from the French national space agency, CNES. IUCAF was a sponsor and organizer of the RFI2016 meeting in Socorro, New Mexico, in October. The IUCAF Chair was one of the conveners of a spectrum-management session that was held during the URSI General Assembly in Montreal in August, 2017.

The IUCAF Chair is a member of the American Astronomical Society's Committee on Light Pollution, Radio Interference, and Space Debris, and is a member of the Steering Committee of the IAU Inter-Division Commission C.B4 on Protection of Existing and Potential Observatory Sites. C.B4 has proposed a Focus Meeting at the upcoming IAU General Assembly in Vienna in August 2018. The Immediate Past Chair of IUCAF, Masatoshi Ohishi, is the official liaison between the IAU and the ITU. IUCAF member S. Ananthakrishnan was a Vice President of URSI and a member of RAFCAP that represents the interests of radio astronomy in the Asia-Pacific Region, ITU-R Region 3 (see http://www.atnf.csiro.au/rafcap/). Tasso Tzioumis is the Chair of RAFCAP and Chair of ITU-R Working Party 7D (Radio Astronomy). Wim van Driel is the Chair of CRAF, representing radio astronomy within the CEPT nations (see http://www.astron.nl/craf/).

9. Publications and Reports

IUCAF has a permanent Web address, http://www.iucaf.org/, where the latest updates on the organization's activities are made available. All contributions to IUCAF-sponsored meetings are made available on this Web site.

10. IUCAF'S Concerns

IUCAF interests and activities range from preserving what has been achieved through regulatory measures or mitigation techniques, to looking far into the future of high-frequency use, giant radio-telescope use, and large-scale distributed radio telescopes. IUCAF sees a busy year ahead, during which it will vigorously pursue the full range of its possible activities.

Current priorities for the coming year are largely focused on responding to the many items of concern to radio astronomy on the agenda of the next World Radiocommunication Conference, WRC-19. These include the increasingly intrusive presence of electronics for radar and telecommunication on automobiles, the use of mm-wave spectrum for train control and Wi-Fi, planning for 5G mobile broadband at frequencies up to 86 GHz, and the use of high-altitude platforms (in constant view of radio telescopes) for radio communication.

WRC-19 aside, several new constellations, consisting of thousands of satellites, for global wireless broadband are in various stages of approval, and will require careful coordination. Close monitoring and coordination among radio astronomers will also be required following the launch of a new constellation by Iridium, the operations of which have proven so problematic for radio astronomy over the past 20 years.

Succession planning is also becoming a subject of major concern as the IUCAF membership ages.

11. Acknowledgements

IUCAF is grateful for the organizational and financial support that has been given by ICSU, IAU, URSI, and COSPAR over many years. IUCAF also recognizes the support given by radio-astronomy observatories, universities, and national funding agencies to individual members, allowing them to participate in the work of IUCAF.

Harvey Liszt, Chair
Charlottesville, Virginia, USA
IUCAF website: http://www.iucaf.org
IUCAF contact: iucafchair@iucaf.org

URSI Conference Calendar

September 2017

RADIO 2017
IEEE Radio and Antenna Days of the Indian Ocean
Cape Town, South Africa, 25-28 September 2017
Contact: IEEE RADIO 2017 Conference Secretariat, , Email: radio2017@radiosociety.org, http://www.radiosociety.org/radio2017/index.php

October 2017

ISAP 2017
Phuket, Thailand, 30 October - 2 November
Contact: Dr. Titipong Lertwiriyaprapa, King Mongkut's University of Technology North Bangkok, 1518 Pracharat 1 Rd., Bangsue, Bangkok, Thailand 10800, E-mail: secretary@isap2017.org,http://www.isap2017.org

December 2017

International Workshop on Metamaterials-by-Design: Theory, Methods and Applications to Communications and Sensing
Madrid, Spain, 14-15 December 2017
Contact: Prof. Francisco Medina-Mena, Universidad de Sevilla, Avenida Reina Mercedes s/n, 41012 Sevilla, Spain, E-mail: medina@us.es

January 2018

USNC-URSI National Radio Science Meeting 2018
Boulder, CO, USA , 4-7 January 2018
Contact: Dr. David R. Jackson, Department of ECE, University of Houston, Houston, TX 77204-4005, USA, Fax: 713-743-4444, E-mail: djackson@uh.edu; Logistics: Christina Patarino, E-mail: christina.patarino@colorado.edu, Fax: 303-492-5959, https://nrsmboulder.org/

March 2018

Gi4DM 2018
Kyrenia, Turkish Republic of Northern Cyprus, 14-18 March 2018
Contact: K2 Conference and Event Management Kosuyolu Mh. Ali Nazime Sk. No: 45 Kosuyolu 34718 Kadikoy / Istanbul Phone: +90 (216) 428 95 51 - Fax: +90 (216) 428 95 91 E-mail: gi4dm@k2-events.com, http://www.gi4dm2018.org

May 2018

AT-RASC 2018
Second URSI Atlantic Radio Science Conference
Gran Canaria, Spain, 28 May – 1 June 2018
Contact: Prof. Peter Van Daele, URSI Secretariat, Ghent University – INTEC, Technologiepark-Zwijnaarde 15, B-9052 Gent, Belgium, Fax: +32 9-264 4288, E-mail address: E-mail: peter.vandaele@intec.ugent.be, http://www.at-rasc.com

July 2018

COSPAR 2018
42nd Scientific Assembly of the Committee on Space Research (COSPAR) and Associated Events
Pasadena, CA, USA, 14 - 22 July 2018
Contact: COSPAR Secretariat (cospar@cosparhq.cnes.fr) http://www.cospar-assembly.org

March 2019

C&RS "Smarter World"
18th Research Colloquium on Radio Science and Communications for a Smarter World
Dublin, Ireland, 8-9 March 2019
Contact: Dr. C. Brennan (Organising Cttee Chair) http://www.ursi2016.org/content/meetings/mc/Ireland-2017-CRS Smarter World CFP.pdf

AP-RASC 2019
2019 URSI Asia-Pacific Radio Science Conference
New Delhi, India, 9-15 March 2019
Contact: Prof. Amitava Sen Gupta, E-mail: sengupto53@yahoo.com

May 2019

EMTS 2019
2019 URSI Commission B International Symposium on Electromagnetic Theory
San Diego, CA, USA, 27-31 May 2019
Contact: Prof. Sembiam R. Rengarajan, California State University, Northridge, CA, USA, Fax +1 818 677 7062, E-mail: srengarajan@csun.edu

URSI cannot be held responsible for any errors contained in this list of meetings

Information for Authors

Content

The *Radio Science Bulletin* is published four times per year by the Radio Science Press on behalf of URSI, the International Union of Radio Science. The content of the *Bulletin* falls into three categories: peer-reviewed scientific papers, correspondence items (short technical notes, letters to the editor, reports on meetings, and reviews), and general and administrative information issued by the URSI Secretariat. Scientific papers may be invited (such as papers in the *Reviews of Radio Science* series, from the Commissions of URSI) or contributed. Papers may include original contributions, but should preferably also be of a sufficiently tutorial or review nature to be of interest to a wide range of radio scientists. The *Radio Science Bulletin* is indexed and abstracted by INSPEC.

Scientific papers are subjected to peer review. The content should be original and should not duplicate information or material that has been previously published (if use is made of previously published material, this must be identified to the Editor at the time of submission). Submission of a manuscript constitutes an implicit statement by the author(s) that it has not been submitted, accepted for publication, published, or copyrighted elsewhere, unless stated differently by the author(s) at time of submission. Accepted material will not be returned unless requested by the author(s) at time of submission.

Submissions

Material submitted for publication in the scientific section of the *Bulletin* should be addressed to the Editor, whereas administrative material is handled directly with the Secretariat. Submission in electronic format according to the instructions below is preferred. There are typically no page charges for contributions following the guidelines. No free reprints are provided.

Style and Format

There are no set limits on the length of papers, but they typically range from three to 15 published pages including figures. The official languages of URSI are French and English: contributions in either language are acceptable. No specific style for the manuscript is required as the final layout of the material is done by the URSI Secretariat. Manuscripts should generally be prepared in one column for printing on one side of the paper, with as little use of automatic formatting features of word processors as possible. A complete style guide for the *Reviews of Radio Science* can be downloaded from http://www.ips.gov.au/IPSHosted/NCRS/reviews/. The style instructions in this can be followed for all other *Bulletin* contributions, as well. The name, affiliation, address, telephone and fax numbers, and e-mail address for all authors must be included with

All papers accepted for publication are subject to editing to provide uniformity of style and clarity of language. The publication schedule does not usually permit providing galleys to the author.

Figure captions should be on a separate page in proper style; see the above guide or any issue for examples. All lettering on figures must be of sufficient size to be at least 9 pt in size after reduction to column width. Each illustration should be identified on the back or at the bottom of the sheet with the figure number and name of author(s). If possible, the figures should also be provided in electronic format. TIF is preferred, although other formats are possible as well: please contact the Editor. Electronic versions of figures *must* be of sufficient resolution to permit good quality in print. As a rough guideline, when sized to column width, line art should have a minimum resolution of 300 dpi; color photographs should have a minimum resolution of 150 dpi with a color depth of 24 bits. 72 dpi images intended for the Web are generally *not* acceptable. Contact the Editor for further information.

Electronic Submission

A version of Microsoft *Word* is the preferred format for submissions. Submissions in versions of T_EX can be accepted in some circumstances: please contact the Editor before submitting. *A paper copy of all electronic submissions must be mailed to the Editor, including originals of all figures.* Please do *not* include figures in the same file as the text of a contribution. Electronic files can be send to the Editor in three ways: (1) By sending a floppy diskette or CD-R; (2) By attachment to an e-mail message to the Editor (the maximum size for attachments *after* MIME encoding is about 7 MB); (3) By e-mailing the Editor instructions for downloading the material from an ftp site.

Review Process

The review process usually requires about three months. Authors may be asked to modify the manuscript if it is not accepted in its original form. The elapsed time between receipt of a manuscript and publication is usually less than twelve months.

Copyright

Submission of a contribution to the *Radio Science Bulletin* will be interpreted as assignment and release of copyright and any and all other rights to the Radio Science Press, acting as agent and trustee for URSI. Submission for publication implicitly indicates the author(s) agreement with such assignment, and certification that publication will not violate any other copyrights or other rights associated with the submitted material.

Become An Individual Member of URSI

The URSI Board of Officers is pleased to announce the establishment of Individual Fellowship (FURSI), Individual Membership (MURSI), and Individual Associate Membership (AMURSI). By joining URSI, Individual Associate Members, Individual Members, and Fellows secure recognition with their peers, are better connected to URSI Headquarters, and are better connected to their National Committees. Each can then better provide support to the other. Other benefits include discounted registration fees at URSI conferences (beginning with the 2018 URSI AT RASC) and at some conferences cosponsored by URSI (beginning with some conferences run by IEEE AP-S), a certificate of membership, and e-mail notification of the availability of the electronic edition of the URSI *Radio Science Bulletin*.

Fellowship is by invitation only. Membership and Associate Membership can be applied for through the online forms available at **www.ursi.org/membership.php**, or at **www.ursi.org**